AD-A261 062

REPORT DOCUMENTATION PAGE

Form Approved
OMB No. 0704-0188

2

2. REPORT DATE: 10/12/1992

3. REPORT TYPE AND DATES COVERED: FINAL - 8/15/89 - 8/14/92

4. TITLE AND SUBTITLE

Active Control of NITINOL-Reinforced Structural Composites

5. FUNDING NUMBERS

DAAL03-89-G-0084

6. AUTHOR(S)

A.Baz

DTIC ELECTE FEB 19 1993 S E D

7. PERFORMING ORGANIZATION NAME(S) AND ADDRESS(ES)

The Catholic University of America
Mechanical Engineering Dept.
620 Michigan Ave., NE.
Washington, DC 20064

8. PERFORMING ORGANIZATION REPORT NUMBER

9. SPONSORING/MONITORING AGENCY NAME(S) AND ADDRESS(ES)

U. S. Army Research Office
P. O. Box 12211
Research Triangle Park, NC 27709-2211

10. SPONSORING/MONITORING AGENCY REPORT NUMBER

ARO 27216.6-EG-SM

11. SUPPLEMENTARY NOTES

The view, opinions and/or findings contained in this report are those of the author(s) and should not be construed as an official Department of the Army position, policy, or decision, unless so designated by other documentation.

12a. DISTRIBUTION/AVAILABILITY STATEMENT

Approved for public release; distribution unlimited.

12b. DISTRIBUTION CODE

93-03461

13. ABSTRACT (Maximum 200 words)

The rapidly growing technology of the SHAPE MEMORY NICKEL-TITANIUM ALLOY (NITINOL) is utilized to develop SMART composite materials that are capable of adapting intelligently to internal and external excitations. The NITINOL fibers are embedded into the composite matrix, at optimal locations and orientations, to sense and control the static and dynamic characteristics of the resulting SMART composite. With such built-in self-inspecting and controlling capabilities, the performance of the SMART composite can be optimized and tailored, in real time, to match changes in the operating conditions.

Emphasis has been placed on controlling the static, dynamic and thermal characteristics of anisotropic NITINOL-reinforced beams. Furthermore, the sensing capabilities of the NITINOL fibers are investigated by using them as distributed strain gages to monitor the physical and modal displacements of NITINOL-reinforced composites. Finite element models are developed to predict structural stability and the static, dynamic and thermal behavior of NITINOL-reinforced composite beams. The theoretical predictions of these models are validated experimentally.

14. SUBJECT TERMS	15. NUMBER OF PAGES
	16. PRICE CODE

17. SECURITY CLASSIFICATION OF REPORT	18. SECURITY CLASSIFICATION OF THIS PAGE	19. SECURITY CLASSIFICATION OF ABSTRACT	20. LIMITATION OF ABSTRACT
UNCLASSIFIED	UNCLASSIFIED	UNCLASSIFIED	UL

NSN 7540-01-280-5500

Standard Form 298 (Rev. 2-89)
Prescribed by ANSI Std. Z39-18
298-102

FINAL REPORT

ACTIVE CONTROL OF NITINOL-REINFORCED

STRUCTURAL COMPOSITES

A.Baz

(Grant # DAAL03-89-G-0084)

Composites Engineering, Vol. 2, Nos 5–7, pp. 527–542, 1992.
Printed in Great Britain.

0961-9526/92 $5.00 + .00

THERMO-DYNAMIC CHARACTERISTICS OF NITINOL-REINFORCED COMPOSITE BEAMS

A. BAZ and J. RO

Mechanical Engineering Department, The Catholic University of America, Washington, DC 20064, U.S.A.

(*Received* 6 *March* 1992; *accepted* 20 *March* 1992)

Abstract—The dynamic characteristics of flexible composite beams are controlled by heating sets of shape memory alloy (**NITINOL**) fibers embedded along the neutral axes of these beams. The activation of the shape memory effect of the fibers increases the elastic energy and enhances the stiffness of the composite beams. With such capabilities, the vibration modes of the beams can be tailored and shifted away from the excitation frequency band in order to avoid undesirable vibrations.

Emphasis is placed, in the present study, on the effect of **intentional** electrical heating of a selected subset of the NITINOL fibers on the overall dynamics of the beams. The effect of the associated thermal energy propagating through the composite on the **unintentional** thermal activation of additional subsets of the NITINOL fibers is accounted for. Such an effect is not only significant but also essential to the thorough understanding of the operation of NITINOL-reinforced composites.

Finite element models are developed to describe the interaction between the thermal and dynamic characteristics of the NITINOL composites as well as the interaction between the **intentional** and **unintentional** activation of the NITINOL fibers. The models are experimentally validated and close agreement is obtained between the theoretical predictions and the experimental results. The mathematical models and procedures described in this paper provide an invaluable means of predicting **realistic** performance of NITINOL-reinforced composites.

NOMENCLATURE

$[A]$	interpolating function of beam deflection
$[A_i]$	ith element of $[A]$
A_m	cross-sectional area of the beam
$[B]$	matrix of the first derivatives of the nodal interpolating functions
$[C]$, $[D]$	first and second derivatives of the interpolating function of beam deflection
E_m	Young's modulus of the beam
$[F]$	vector of external loads acting on the beam
h	convective heat transfer coefficient
I_m	area moment of inertia of the beam
k	thermal conductivity of the beam
$[k^e_{1,2,3}]$	matrices given by eqns (16), (17) and (18), respectively
$[K_e]$	stiffness matrix of the beam element
l_y, l_z	direction cosines of outward normals to the beam boundaries
L	length of the beam element and NITINOL fiber
M_i	external moment acting at the ith node
$[M_e]$	mass matrix of the beam element
$m_e(i,j)$	the element i,j of the mass matrix
$[N]$	interpolating function of the beam temperature
N_i	interpolating function of the ith node
p	number of vertices of the element
$P_{m,n,t}$	mechanical, net and thermal axial loads acting on the beam
$[P^e]$	matrix given by eqn (19)
q_n	generalized coordinate of the nth vibration mode of the NITINOL fiber
$\ddot{q}_n$	generalized acceleration of the nth vibration mode of the NITINOL fiber
Q	heat flux per unit area
$S_{1,2}$	boundaries of the NITINOL fibers and the beam, respectively
t	time
T_0	initial tension in a NITINOL fiber
T_t	total tension in a NITINOL fiber
V_i	shear force acting at the ith node
w	transverse deflection of the beam and NITINOL fibers
x, y, z	Cartesian coordinates along the beam neutral axis and cross-section, respectively

Greek letters

α	thermal diffusivity of the beam
$[\delta]$	the deflection vector of the beam element
ϑ_i	angular deflection of the ith node
Θ	temperature at any location (y, z) of the beam cross-section
Θ_a	ambient temperature
$[\Theta^e]$	vector of the nodal temperatures of the element
ϕ_n	mode shape of the nth mode
ω_n	natural frequency of the nth mode.

1. INTRODUCTION

Considerable attention has been devoted recently to the utilization of the Shape Memory NIckel-TItanium alloy (**NITINOL**) in developing **SMART** composites that are capable of adapting intelligently to external disturbances (Ikegami *et al.*, 1990; Rogers *et al.*, 1991; Baz *et al.*, 1990, 1991a, b). Such wide acceptance of NITINOL stems from its unique behavior when it is subjected to particular heating and cooling strategies. For example, the alloy becomes soft when it is cooled below its martensite transformation temperature and becomes about four times stiffer when it is heated above its austenite transformation temperature (Funakubo, 1987). Furthermore, if the alloy is trained to have a particular shape while in its austenite phase, it will memorize this shape. If the alloy is then cooled to its martensite phase and subjected to plastic deformation, it will return to its **memorized** shape when it is heated above the austenite transformation temperature. The phase transformation from martensite to austenite produces significant forces as the alloy recovers its original shape. The alloy acts as an actuator transforming thermal energy into mechanical energy (Perkins, 1975; Duerig *et al.*, 1990). Accordingly, if the NITINOL fibers are embedded inside a composite matrix at optimal locations, they can be used to control the static and dynamic characteristics of the resulting **SMART** composite. The control action is generated by the described stiffening of the NITINOL fibers and/or the shape memory effect. With such built-in control capabilities, the performance of the **SMART** composites can be optimized and tailored to match changes in the operating conditions.

It is therefore the purpose of this study to develop a thorough understanding of the fundamentals governing the operation of NITINOL-reinforced composite beams. The individual contributions of the composite matrix, the NITINOL fibers and the shape memory effect to the overall dynamic performance of the composite beams will be determined. Also, the influence of the temperature distribution inside the composite, which results from the activation of a small subset of the NITINOL fibers, on the overall performance of the entire beam will be addressed both theoretically and experimentally. Such an important interaction between the thermal and dynamic characteristics of the NITINOL-reinforced composites has not been addressed in the previous analyses of Rogers *et al.* (1991) and Jia and Rogers (1989). In these studies, the NITINOL-reinforced composites have been considered to operate isothermally even though the activation and deactivation of the NITINOL fibers subject these composites to non-uniform temperature fields. Furthermore, the effects of **intentional** electrical heating of a selected subset of the NITINOL fibers and the associated thermal energy propagating through the composite on the **unintentional** thermal activation of additional susbsets of the fibers have not been considered by Rogers *et al.* (1991) and Jia and Rogers (1989). These effects significantly alter the dynamics of NITINOL-reinforced composites, particularly those made of multi-lamina where the **intentional** electrical activation of a NITINOL lamina, by an active controller, will generate enough heat to activate thermally and **unintentionally** the adjacent NITONOL laminas. The phenomena associated with **intentional** electrical activation and the associated **unintentional** thermal activation will be addressed, in detail, in the present study.

The present paper is organized in five sections. In Section 1 a brief introduction is given. In Sections 2 and 3 the dynamic and thermal models of the NITINOL-reinforced composites are presented, respectively. The experimental behavior of a single and two-layer NITINOL-reinforced composite is given in Section 4, both in the time and frequency domains. Section 5 summarizes the results and the conclusions of the study.

2. THE DYNAMICS OF NITINOL-REINFORCED COMPOSITE BEAMS

In the present study, the NITINOL-reinforced composites are made by embedding the NITINOL fibers inside vulcanized rubber sleeves placed along the neutral axes of these composite beams, as shown in Fig. 1. In this arrangement, the NITINOL fibers are free to move during the phase transformation process in order to avoid degradation and/or destruction of the shape memory effect which may result when the fibers are completely bonded inside the composite matrix.

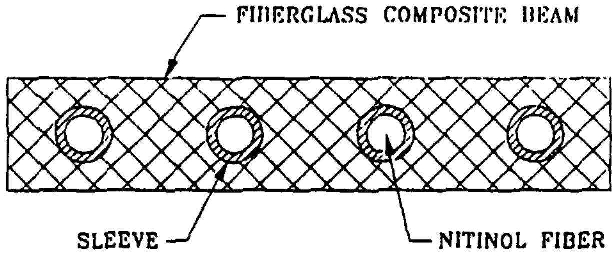

Fig. 1. A schematic drawing of the cross-section of a NITINOL-reinforced composite beam.

The dynamic characteristics of this class of NITINOL-reinforced beams are obtained by dividing each beam into finite elements. The forces typically acting on any of these elements are displayed in Fig. 2 along with the associated nodal displacements. The stiffness and mass matrices of each beam element are derived in Sections 2.1 and 2.2, respectively, using the theory of Bernoulli-Euler beams. The overall stiffness and mass matrices of the entire beam are obtained by assembling the stiffness and mass matrices of the individual elements (Paz, 1991).

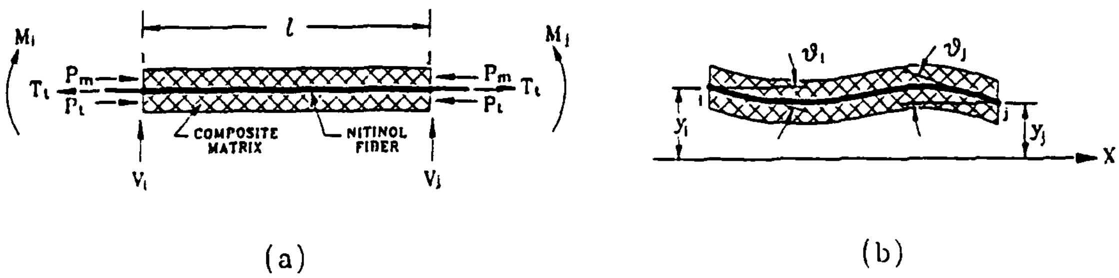

Fig. 2. NITINOL-reinforced beam element with forces and resulting displacements.

2.1. *The stiffness matrix*

The element stiffness $[\mathbf{K}_e]$ is made up of the flexural rigidity of the beam, the geometric stiffness that accounts for the axial and thermal loading as well as the stiffness imparted by the elasticity of the NITINOL fibers. The combined stiffness of the element is obtained using the principle of conservation of energy and equating the work done by external loads to the strain energies stored in the element as follows:

Sum of work done by external loads = Sum of stored strain energies

or

$$\tfrac{1}{2}[\delta]^{\mathrm{T}}[F] + P_m/2\int_0^L (\mathrm{d}w/\mathrm{d}x)^2\,\mathrm{d}x + P_t/2\int_0^L (\mathrm{d}w/\mathrm{d}x)^2\,\mathrm{d}x$$

$$= E_m I_m/2\int_0^L (\mathrm{d}^2w/\mathrm{d}x^2)^2\,\mathrm{d}x + T_t/2\int_0^L (\mathrm{d}w/\mathrm{d}x)^2\,\mathrm{d}x \tag{1}$$

where the terms on the left-hand side denote the work done by the transverse loads and moments, the axial mechanical loads $\mathbf{P}_m$ and axial thermal loads $\mathbf{P}_t$, respectively. The terms on the right-hand side define the strain energy stored by virtue of the flexural rigidity $E_m I_m$ of the beam and the energy stored in the NITINOL fibers due to their transverse deflection $\mathbf{w}$ while under tension $\mathbf{T}_t$, respectively.

In eqn (1), the thermal loads $\mathbf{P}_t$ is generated by changes in the temperature $\Delta\Theta$ of the element caused by changes in the ambient temperature or by the activation and de-activation of the NITINOL fibers. It is given by

$$P_t = \alpha\,\Delta\Theta\,E_m A_m, \tag{2}$$

where α is the thermal expansion coefficient of the composite, E_m is its modulus of elasticity, and A_m is the cross-sectional area of the beam.

Equation (1) reduces to

$$[\delta]^{\mathrm{T}}[F] = E_m I_m \int_0^L (\mathrm{d}^2 w/\mathrm{d}x^2)^2\,\mathrm{d}x - P_n \int_0^L (\mathrm{d}w/\mathrm{d}x)^2\,\mathrm{d}x, \tag{3}$$

where $\mathbf{P}_n$ is the net axial force given by

$$P_n = (P_m + P_t - T_t). \tag{4}$$

Defining a proper displacement function for the composite beam element, one can write the deflection $\mathbf{w}$ as

$$w = [A][\delta], \tag{5}$$

where the elements of matrix $[A]$ are a function of $\mathbf{x}$ (Fenner, 1975).

Accordingly, $\mathrm{d}w/\mathrm{d}x$ and $\mathrm{d}^2w/\mathrm{d}x^2$ can be obtained by differentiating eqn (5) with respect to x to yield

$$\mathrm{d}w/\mathrm{d}x = [C][\delta] \qquad \text{and} \qquad \mathrm{d}^2w/\mathrm{d}x^2 = [D][\delta]. \tag{6}$$

If the stiffness matrix $[K_e]$ of the element is defined by the following relationship

$$[F] = [K_e][\delta], \tag{7}$$

then $[K_e]$ can be determined by combining eqns (3), (6) and (7) as follows:

$$[K_e] = E_m I_m \int_0^L [D]^{\mathrm{T}}[D]\,\mathrm{d}x - P_n \int_0^L [C]^{\mathrm{T}}[C]\,\mathrm{d}x. \tag{8}$$

The element stiffness matrix $[K_e]$, given by eqn (8), consists of two components: the conventional transverse stiffness and the geometric stiffness that combines the effect of the axial mechanical loads, axial thermal loads and the tension of the NITINOL reinforcing fibers. Equation (8) also represents the basic equation for understanding the role that the NITINOL fibers can play in controlling the stiffness of the composite beam. For example, if the initial fiber tension $\mathbf{T}_0$, resulting from the pre-strain alone, is high enough to counter-balance the mechanical and thermal effects (i.e. $P_n = 0$), then the beam stiffness can be maintained unchanged. For higher pre-strain levels, the beam stiffness can be enhanced. Further enhancement can be achieved when the shape memory effect of the NITINOL fibers is activated by heating the fibers above their phase transformation temperature. The additional tension, induced into the fibers by the phase recovery forces, makes the net axial load P_n negative and accordingly increases the overall stiffness of the beam. However, it is essential that the total tension in the NITINOL fibers, i.e. the sum of the tension due to the pre-strain and the phase recovery force, must exceed the mechanical and thermal loads and compensate for the softening effect in the matrix resulting from heating the NITINOL fibers inside the composite matrix.

2.2. *The mass matrix*

The element $\mathbf{m}_e(i,j)$ of the mass matrix $[\mathbf{M}_e]$ of the beam element is obtained using the consistent mass formulation (Zienkiewicz and Taylor, 1989) as follows:

$$m_e(i,j) = \rho_m A_m \int_0^L A_i A_j\,\mathrm{d}x \tag{9}$$

where A_i and A_j are the ith and jth elements of the vector A given by eqn (5). Also in eqn (9), ρ_m denotes the density of the composite beam.

The classical finite element approach is used to form the equations of motion of the assembly of several beam elements along with the appropriate boundary conditions. The solution of the eigenvalues of the resulting homogeneous equations gives the natural frequencies of the composite beam as influenced by the properties of the matrix and the NITINOL fibers. It is important to note that these properties are influenced by the temperature distribution inside the beam which is developed by virtue of activating and de-activating the NITINOL fibers. A study of the temperature distribution inside NITINOL-reinforced beams is presented in Section 3.

The analysis presented here is for an orthotropic laminate that has a single layer of unidirectional NITINOL fibers. Such an analysis can be used along with the classical laminate theory to assemble the stiffness matrix for a multi-laminate composite beam. A similar approach is carried out for modeling the static and dynamic characteristics of NITINOL-reinforced composite plates (Ro, 1992).

3. THERMAL CHARACTERISTICS OF NITINOL-REINFORCED COMPOSITE BEAMS

The thermal characteristics of NITINOL-reinforced composite beams are influenced primarily by the temperature distribution inside the composite. A thermal finite element model is developed to determine steady-state and transient temperature distributions resulting from different activation strategies of the NITINOL fibers. The theoretical predictions are compared with experimental measurements in order to validate the thermal model.

It is important here to note that although the finite element model used in predicting the beam dynamics is a one-dimensional model, with the single dimension taken along the beam neutral axis, the thermal model is considered to be two-dimensional model to predict the temperature distribution over the beam cross-section. Such a distinction is made because the temperature distribution, along the beam neutral axis, is assumed to be uniform. This assumption is confirmed experimentally and is attributed to the fact that the NITINOL fibers are oriented parallel to the neutral axis (Baz *et al.*, 1992). The beam temperature, however, varies only over the cross-section and its magnitude depends on the number and location of the activated or de-activated NITINOL fibers. The resulting temperature distribution can be used to compute an average modulus of elasticity of the composite. The average temperature rise above ambient can also be used to compute the axial thermal loading on the beam $\mathbf{P}_t$ which results from fixing the two ends of the beam.

The two-dimensional thermal modeling of the beam is favored over a one-dimensional lumped-parameter approach because it provides a more accurate simulation of the thermal state of the beam.

THE THERMAL FINITE ELEMENT MODEL

The energy balance equation that governs the heat transfer across the beam can be written, in a two-dimensional Cartesian coordinate system, as follows

$$\frac{\partial^2\Theta}{\partial y^2} + \frac{\partial^2\Theta}{\partial z^2} + \frac{\dot{Q}}{k} = \frac{1}{\alpha}\frac{\partial\Theta}{\partial t} \tag{10}$$

where Θ is the beam temperature at time t and location (y, z) as defined in Fig. 3. In eqn (10), $\dot{Q}$ defines the rate of heat generated per unit area during the activation of the NITINOL fibers. Also, k denotes the conductivity of the beam and α its thermal diffusivity.

The above equation is subject to the following boundary and initial conditions

$$k\left[\frac{\partial\Theta}{\partial y}l_y + \frac{\partial\Theta}{\partial z}l_z\right] + Q = 0 \qquad \text{on boundary } S_1, \tag{11}$$

$$k\left[\frac{\partial\Theta}{\partial y}l_y + \frac{\partial\Theta}{\partial z}l_z\right] + h(\Theta - \Theta_a) = 0 \qquad \text{on boundary } S_2, \tag{12}$$

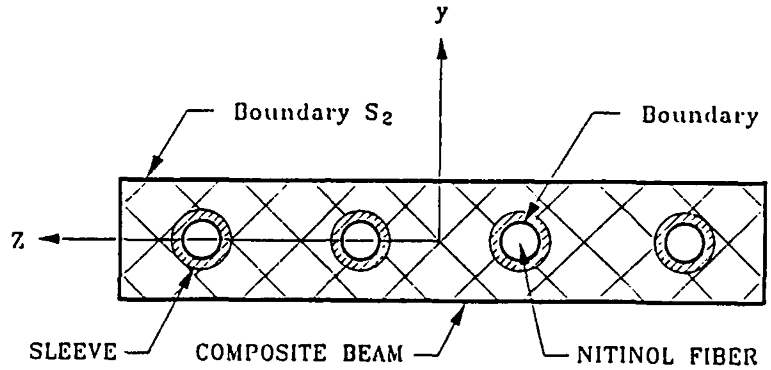

Fig. 3. Schematic drawing of the beam cross-section with heat transfer boundaries.

and

$$\Theta(y, z, t = 0) = \Theta_0(y, z) \qquad \text{on the beam cross section.} \tag{13}$$

Equation (11) defines the condition at the NITINOL fiber circular boundary S_1 on which the heat flux **Q** is specified, and eqn (12) specifies the conditions at the beam outer boundary S_2 where the interaction with the ambient temperature Θ_a is through convective heat transfer with coefficient **h**. The boundaries S_1 and S_2 are defined in Fig. 3. In eqns (11) and (12), l_y and l_z denote the direction cosines of the outward normals to the boundaries. Equation (13) describes the initial temperature distribution over the beam cross-section at time $t = 0$.

Assuming a linear interpolating function $[N]$ with triangular elements that have isotropic thermal properties, then the temperature Θ at any **y**, **z** and **t** can be expressed in terms of the nodal temperatures $[\Theta^e]$ as follows

$$\Theta = [N][\Theta^e]. \tag{14}$$

Using the Galerkin method along with the assumed interpolating functions, one can write the following finite element equation (Rao, 1988)

$$[k_1^e][\dot{\Theta}^e] + ([k_2^e] + [k_3^e])[\Theta^e] = [P^e], \tag{15}$$

where

$$[k_1^e] = \int_{A^e}\!\!\int k/\alpha[N]^T[N]\,\mathrm{d}A, \tag{16}$$

$$[k_2^e] = \int_{S_2^e} h[N]^T[N]\,\mathrm{d}S_2, \tag{17}$$

$$[k_3^e] = \int_{A^e}\!\!\int k[B]^T[B]\,\mathrm{d}A, \tag{18}$$

and

$$[P^e] = \int_{A^e}\!\!\int \dot{Q}[N]^T\,\mathrm{d}A - \int_{S_1^e} Q[N]^T\,\mathrm{d}S_1 + \int_{S_2^e} h\Theta_a[N]^T\,\mathrm{d}S_2 \tag{19}$$

with

$$[B] = \begin{bmatrix} \partial N_1/\partial y & \partial N_2/\partial y & \dots & \partial N_p/\partial y \\ \partial N_1/\partial z & \partial N_2/\partial z & \dots & \partial N_p/\partial z \end{bmatrix} \tag{20}$$

where subscript **p** is the number of vertices of the element ($p = 3$ for a triangular element).

The individual element equations are assembled to form the overall equation of the NITINOL-composite beam which can be solved for the nodal temperatures. The solution is based on a Crank-Nicolson trapezoidal scheme (Hughes, 1977).

The thermal finite element model developed in Section 3 is used to generate the temperature distribution over the beam cross-section which in turn is utilized to compute the average properties of the beam, as for example its modulus of elasticity, under different operating conditions. The theoretical predictions of the thermal characteristics will be compared with experimental measurements, obtained in Section 4, in order to check the validity of the thermal model.

4. EXPERIMENTAL CHARACTERISTICS OF A NITINOL-REINFORCED BEAM

4.1. *Experimental set-up, materials and methods*

The characteristics of NITINOL-reinforced beams are computed using the developed dynamic and thermal models. The theoretical predictions are experimentally validated using a composite beam made of randomly oriented glass fibers embedded in a low cure temperature polyester resin. The beam is 30 cm long, 2.5 cm wide and 0.156 cm thick mounted in a clamped–clamped arrangement. The temperature dependence of the modulus of elasticity of the beam, shown in Fig. 4, is obtained experimentally using the **D**ynamic, **M**echanical, and **T**hermal **A**nalyzer **(DMTA)** of Polymer Laboratories Ltd (1990).

Four NITINOL 55 fibers, that are 0.55 mm in diameter, are embedded inside the beam through vulcanized rubber sleeves that have an outer diameter of 0.95 mm. The NITINOL fibers used have an austenite transformation temperature of about 50°C. The performance of the composite beam is monitored when different subsets of the NITINOL fibers are **intentionally** activated by a controlled electrical current. Monitored also is the **unintentional** activation of the remaining NITINOL fibers which results from the thermal energy propagating from the electrically activated fibers. The effect of such an **unintentional** activation on the overall performance of the NITINOL-reinforced beam is determined, in detail, for different **intentional** activation strategies.

The experimental set-up used in measuring the interaction between the **intentional** electrical and **unintentional** thermal activation of the NITINOL fibers is shown in Fig. 5. In the figure, the beam is clamped in a fixed-fixed arrangement and the NITINOL fibers are divided into two sets which are separately clamped. The first set is electrically activated whereas the second set is activated by the **unintentional** thermal energy propagating from the first set through the composite beam. In the arrangement shown in Fig. 5, the first set includes fibers number 1, 2 and 4 while the second set is made only of fiber number 3. The phase recovery forces developed by each set of fibers are separately measured using two separate load cells.

The time history of the phase recovery forces developed by each set of fibers is sampled by a computer when the first set is subject to a step electrical current. The corresponding time histories of the temperatures generated in the NITINOL fibers and the composite beam are also monitored by the computer. When steady-state conditions are attained the modes of vibration of the beam are measured using a modally tuned impact hammer (Ewins, 1984).

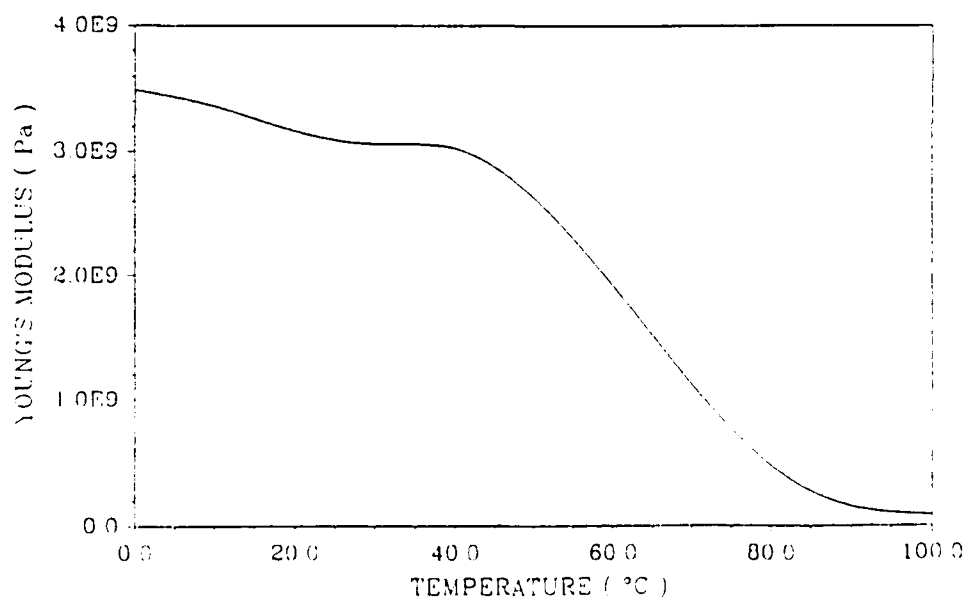

Fig. 4. Effect of operating temperature on modulus of elasticity of the test fiberglass composite beam.

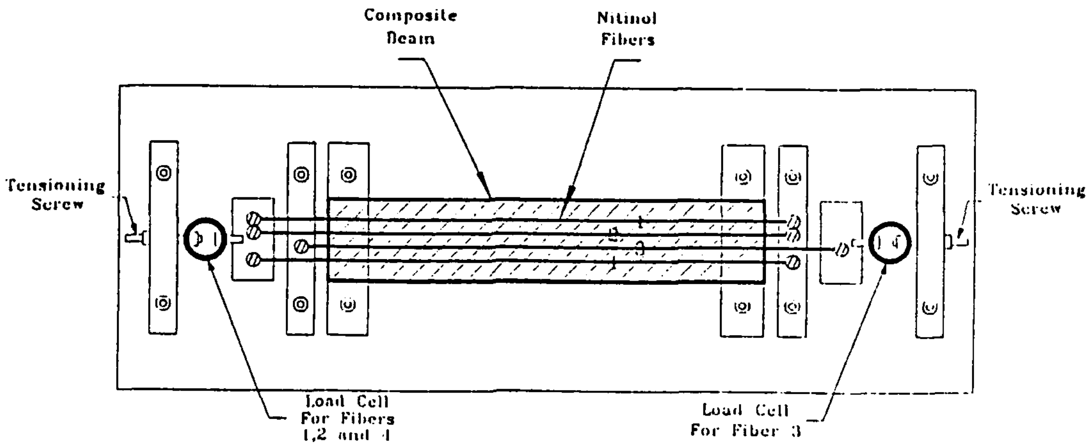

Fig. 5. Experimental set-up used in monitoring the performance of NITINOL-reinforced beams.

4.2. *Experimental results*

A. *Electrical activation of three fibers*

A.1. *Phase recovery forces*

Figures 6a and 6b show the time response of the phase recovery forces developed by the **intentional** electrical activation of fibers 1, 2 and 4, and the **unintentional** thermal activation of fiber 3, respectively. In the displayed characteristics, all the NITINOL fibers are initially pre-tensioned to 26.6 N per fiber and the electrically activated fibers are subjected to a step electric heating of 5.4 W per fiber. Figure 6a shows that the phase recovery forces of the electrically activated fibers quickly rise to their peak value of 66 N per fiber. On the other hand, Fig. 6b indicates that fiber number 3, which is not **intentionally** activated by the electrical current, experiences a delay of about 100 s before its starts developing its phase recovery forces. This time delay is the time needed for the thermal energy propagating from the electrically activated fibers to reach and heat fiber 3 above its phase transformation temperature. Following this time delay, the phase recovery force builds up relatively slowly to a peak value of 50.4 N which is a very large force that cannot be neglected. The slow rise to the peak force is attributed primarily to the thermal capacitance of the composite beam and to the heat lost to the surroundings across the beam surfaces. Hence, the resulting **unintentional** thermal activation of the NITINOL fiber number 3 changes the total tensile force $\mathbf{T}_t$ of the reinforcing fibers and the total elastic energy of the beam. These changes are rather complex and mainly depend on the temperature distribution inside the composite beam. In addition, such changes are significant and must be accounted for as they alter the stiffness and the dynamics of the entire beam, as will be shown in what follows.

A.2. *Modes of vibration*

The effect of different activation strategies on the first threee modes of vibration of the NITINOL-reinforced composite beam is shown in Figs 7a and 7b when the initial tension is 26.6 N per fiber. These results are obtained after steady-state temperatures and forces are attained. Comparisons are also given with the modes of the beam with unactivated fibers. For instance, when fibers 1, 2 and 4 are electrically activated while fiber 3 is thermally activated, the first three modes of vibration are found to be 94.9, 192.5 and 318.7 Hz, respectively. This is in comparison to 87.9, 184.92 and 315.0 Hz when all the fibers are unactivated. The increase in the three modes of vibration, of 7.9%, 4.1% and 1.15%, respectively, is attributed to the increase in the fiber's tension developed by both the **intentional** electrical and the **unintentional** thermal activation of these fibers. In order to isolate the two effects, fiber 3 is replaced by another NITINOL fiber which has a very high phase transformation temperature of 100°C. In this manner the thermal energy propagating through the beam will not result in a high enough temperature to

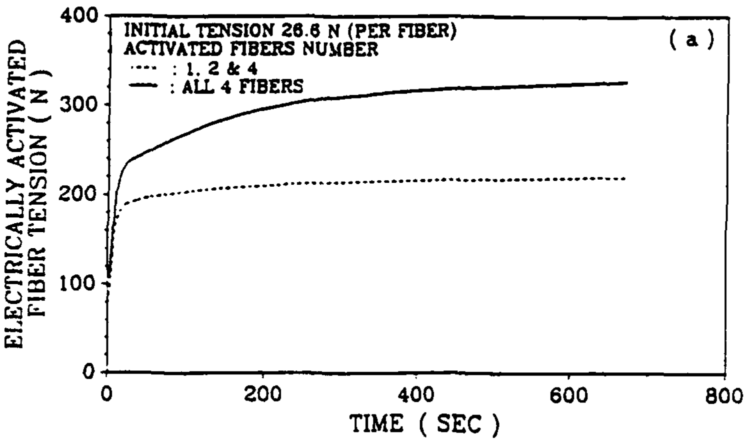

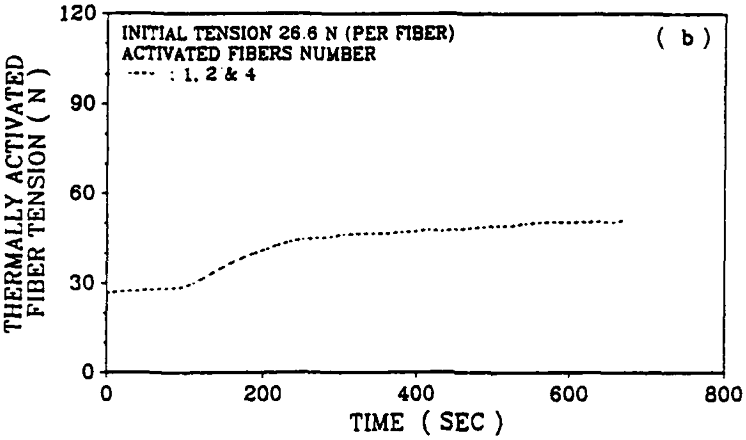

Fig. 6. Time history of the recovery forces with three activated NITINOL fibers. (a) Electrically activated, (b) thermally activated.

induce the thermal activation of fiber 3. Accordingly, the initial tension applied to fiber 3 will remain unchanged at 26.6 N even after the electrical activation of fibers 1, 2 and 4. This is not the case with the original low phase transformation temperature fiber where the tension increased from 26.6 to 50.4 N following the electrical activation of fibers 1, 2 and 4. In this way the effect of **unintentional** thermal activation on the beam dynamics can be isolated and quantified.

The modes of vibration measured with the high phase transformation temperature fiber are 92.3, 182.5 and 291.3 Hz. This corresponds to an increase of 5.02%, −0.53% and −7.5% as compared to the modes of vibration with unactivated fibers. Accordingly, the thermal activation accounts for about 36.4%, 113% and 752% of the total increase in the normal modes. Such percentages are very significant and cannot be neglected. For the sake of completion, the effect of activating all the four fibers electrically on the natural frequencies of the beam is shown in Fig. 7b along with the frequencies obtained with all fibers unactivated.

A.3. *Temperature distribution*

In order to develop a thorough understanding of the effect of **unintentional** thermal activation, it is necessary to consider the temperature distribution over the cross-section of the composite beam shown in Fig. 8a. Figure 8b shows the theoretical temperature distribution when fibers 1, 2 and 4 are electrically activated, and Fig. 8c shows the corresponding distribution when all the four fibers are electrically energized. The distributions displayed represent the steady-state distributions obtained by the thermal finite element model after 700 s from the initiation of the step heating of the NITINOL fibers. It is evident from Figs 8b and 8d that the electrical activation of fibers 1, 2 and 4 generates temperatures around fiber 3 in excess of its phase transformation temperature.

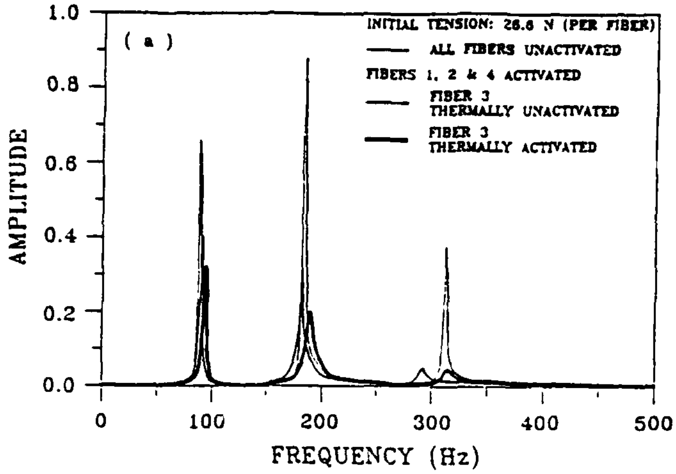

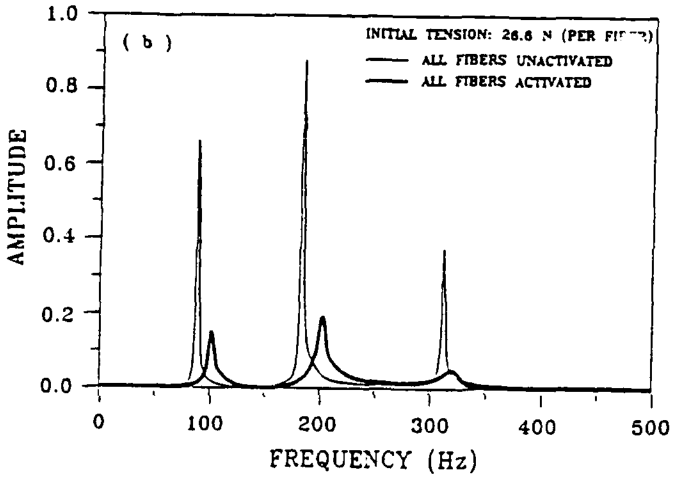

Fig. 7. Natural frequencies of NITINOL-reinforced beam. (a) Three activated fibers, (b) four activated fibers.

Under such conditions, the phase transformation is induced thermally and fiber 3 starts developing its phase recovery force. The extent of completion of the phase transformation process and the magnitude of the force developed depend on how high the beam temperature becomes in relation to the phase transformation temperature.

Figure 8d shows also that the rise of the beam temperature, near fiber 3, is rather slow because of the thermal capacitance of the beam and also because of the heat losses to the environment across its surfaces. Accordingly, there is a time period before the beam temperature rises to the phase transformation temperature and before fiber 3 starts generating its phase recovery force. During that period of time and until steady-state conditions are attained, the dynamics of the beam will be continuously varying. Predictions of such behavior are only possible through the interaction between the thermal and dynamic finite element models.

Comparison between the theoretical and the experimental temperatures of the activated NITINOL fiber and the beam surface are shown in Figs 8d and 8e when three and four fibers are electrically activated, respectively. It is evident that theoretical predictions are in close agreement with the experimental results.

B. *Electrical activation of two fibers*

B.1. *Phase recovery forces*

The effect of electrically activating two NITINOL fibers (1 and 2, 1 and 4, or 2 and 4) on the phase recovery forces developed by the thermal activation of the remaining two fibers is shown in Fig. 9. Figure 9a shows the forces developed by the electrically

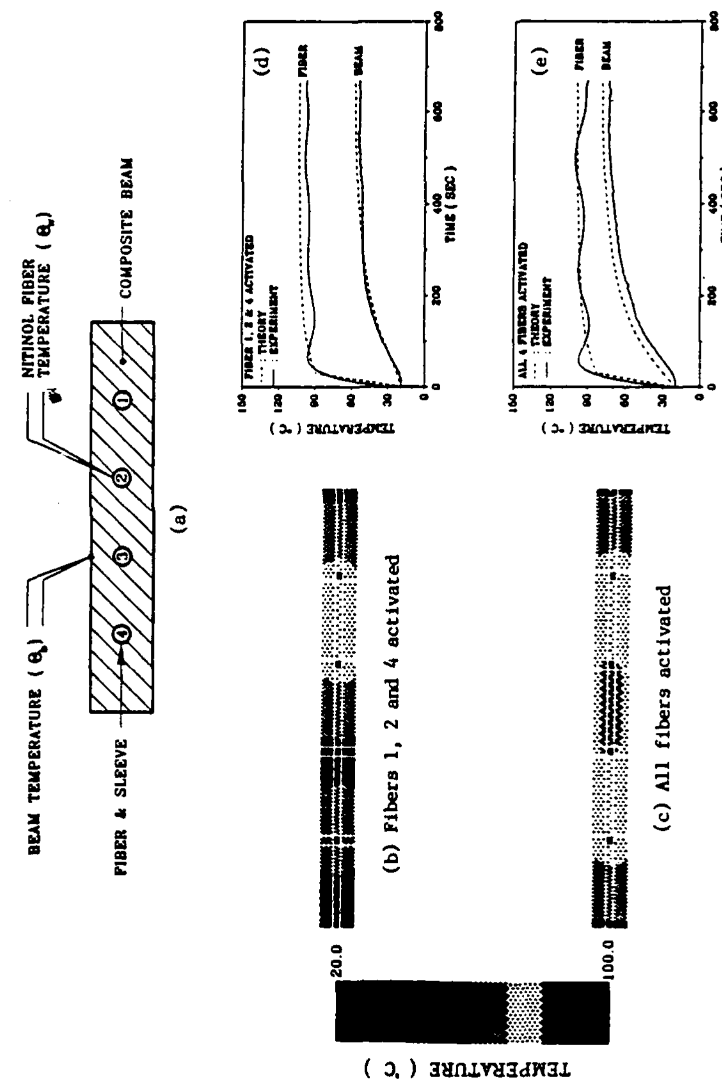

Fig. 8. Temperature distribution over the beam cross-section with three and four activated fibers.

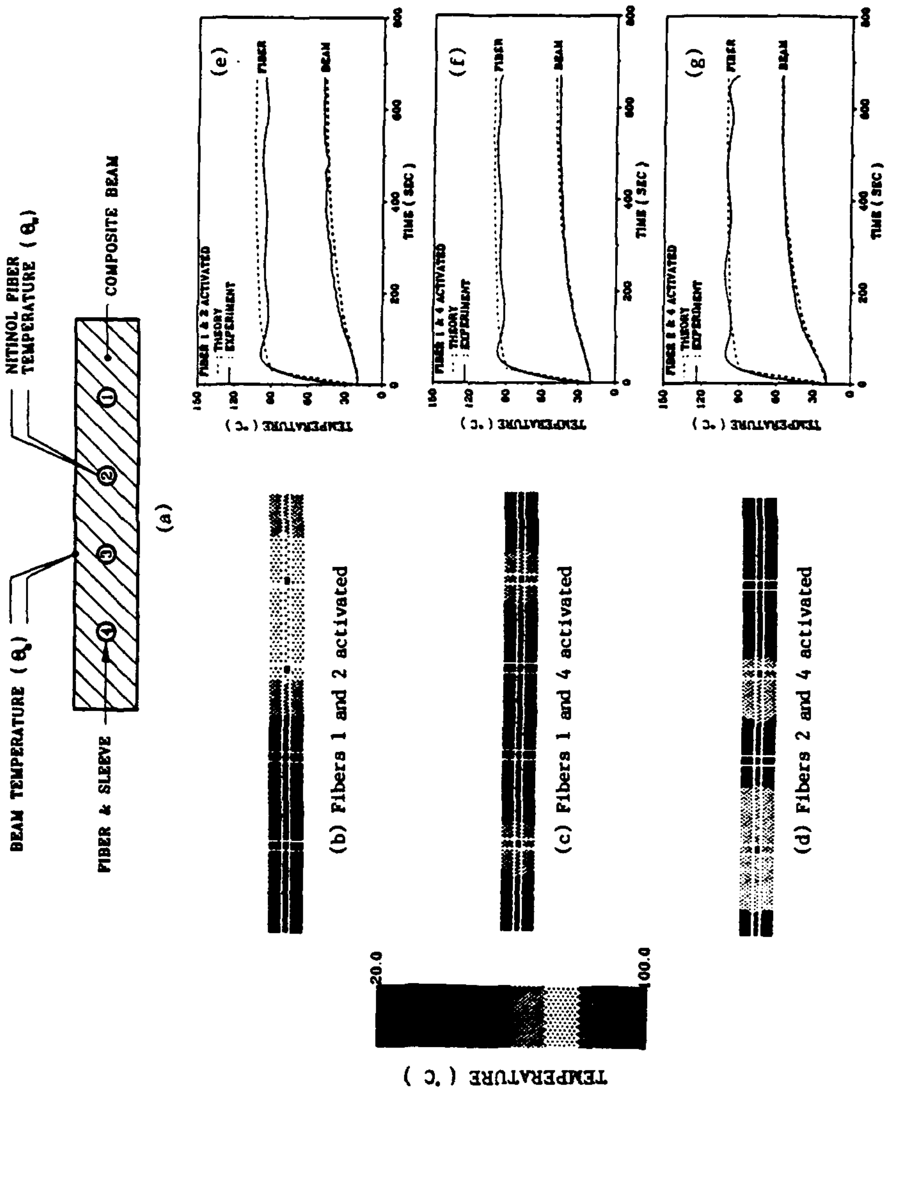

Fig. 11. Temperature distribution over the beam cross-section with two activated fibers.

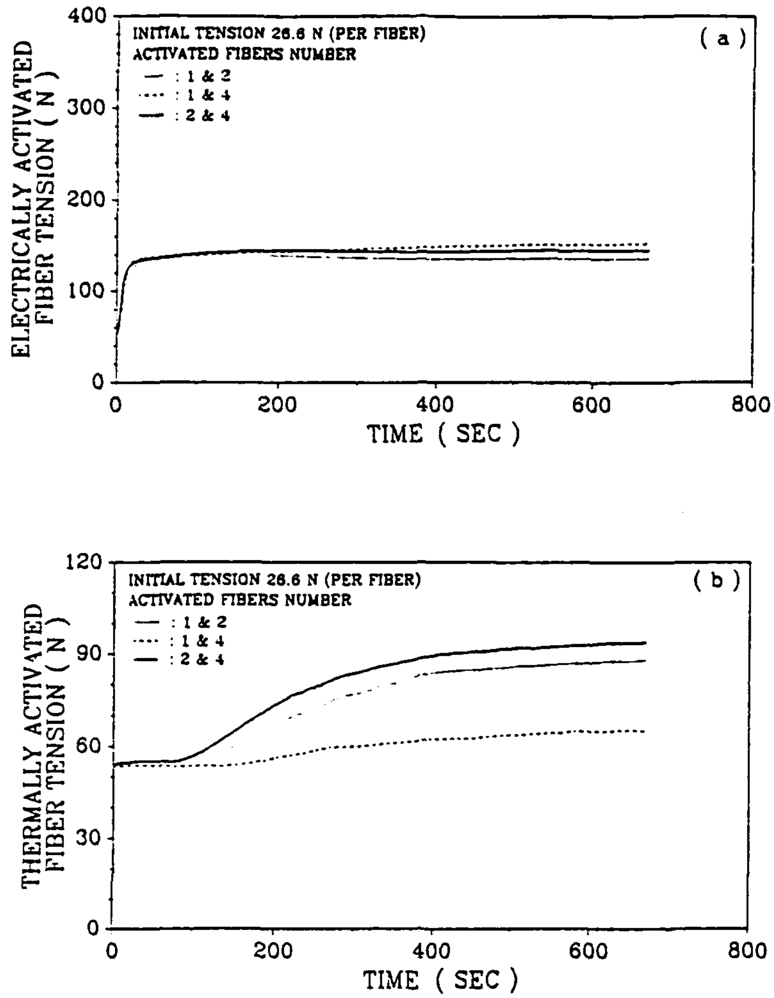

Fig. 9. Time history of the recovery forces with two activated NITINOL fibers.
(a) Electrically activated, (b) thermally activated.

activated fibers and Fig. 9b shows the corresponding forces developed by the remaining thermally activated fibers. The magnitude of the forces developed by the electrically activated fibers is exactly the same, irrespective of their location. However, the magnitude of forces generated by the thermally activated fibers depends on their location, inside the beam, relative to the location of the electrically activated fibers. The least forces are developed when the electrically activated fibers are located near the edges of the beam (fibers 1 and 4) where most of their generated thermal energy will be lost to the surrounding. The remaining portion of the thermal energy will propagate inside the beam to thermally activate the remaining two fibers (2 and 4). Higher forces are developed when the electrically activated fibers (1 and 2, or 2 and 4) are located away from the beam edges. For instance, when fibers 2 and 4 are electrically activated they produce a total force of about 132 N while the thermally activated fibers (1 and 3) develop a total force of about 95 N. Definitely, the magnitude of such **unintentionally** generated forces cannot be neglected.

It is again evident that the interaction between the electrical and thermal activations plays a very important role in determining the total tension developed by the NITINOL reinforcement which in turn determines the dynamic behavior of the entire composite beam.

B.2. *Modes of vibration*

The effect of diferent electrical activation strategies of two fibers on the modes of vibration of the beam is shown in Fig. 10 and the results are summarized in Table 1. These results are obtained after steady-state temperatures and forces are attained.

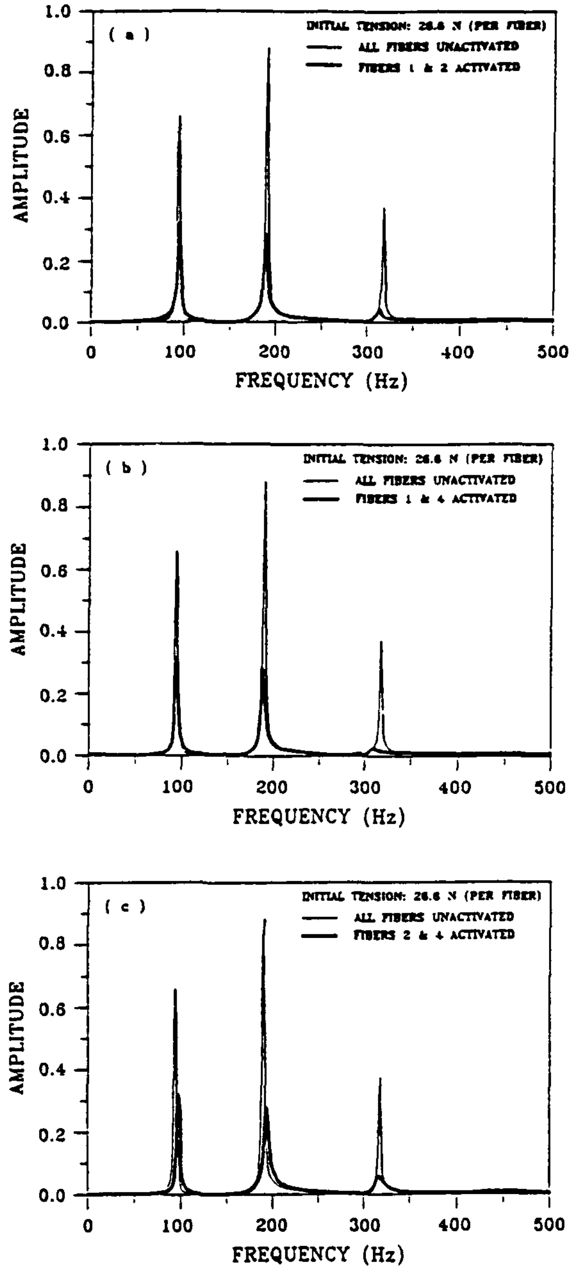

Fig. 10. Natural frequencies of a NITINOL-reinforced beam with two activated fibers. (a) Fibers 1 and 2, (b) fibers 1 and 4, and (c) fibers 2 and 4.

Table 1 and Fig. 10 indicate that the dynamic performance of the composite beam, is significantly influenced by the different electrical activation strategies. This is in spite of the fact that two fibers are always activated in all these strategies. The studies of Rogers *et al.* (1991) and Jia and Rogers (1989) predict that the beam performance remains the same for all the cases considered.

Table 1. Effect of activation strategy of two fibers on the modes of vibration of the beam

Number of fibers activated	Modes of vibration (Hz)		
	First	Second	Third
None	87.9	184.9	315.0
All	100.1	202.5	323.7
1 and 4	88.4	182.5	305.0
1 and 2	88.8	183.8	307.4
2 and 4	93.5	190.1	315.0

Furthermore, it is interesting to note that when the effect of the **unintentional** thermal activation is negligible, as when fibers 1 and 4 are electrically activated, the beam becomes less stiff than a beam with unactivated fibers. This is clearly manifested by the drop in the frequencies of the second and third modes of vibration. Such a drop is attributed to the fact that the phase recovery forces generated by fibers 1 and 4 are not high enough to compensate for the softening effect of the matrix modulus due to the heating of the fibers. However, when the **unintentional** thermal activation effect becomes significant, as when fibers 2 and 4 are electrically activated, the beam performance is considerably enhanced. This is evident from the significant increase in the natural frequencies of the beam. The improved performance is due to the additional recovery forces developed by the **unintentional** thermal activation of fibers 1 and 3.

B.3. *Temperature distribution*

The interaction between the thermal and dynamic behavior of the beam can best be understood by considering the temperature distributions across the cross-section of the NITINOL-reinforced beam for different activation strategies. Figure 11 displays such temperature distributions along with comparisons between the theoretical and experimental temperatures of the activated NITINOL fibers and the beam surface. Close agreement between the theoretical and experimental results is evident.

4.3. *Further comparisons between theory and experiments*

Figure 12 shows comparison between the theoretical and the experimental natural frequencies of the beam for different activation strategies and different initial fiber tensions. The effect of interaction between the electrical and thermal activation of the NITINOL fibers is taken into consideration in these results. Close agreement is also evident between the theoretical predictions and experimental measurements.

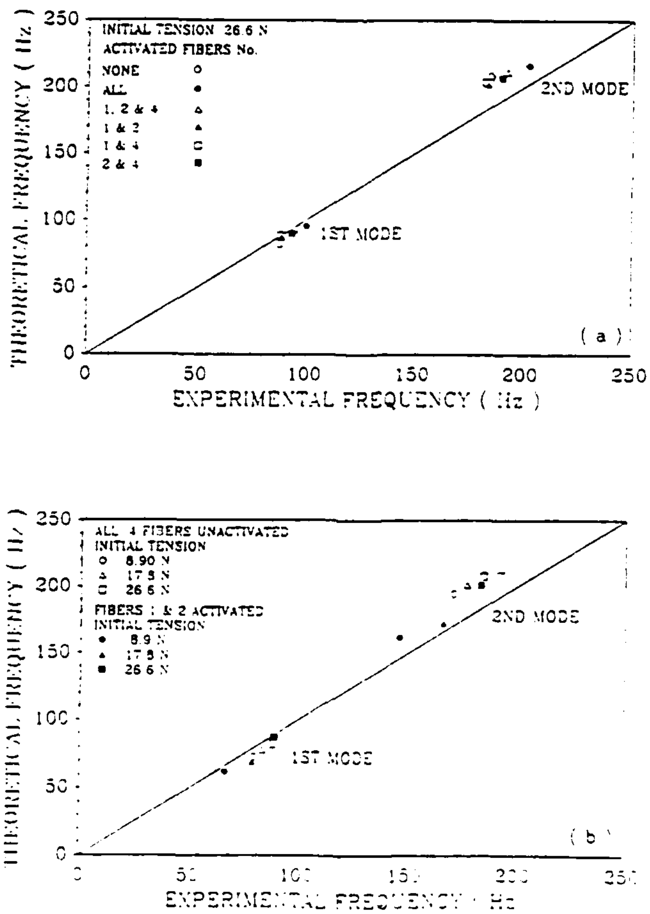

Fig. 12. Comparisons between theoretical and experimental natural frequencies of the beam. (a) Different activation, (b) different initial tension.

5. CONCLUSIONS

The dynamic and thermal characteristics of NITINOL-reinforced composite beams have been presented. The fundamental issues governing the behavior of this new class of **SMART** composites have been introduced. Particular emphasis has been placed on the interaction between the **intentional** electrical activation of subsets of the NITINOL fibers, by an active controller, and the associated **unintentional** activation of neighboring NITINOL fibers. It is shown that such an interaction plays a significant role in determining the dynamic behavior of the entire composite beam. Furthermore, such interaction cannot be neglected as in the previous studies of Rogers *et al.* (1991) and Jia and Rogers (1989).

It is also shown that the dynamic and thermal models developed in this study enable the accurate prediction of the behavior of NITINOL-reinforced composite beams. With such models it would be possible to design NITINOL-reinforced composites that have continuously tunable structural characteristics to adapt to changes in the operating conditions. These features will be particularly useful in many critical structures that are intended to operate autonomously for long durations in isolated environments such as defense vehicles, space structures and satellites.

Acknowledgements—This work is funded by a grant from the U.S. Army Research Office (Grant number DAAL03-89-G-0084). Special thanks are due to Dr Gary Anderson, the technical monitor and Chief of the Structures and Dynamics Branch of ARO, for his invaluable and continuous technical inputs.

REFERENCES

Bathe, K. J. and Wilson, E. L. (1976). *Numerical Methods in Finite Element Analysis*. Prentice-Hall, Englewood Cliffs, New Jersey.

Baz, A., Iman, K. and McCoy, J. (1990). Active control of flexible beams using shape memory actuators. *J. Sound Vibr.* **140**(3), 437–456.

Baz, A., Poh, S. and Gilheany, J. (1990). A multi-mode distributed sensor for vibrating beams. ASME Winter Annual Meeting, Atlanta, GA, Dec. 1991.

Baz, A., Poh, S., Ro, S., Mutua, M. and Gilheany, J. (1992). Active control of NITINOL-reinforced composite beams. In *Intelligent Structural Systems* (Edited by H. S. Tzou and G. Anderson). Kluwer, The Netherlands.

Baz, A., Ro, J., Mutua, M. and Gilheany, J. (1991b). Active control of buckling of NITINOL-reinforced composite beams. In *Active Materials and Adaptive Structures Conf.*, Arlington, VA. November 1991.

Baz, A. and Tampe, L. (1989). Active control of buckling of flexible beams. In *Proc. ASME Design Technical Conf.*, Montreal, Canada, Vol. 1. DE-16, pp. 211–218, Sept. 1989.

Duerig, T. W., Melton, K. N., Stockel, D. and Wayman, C. (1990). *Engineering Aspects of Shape Memory Alloys*. Butterworth Heineman, London.

Ewins, D. J. (1984). *Modal Testing: Theory and Practice*. Research Studies Press, Letchworth, U.K.

Fenner, R. T. (1975). *Finite Element Methods for Engineers*. Macmillan, London.

Funakubo, H. (1987). *Shape Memory Alloys*. Gordon and Breach, New York.

Hughes, T. J. (1977). Unconditionally stable algorithm for nonlinear heat conduction. In *Computer Methods in Applied Mechanics and Engineering*, Vol. 10, pp. 135–139.

Ikegami, R., Wilson, D. and Laakso, J. (1990). Advanced composites with embedded sensors and actuators (ACESA). Edwards AFB Technical Report No. AL-TR-90-022 (FO4611-88-C-0053).

Jia, J. and Rogers, C. (1989). Formulation of a laminated shell theory incorporating embedded distributed actuators. In *Proc. ASME Winter Annual Meeting* (*Adaptive Structures*—AD Vol. 15), pp. 25–34. ASME, New York.

Paz, M. (1991). *Structural Dynamics: Theory and Computations*. Van Nostrand Reinhold, Australia.

Perkins, J. (1975). *Shape Memory Effect in Alloys*. Plenum Press, New York.

Polymer Laboratories, Ltd. (1990). PL-DMTA, MKII Dynamic Mechanical Thermal Analyser. Loughborough, U.K.

Rao, S. S. (1988). *The Finite Element Method in Engineering*, Second Edn. Pergamon Press, Oxford.

Rogers, C., Liang, C. and Jia, J. (1991). Structural modification of simply-supported laminated plates using embedded shape memory alloy fibers. *Compt. Struct.* **38**(5/6), 569–580.

Zienkiewicz, O. C. and Taylor, R. L. (1989). *The Finite Element Method*, Vol. 1, Fourth Edn. McGraw-Hill, New York.

Intelligent Structural Systems

edited by

H. S. TZOU

Department of Mechanical Engineering,
University of Kentucky,
Lexington, U.S.A.

and

G. L. ANDERSON

Engineering Science Division,
U.S. Army Research Office,
North Carolina, U.S.A.

KLUWER ACADEMIC PUBLISHERS

DORDRECHT / BOSTON / LONDON

ACTIVE CONTROL OF NITINOL-REINFORCED COMPOSITE BEAM

A. BAZ, S. POH, J. RO, M. MUTUA and J. GILHEANY
Department of Mechanical Engineering
The Catholic University of America
Washington, DC 20064

1. INTRODUCTION

Considerable attention has been devoted recently to the utilization of the Shape Memory NIckel-TItanium alloy (NITINOL) in developing SMART composites that are capable of adapting intelligently to external disturbances (Ikegami et al. 1990, Rogers et al. 1991, and Baz et al. 1990 and 1991). Such wide acceptance of NITINOL stems from its unique behavior when it is subjected to particular heating and cooling strategies. For example, the alloy becomes soft when it is cooled below its martensite transformation temperature and becomes about four times stiffer when it is heated above its austenite transformation temperature (Funakubo 1987). Furthermore, if the alloy is trained to have a particular shape while in its austenite phase, it will memorize this shape. If the alloy is then cooled to its martensite phase and subject to plastic deformation, it will return to its memorized shape when it is heated above the austenite transformation temperature. The phase transformation from martensite to austenite produces significant forces as the alloy recovers its original shape. The alloy acts as an actuator transforming thermal energy into mechanical energy (Perkins 1975 and Duerig et al. 1990). Accordingly, if the NITINOL fibers are embedded inside a composite matrix at optimal locations, they can be used to control the static and dynamic characteristics of the resulting SMART composite. The control action is generated by the described stiffening of the NITINOL fibers and/or the shape memory effect. With such built-in control capabilities, the performance of the SMART composites can be optimized and tailored to match changes in operating conditions.

Emphasis is placed, in the present work, on using the shape memory

H. S. Tzou and G. L. Anderson (eds.), Intelligent Structural Systems, 169–212.

effect of the NITINOL fibers to control the performance of fiberglass composite beams. The NITINOL fibers are embedded inside vulcanized rubber sleeves placed along the neutral axes of these composite beams as shown in Figure (1). In this arrangement, the fibers are free to move during the phase transformation process in order to avoid degradation and/or destruction of the shape memory effect which may result when the fibers are completely bonded inside the composite matrix.

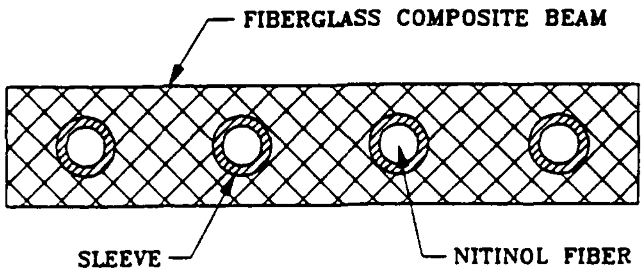

Figure (1) - A schematic drawing of the cross section of a NITINOL-reinforced composite beam

The basic phenomena governing the thermo-dynamic performance of the NITINOL fibers and NITINOL-reinforced composites will be presented. The NITINOL fibers will be utilized to control the buckling and the flow-induced vibrations of NITINOL-reinforced fiberglass composite beams.

2. CHARACTERISTICS OF THE NITINOL FIBERS

Knowledge of the thermal and dynamic behavior of the shape memory NITINOL fibers is essential to the understanding of their role in controlling the performance of NITINOL-reinforced composites. The thermo-dynamic behavior of the NITINOL fibers has been extensively studied throughout the last two decades (Funakubo 1987, Perkins 1975, Jackson et al. 1972). However, we will present a different outlook which will be crucial in developing the basic principles governing the performance of NITINOL-reinforced composites.

Emphasis is placed on studying the effect of the operating temperature and the pre-strain level on the recovery forces and, most importantly, on the natural frequencies of end-restrained NITINOL fibers. Such end-restrained fibers constitute the basic building block of NITINOL-reinforced composites.

Figure (2) shows a schematic drawing of the experimental set-up used to determine such thermo-dynamic characteristics. In the set-up, the NITINOL fiber is clamped in a holder at one end and connected to a load cell at the other end. The load cell monitors the pre-strain level of the fiber when it is in its martensitic phase. It also provides continuous measurements of the recovery force when the fiber undergoes its phase transformation due to external electric heating. The fiber temperature is monitored by a thermocouple bonded to the NITINOL fiber. The fiber assembly is mounted on an sliding table which is connected to a mechanical shaker. Random excitations are used to drive the shaker and the table, thus applying a transverse displacement to the fixed ends of the NITINOL fiber. The resulting oscillations of the fiber are measured by a non-contacting magnetic sensor mounted on the table. The shape memory effect of the NITINOL fiber is energized electrically and the resulting fiber temperature, recovery force and amplitude of oscillation are continuously sampled by a digital computer.

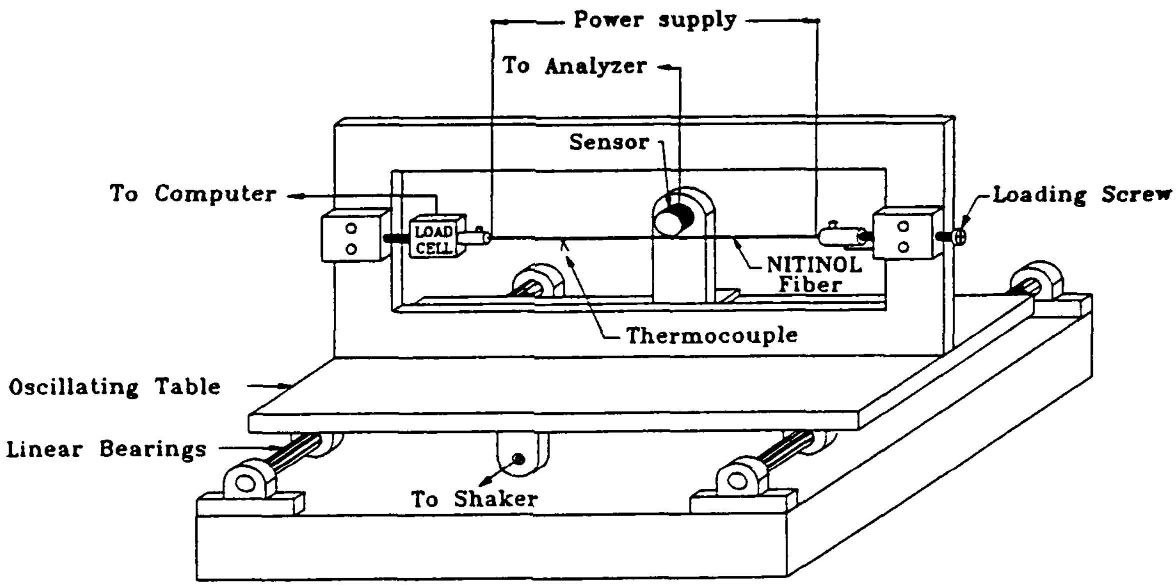

Figure (2) - Experimental set-up for monitoring thermo-dynamic behavior of NITINOL fibers.

The effect of the pre-strain level on the recovery force, as a function of time during a heating and cooling cycle, and force-temperature characteristics are shown in Figures (3-a), and (3-b) respectively. The recovery force increases almost linearly with increasing pre-strain levels. Such characteristics conform with published results.

The new outlook on the thermo-dynamic characteristics of the NITINOL fibers is demonstrated by the effect of the pre-strain on the natural frequencies of the fiber as shown in Figure (4). The figure displays the spectrum analysis of the amplitude of oscillation of the fiber, at different pre-strain levels, with and without the activation of the shape memory effect.

Figure (4) indicates that activating the shape memory effect results in a significant increase of the natural frequency of the fiber which becomes more pronounced with increasing pre-strain levels.

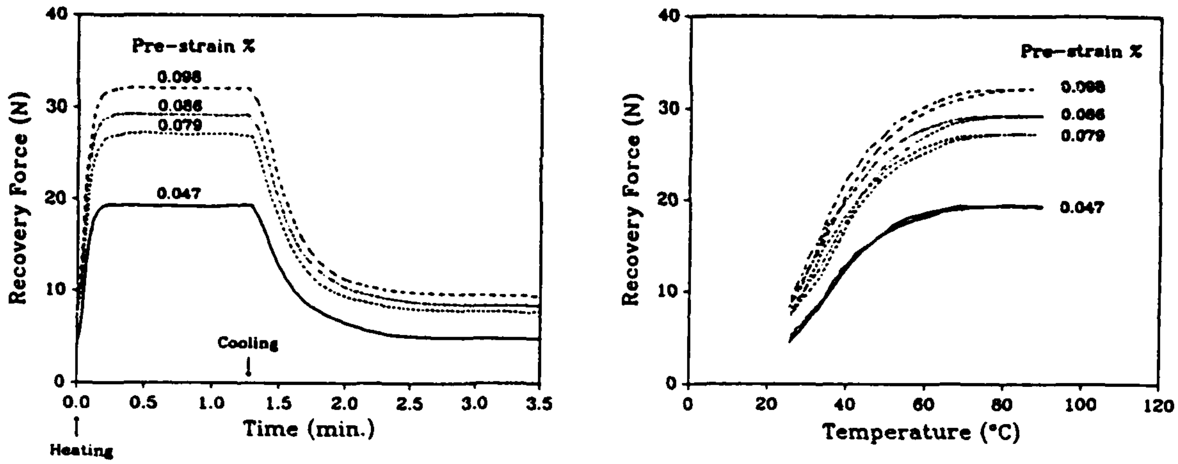

Figure (3) - Effect of pre-strain on recovery force, and force-temperature characteristics of a 30 cm long 22 mil NITINOL fiber.

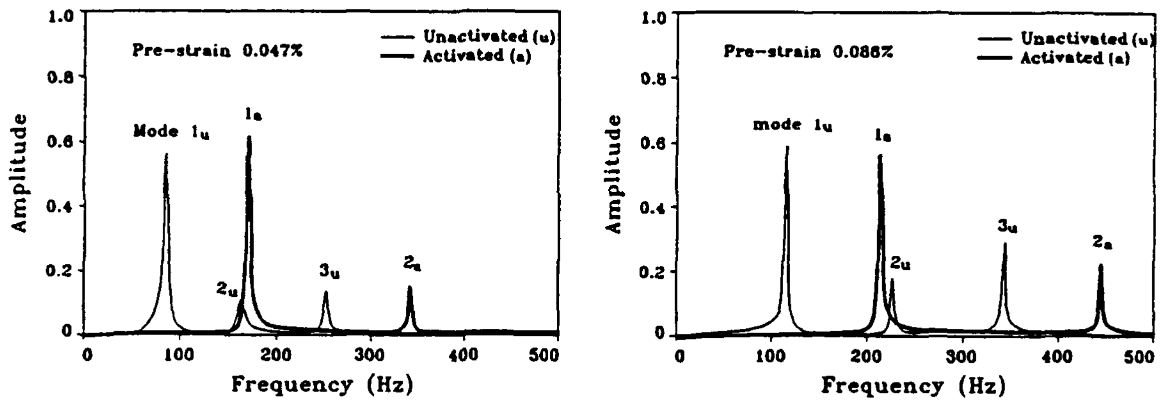

Figure (4) - Effect of pre-strain on the natural frequencies of unactivated (u) and activated (a) NITINOL fibers.

A better understanding of the underlying phenomena can be obtained by treating the NITINOL fiber using the classical theory of vibrating strings. The wave equation for transverse vibrations of a undamped freely vibrating string, which is tightly stretched with a tension T_o, is given by (James et al. 1989)

$$\frac{\partial^2 w}{\partial x^2} = \frac{1}{c^2} \frac{\partial^2 w}{\partial t^2} , \qquad (1)$$

where w is the transverse deflection of the string at a distance x along the string at time t. In equation (1), the constant c is the wave propagation speed given by

$$c = \sqrt{T_o / \rho_L} \quad , \tag{2}$$

where ρ_L is the mass per unit length of the string.

Using conventional separation of variables approach for a string of length L which is fixed at both ends, the transverse deflection w is written as

$$w = \sum_{n=1}^{\infty} \phi_n q_n \quad , \tag{3}$$

where ϕ_n and q_n are the mode shape and the generalized coordinate for the nth mode of vibration respectively. Using equation (3), equation (1) reduces to

$$\ddot{q}_n + \omega_n^2 q_n = 0 \; , \qquad \text{for } n=1,\ 2,\ .. \tag{4}$$

where ω_n is the natural frequency of a fixed-fixed string given by

$$\omega_n = (n \pi / L) \sqrt{T_o / \rho_L} \qquad \text{for } n=1,\ 2,\ .. \tag{5}$$

Accordingly, the natural frequency of the string is proportional to the square root of its tension. Using this relationship, the effect of the pre-strain (or the initial tension) of the NITINOL fibers on the first natural frequency of the unactivated and activated fiber is shown in Figure (5). Two distinct linear characteristics are observed with a significant increase in the natural frequency when the fiber is activated. A unified characteristic can be obtained when the effect of total tension T_t, which is the sum of the initial tension and the phase transformation force of the activated fibers, is considered as shown in Figure (6). The natural frequencies of the unactivated and activated fiber fall on a single straight line which has a slope of($n/2L \sqrt{\rho_L}$). In this analysis the effect of thermal expansion on the fiber tension is negligible as compared to the phase transformation force.

Therefore, the classical theory of vibrating strings can be used to predict the dynamics of unactivated as well as activated NITINOL fibers. Accordingly, the theory of vibrating strings can be utilized to determine the strain energy stored in NITINOL fibers embedded inside composite beams as the beams deflect from their equilibrium position under the action of external loads. Using this approach to determine the thermo-dynamic behavior of NITINOL fibers, it is possible to develop a thorough understanding of the static and dynamic performance of NITINOL-reinforced composites.

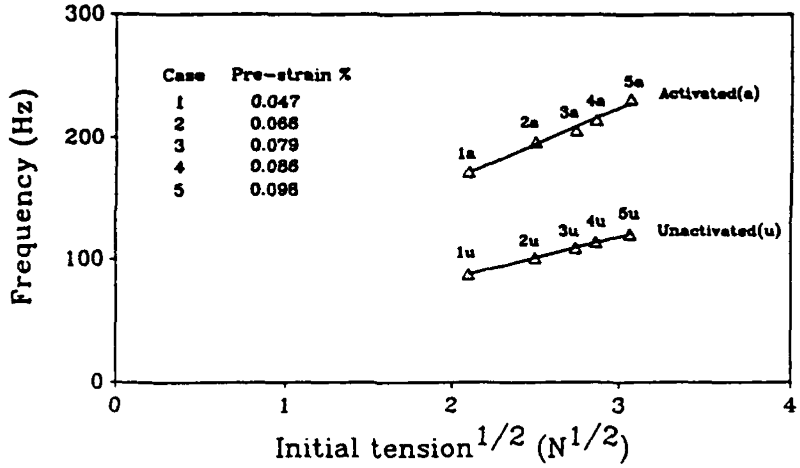

Figure (5) - Effect of pre-strain (initial tension) on the first natural frequency of unactivated and activated NITINOL fiber.

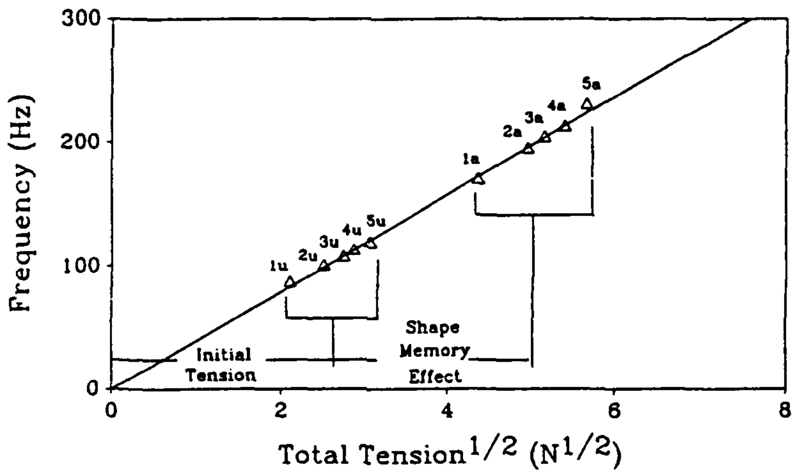

Figure (6) - Effect of total tension on the first natural frequency of unactivated and activated NITINOL fiber.

3. CHARACTERISTICS OF NITINOL-REINFORCED COMPOSITE BEAMS

3.1. STATIC CHARACTERISTICS

The static characteristics of NITINOL-reinforced composite beams are primarily governed by their stiffness. The beam stiffness is made up of different components which include: the flexural rigidity of the beam, the geometric stiffness that accounts for the axial and thermal loading as well as the stiffness imparted by the elasticity of the NITINOL fibers. The individual components of the beam stiffness can be determined by considering the NITINOL-reinforced beam element shown in Figure (7) with the forces acting on it and the associated displacements. The combined stiffness of the element can be obtained using the principle of conservation of energy and equating the work done by external loads to the strain energies stored in the element. In the present analysis, the theory of Bernoulli-Euler beams is used with the assumption of small deflections.

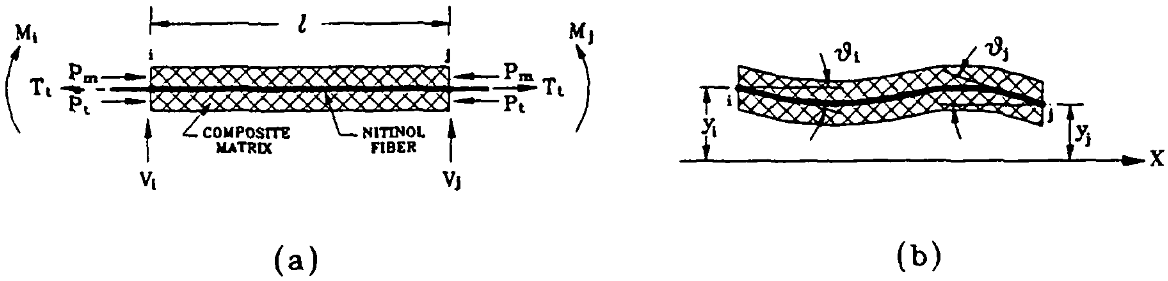

Figure (7) - NITINOL-reinforced beam element with forces and resulting displacements

3.1.1. EXTERNAL WORK

The work done by the external loads includes:

a. work done by transverse loads and moments (W_1)

This work is given by

$$W_1 = 1/2\ [\delta]^T\ [F], \tag{6}$$

where $[\delta]$ and $[F]$ are the displacement and transverse loads vectors, respectively, given by

$$[\delta] = [w_i \quad \vartheta_i \quad w_j \quad \vartheta_j]^T, \tag{7}$$

and

$$[F] = [V_i \quad M_i \quad V_j \quad M_j]^T, \tag{8}$$

with w_i and ϑ_i are the linear and angular deflections of node i, respectively and V_i and M_i are the shear and moment acting at node i, respectively.

b. work done by the axial mechanical loads (W_{2m})

W_{2m} is given by

$$W_{2m} = P_m / 2 \int_0^L (dw/dx)^2 \, dx, \tag{9}$$

where P_m is the external axial compressive load acting along the neutral axis of the beam element.

c. work done by the axial thermal loads (W_{2t})

W_{2t} represents the work done by the thermal loads P_t on the beam element due to changes in the temperature $\Delta\Theta$ of the element caused by changes in the ambient temperature or during the activation and de-activation of the NITINOL fibers. It is given by

$$W_{2t} = P_t / 2 \int_0^L (dw/dx)^2 \, dx, \tag{10}$$

where P_t is given by

$$P_t = \alpha \, \Delta\Theta \, E_m \, A_m, \tag{11}$$

where α is the thermal expansion coefficient of the composite, E_m is its modulus of elasticity and A_m is the beam cross sectional area.

3.1.2. STORED STRAIN ENERGY

The stored strain energy consists of two components:

a. strain energy of beam (W_3)

The energy stored in the beam element due to its bending is given by

$$W_3 = E_m \, I_m / 2 \int_0^L (d^2w/dx^2)^2 \, dx \tag{12}$$

where $E_m \, I_m$ is the flexural rigidity of the beam.

b. strain energy of NITINOL fibers (W_4)

Considering the NITINOL fiber as a string with a tension T which is displaced laterally a distance w from the neutral axis of the beam. Then its stored strain energy W_4 is given by

$$W_4 = T / 2 \int_0^L (dw/dx)^2 \, dx. \tag{13}$$

Equating the sum of the work done by the external forces F, P_m and P_t to the sum of the strain energies stored in beam and NITINOL fibers gives

$$W_1 + W_{2m} + W_{2t} = W_3 + W_4. \tag{14}$$

Substituting equations (6), (9), (10), (12) and (13) into equation (14) yields

$$[\delta]^T[F] = E_m I_m \int_0^L (d^2w/dx^2)^2 \, dx - P_n \int_0^L (dw/dx)^2 \, dx, \tag{15}$$

where P_n is the net axial force give by

$$P_n = (P_m + P_t - T). \tag{16}$$

Defining a cubic displacement function for the composite beam element, of the following form

$$w = a + b x + c x^2 + d x^3 \tag{17}$$

where a, b, c and d are constants that can be calculated in terms of the deflections of the nodes i and j bounding the beam element. Then equation (17) can be rewritten as

$$w = [A] \; [\delta], \tag{18}$$

where the elements of matrix [A] are function of x (Fenner 1975).

Accordingly, dw/dx and d^2w/dx^2 can be obtained by differentiating equation (18) with respect to x to yield

$$dw/dx = [C] \; [\delta] \quad \text{and} \quad d^2w/dx^2 = [D] \; [\delta], \tag{19}$$

where the matrices [C] and [D] are given by

$$[C] = \frac{d}{dx}([A]) \qquad \text{and} \qquad [D] = \frac{d^2}{dx^2}([A]), \tag{20}$$

The following relationships can also be obtained from equation (19)

$$(dw/dx)^2 = [\delta]^T[C]^T[C][\delta] \quad \text{and} \quad (d^2w/dx^2)^2 = [\delta]^T[D]^T[D][\delta]. \tag{21}$$

If the stiffness matrix $[K_e]$ of the element is defined by the following relationship

$$[F] = [K_e]\ [\delta], \tag{22}$$

then, $[K_e]$ can be determined by combining equations (15), (21) and (22) as follows

$$[K_e] = E_m\ I_m \int_0^L [D]^T[D]\ dx - P_n \int_0^L [C]^T[C]\ dx \tag{23}$$

It can be seen from equation (23), that the element stiffness matrix $[K_e]$ consists of two components: the conventional transverse stiffness and the geometric stiffness that combines the effect of the axial mechanical loads, axial thermal loads and the tension of the NITINOL reinforcing fibers. Equation (23) also represents the basic equation for understanding the role that the NITINOL fibers can play in controlling the static characteristics of the composite beam. For example, if the beam is not reinforced by NITINOL fibers (i.e. $T = 0$) and the mechanical and thermal loads induce compressive stresses in the beam, then the geometric stiffness will increase and the total element stiffness will decrease. When the combined effect of the mechanical and thermal loads reaches a critical magnitude such that the geometric stiffness becomes equal to the flexural stiffness of the beam, the beam stiffness vanishes and the beam becomes elastically unstable. Subjecting the beam to any additional external disturbance will cause the beam to buckle.

It should be pointed out that the thermal loading, as it increases the geometric stiffness, also decreases the flexural stiffness of the beam because it reduces its effective Young's modulus E_m. Such a dual effect makes the beam buckle under smaller thermal loads than under pure mechanical loading.

However, the critical load of the un-reinforced beam can be increased by embedding pre-strained NITINOL fibers into the beam. If the tension T, resulting from the pre-strain alone, is high enough to counter-balance the mechanical and thermal effects then the beam stiffness can be maintained unchanged. For higher pre-strain levels, the beam stiffness can be enhanced. Further enhancement can be achieved when the shape memory effect of the NITINOL fibers is activated by heating the fibers above their phase transformation temperature. The additional tension, induced into the fibers by the phase recovery forces, makes the net axial load P_n negative and increases accordingly the overall stiffness of the beam element. However, it is essential that the total tension in the NITINOL fibers, i.e., the sum of the tension due to the pre-strain and the phase recovery force, must exceed the mechanical and thermal loads and compensate for the softening effect in the matrix resulting from heating the NITINOL fibers inside the composite matrix.

Therefore, effective control of the stiffness of NITINOL-reinforced composites can be achieved by proper selection of the initial pre-strain level of the NITINOL fibers. This selection is particularly crucial, in view of the results of Figure (3), as the pre-strain level determines the generated levels of recovery forces.

The finite element model of the NITINOL-reinforced beams describes the interaction between the external loads, operating conditions and the geometrical and physical parameters of the composite beam and the NITINOL fibers. It defines how the NITINOL fibers can be utilized to tailor the stiffness of the composite to compensate for environmental and operating conditions and disturbances. The stiffness obtained for the individual elements of the beam can be assembled using the classical finite element approach (Fenner 1975). The assembled model can then be subjected to the appropriate boundary conditions in order to compute the deflections corresponding to particular external loading conditions. The analysis presented is for an orthotropic laminate that has a single layer of unidirectional NITINOL fibers. Such an analysis can be used along with the classical laminate theory to assemble the stiffness matrix for a multi-laminate composite beam. Similar approach can be carried out for modeling the static and dynamic characteristics of NITINOL-reinforced composite plates.

The finite element model developed will be validated with experimental results obtained with fiberglass composite beams.

3.2. DYNAMIC CHARACTERISTICS

The dynamic characteristics of NITINOL-reinforced beams are obtained by combining the stiffness matrix $[K_e]$ with the mass matrix $[M_e]$ of the beam to form the following element equation of motion

$$[M_e]\ [\ddot{\delta}] + [K_e]\ [\delta] = [F], \tag{24}$$

where $[\ddot{\delta}]$ is the nodal acceleration vector. The elements $m_e(i,j)$ of the element mass matrix $[M_e]$ are obtained using the consistent mass formulation (Zienkiewicz and Taylor 1989) as follows

$$m_e(i,j) = \rho_m\ A_m \int_0^L [A_i]\ [A_j]\ dx \tag{25}$$

where $[A_i]$ and $[A_j]$ are the ith and jth elements of the vector A given by equation (18).

The classical finite element approach is used to form the equations of motion of the assembly of several beam elements and the appropriate boundary conditions are then applied. The solution of the eigenvalues of the resulting homogeneous equations give the natural frequencies of the composite beam as influenced by the properties of the matrix and the NITINOL fibers. It is important to note that these properties are influenced by the temperature distribution inside the beam which is developed by virtue of activating and de-activating the NITINOL fibers. A study of the temperature distribution inside NITINOL-reinforced beams will be presented in the following section.

3.3. THERMAL CHARACTERISTICS

The thermal characteristics of NITINOL-reinforced composite beams are influenced primarily by the temperature distribution inside the composite. A thermal finite element model is developed to determine steady-state and transient temperature distribution resulting from different activation strategies of the NITINOL fibers. The theoretical predictions are compared with experimental measurements in order to validate the thermal model.

It is important here to note that although the finite element model used in predicting the beam dynamics is a one-dimensional model, with the single dimension taken along the beam neutral axis, the thermal model is considered to be a two-dimensional model to predict the temperature distribution over the beam cross section. Such a distinction is made because the temperature distribution, along the beam neutral axis, is assumed to be uniform. This assumption is confirmed experimentally and is attributed to the fact that the NITINOL fibers are oriented parallel to the neutral axis. The beam temperature, however, varies only over the cross section and its magnitude depends on the number and location of the activated or de-activated NITINOL fibers. The resulting temperature distribution can be used to compute an average Young's modulus of the composite. The average temperature rise above the ambient can also be used to compute the axial thermal loading on the beam P_t which results from fixing the two ends of the beam.

The two-dimensional thermal modeling of the beam is favored over a one-dimensional lumped-parameter approach because it provides more accurate simulation of the thermal state of the beam.

3.3.1 THERMAL FINITE ELEMENT MODEL

The energy balance equation that governs the heat transfer across the beam can be written, in two-dimensional cartesian coordinate system , as follows

$$\frac{\partial^2\theta}{\partial y^2} + \frac{\partial^2\theta}{\partial z^2} + \frac{\dot{Q}}{k} = \frac{1}{\alpha}\frac{\partial \theta}{\partial t} \qquad (26)$$

where θ is the beam temperature at time t and location (y,z) as defined in Figure (8). In equation (26), $\dot{Q}$ defines the rate of heat generated per unit area during the activation of the NITINOL fibers. Also, k denotes the conductivity of the beam and α its thermal diffusivity.

The above equation is subject to the following boundary and initial conditions

$$k\left[\frac{\partial \theta}{\partial y}\ell_y + \frac{\partial \theta}{\partial z}\ell_z\right] + Q = 0 \qquad \text{on boundary } S_1, \qquad (27)$$

$$k\left[\frac{\partial \theta}{\partial y}\ell_y + \frac{\partial \theta}{\partial z}\ell_z\right] + h\,(\theta - \theta_a) = 0 \qquad \text{on boundary } S_2, \qquad (28)$$

and $$\theta\,(y,\, z,\, t=0) = \theta_o\,(y,\, z) \qquad \text{on beam cross section} \qquad (29)$$

Equation (27) defines the condition at the NITINOL fiber circular boundary S_1 on which the heat flux Q is specified, and equation (28) specifies the conditions at the beam outer boundary S_2 where the interaction with the ambient temperature θ_a is through convective heat transfer with coefficient h. The boundaries S_1 and S_2 are defined in Figure (8). In equations (27) and (28), ℓ_y and ℓ_z denote the direction cosines of the outward normals to the boundaries. Equation (29) describes the initial temperature distribution over the beam cross section at time t = 0.

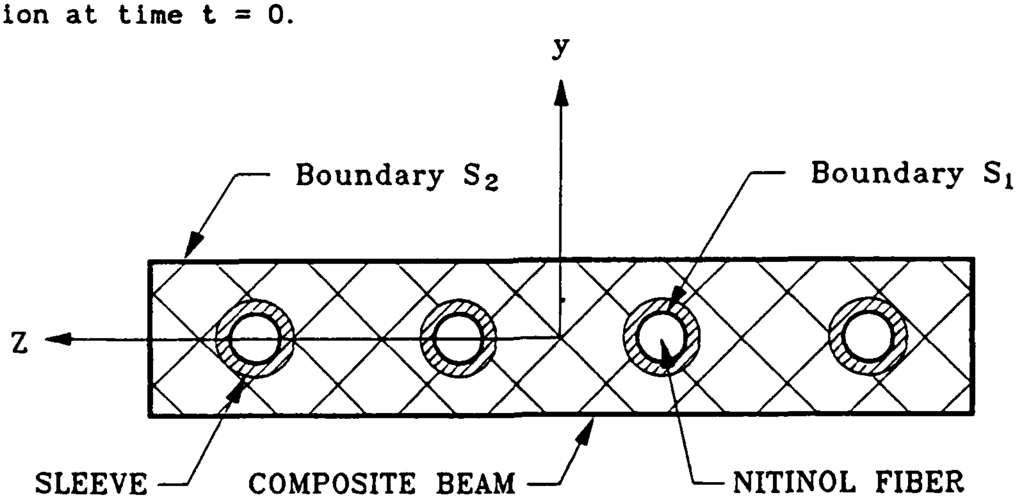

Figure (8) - Schematic drawing of beam cross section with heat transfer boundaries.

Assuming a linear interpolating function [N] with triangular elements that have isotropic thermal properties, then the temperature θ at any y, z and t can be expressed, in terms of the nodal temperatures $[\theta^e]$ as follows

$$\theta = [N]\ [\theta^e], \tag{30}$$

Using Galerkin method along with assumed interpolating functions, one can write the following finite element equation (Rao 1988)

$$[k_1^e]\ [\dot{\theta}^e] + \Big([k_2^e] + [k_3^e]\Big)\ [\theta^e] = [P^e], \tag{31}$$

where
$$[k_1^e] = \iint_{A^e} k/\alpha\ [N]^T\ [N]\ dA\ , \tag{32}$$

$$[k_2^e] = \int_{S_2^e} h\ [N]^T\ [N]\ dS_2\ , \tag{33}$$

$$[k_3^e] = \iint_{A^e} k\ [B]^T\ [B]\ dA\ , \tag{34}$$

and
$$[P^e] = \iint_{A^e} \dot{Q}\ [N]^T\ dA - \int_{S_1^e} Q\ [N]^T\ dS_1 + \int_{S_2^e} h\ \theta_a\ [N]^T\ dS_2. \tag{35}$$

with
$$[B] = \begin{bmatrix} \partial N_1/\partial y & \partial N_2/\partial y & \dots & \partial N_p/\partial y \\ \partial N_1/\partial z & \partial N_2/\partial z & \dots & \partial N_p/\partial z \end{bmatrix} \tag{36}$$

where subscript p is the number of vertices of the element (p=3 for triangular element).

The individual element equations are assembled to form the overall equation of the NITINOL-composite beam equation which can be solved for the nodal temperatures. The solution is based on a Crank-Nicolson trapezoidal scheme (Hughes 1977).

3.4. NUMERICAL AND EXPERIMENTAL RESULTS

3.4.1. BASIC CHARACTERISTICS OF BEAM

The characteristics of NITINOL-reinforced beams are computed using the developed static, dynamic and thermal models. The theoretical predictions are compared with experimental results obtained with a composite beam made of randomly oriented glass fibers embedded in a low cure temperature polyester resin. The beam is 30 cm long, 2.5 cm wide and 0.156 cm thick mounted in clamped-clamped arrangement. The temperature dependence of Young's modulus of the beam, shown in Figure (9), is obtained experimentally using the Dynamic, Mechanical, and Thermal Analyzer (DMTA) of Polymer Laboratories, Ltd (1990).

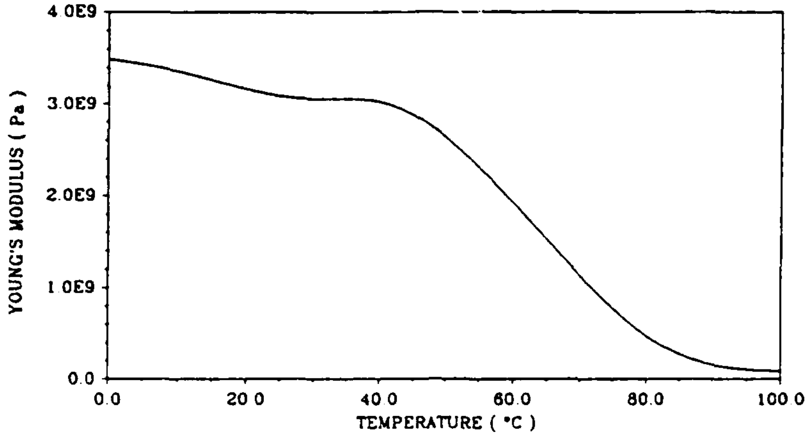

Figure (9) - Effect of operating temperature on Young's modulus of the test fiberglass composite beam

Four NITINOL 55 fibers, that are 0.55 mm in diameter, are embedded inside the beam through vulcanized rubber sleeves that have outer diameter of 0.95 mm. Two sets of NITINOL fibers were used. The first set consisted of trained fibers that have austenite transformation temperature of 50^{o}C. The second set however is untrained and accordingly, the shape memory effect has not been imparted to it. The two sets are inserted, one at a time, inside the sleeves and the effect of the shape memory and the associated phase recovery forces on the performance of the composite beam are monitored when the beam is exposed to different ambient temperatures. The experimental set-up, shown in Figure (10), is placed inside a temperature-controlled chamber to determine the natural frequencies of the fixed-fixed beam as a function of the ambient temperature. The set-up is very similar to that used in studying the thermo-dynamic characteristics of the NITINOL fibers. However, instead of activating the NITINOL fibers electrically, the fibers are activated thermally by controlling the temperature of the environmental chamber. The measurements are carried out after steady-state and thermal equilibrium conditions are attained. Under these conditions, the composite matrix and the NITINOL fibers are all at the same equilibrium temperature. At each equilibrium temperature, the composite beam is subjected to random vibrations and the resulting response is monitored by an micro-accelerometer bonded to the beam. The response is analyzed in the frequency domain to determine the modes of vibration of the composite beam.

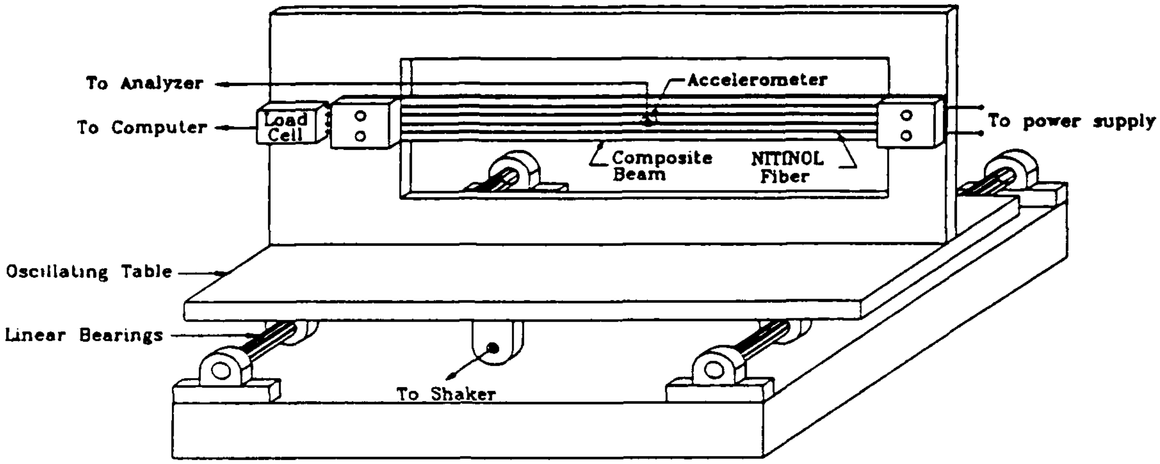

Figure (10) - Experimental set-up used in monitoring the performance of NITINOL-reinforced beams

3.4.2. THE STATIC AND DYNAMIC CHARACTERISTICS

Figure (11-a) shows the measured changes in the first natural frequency of the beam when it is reinforced with untrained fibers which are pre-strained at different levels. The changes are normalized with respect to the natural frequency ω_b of the un-reinforced beam measured at 25^{o}C. The normalized characteristics of the un-reinforced beam are also plotted to serve as a datum for defining the effect of reinforcing the beam with NITINOL fibers and also the effect of the pre-strain level. It can be seen that the frequency of the un-reinforced beam drops as the ambient temperature increases and when the temperature exceeds 40^{o}C the beam losses its elastic stability and start to buckle. The drop in the natural frequency of the un-reinforced beam is attributed to the softening of the matrix which is clearly demonstrated by the loss in the Young's modulus of the beam as shown in Figure (9).

Reinforcing the beam with pre-strained untrained NITINOL fibers considerably increases the natural frequency of the beam. The extent of the upward shift in natural frequency increases with increased pre-strain level. An increase of about 40% is obtained at room temperature when the pre-strain level is only 0.26%. However, as the ambient temperature increases the frequency shift drops in a manner similar to the characteristics of the plain un-reinforced beam. Such a drop is again attributed to the softening effect of the matrix and the fact that the untrained NITINOL fibers act as a static pre-tensioning device that produce constant tension which is independent of temperature. Therefore, the frequency enhancement is only generated by the reinforcement and the pre-strain effects, and not by the shape memory effect.

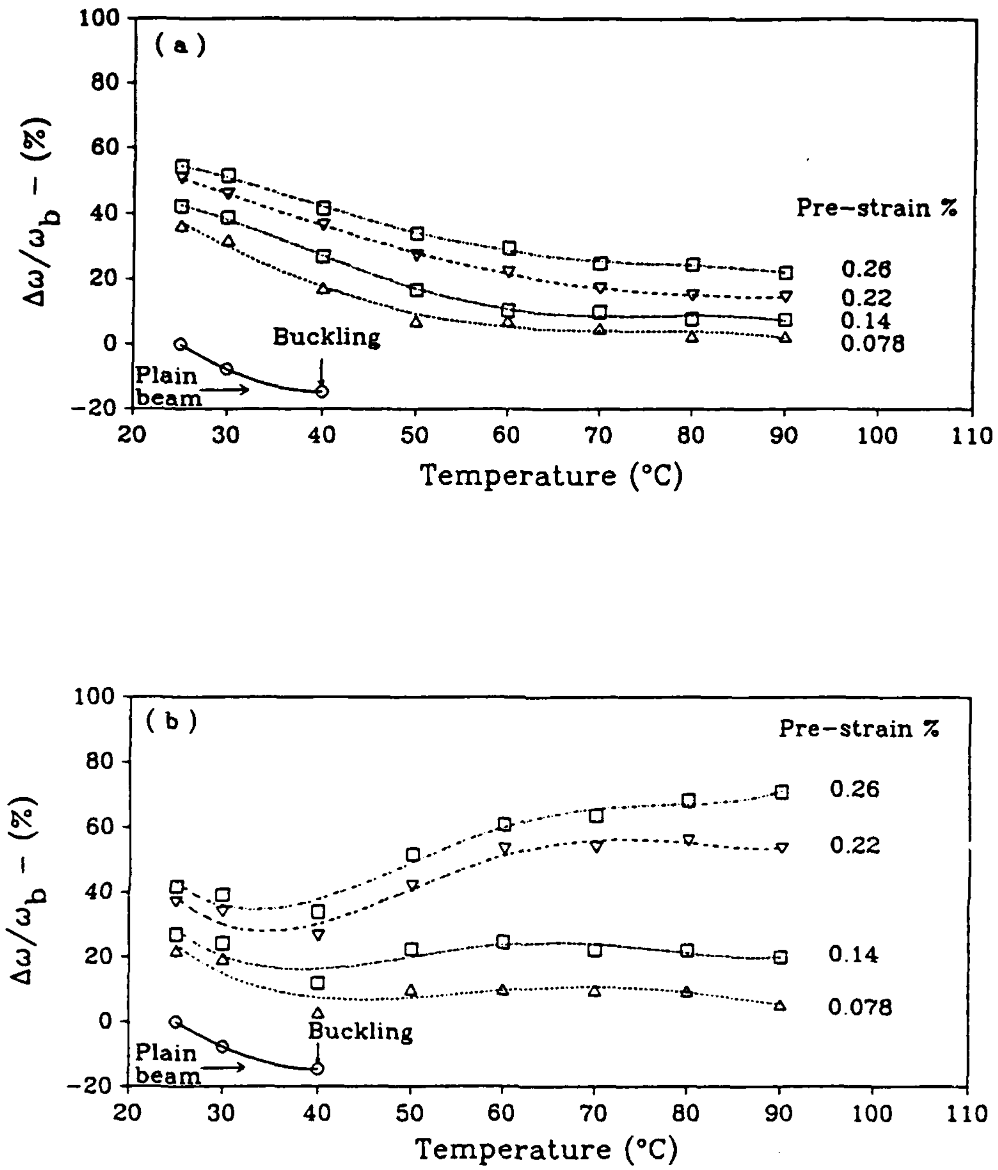

Figure (11) - Effect of the ambient temperature and pre-strain level on enhancing the first mode of vibration of clamped-clamped composite beam reinforced with NITINOL fiber without (a) and with (b) shape memory.

It is important to note that considerably higher increases in natural frequency can be obtained by further increases of the pre-strain level to its maximum permissible level of 6%.

However, a greater frequency shift can be achieved by imparting the shape memory effect to the NITINOL fibers. The fibers are trained over 250 cycles using the procedure outlined by Johnson (1984). The trained fibers are inserted into the composite beam to replace the untrained set, the frequency shifts become significant, particularly at high ambient temperatures. This is clearly demonstrated in Figure (11-b). For temperatures between room temperature and 40^{o}C, the frequency shifts obtained are similar to those with the untrained fibers within experimental accuracy. But, once the ambient temperature exceeds the 50^{o}C temperature, which is the austenite phase transformation temperature, the frequency shift characteristics changes from a gradually decaying trend and develops a gradually increasing profile. Such a sudden change is a reflection of the contribution of the phase recovery forces developed by the shape memory effect which is illustrated in Figure (12).

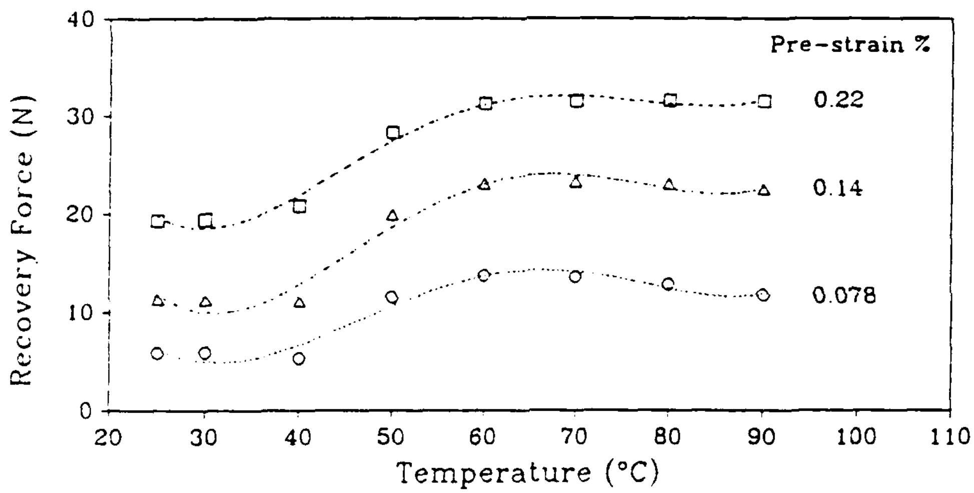

Figure (12) - Effect of pre-strain level and ambient temperature on the phase recovery forces of trained NITINOL fibers.

The shape memory effect generates strain energy in the NITINOL fibers to counterbalance the softening effect of the composite matrix with increasing temperature. The amount of strain energy developed, depends on the initial pre-strain level, it can merely compensate for the softening effect to maintain the beam frequency at nearly a constant value which is independent of ambient temperature as shown for pre-strain level of 0.078%. It can also increase the beam frequency as the ambient temperature increases as indicated for pre-strain levels of 0.22 and 0.26%. With pre-strain level of 0.26%, the frequency increase reaches about 70% of that at ambient temperature of 90^{o}C as compared to 18% increase when untrained fibers are used. In this way, the individual contributions of the pre-strain, matrix softening and shape memory effect on the frequency shift are isolated. This facilitates checking the validity of the mathematical models against the experimental results.

Comparisons between the theoretical predictions and the measurements are shown in Figures (13-a) and (13-b) for NITINOL fibers without and with shape memory effect, respectively. The figures include comparisons for the first and second modes of vibrations. Close agreement between theory and experiments is evident.

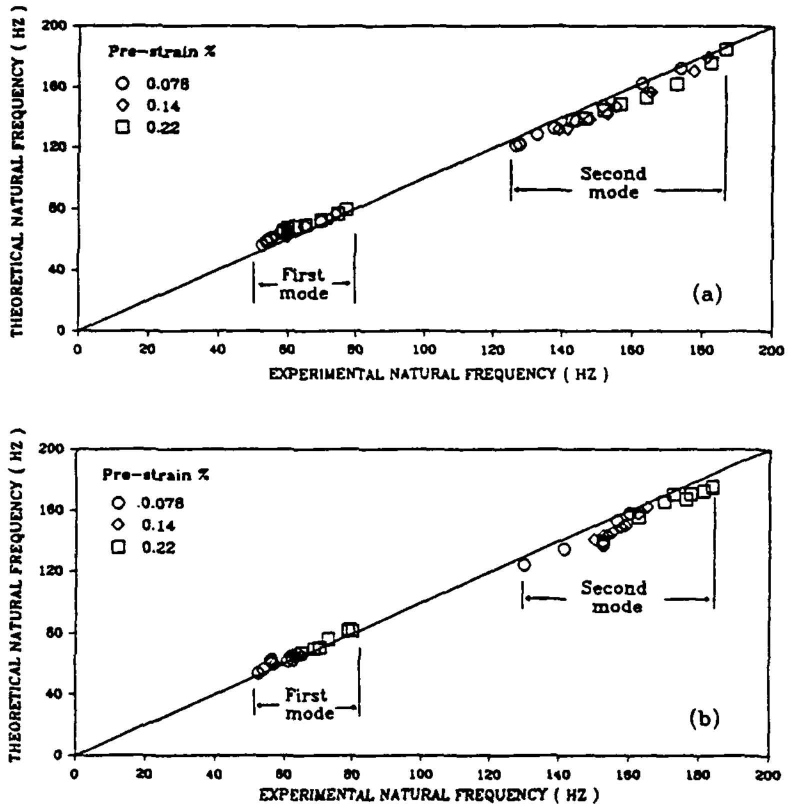

Figure (13) - Comparison between the theoretical and experimental frequencies of composite beam reinforced with NITINOL fibers without (a) and with shape memory (b).

3.4.3. THERMAL CHARACTERISTICS OF BEAM

The thermal finite element model developed in section 3.3.1 is used to generate the temperature distribution over the beam cross section which in turn is utilized to compute the average Young's modulus of the beam under different operating conditions. Such thermal characteristics will be presented in this section and compared with experimental results in order to check the validity of the theoretical predictions.

Figure (14) shows a sample of the finite element mesh used in the analysis of the temperature field in the NITINOL-reinforced beam.

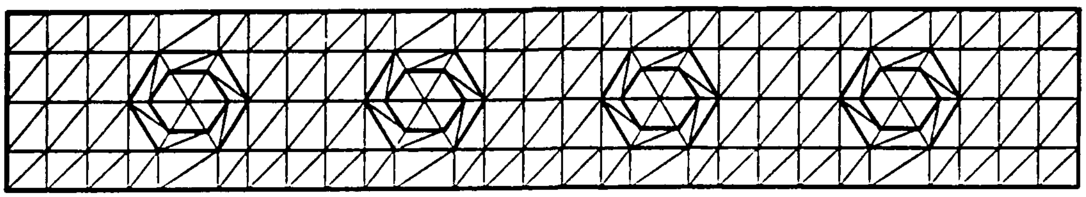

Figure (14) - The finite element mesh of the thermal model of the NITINOL-reinforced beam.

Figures (15), (16) and (17) show the steady-state temperature and Young's modulus distributions over the cross section of the beam when activating all the four fibers, the two extreme fibers, and the middle two fibers, respectively. It is evident that the activation strategy, as well as the number and location of the activated fibers, result in dramatic variations of the temperature and Young's modulus distribution. These variations influence the static and dynamic characteristics of the composite beam. Hence, integration of the thermal and mechanical models is essential to the understanding and the prediction of the behavior of NITINOL-reinforced composites.

Comparisons are shown in Figures (15) through (17) with the experimental results when the fibers are activated electrically with 8.3 watts/fiber and when steady-state conditions are attained after 720 seconds. The temperature distribution is also monitored during the 720 second period required to reach steady-state at six different locations. Figure (18) displays the spatial distribution of these measurement stations.

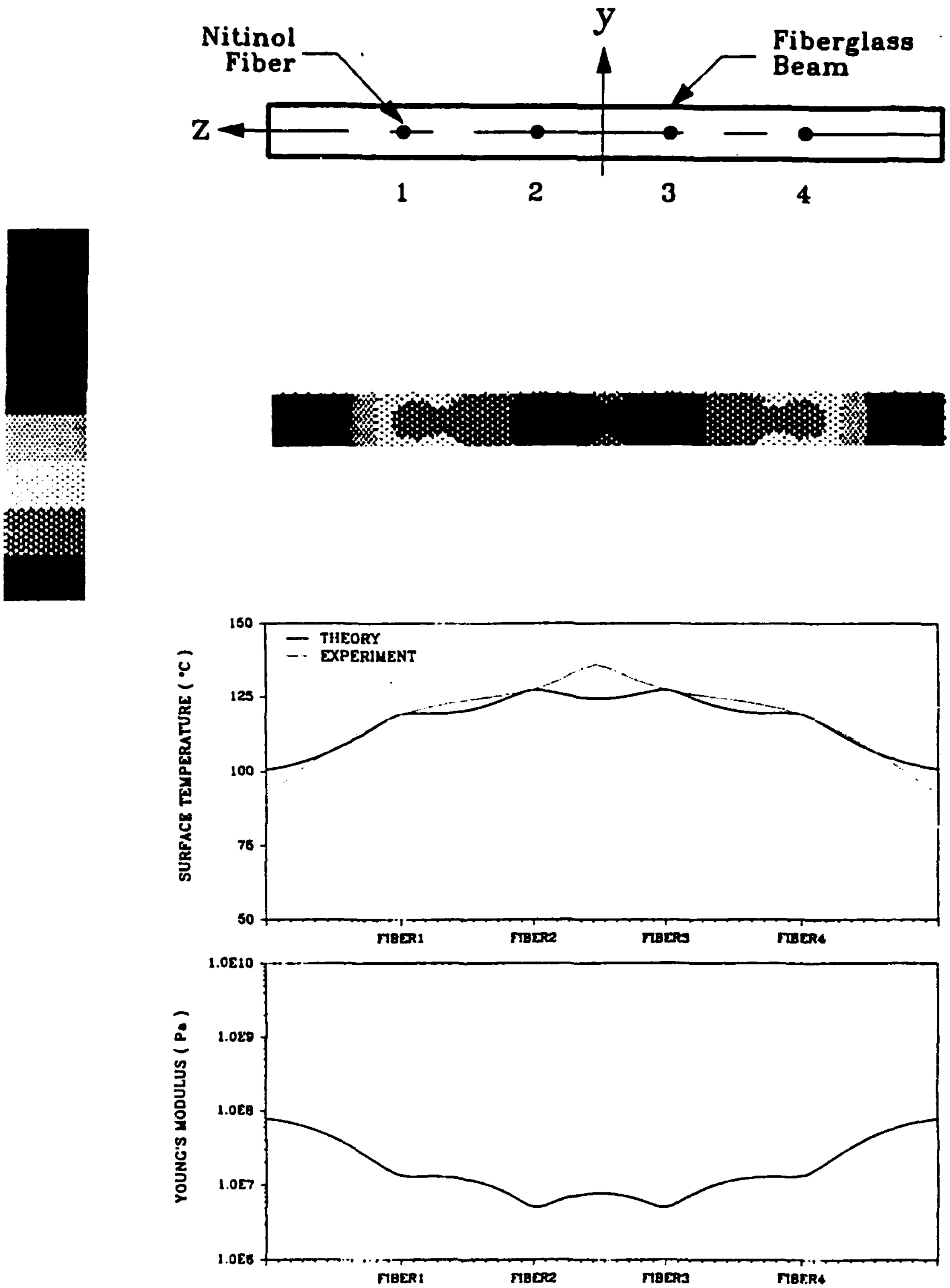

Figure 15 - Temperature and Young's modulus distribution over beam cross section when all four NITINOL fibers are activated

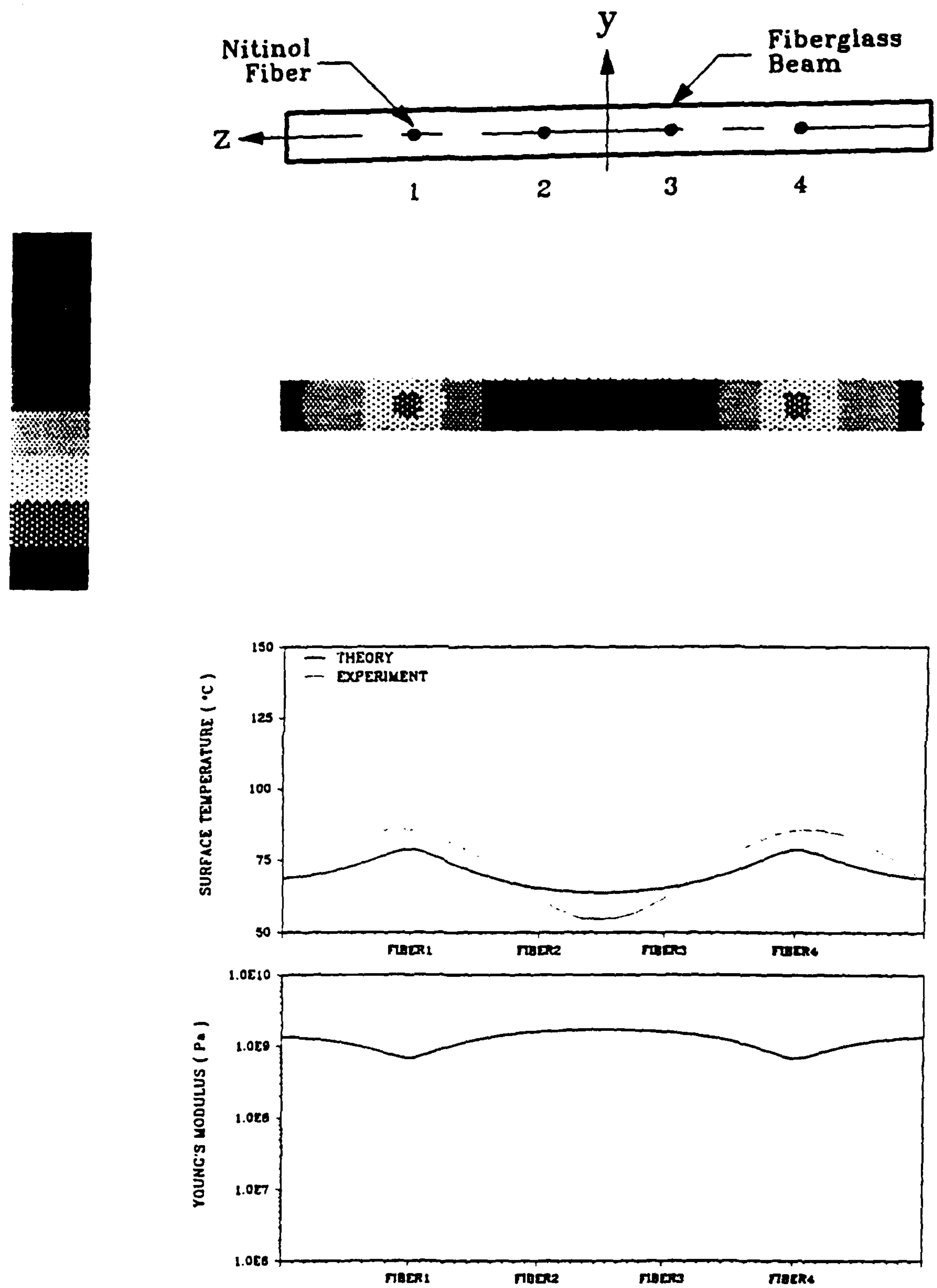

Figure 16 - Temperature and Young's modulus distribution over beam cross section when the two extreme NITINOL fibers are activated

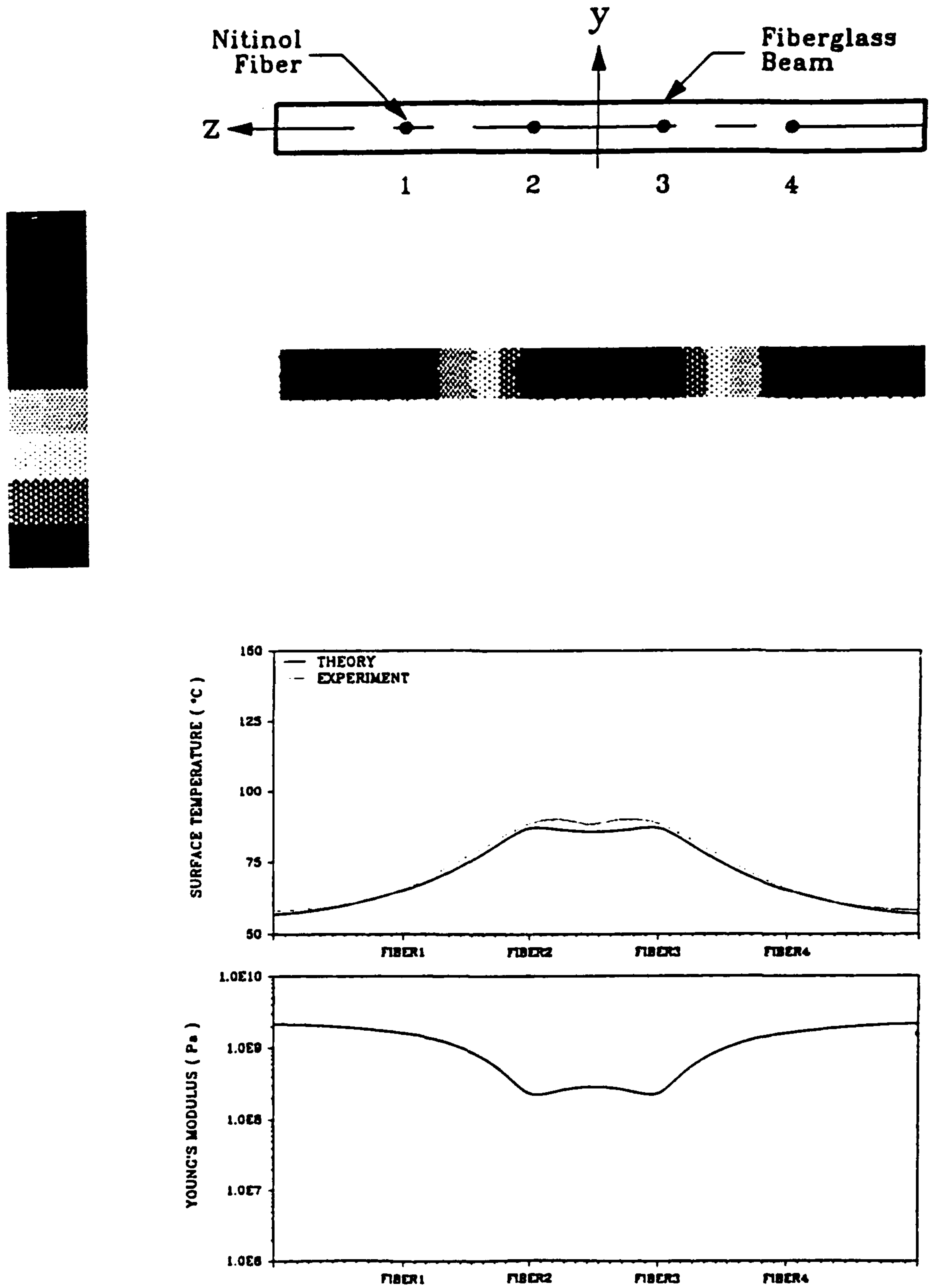

Figure 17 - Temperature and Young's modulus distribution over beam cross section when the two middle NITINOL fibers are activated

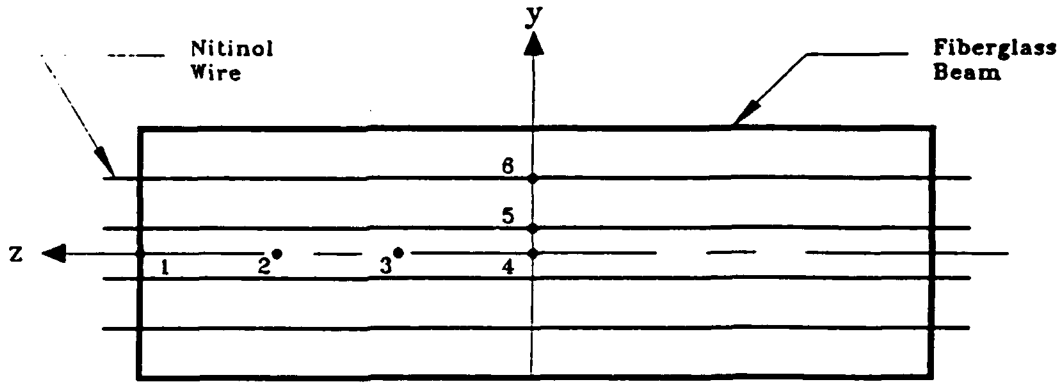

Figure (18) - Spatial distribution of temperature measurement stations

Figures (19-a) and (19-b) show comparisons between the experimental and theoretical temperature distributions over the beam cross section at three stations located on the outer surface of the beam. Close agreement between theory and experiment is evident.

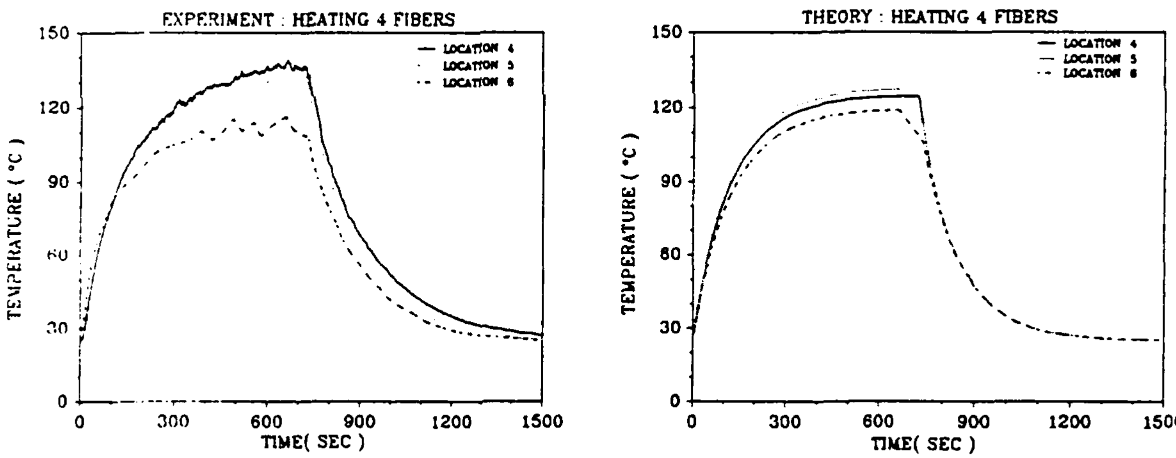

Figure (19) - Comparison between theoretical and experimental surface temperature distributions over beam cross sections with all four NITINOL fibers activated.

Figure (20) shows the experimental surface temperature of the beam along its longitudinal axis. It is clear that the temperature is practically constant along the beam longitudinal axis. Such measurements validate the assumption used in deriving the thermal model and justify the use of the two-dimensional simulation of the beam.

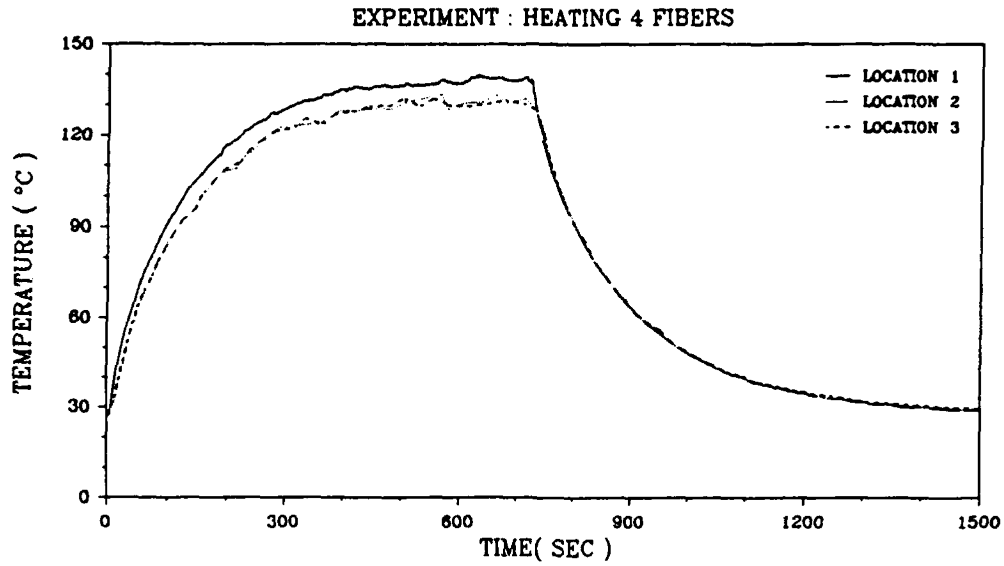

Figure (20) - Experimental surface temperature of the beam along its longitudinal axis.

4. APPLICATIONS OF NITINOL-REINFORCED COMPOSITE BEAMS

The feasibility of utilizing NITINOL-reinforcing fibers to actively control the buckling and flow-induced vibrations of composite beams are demonstrated in this section.

4.1. ACTIVE BUCKLING CONTROL

The new trend of designing light weight and large structures render these structures to be more susceptible to failure due to buckling. Baz and Tampe (1989) were successful in to enhancing the buckling characteristics of long slender beams by using external helical shape memory actuators. In the present study, actuators in the form of NITINOL fibers are embedded inside the long slender beams. With such a configuration, beams can be manufactured from light weight sections that have built-in capabilities for withstanding failure due structural instabilities. It was shown theoretically in section 2 that NITINOL-reinforced composite beams can have enhanced buckling characteristics depending on the pre-strain level of the NITINOL fibers in comparison with the external mechanical and thermal loads acting on these beams. The validation of such theoretical model is experimentally demonstrated in this section.

4.1.1. THE EXPERIMENTAL SET-UP

Figure (21) shows a schematic drawing of the experimental set-up used in actively controlling the buckling of a NITINOL-reinforced beam. The beam dimensions are 63.75 cm by 2.5 cm by 0.44 cm. The beam is reinforced by eight o.55 mm NITINOL fibers which are embedded symmetrically along the neutral axis of the beam.

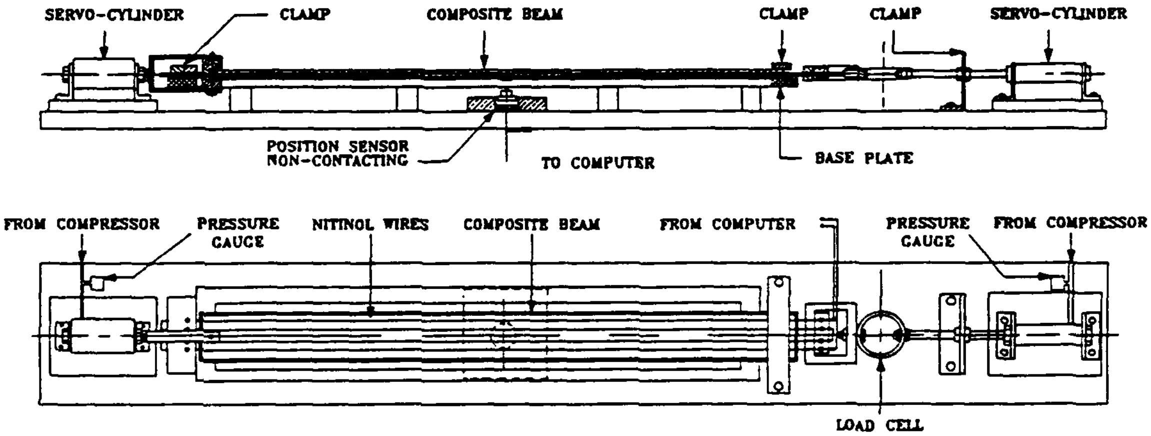

Figure (21) - Schematic drawing of the active buckling control experiment.

One end of the beam is clamped to a fixed base and the other end is connected to the piston of a loading cylinder. The cylinder is pressurized by compressed air from the storage tank of an air compressor. The increasing compressive load applied by the load cylinder to the beam will eventually cause the beam to buckle. The resulting deflection of the beam is monitored continuously by two non-contacting sensors which are placed on both sides of the beam. The sensors also serve as physical stops to prevent excessive deflection once buckling has occured. The output signals of the sensors are sent to a micro-computer via a set of analog-to-digital converters. The processing these signals is shown in the controller block diagram shown in Figure (22). When the beam deflection exceeds a pre-set value of a dead-band, the controller is turned on using a proportional controller with a saturation limit. The control action is sent via a

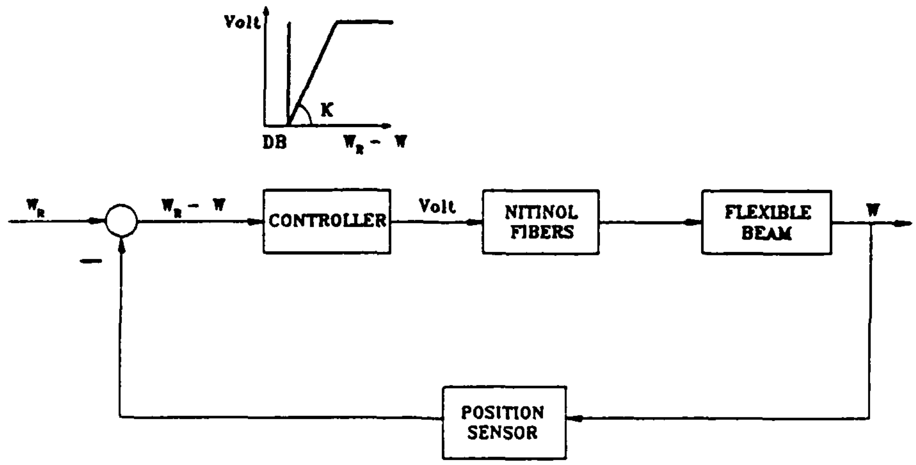

Figure (22) - Block diagram of the active buckling control system

digital-to-analog converter to a power amplifier to activate the NITINOL fibers embedded inside the compressively loaded composite beam. The activation of the NITINOL fibers will compensate for the monitored deflection and the phase recovery forces developed in the fibers will attempt to bring the beam back to its undeflected position.

It is important here to note that the controller dead-band is essential to prevent chattering of the controller as observed by Baz, Iman and McCoy (1990). Also, the saturation limiting of the maximum voltage applied to the NITINOL fibers is necessary to avoid destruction of the shape memory effect of the NITINOL fibers due to excessive heating.

In the active buckling control system described, the NITINOL reinforcing fibers are clamped at one end to the fixed base and at the other end to pre-tensioning cylinder via a load cell. The load cell monitors the initial value of the pre-tension applied to the NITINOL fibers by the pre-tensioning cylinder. The load cell also continuously measures the phase recovery forces developed in the NITINOL fibers as they undergo their phase transformation.

4.1.2. EXPERIMENTAL RESULTS

Figure (23) shows a comparison of the performance with and without the active buckling control. The results displayed are for a NITINOL-reinforced beam with each of the eight fibers has an initial tension of 33.7 N which corresponds to an initial pre-strain of 0.35%. For the controlled cases, the controller dead band corresponds to deflection error of 0.0176 mm and the controller gain is 2727 volt/mm. The saturation limit is 6 volts/fiber and the maximum current is 1.6A.

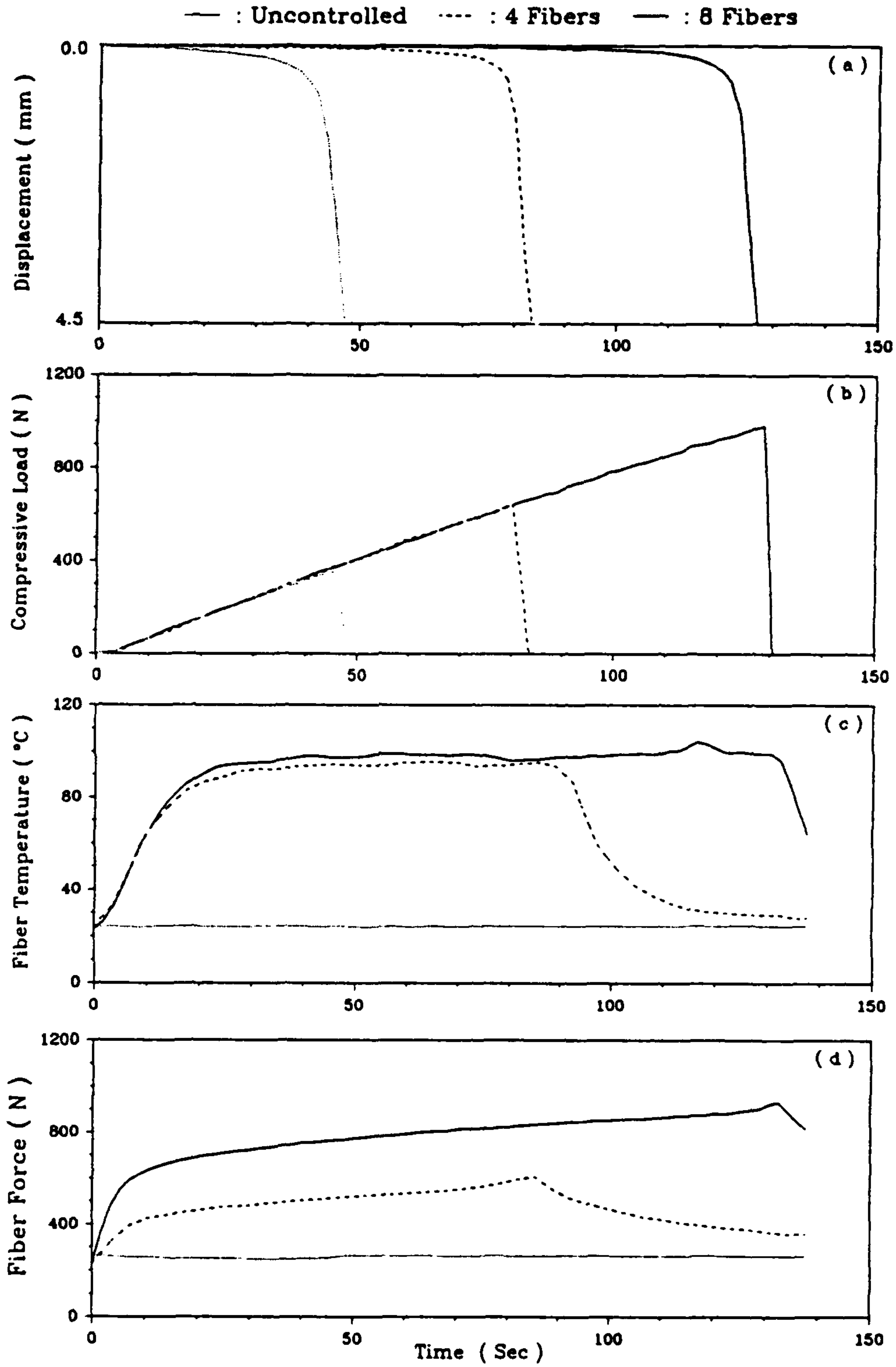

Figure (23) - Performance of active buckling control system with 0, 4 and 8 NITINOL fibers activated with a dead band = 0.0176 mm and control gain = 2727 volts/mm.

In Figure (23-a), the deflection of the beam resulting from the application of a gradually increasing compressive load is shown. The rate of load increase is 500 N/min as shown in Figure (23-b). It can be observed that the uncontrolled beam buckles when the compressive axial loads starts exceeding 330 N. However, when all eight NITINOL fibers are activated, the beam can withstand axial loads up to 950 N before it starts to buckle. Therefore, with the NITINOL reinforcement, it is possible to triple the critical buckling load of the beam. With four activated fibers, the critical buckling load is about 700 N which corresponds to about double the critical load of the uncontrolled beam. Figure (23-c) shows the corresponding time history of the temperature of the NITINOL fibers due to the activation and de-activation of the controller. In Figure (23-d), the time history of the phase recovery forces developed in the NITINOL fibers is shown. The tension in the fibers remains equal to the initial pre-tension, i.e. 33.7N x 8 = 269.6N, for the uncontrolled case. However, the tension increases to approximately 1000 N when eight NITINOL fibers are activated.

With such capability, it is possible to energize different sets of the NITINOL fibers to counterbalance the external loading condition and avoid buckling of the composite beam. Therefore, for small external loads, it is only necessary to energize a few fibers, but as the load increases, the controller can energize a larger number of fibers to maintain the beam in its undefelected form.

The effect of varying the controller parameters on the performance of the active control system is shown in Figures (24), (25) and (26). In Figure (24), the effect of varying the control dead-band on the system performance is shown. In this case, the controller will be off until the beam deflection exceeds the dead band. Once the deflection exceeds the dead band , the controller is energized. This is accomplished by the heating of the NITINOL fibers and the development of the phase recovery forces as shown in Figures (24-c) and (24-d), respectively. For the range of dead bands considered, between 0.0176 mm and 0.528 mm, the effect on the critical buckling loads is insignificant.

The effect of varying the controller gain from 2727 volt/mm to 136.35 volt/mm on the system performance is shown in Figure (25). This effect varies the slope of temperature rise of the NITINOL fibers and, in turn, the rate at which the corresponding phase transformation forces are recovered. Changing the controller gain is found to influence to some extent the critical buckling load. For example, when the controller gain is 2727 volt/mm the critical buckling load is 950 N and when the gain is reduced to 136.35 volt/mm the critical buckling load become about 850. Therefore, reducing the controller gain by a factor of 1/20 only results in a 10.5% reduction in the critical buckling load.

The effect that the pre-tension has on the system performance is shown in Figure (26) for dead band of 0.0176 mm and controller gain of 2727 volts/mm. It is clear from the results obtained that , the pre-tension plays the most crucial role in controlling the buckling of

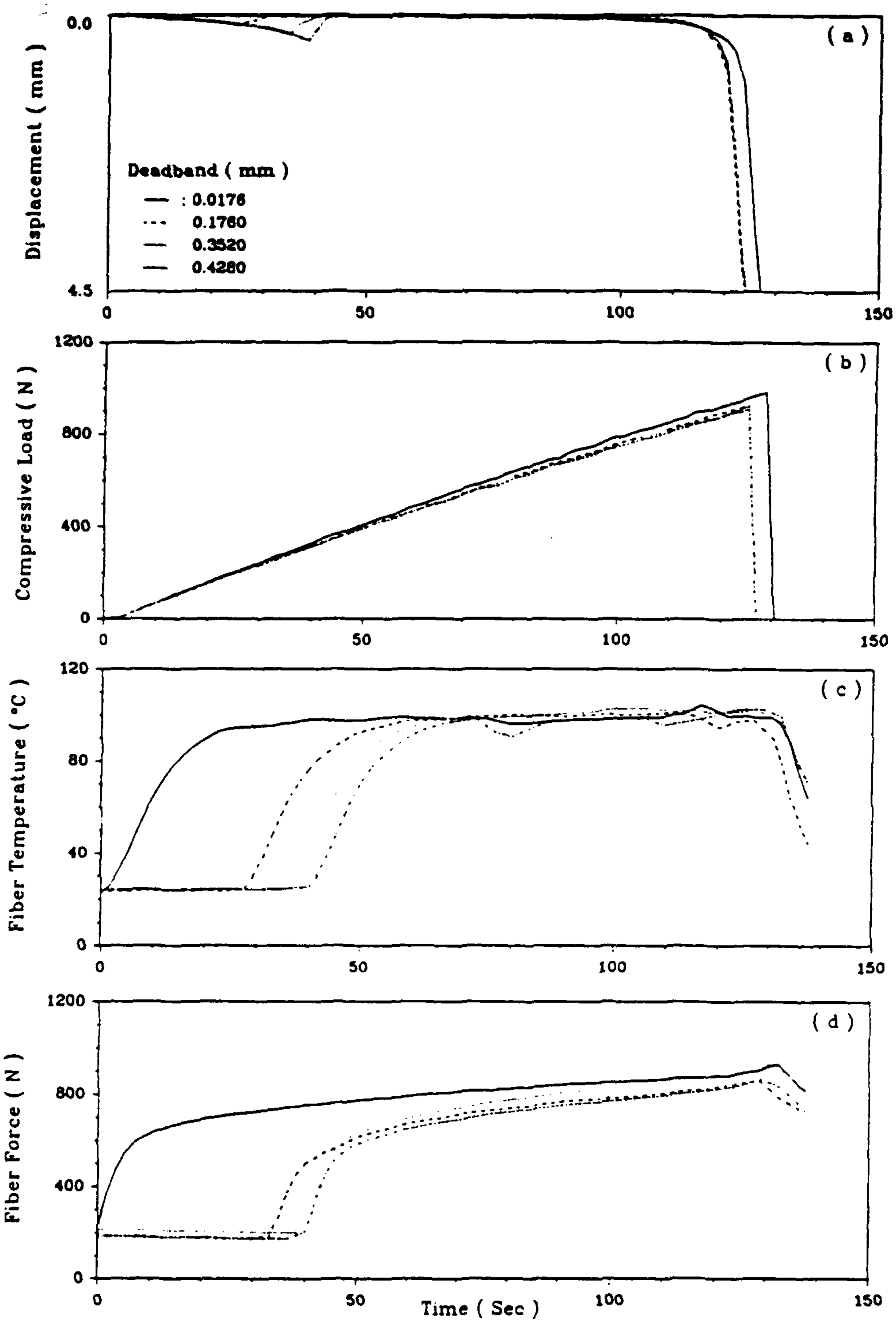

Figure (24) - Effect of controller dead band on the performance of the active control system when the controller gain is 2727 volts/mm), the initial pre-tension/fiber = 33.7N and 8 fibers are activated.

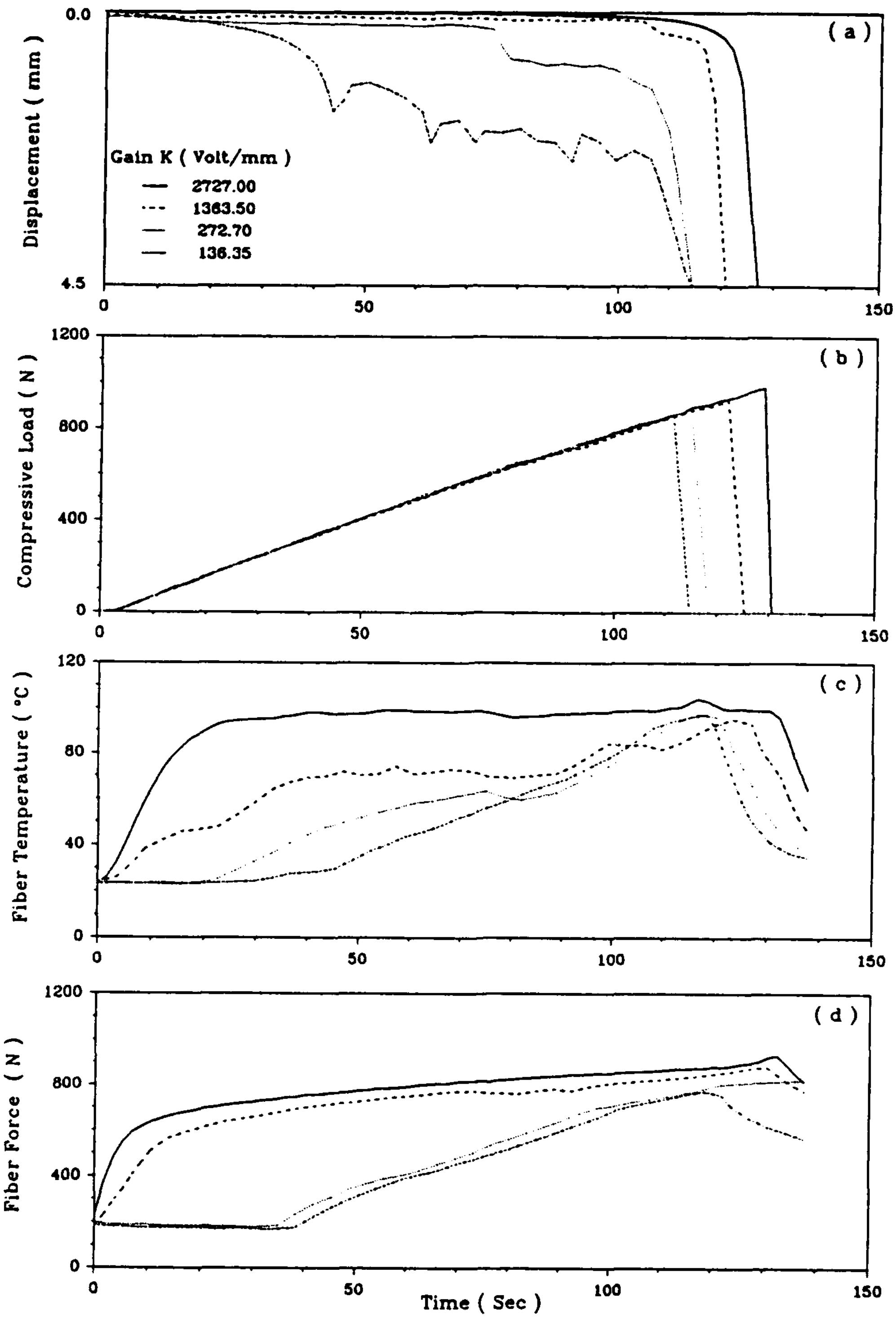

Figure (25) - Effect of controller gain on the performance of the active control system when the dead band is 0.0176 mm, the initial pre-tension/fiber = 33.7N and 8 fibers are activated.

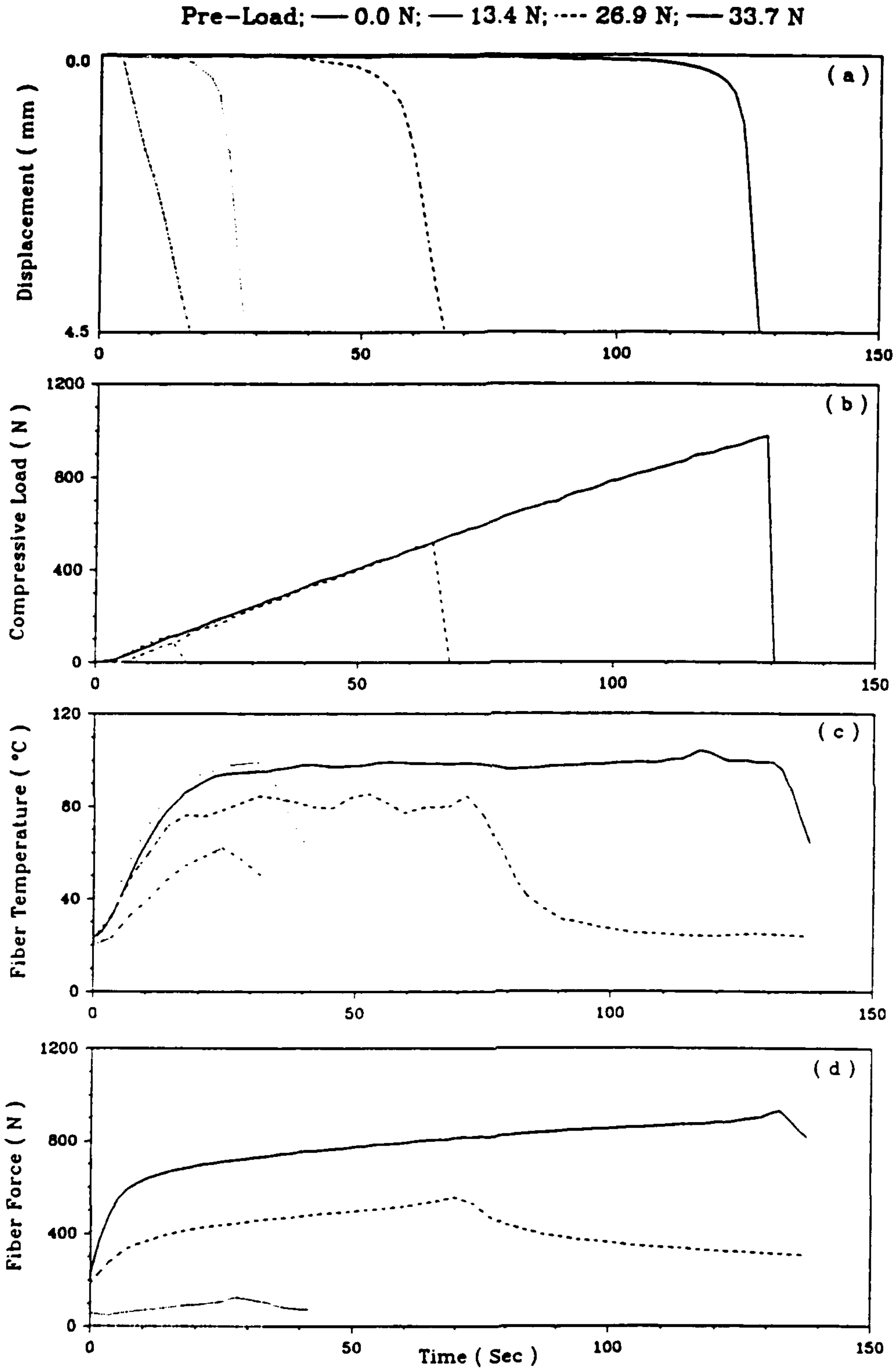

Figure (26) - Effect of initial pre-tension on the performance of the active control system when the dead band is 0.0176 mm, the controller gain is 2727 volts/mm and 8 fibers are activated.

the beam. Increasing the tension from 0.0 N/fiber to 33.7 N/fiber increases the critical buckling load from about 100 N to 950 N, respectively.

4.1.3. COMPARISON BETWEEN THEORY AND EXPERIMENTS

The mechanism of actively controlling the buckling of the NITINOL-reinforced beam can best be understood by considering Figure (27-a). The figure represents the theoretical prediction of the buckling characteristics of actively controlled NITINOL-reinforced beams. In the figure, the applied axial load is increased gradually at a linear rate of 500 N/min. For the uncontrolled beam, the critical buckling load is fixed at 320 N and remain unchanged with time. This load corresponds to a pre-tension of 33.5 N/fiber. When the applied load becomes equal to the critical buckling load, the beam is on the verge of elastic instability. The beam will buckle once the applied load exceeds the fixed critical buckling load. For the case of controlled beam, the beam starts at time $t = 0$ with the same buckling load as the uncontrolled beam. When the controller senses any deflection greater than the dead band due to the application of the external load, the buckling characteristics of the beam is enhanced as represented by the dashed characteristics. The activation of the NITINOL fibers makes the beam less susceptible to buckling as the critical buckling load is increased to become 850 N instead of the original uncontrolled load of 320 N. Accordingly, the controlled beam will not buckle until the applied load exceeds the theoretically predicted limit of 850 N.

The effect of varying the pre-tension levels on the theoretical prediction of the critical buckling load is shown in Figure (27-b) along with the corresponding experimental results. It is evident that there is a close agreement between theory and experiment.

4.2. ACTIVE CONTROL OF FLOW-INDUCED VIBRATIONS

The phenomenon of vibrations induced by the flow of fluids past flexible structures has been of concern for many years. This concern is attributed to the detrimental effects that such vibrations can have on the integrity of these structures. Several attempts have been made to passively and actively control the flow-induced vibrations of various structural members. For example, Baz and Ro (1991) utilized a direct velocity feedback controller to control the vortex-induced vibrations of a flexible cylinder. The control system relied in its operation on an electromagnetic actuator to provide the control action necessary to resist the flow-induced vibration. Baz and Kim (1992) developed a modal space control method to control the vortex-induced vibrations of a flexible cylinder using piezo-electric actuators.

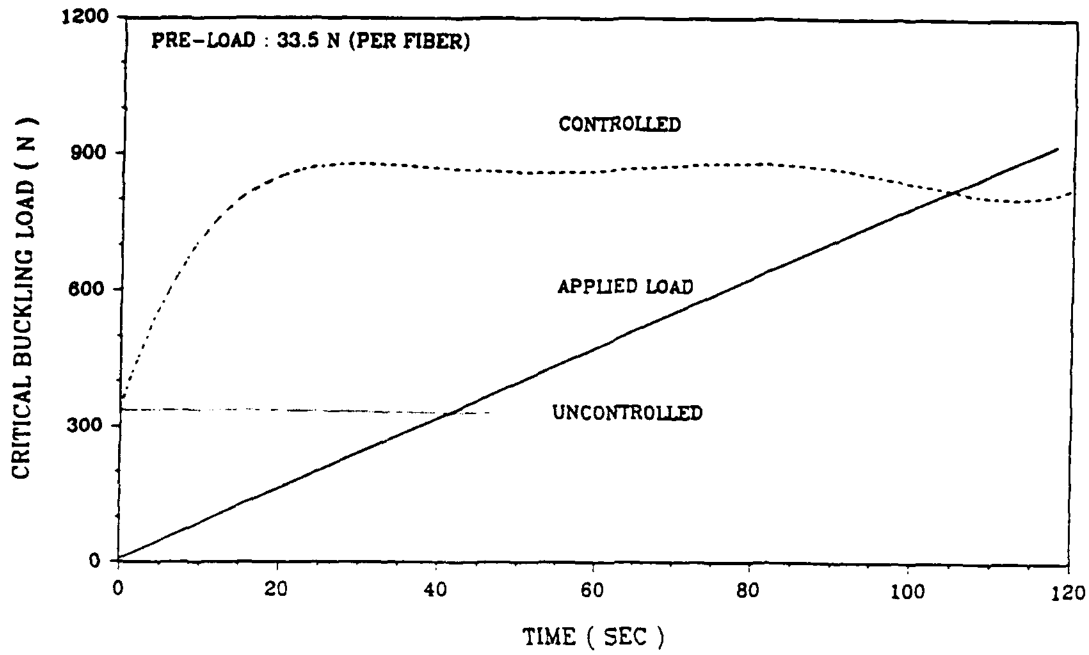

Figure (27-a) - Theoretical prediction of critical buckling load of controlled and uncontrolled beams.

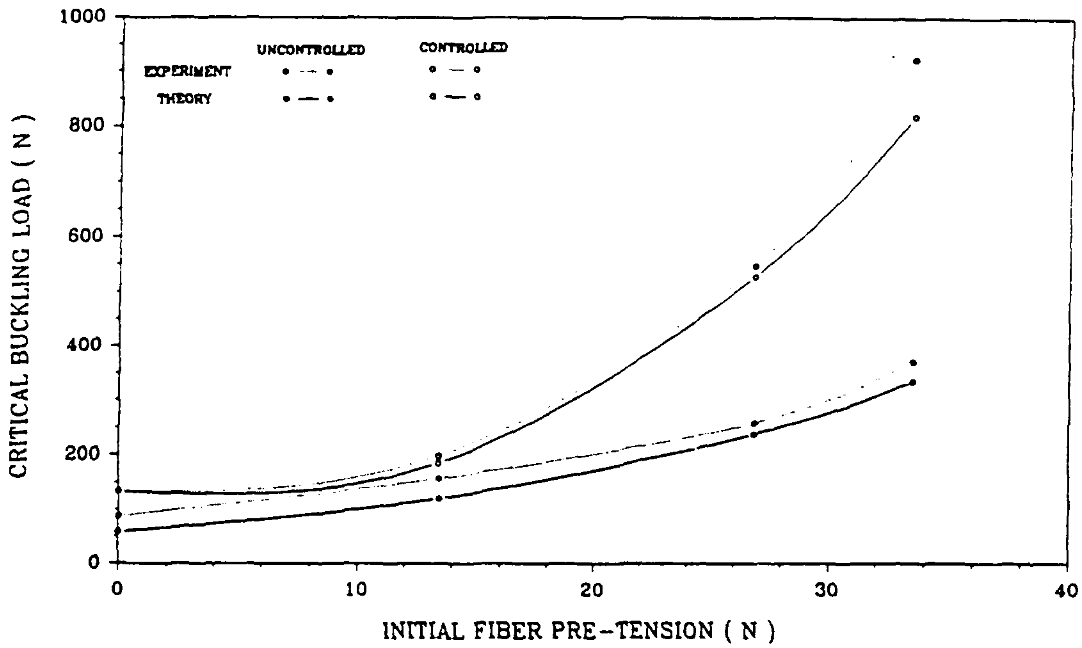

Figure (27-b) - Comparison between theoretical and experimental critical buckling loads as function of the initial fiber pre-tension.

In this study, NITINOL fibers are used as embedded actuators to control the flow-induced vibrations of NITINOL-reinforced composite beams. The control action used is of the ON-OFF type. When undesirable vibrations are detected, the NITINOL fibers are activated. The strain energy generated in the fibers by the phase transformation makes the beam stiffer and shifts its natural frequencies away from the excitation frequency. This modal tuning of the beam dynamics in response to the external disturbances can result in reducing the amplitude of vibration of the beam to acceptable limits. This will only be true if the flow-induced vibrations have a narrow frequency band. For broad band excitations, the modal tuning mechanism will not be effective in attenuating the induced vibrations as it merely shifts the vibration energy to higher frequency bands. However, in NITINOL-reinforced composites an additional mechanism can play a dominant role in the suppression of broad band vibrations. This mechanism is generated by the temperature-dependent damping characteristics of the composite matrix as shown in Figure (28). These characteristics are obtained experimentally using the Dynamic, Mechanical , and Thermal Analyzer (DMTA).

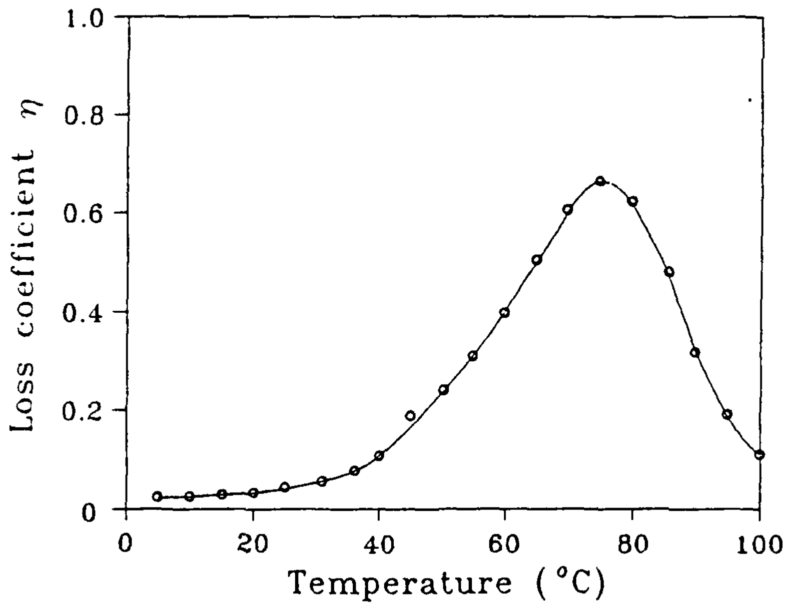

Figure (28) - Loss coefficient of fiberglass composite beam

When the NITINOL fibers are activated, the temperature of the matrix increases as indicated in section 3.4.3. Such a temperature increase is accompanied with an increase in the loss coefficient of the matrix as displayed in Figure (28). Operation at a temperature corresponding to the maximum loss coefficient is essential to achieve maximum structural damping. At that temperature, the dissipation of the vibration energy will be maximum and the attenuation of broad band vibrations will also be maximum.

Therefore, in NITINOL-reinforced composites, the interaction between the modal tuning and the enhanced damping characteristics is crucial in controlling both narrow and broad band vibrations.

4.2.1. TEST BEAM AND FACILITY

Figure (29) shows a schematic drawing of the test beam mounted in a clamped-clamped configuration inside a low speed wind tunnel. The beam is 30 cm long, 2.5 cm wide and 0.156 cm thick. It is made of fiberglass/polyester resin composite with four embedded NITINOL fibers. The fibers are 0.55 mm in diameters and are inserted inside 0.95 mm vulcanized rubber sleeves. The elastic and damping characteristics of the beam are shown in Figures (9) and (28) respectively.

The beam is mounted inside a 30 cm x 30 cm test section of a low speed wind tunnel and is subjected to flow speeds between 4.8 and 8.3 m/s.

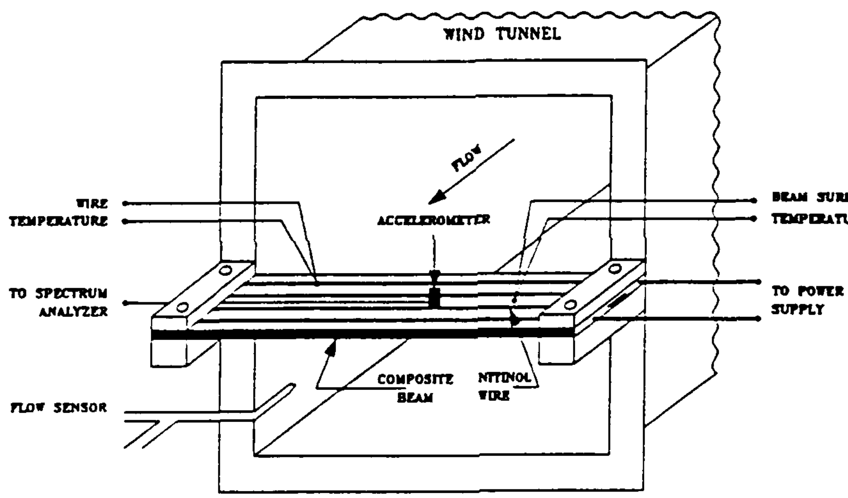

Figure (29) - A schematic drawing of a NITINOL-reinforced beam mounted inside a low-speed wind tunnel.

The NITINOL fibers have an initial pre-tension of 17.6 N each and are electrically activated by applying a voltage of 4.5 V across each fiber. This generates a current of 1.85 A and a total of 8.325 watts are dissipated in the composite beam. The resulting shift of the first three natural frequencies of the beam are shown in Figure (30). The figure shows the time history of the frequency shift when all the four fibers are activated for two minutes and then de-activated for the remaining six minutes.

The effect of varying the number of activated fibers on the frequency shift of the first three modes is shown in Figure (31-a)

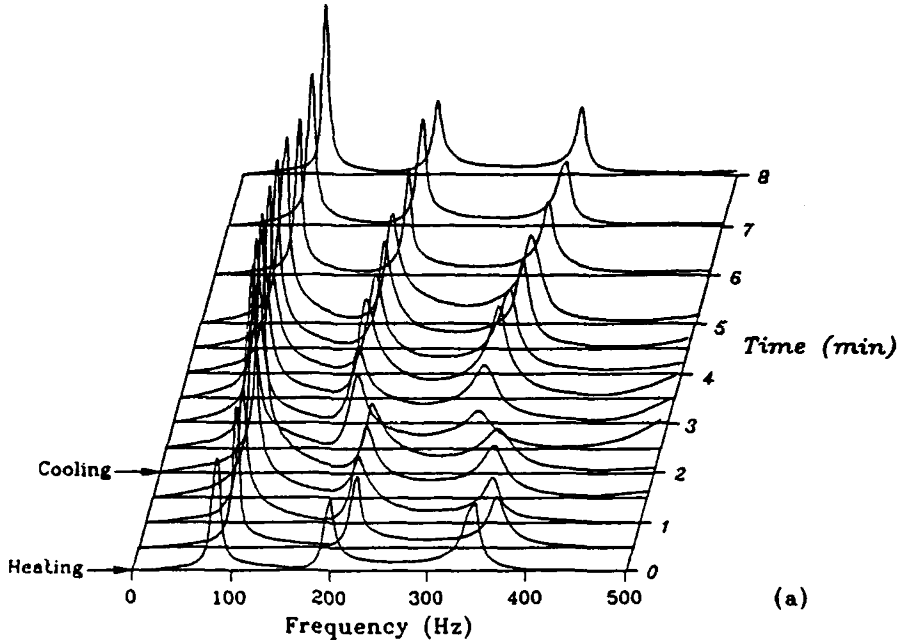

Figure (30) - The shift of the first three modes of the NITINOL-reinforced beam during the activation and de-activation cycles of all the four NITINOL fibers

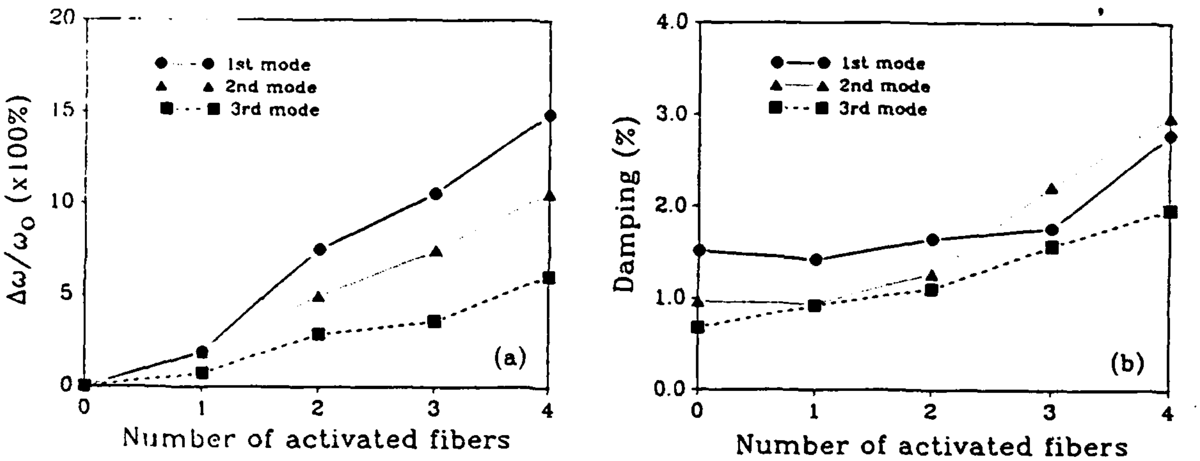

Figure (31) - Effect of number of activated NITINOL fibers on the frequency shift and damping ratio of the first three modes of the NITINOL-reinforced beam.

after steady-state conditions are attained. The results displayed in the figure are normalized with respect to the natural frequencies measured at 25°C. The corresponding variation of the modal damping is shown in Figure (31-b). The figure clearly indicates that increasing the number of activated fibers results in enhancing the damping characteristics of the beam. This is attributed to the increase in the beam temperature when the number of activated fibers is increased. This in turn makes the composite matrix of the beam operate near the point of maximum loss coefficient shown in Figure (28).

4.2.2. EXPERIMENTAL RESULTS

The performance of the NITINOL-reinforced composite beam subjected to flow-induced vibrations is monitored at different flow speeds with and without the activation of the NITINOL fibers. The experiments aim at demonstrating the feasibility of NITINOL fibers in attenuating the flow-induced vibrations.

Figure (32) shows the spectra of the amplitude of vibration of the beam as measured at different flow speeds ranging between 4.8 m/s and 8.32 m/s. The figure also shows a comparison between the amplitudes of

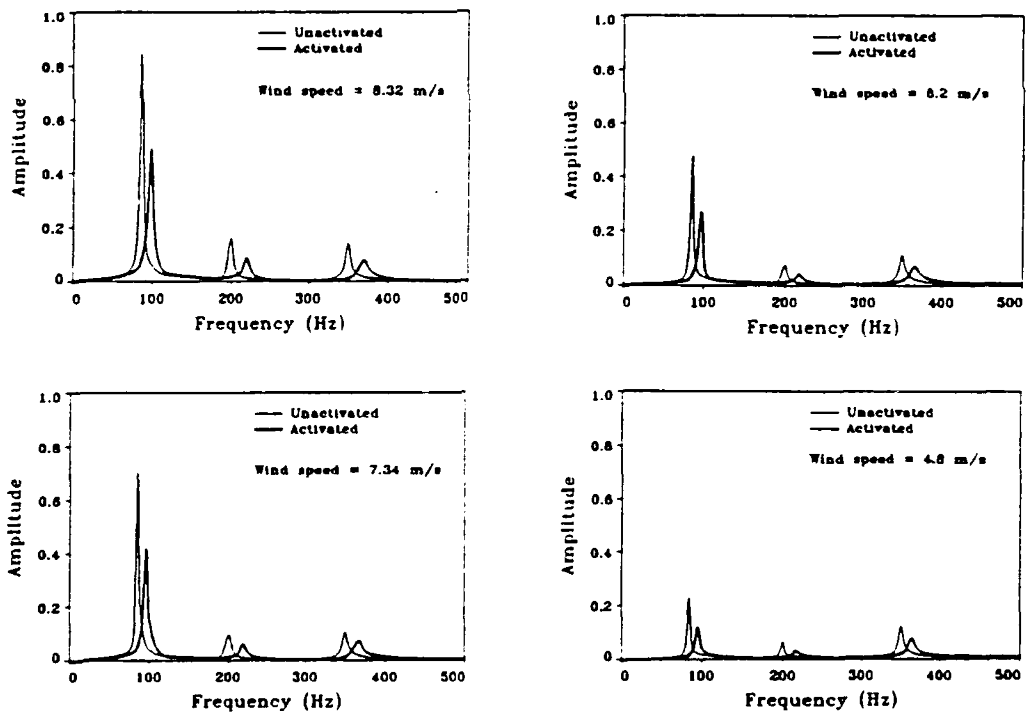

Figure (32) - Spectra of the amplitudes of vibration of the NITINOL-reinforced beam at different flow speeds with and without the activation of the four NITINOL fibers.

THIS

PAGE

IS

MISSING

IN

ORIGINAL

DOCUMENT

207

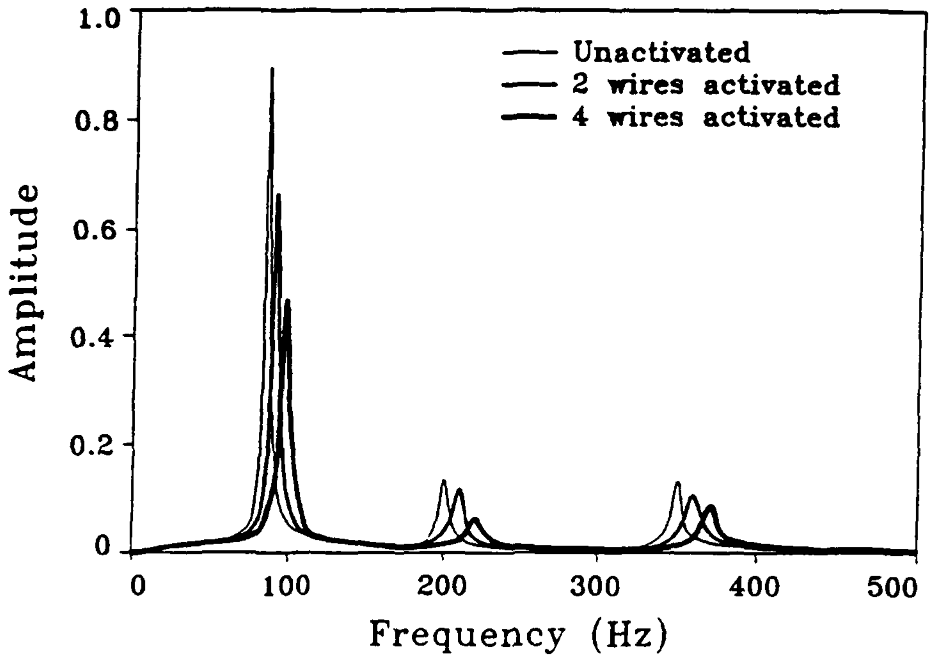

Figure (34) - Effect of activating different numbers of NITINOL fibers on the spectra of the amplitude of flow-induced vibration at flow speed = 8.32 m/s

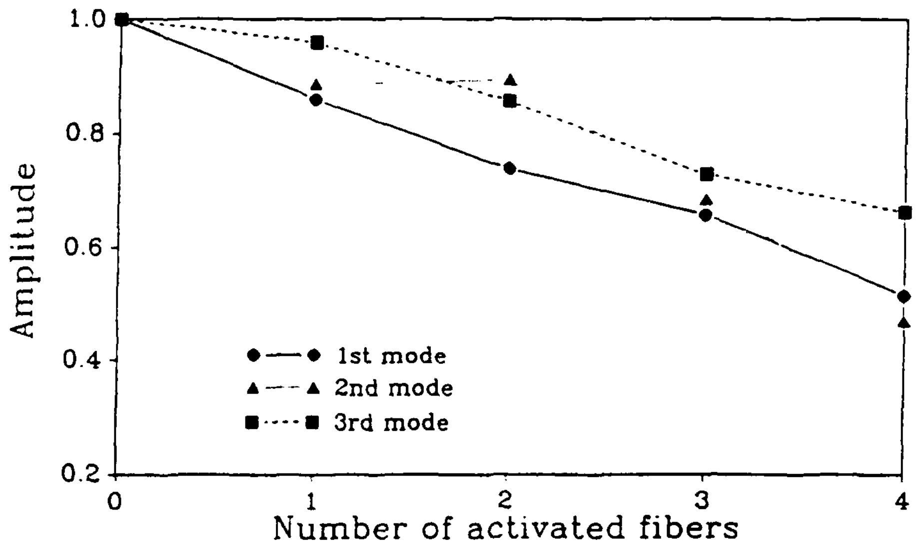

Figure (35) - Effect of number of activated NITINOL fibers on the amplitude of flow-induced vibration at flow speed of 8.32 m/s

Emphasis has been placed in the presentation on the actuation capabilities of the NITINOL fibers. Extensive efforts are, however, in progress to use the NITINOL fibers to extract modal and physical displacements of structures with multi-modes of vibration (Baz, Poh and Gilheany 1991).

With such built-in sensing and controlling capabilities, NITINOL-reinforced composites can provide a means for continuously tuning the structural characteristics to adapt to changes in the operating conditions. These features will be particularly useful in many critical structures that are intended to operate autonomously for long durations in isolated environment such as defense vehicles, space structures and satellites.

ACKNOWLEDGEMENTS

This work is funded by a grant from the US Army Research Office (Grant number DAAL03-89-G-0084). Special thanks are due to Dr. Gary Anderson, the technical monitor and Chief of the Structures and Dynamics Branch of ARO, for his invaluable and continuous technical inputs.

NOMENCLATURE

[A]	interpolating function of beam deflection
$[A_i]$	ith element of [A]
A_m	cross sectional area of beam
[B]	matrix of first derivatives of the nodal interpolating functions
c	wave propagation speed
[C], [D]	first and second derivatives of interpolating function of beam deflection
E_m	Young's modulus of beam
[F]	vector of external loads acting on beam
h	convective heat transfer coefficient
I_m	area moment of inertia of beam
k	thermal conductivity of beam
$[k^e_{1,2,3}]$	matrices given by equations (32), (33) and (34) respectively
$[K_e]$	stiffness matrix of beam element
ℓ_y, ℓ_z	direction cosines of outward normals to beam boundaries
L	length of beam element and NITINOL fiber
M_i	external moment acting at ith node
$[M_e]$	mass matrix of beam element
$m_e(i,j)$	the element i,j of the mass matrix
[N]	interpolating function of beam temperature
N_i	interpolating function of ith node
p	number of vertices of element
$P_{m,n,t}$	mechanical, net and thermal axial loads acting on beam
$[P^e]$	matrix given by equation (35)
q_n	generalized coordinate of the nth vibration mode of NITINOL fiber
$\ddot{q}_n$	generalized acceleration of the nth vibration mode of NITINOL fiber
Q	heat flux per unit area
$S_{1,2}$	boundaries of the NITINOL fibers and beam respectively
t	time
T_o	initial tension in a NITINOL fiber
T_t	total tension in a NITINOL fiber
V_i	shear force acting at the ith node
w	transverse deflection of beam and NITINOL fibers
W_1	work done by transverse loads
W_{2m}	work done by mechanical axial loads
W_{2t}	work done by thermal axial loads
W_3	strain energy of beam
W_4	strain energy of NITINOL fiber
x, y, z	cartesian coordinates along beam neutral axis and cross section respectively

Greek letters

α	thermal diffusivity of beam
$[\delta]$	the deflection vector of beam element
ϑ_i	angular deflection of ith node
Θ	temperature at any location (y,z) of beam cross section
Θ_a	ambient temperature
$[\Theta^e]$	vector of nodal temperatures of element
ϕ_n	mode shape of the nth mode
ω_n	natural frequency of the nth mode

NOMENCLATURE

[A]	interpolating function of beam deflection
$[A_i]$	ith element of [A]
A_m	cross sectional area of beam
[B]	matrix of first derivatives of the nodal interpolating functions
c	wave propagation speed
[C], [D]	first and second derivatives of interpolating function of beam deflection
E_m	Young's modulus of beam
[F]	vector of external loads acting on beam
h	convective heat transfer coefficient
I_m	area moment of inertia of beam
k	thermal conductivity of beam
$[k^e_{1,2,3}]$	matrices given by equations (32), (33) and (34) respectively
$[K_e]$	stiffness matrix of beam element
ℓ_y, ℓ_z	direction cosines of outward normals to beam boundaries
L	length of beam element and NITINOL fiber
M_i	external moment acting at ith node
$[M_e]$	mass matrix of beam element
$m_e(i,j)$	the element i,j of the mass matrix
[N]	interpolating function of beam temperature
N_i	interpolating function of ith node
p	number of vertices of element
$P_{m,n,t}$	mechanical, net and thermal axial loads acting on beam
$[P^e]$	matrix given by equation (35)
q_n	generalized coordinate of the nth vibration mode of NITINOL fiber
$\ddot{q}_n$	generalized acceleration of the nth vibration mode of NITINOL fiber
Q	heat flux per unit area
$S_{1,2}$	boundaries of the NITINOL fibers and beam respectively
t	time
T_o	initial tension in a NITINOL fiber
T_t	total tension in a NITINOL fiber
V_i	shear force acting at the ith node
w	transverse deflection of beam and NITINOL fibers
W_1	work done by transverse loads
W_{2m}	work done by mechanical axial loads
W_{2t}	work done by thermal axial loads
W_3	strain energy of beam
W_4	strain energy of NITINOL fiber
x, y, z	cartesian coordinates along beam neutral axis and cross section respectively

Active buckling control of nitinol-reinforced composite beams

A. Baz, J. Ro, M. Mutua and J. Gilheany

Mechanical Engineering Department, The Catholic University of America, Washington, DC 20064

ABSTRACT

The buckling characteristics of flexible fiberglass composite beams are actively controlled by activating optimal sets of a shape memory alloy (NITINOL) wires which are embedded along the neutral axes of the beams. With such active control capabilities, the beams can be manufactured from light weight sections without compromising their elastic stability. This feature will be invaluable in building light weight structures that have high resistance to failure due to buckling.

A finite element model is developed to analyze the individual contributions of the fiberglass-resin laminate, the NITINOL wires, and the shape memory effect to the overall performance of the composite beams. A closed-loop computer-controlled system is built to validate the finite element model. The system is used to control the buckling of a fiberglass polyester resin beam which is 63.75 cm long, 0.45 cm thick and 2.54 cm wide reinforced with 8 NITINOL - 55 wires that are 0.55 mm in diameter. The results obtained confirm the developed theoretical model and indicate that the critical buckling load can be increased three times when compared to the uncontrolled beam.

1. INTRODUCTION

Considerable attention has been devoted recently to the utilization of the Shape Memory NIckel-TItanium alloy (NITINOL) in developing SMART composites that are capable of adapting intelligently to external disturbances (Ikegami et al. 1990, Rogers et al. 1991, and Baz et al. 1990 and 1991). Such wide acceptance stems from the fact that NITINOL acts as an actuator converting thermal energy into mechanical energy (Perkins 1975 and Duerig et al. 1990) as it undergoes its unique phase transformation from low temperature martensite to high temperature austenite. During this phase transformation process large phase recovery forces are generated and thereby alter the strain energy of the composite inside which the NITINOL fibers are embedded. With such capabilities, the static and dynamic performance of the SMART composites can be optimized and tailored to match changes in the operating conditions.

Emphasis is placed, in the present work, on using the shape memory effect of the NITINOL fibers in controlling the buckling of fiberglass composite beams. The NITINOL fibers are embedded inside vulcanized rubber sleeves placed along the neutral axes of these composite beams as shown in

Figure (1). In this arrangement, the fibers are free to move during the phase transformation process in order to avoid degradation and/or destruction of the shape memory effect which may result when the fibers are completely bonded inside the composite matrix. The NITINOL fibers are trained to memorize the shape of the unbuckled beam and when the beam is deflected under the action of external compressive loads, the controller activates the NITINOL fibers by heating them above their transformation temperature. The generated phase recovery forces bring the beam back to its memorized undeflected position. The present study is motivated by the work of Baz and Tampe (1989) where external helical shape memory actuators are used to enhance the buckling characteristics of long slender beams.

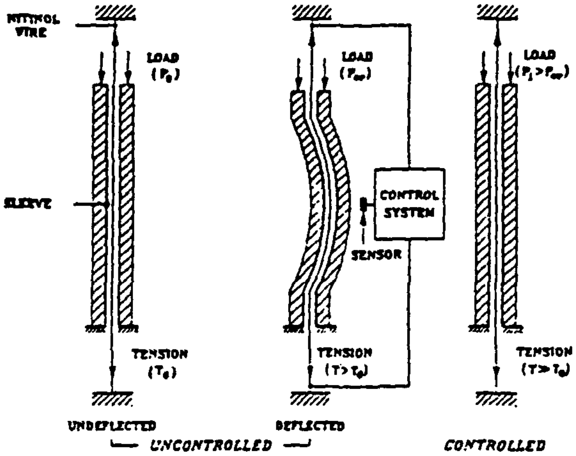

Figure (1) - Principle of buckling control of NITINOL-reinforced composites

2. STATIC CHARACTERISTICS OF NITINOL-REINFORCED BEAMS

The static characteristics of NITINOL-reinforced composite beams are primarily governed by their stiffness. The overall beam stiffness is made up of the following components: the flexural rigidity of the beam, the geometric stiffness that accounts for the axial and thermal loading as well as the stiffness imparted by the elasticity of the NITINOL fibers. These individual components of the beam stiffness can be determined by considering the NITINOL-reinforced beam element shown in Figure (2) with the forces acting on it and the associated displacements. The combined stiffness of the element can be obtained using the principle of conservation of energy and equating the work done by external loads to the strain energies stored in the element. In the present analysis, the theory of Bernoulli-Euler beams is used with the assumption of small deflections.

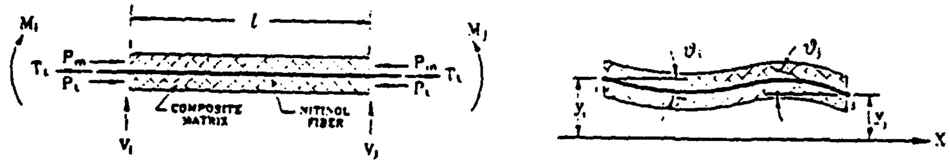

(a) (b)

Figure (2) - NITINOL-reinforced beam element with forces and displacements

2.1 External Work

The work done by the external loads includes:

a. work done by transverse loads and moments (W_1): This work is given by

$$W_1 = 1/2\ [\delta]^T\ [F], \tag{1}$$

where $[\delta]$ is deflection vector and $[F]$ is transverse load vector.

b. work done by the axial mechanical loads (W_{2m}): W_{2m} is given by

$$W_{2m} = P_m\ /\ 2 \int_0^L (dw/dx)^2\ dx, \tag{2}$$

where P_m is the external axial compressive load acting on the beam.

c. work done by the axial thermal loads (W_{2t}): W_{2t} represents the work done by the thermal loads P_t on the beam element due to changes in the temperature $\Delta\theta$ of the element caused by changes in the ambient temperature or during the activation and de-activation of the NITINOL fibers. It is given by

$$W_{2t} = P_t\ /\ 2 \int_0^L (dw/dx)^2\ dx, \tag{3}$$

where P_t is

$$P_t = \alpha\ \Delta\theta\ E_m\ A_m, \tag{4}$$

where α is the thermal expansion coefficient of the composite, E_m is its modulus of elasticity and A_m is the beam cross sectional area.

2.2 Stored strain energy

The stored strain energy consists of two components:

a. strain energy of beam (W_3): The energy stored in the beam element due to its bending is given by

$$W_3 = E_m\ I_m\ /\ 2 \int_0^L (d^2w/dx^2)^2\ dx, \tag{5}$$

where $E_m\ I_m$ is the flexural rigidity of the beam.

b. strain energy of NITINOL fibers (W_4): Considering the NITINOL fiber as a string with a tension T which is displaced laterally a distance w from the neutral axis of the beam. Then its stored strain energy W_4 is given by

$$W_4 = T\ /\ 2 \int_0^L (dw/dx)^2\ dx. \tag{6}$$

Equating the sum of the work done by the external forces F, P_m and P_t to the sum of the strain energies stored in the beam and the NITINOL fibers gives

$$W_1 + W_{2m} + W_{2t} = W_3 + W_4. \tag{7}$$

Substituting equations (1), (2), (3), (5) and (6) into equation (7) yields

$$[\delta]^T[F] = E_m\ I_m \int_0^L (d^2w/dx^2)^2\ dx - P_n \int_0^L (dw/dx)^2\ dx, \tag{8}$$

where P_n is the net axial force give by

$$P_n = (\ P_m + P_t - T). \tag{9}$$

Defining a proper displacement function for the composite beam element, one can write the beam deflection w as

$$w = [A]\ [\delta], \tag{10}$$

where the elements of matrix [A] are function of x (Fenner 1975).

Accordingly, dw/dx and d^2w/dx^2 can be obtained by differentiating equation (10) with respect to x to yield

$$dw/dx = [C]\ [\delta] \quad \text{and} \quad d^2w/dx^2 = [D]\ [\delta]. \tag{11}$$

If the stiffness matrix $[K_e]$ of the element is defined by the following relationship

$$[F] = [K_e]\ [\delta], \tag{12}$$

then, $[K_e]$ can be determined by combining equations (8), (11) and (12) as follows

$$[K_e] = E_m\ I_m \int_0^L [D]^T[D]\ dx - P_n \int_0^L [C]^T[C]\ dx. \tag{13}$$

The element stiffness matrix $[K_e]$ of equation (13) consists of two components: the conventional transverse stiffness and the geometric stiffness that combines the effect of the axial mechanical loads, axial thermal loads and the tension of the NITINOL reinforcing fibers. Equation (13) also represents the basic equation for understanding the role that the NITINOL fibers can play in controlling the static characteristics of the composite beam. For example, if the beam is not reinforced by NITINOL fibers (i.e. T = 0) and the mechanical and thermal loads induce compressive stresses in the beam, then the geometric stiffness will increase and the total element stiffness will decrease. When the combined effect of the mechanical and thermal loads reaches a critical magnitude such that the geometric stiffness becomes equal to the flexural stiffness of the beam, the beam stiffness vanishes and the beam becomes elastically unstable. Subjecting the beam to any additional external disturbance will cause the beam to buckle.

It should be pointed out that the thermal loading, as it increases the geometric stiffness, also decreases the flexural stiffness of the beam because it reduces its effective modulus of elasticity E_m. Such a dual effect makes the beam buckle under smaller thermal loads than under pure mechanical loading.

However, the critical load of the un-reinforced beam can be increased by embedding pre-strained NITINOL fibers into the beam. If the tension T, resulting from the pre-strain alone, is high enough to counter-balance the mechanical and thermal effects then the beam stiffness can be maintained unchanged. For higher pre-strain levels, the beam stiffness can be enhanced. Further enhancement can be achieved when the shape memory effect of the NITINOL fibers is activated by heating the fibers above their phase transformation temperature. The additional tension, induced into the fibers by the phase recovery forces, makes the net axial load P_n negative and accordingly increases the overall stiffness of the beam element. However, it is essential that the total tension in the NITINOL fibers, i.e., the sum of the tension due to the pre-strain and the phase recovery force, must exceed the mechanical and thermal loads and compensate for the softening effect in the matrix resulting from heating the NITINOL fibers inside the composite matrix.

Therefore, effective control of the stiffness of NITINOL-reinforced composites can be achieved by proper selection of the initial pre-strain level of the NITINOL fibers. This selection is particularly crucial as the pre-strain level determines the generated levels of recovery forces.

3. THE EXPERIMENTAL SET-UP AND RESULTS

3.1. Experimental set-up

Figure (3) shows a schematic drawing of the experimental set-up used in actively controlling the buckling of a NITINOL-reinforced beam. The beam dimensions are 63.75 cm by 2.5 cm by 0.44 cm. The beam is reinforced by eight 0.55 mm NITINOL fibers which are embedded symmetrically along the neutral axis of the beam.

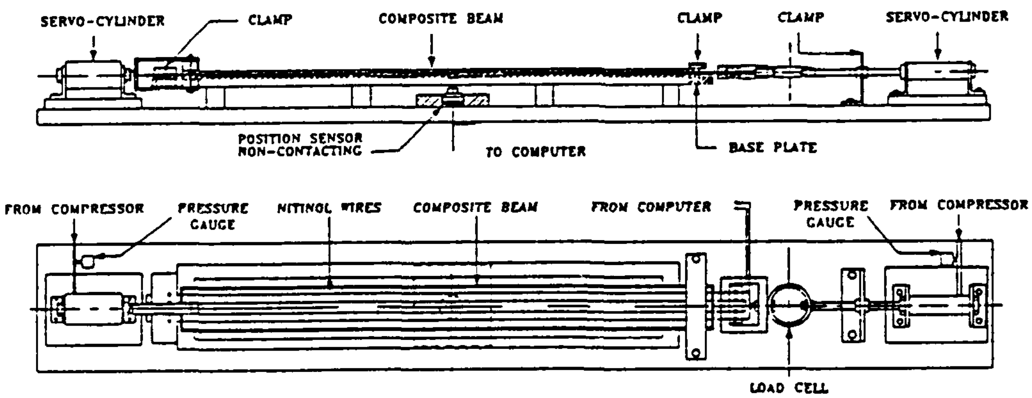

Figure (3) - Schematic drawing of the active buckling control experiment.

The right end of the beam is clamped to a fixed base and the left end is connected to the piston of a loading cylinder. The cylinder is pressurized by compressed air from the storage tank of an air compressor. The increasing compressive load applied by the load cylinder to the beam will eventually cause the beam to buckle. The resulting deflection of the beam is monitored continuously by a non-contacting sensor which is placed at the mid-span of the beam. The sensor also serves as physical stop to prevent excessive deflection once buckling has occured. The output signals of the sensor is sent to a micro-computer via a set of analog-to-digital converters. The processing of the sensor's signal is shown in the controller block diagram shown in Figure (4). When the beam deflection exceeds a pre-set value of a dead-band, the controller is turned on using a

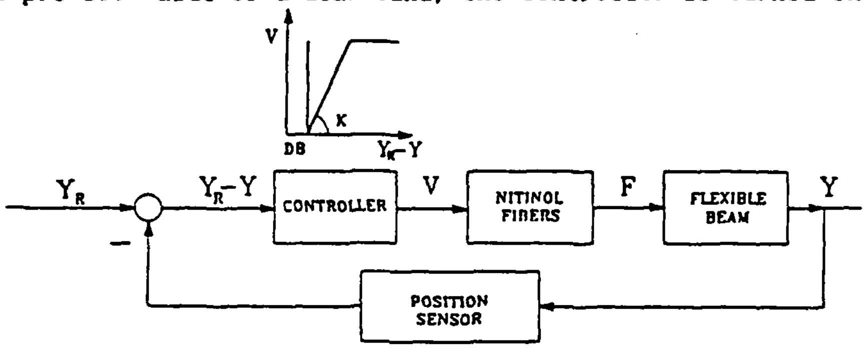

Figure (4) - Block diagram of the active buckling control system

proportional controller with a saturation limit. The control action is sent via a digital-to-analog converter to a power amplifier to activate the NITINOL fibers embedded inside the compressively loaded composite beam. The activation of the NITINOL fibers will compensate for the monitored deflection and the phase recovery forces developed in the fibers will attempt to bring the beam back to its undeflected position.

In the active buckling control system described, the NITINOL reinforcing fibers are clamped at one end to the fixed base and at the other end to pre-tensioning cylinder via a load cell. The load cell monitors the initial value of the pre-tension applied to the NITINOL fibers by the pre-tensioning cylinder. The load cell also continuously measures the phase recovery forces developed in the NITINOL fibers as they undergo their phase transformation.

3.2. Experimental Results

Figure (5) shows a comparison of the performance with and without the active buckling control. The results displayed are for a NITINOL-reinforced beam with each of the eight fibers has an initial tension of 33.7 N which corresponds to an initial pre-strain of 0.35%. For the controlled cases, the controller dead band corresponds to deflection error of 0.0176 mm and the controller gain is 2727 volt/mm. The saturation limit is 6 volts/fiber and the maximum current is 1.6A.

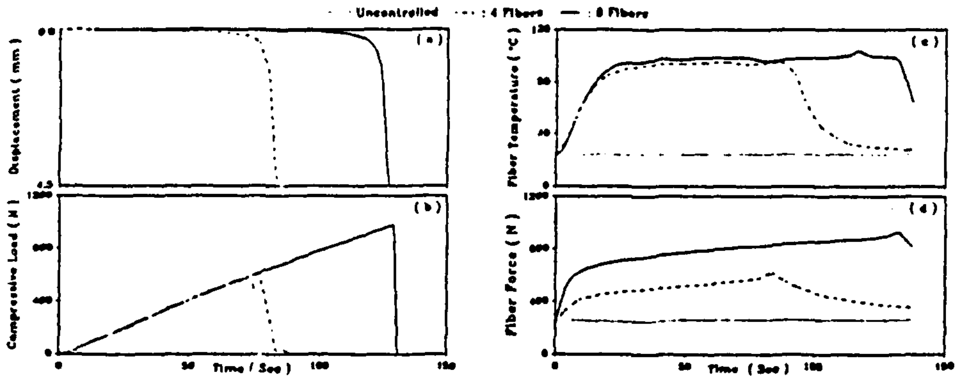

Figure (5) - Performance of buckling controller with 0, 4 and 8 NITINOL fibers activated (dead band = 0.0176 mm, gain = 2727 volts/mm).

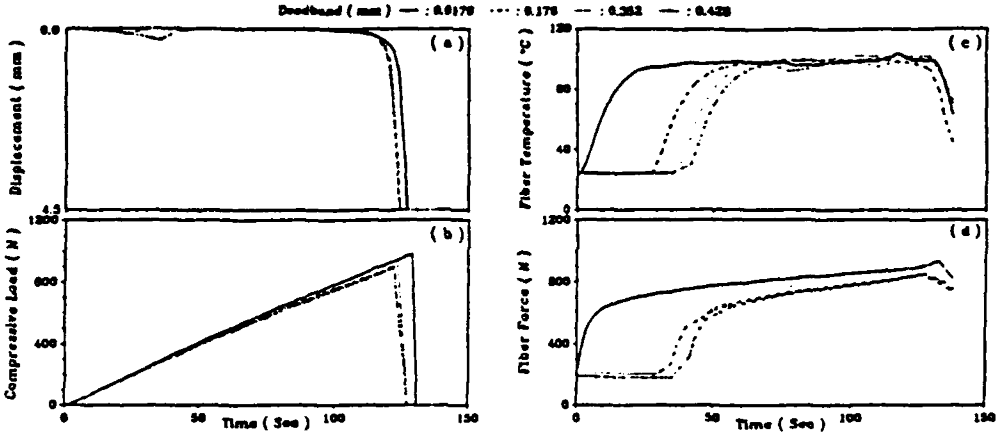

Figure (6) - Effect of dead band (gain = 2727 volts/mm, initial pre-tension/fiber = 33.7N and 8 fibers are activated).

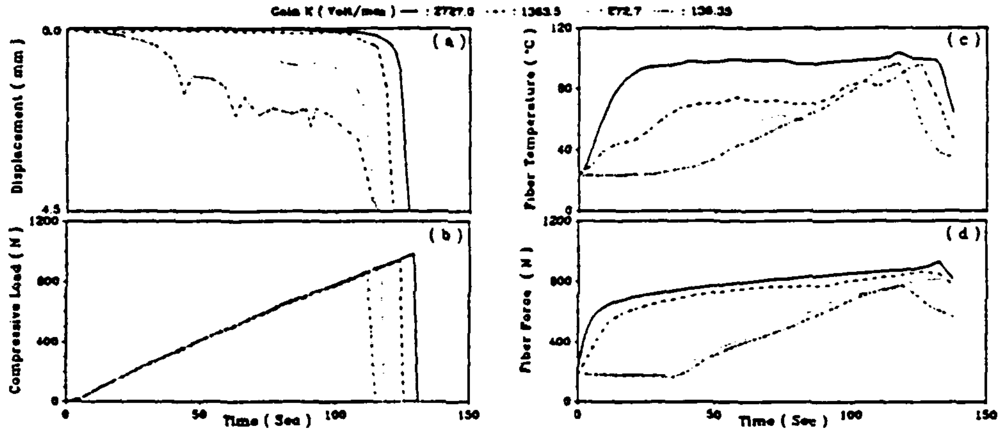

Figure (7) - Effect of controller gain (dead band = 0.0176 mm, initial pre-tension/fiber = 33.7N and 8 fibers are activated).

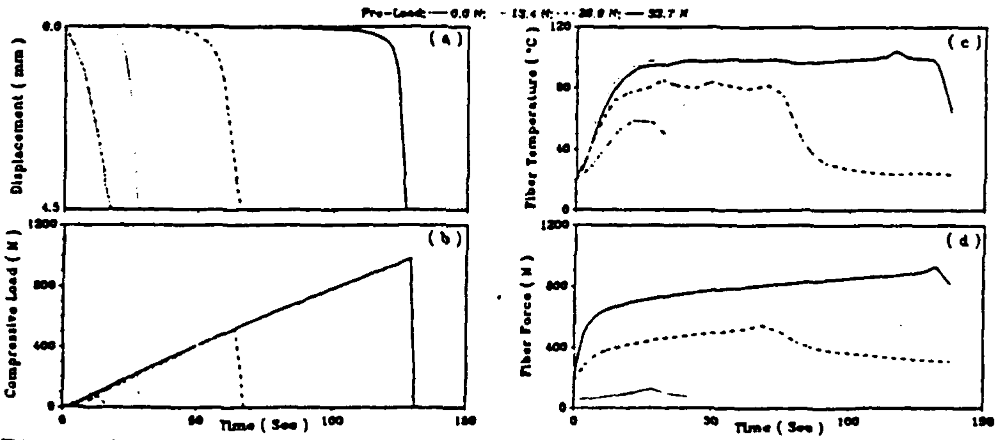

Figure (8) - Effect of initial pre-tension (dead band = 0.0176 mm, gain = 2727 volts/mm and 8 fibers are activated).

In Figure (5-a), the deflection of the beam resulting from the application of a gradually increasing compressive load is shown. The rate of load increase is 500 N/min as shown in Figure (5-b). It can be observed that the uncontrolled beam buckles when the increasing compressive axial load exceeds 330 N. However, when all eight NITINOL fibers are activated, the beam can withstand axial loads up to 950 N before it begins to buckle. Therefore, with the NITINOL reinforcement it is possible to almost triple the critical buckling load of the beam. With four activated fibers, the critical buckling load is about 700 N which corresponds to about double the critical load of the uncontrolled beam. Figure (5-c) shows the corresponding time history of the temperature of the NITINOL fibers due to the activation and de-activation of the controller. In Figure (5-d), the time history of the phase recovery forces developed in the NITINOL fibers is shown. The tension in the fibers remains equal to the initial pre-tension, i.e. 33.7N x 8 = 269.6N, for the uncontrolled case. However, the tension increases to approximately 1000 N when eight NITINOL fibers are activated.

It is also possible to energize different sets of the NITINOL fibers to counterbalance the external loading condition in order to prevent buckling of the composite beam. For small external loads it is only necessary to energize a few fibers, but if the load increases the controller can energize a larger number of fibers to maintain the beam in its undefelected form.

The effect of varying the controller parameters on the performance of the active control system is shown in Figures (6), (7) and (8). In Figure (6), the effect of varying the control dead-band on the system performance is shown. In this case, the control action is only generated when the beam deflection exceeds the dead band. This is accomplished by the heating of the NITINOL fibers and the development of the phase recovery forces as shown in Figures (6-c) and (6-d), respectively. For the range of dead bands considered, between 0.0176 mm and 0.528 mm, the effect on the critical buckling loads is insignificant.

The effect of decreasing the controller gain from 2727 volt/mm to 136.35 volt/mm on the system performance is shown in Figure (7). This effect decreases the slope of temperature rise of the NITINOL fibers and, in turn, the rate at which the corresponding phase transformation forces are recovered. Changing the controller gain is found to influence to some extent the critical buckling load. For example, when the controller gain is 2727 volt/mm the critical buckling load is 950 N and when the gain is reduced to 136.35 volt/mm the critical buckling load become about 850N. Therefore, reducing the controller gain by a factor of 1/20 only results in a 10.5% reduction in the critical buckling load.

The effect that the pre-tension has on the system performance is shown in Figure (8) for a dead band of 0.0176 mm and controller gain of 2727 volts/mm. It is clear from the results obtained that , the pre-tension plays the most crucial role in controlling the buckling of the beam. Increasing the tension from 0.0 N/fiber to 33.7 N/fiber increases the critical buckling load from about 100 N to 950 N, respectively.

4. COMPARISON BETWEEN THEORY AND EXPERIMENTS

The mechanism of actively controlling the buckling of the NITINOL-reinforced beam can best be understood by considering Figure

(9-a). The figure represents the theoretical prediction of the buckling characteristics of actively controlled NITINOL-reinforced beams. In the figure, the applied axial load is increased gradually at a linear rate of 500 N/min. For the uncontrolled beam, the critical buckling load is fixed at 320 N and remains unchanged with time. This load corresponds to a pre-tension of 33.5 N/fiber. When the applied load becomes equal to the critical buckling load, the beam is on the verge of elastic instability. The beam will buckle once the applied load exceeds the fixed critical buckling load. At time t = 0, the controlled beam has the same buckling load as the uncontrolled beam. But, when the controller senses any deflection greater than the dead band due to the application of the external load, the buckling characteristics of the beam is enhanced as represented by the dashed characteristics. The activation of the NITINOL fibers makes the beam less susceptible to buckling as the critical buckling load is increased to become 850 N instead of the original uncontrolled load of 320 N. Accordingly, the controlled beam will not buckle until the applied load exceeds the theoretically predicted limit of 850 N. The effect of varying the pre-tension levels on the theoretical prediction of the critical buckling load is shown in Figure (9-b) along with the corresponding experimental results. It is evident that there is a close agreement between theory and experiment.

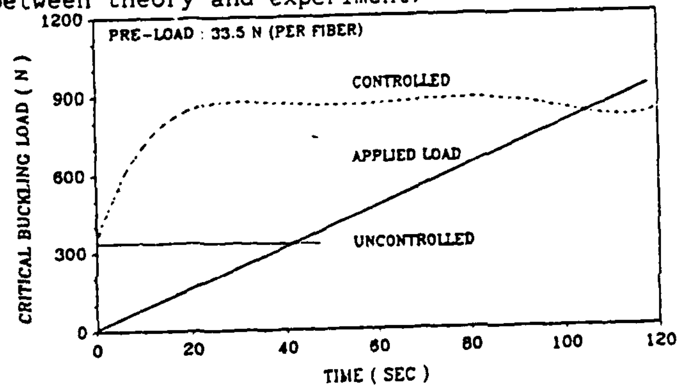

Figure (9-a) - Theoretical prediction of critical buckling load of controlled and uncontrolled beams.

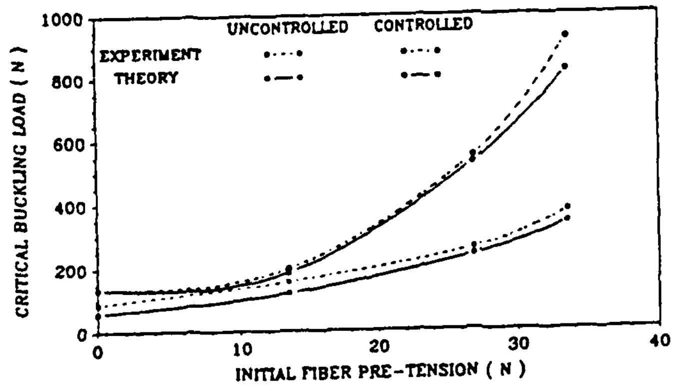

Figure (9-b) - Comparison between theoretical and experimental critical buckling loads as function of the initial fiber pre-tension.

5. CONCLUSIONS

The buckling characteristics of NITINOL-reinforced composite beams have been presented. The fundamental issues governing the behavior of this new class of SMART composites have been introduced. Applications of NITINOL reinforcing fibers in the control of buckling have been successfully demonstrated.

Emphasis has been placed in the presentation on the actuation capabilities of the NITINOL fibers. Extensive efforts are, however, in progress to use the NITINOL fibers to extract modal and physical displacements of structures with multi-modes of vibration (Baz, Poh and Gilheany 1991).

With such built-in sensing and controlling capabilities, NITINOL-reinforced composites can provide a means for continuously tuning their structural characteristics to adapt to changes in the operating conditions. These features will be particularly useful in many critical structures that are intended to operate autonomously for long durations in isolated environment such as defense vehicles, space structures and satellites.

REFERENCES

Baz, A., and Tampe, L., "Active Control of Buckling of Flexible Beams", Proc. of ASME Design Technical Conference, Montreal, Canada, Vol. DE-16, pp.211-218, Sept. 1989.

Baz, A., Iman, K. and McCoy, J., "Active Control of Flexible Beams using Shape Memory Actuators", *J. of Sound & Vibration*, Vol.140, No.3, pp.437-456, 1990.

Baz, A., Poh, S. and Gilheany, J., "A Multi-mode Distributed Sensor for Vibrating Beams", ASME Winter Annual Meeting, Atlanta, GA., Dec. 1991.

Duerig, T.W., Melton, K.N., Stockel, D. and Wayman, C., *Engineering Aspects of Shape Memory Alloys*, Butterworth and Heinemann Ltd., London, 1990.

Fenner, R.T., *Finite Element Methods for Engineers.*, Macmillan Press Ltd., London, 1975.

Ikegami, R., Wilson, D. and Laakso, J. , "Advanced Composites with Embedded Sensors and Actuators (ACESA)", Edwards AFB Technical Report # AL-TR-90-022 (F04611-88-C-0053), 1990.

Perkins, J. *Shape Memory Effect in Alloys*, Plenum Press, New York, 1975.

Polymer Laboratories, Ltd., "PL-DMTA, MKII Dynamic Mechanical Thermal Analyser", Loughborough, United Kingdom, 1990.

Rogers, C., Liang, C. and Jia, J., "Structural Modification of Simply-Supported Laminated Plates using Embedded Shape Memory Alloy Fibers", *Computers & Structures*, Vol.38, No.5/6, pp.569-580, 1991.

ACKNOWLEDGEMENTS

This work is funded by a grant from the US Army Research Office (Grant number DAAL03-89-G-0084). Special thanks are due to Dr. Gary Anderson, the technical monitor and Chief of the Structures and Dynamics Branch of ARO, for his invaluable and continuous technical inputs.

— To appear in J. of Sound & Vibration

A MULTI-MODE DISTRIBUTED SENSOR FOR VIBRATING BEAMS

A. BAZ , S. POH and J. GILHEANY

Mechanical Engineering Department
The Catholic University of America
Washington, DC 20064

NUMBER of PAGES = 28
NUMBER of FIGURES = 8
NUMBER of TABLES = 1
NUMBER of COPIES = 4

Correspondence with

Dr. Amr M. Baz
Professor of Mechanical Engineering
The Catholic University of America
620 Michigan Ave., NE
Washington, DC 20064
Tel: 202-319-5170

A MULTI-MODE DISTRIBUTED SENSOR FOR VIBRATING BEAMS

A. BAZ , S. POH and J. GILHEANY

Mechanical Engineering Department
The Catholic University of America
Washington, DC 20064

ABSTRACT

A new class of distributed sensors is presented which can measure both the modal and physical displacements of vibrating composite beams. The sensor relies in its operation on a set of super-elastic Shape Memory Alloy (**SMA**) wires which are embedded off the neutral axes of the vibrating beams. The wires are arranged in a special manner which allows continuous monitoring of the deflection curve of the beam. The output signals of the **SMA** wires are processed to determine the modal displacements of the beam and the physical displacements at critical discrete points along the beam axis.

The theoretical and experimental performance of the sensor are presented in both the time and frequency domains. Comparisons are given between the experimental performance of the **SMA** distributed sensor and that of conventional laser sensors in order to demonstrate the accuracy and merits of the distributed **SMA** sensor. The results obtained suggest the potential of this new class of sensors as a viable means for controlling the vibrations of flexible composite beams and plates particularly with modal control algorithms. [Work supported by grant from ARO].

1. INTRODUCTION

Considerable interest has been directed recently towards the development of a wide variety of distributed sensors for monitoring the vibration of composite flexible structures. Distinct among these sensors are those relying in their operation on optical fibers [1-2], piezo-electric films [3-4] and Shape Memory Alloy (SMA) wires [5-6] which are embedded in the composite matrix of the flexible structures. By far the most commonly used and researched class of embedded sensors is the optical fibers sensors. These sensors have been developed to monitor not only structural vibrations [1] but also temperature distribution [7], cracks and defects [8] as well as curing of composite matrices [9]. In spite of such wide acceptance, the complexity of the instrumentation and the signal processing algorithms associated with optical fibers sensors still poses many serious challenges that remain to be addressed [10].

Such problems are avoided with the embedded piezo-electric film sensors developed by Lee [3]. These sensors utilize specially shaped piezo-electric films to monitor the modal coordinates of vibrating beams and plates. The shaping of the films aims at isolating the individual modal signals in a manner similar to the modal filtering technique of Meirovitch [11]. Such specially configured piezo-electric films have also been used by Lee et al [4] to monitor uniaxial and pure shear strain rates in vibrating beams. In spite of their on-line and real time measurement capability without the need for any signal processing, the configured piezo-electric films are restricted to the singular structural configuration that they are designed for and are limited to simple and time invarying structures.

The use of shape memory wires as embedded distributed sensors provides a viable alternative to optical fibers and piezo-electric film sensors. The **SMA** sensors require very simple instrumentation and when properly designed, they require very simple signal processing algorithms to extract modal and physical coordinates of the vibrating structures. The sensors rely in their operation on the changes in the electrical resistance of the **SMA** wires when subjected to axial loading in a manner similar to conventional discrete strain gage sensors. This physical property has been successfully utilized in monitoring the position of robotic joints [12]. The **SMA** sensor have also been used at Virginia Polytechnic Institute [5] and Boeing Aerospace [6] to measure a single mode of vibration of composite flexible beams [5-6]. No attempt has been made however to use the **SMA** sensor to monitor several modes of vibration or to extract the modal and physical parameters of vibrating structures.

It is therefore the purpose of this study to develop such a **SMA** sensor which is capable of monitoring multi-modes of vibration of flexible composite beams in order to extract individual modal and physical parameters of these beams. Furthermore, this study documents the performance of such **SMA** sensors, both in the time and frequency domains, and validates their performance by comparison with conventional sensors. It is important to note that the **SMA** sensor relies in its operation on the use of the classical modal decomposition approach [13]. This approach has been recently utilized, by many investigators, to extract the modal displacements of vibrating beams [14-16] and plates [17] from the measurements of a set of discrete sensors. The placement strategy of these discrete sensors is, however, very critical in order to avoid nodes of vibration. This is in contrast to the distributed **SMA** sensor which can be placed at any place along the beam without any concern about the location of the nodes of vibration. Such versatility makes the **SMA** sensor suitable for monitoring the vibration of more complex structures where the location of the nodes of vibration can not be accurately determined particularly for higher order modes.

Accordingly, this paper is organized in four sections and an appendix. In section **1**, a brief introduction is given and section **2** presents the theoretical principles of the sensor. The experimental performance of the sensor is given in section **3** and the conclusions are summarized in section **4**. The calibration of the sensor is described in the appendix.

2. THEORETICAL MODELING OF THE SENSOR

2.1. Monitoring the modal coordinates

The multi-mode distributed **SMA** sensor relies in its operation on a **SMA** wire embedded inside a composite beam as shown in Figure (1). The wire is placed, at a distance **a**, off the neutral axis of the beam. The wire is tapped along its length at different locations **1**, **2**, .. , **N** where **N** is equal to both the number of modal coordinates to be extracted and the number of physical coordinates to be estimated. The changes ΔL_1, ΔL_2, ..and ΔL_N in the lengths L_1, L_2, .. and L_N of the different segments of the wire, due to the vibration of the beam, are monitored continuously by measuring the changes ΔR_1, ΔR_2, .. and ΔR_N in the electrical resistances of these segments such that

$$\Delta L_i = (\Delta R_i \ A) \,/\, \rho_e \qquad \text{for } i=1,\ldots, N \qquad (1)$$

where A is the wire cross sectional area and ρ_e is its electrical resistivity.

The changes in the lengths ΔL_i are related to the curvature of the deflection curve of the beam as it vibrates under the action of the

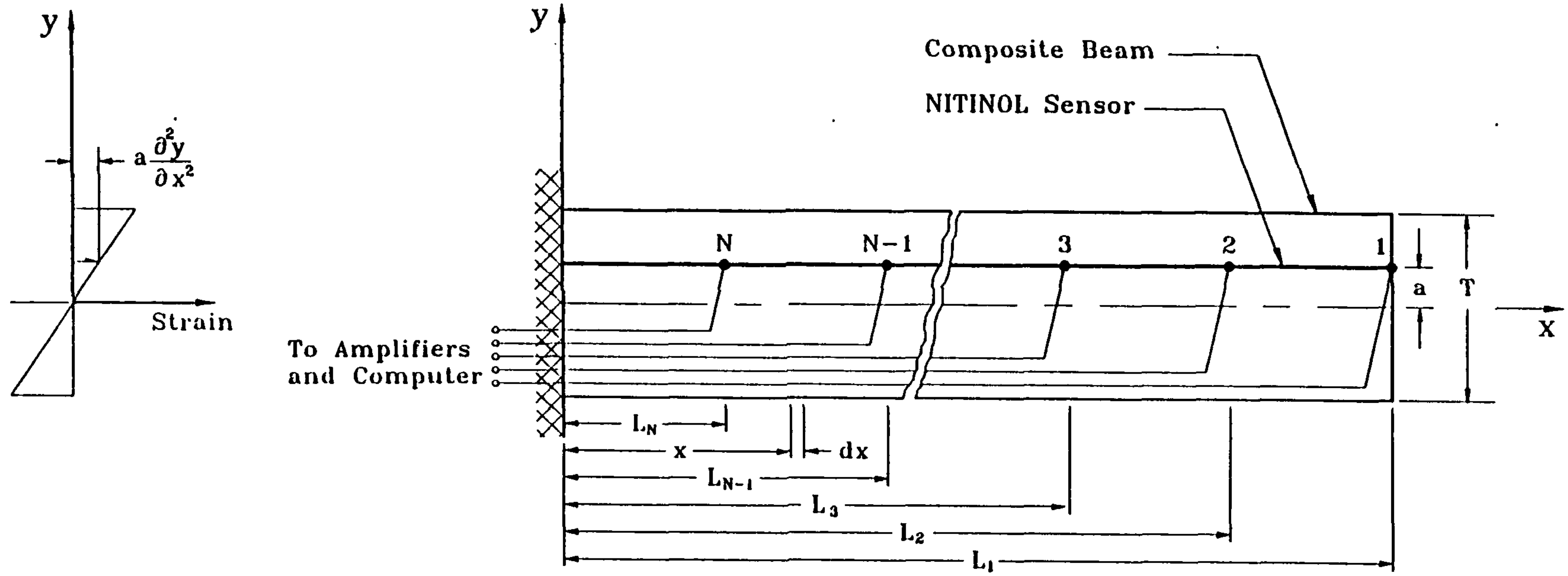

Figure (1) - Schematic drawing of the **SMA** distributed sensor.

external loads. Assuming small deflections and that the **SMA** wire experiences the same linear strains as the host beam in which the wire is embedded, then the changes ΔL_i can be calculated from

$$\Delta L_i = \int_0^{L_i} \varepsilon \, dx = \int_0^{L_i} a \frac{\partial^2 y}{\partial x^2} \, dx \qquad (2)$$

where ε is the axial strain in the wire and **y** is the beam deflection in the transverse direction which obeys the following partial differential equation describing the dynamics of a Bernoulli-Euler beam [13], is

$$E\,I \frac{\partial^4 y}{\partial x^4} + \rho A_b \frac{\partial^2 y}{\partial t^2} = \sum F_i \, \delta(x-x_i) + \sum M_j \, \delta'(x-x_j) \qquad (3)$$

where **EI** is the flexural rigidity of the beam, ρ is the mass density, A_b is the beam cross sectional area, **t** is the time, F_i is a point load acting on the beam at location x_i, M_j is a moment acting on the beam at location x_j, δ is the kronecker delta function and δ' is the unit doublet function. Applying the separation principle [13] to equation (3), the transverse deflection **y**(x, t), at any location **x** and time **t**, can be written as a linear combination of the mode shapes $\phi_i(x)$ of the beam as follows

$$y(x,t) = \sum_{i=1}^{N} \phi_i(x) \, u_i(t) \qquad (4)$$

where $u_i(t)$ and $\phi_i(x)$ are the generalized modal coordinate and the corresponding mode shape respectively for the ith mode. The mode shape $\phi_i(x)$ for a cantilevered beam is given by

$$\phi_i(x) = [\cosh(k_i x) - \cos(k_i x)] - \alpha i \, [\sinh(k_i x) - \sin(k_i x)] \qquad (5)$$

with α_i given by

$$\alpha_i = [\cosh(k_i L_1) + \cos(k_i L_1)] \, / \, [\sinh(k_i L_1) + \sin(k_i L_1)] \qquad (6)$$

and k_i is defined as the wave number of the ith mode which satisfies the following characteristic equation

$$\cos\,(k_i L_1)\,\cosh\,(k_i L_1) + 1 = 0 \qquad (7)$$

Substituting equations (5), (6) and (7) into equation (4) the transverse deflection **y** at any **x** and **t** can be determined. The resulting equation can be used to calculate the beam curvature $\partial^2 y/\partial x^2$ which is in turn can be substituted into equation (2) to calculate the change in lengths ΔL_i.

After some manipulations, the vector of length changes ΔL_i can be calculated from

$$\Delta L_i = a \sum_{j=1}^{N} k_j \left[\left(\sinh(k_j L_i) + \sin(k_j L_i) \right) - \alpha_j \left(\cosh(k_j L_i) - \cos(k_j L_i) \right) \right] u_j \qquad (8)$$

Letting $\mathbf{\Delta L}$ be the vector of length changes given by

$$\mathbf{\Delta L} = [\Delta L_1 \quad \Delta L_2 \quad .. \quad \Delta L_N]^T, \qquad (9)$$

C be a (NxN) matrix whose constant and known entries c_{ij} are given by

$$C_{ij} = a\, k_j \left[\left(\sinh(k_j L_i) + \sin(k_j L_i) \right) - \alpha_j \left(\cosh(k_j L_i) - \cos(k_j L_i) \right) \right], \qquad (10)$$

and **U** be the vector of the beam modal coordinates given by

$$\mathbf{U} = [u_1 \quad u_2 \quad .. \quad u_N]^T \qquad (11)$$

Then substituting equations (8), (10) and (11) into equation (9), it yields the following matrix equation for the vector of length changes

$$\mathbf{\Delta L} = \mathbf{C} \quad \mathbf{U} \qquad (12)$$

indicating that the changes in the lengths ΔL of the different segments of the **SMA** wire are linearly related to the modal coordinates **U** of the composite beam.

Defining ΔR as the vector of resistance changes of the different wire segments , i.e.

$$\Delta R = [\Delta R_1 \quad \Delta R_2 \quad \dots \quad \Delta R_N]^T \tag{13}$$

and substituting for ΔR_i from equation (1), the above equation reduces to

$$\Delta R = A/\rho_e \, \Delta L \tag{14}$$

Combining equations (12) and (14), gives the modal coordinate vector **U** in terms of the resistance changes vector ΔR as follows

$$\mathbf{U} = \rho_e/A \quad \mathbf{C}^{-1} \quad \Delta R \tag{15}$$

i.e. measuring the changes ΔR of the **N** segments of the **SMA** wire can be used to directly calculate the **N** modal coordinates of the vibrating composite beam as the matrix equation (15) represents a set of **N** linear equations in the **N** unknowns u_1, u_2, .. and u_N.

It should be noted that the matrix **C** is always non-singular i.e. a solution for equation (15) always exists, unless two tapping points of the **SMA** wire coincide. This means that the length of the corresponding two wire segments is equal resulting in a matrix **C** with two equal rows. Accordingly, the rank of matrix **C** is reduced to **N-1**. Of course such condition will not occur on purpose. However, if it does occur the sensor can still extract (**N-1**) modal and (**N-1**) physical displacements. In other words, the tapping points of this distributed sensor can be placed any where along the beam even coinciding with any node of vibration. This is not the case with discrete sensors such as conventional strain gages and accelerometers where these sensors should not be placed at nodes of vibration. Such critical placement requirement of the discrete sensors limits their use to simple structures and favors the use of the distributed sensor described in this study.

2.2. Monitoring the physical coordinates

In a similar fashion, the measurements of **ΔR** can also be used to compute the **N** physical coordinates of the vibrating beam. This can be achieved by defining **Y** as a vector of physical coordinates given by

$$\mathbf{Y} = [\ y(L_1) \quad y(L_2) \quad \ldots . \quad y(L_N)]^T \tag{16}$$

Therefore, from equation (4) the following matrix equation can be written

$$\mathbf{Y} = \Phi\, U \tag{17}$$

where

$$\Phi = \begin{bmatrix} \phi_1(L_1) & .. & \phi_N(L_1) \\ \phi_1(L_2) & .. & \phi_N(L_2) \\ \ldots & \ldots & \ldots \\ \phi_1(L_N) & .. & \phi_N(L_N) \end{bmatrix} \tag{18}$$

From equations (15) and (17), the physical transverse displacement vector **Y** of the **N** taping points can be calculated from the measurements of the resistance changes **ΔR** of the **N** segments of the **SMA** wire as follows

$$\mathbf{Y} = \rho_e \,/\, A \quad \Phi \quad \mathbf{C}^{-1}\, \Delta\mathbf{R} \tag{19}$$

Equations (15) and (19) constitute the basic equations that govern describing the capability of the distributed **SMA** sensor in extracting the modal and physical coordinates of a vibrating composite beam from the measurements of resistance changes of **N** segments of the wire. In these equations, the calculation of both the modal and physical coordinates of a beam is shown to be very simple as it is reduced to merely the solution of two sets of simultaneous linear equations.

Equations (15) and (19) will be utilized in the following section to extract the coordinates of an experimental beam and the results obtained will be compared to the results measured by conventional laser sensors.

The above analysis of the **SMA** sensor indicates that the sensor is in effect a multi-mode distributed strain gage. Such distributed nature of the sensor has many inherent advantages. First, it makes the placement of the sensor and its tapping points insensitive to the location of the nodes of vibration. This of course is not the case for conventional discrete strain gages where the sensors can not be placed at these nodes. Second, because the **SMA** sensor relies on integrating the strain along the wire segments, as described by equation (2), its output signal will be less noisy than that of conventional strain gages and high signal-to-noise ratios can be obtained. Third and because of its embedded nature the **SMA** sensor can also detect structural failures by monitoring the failure of any wire segment. These advantages make the **SMA** sensor suitable for accurately monitoring the vibration and integrity of complex SMART composites.

Worth noting also is that the theory developed for the **SMA** sensor is based on the knowledge of the mode shapes of the beam or the structure inside which it is embedded. However, the cantilevered beam example given in this study can be easily extended to beams with other boundary conditions.

3. EXPERIMENTAL PERFORMANCE OF THE DISTRIBUTED SENSOR

3.1. Experimental set-up

Figure (2) shows a schematic layout of the experimental set up used

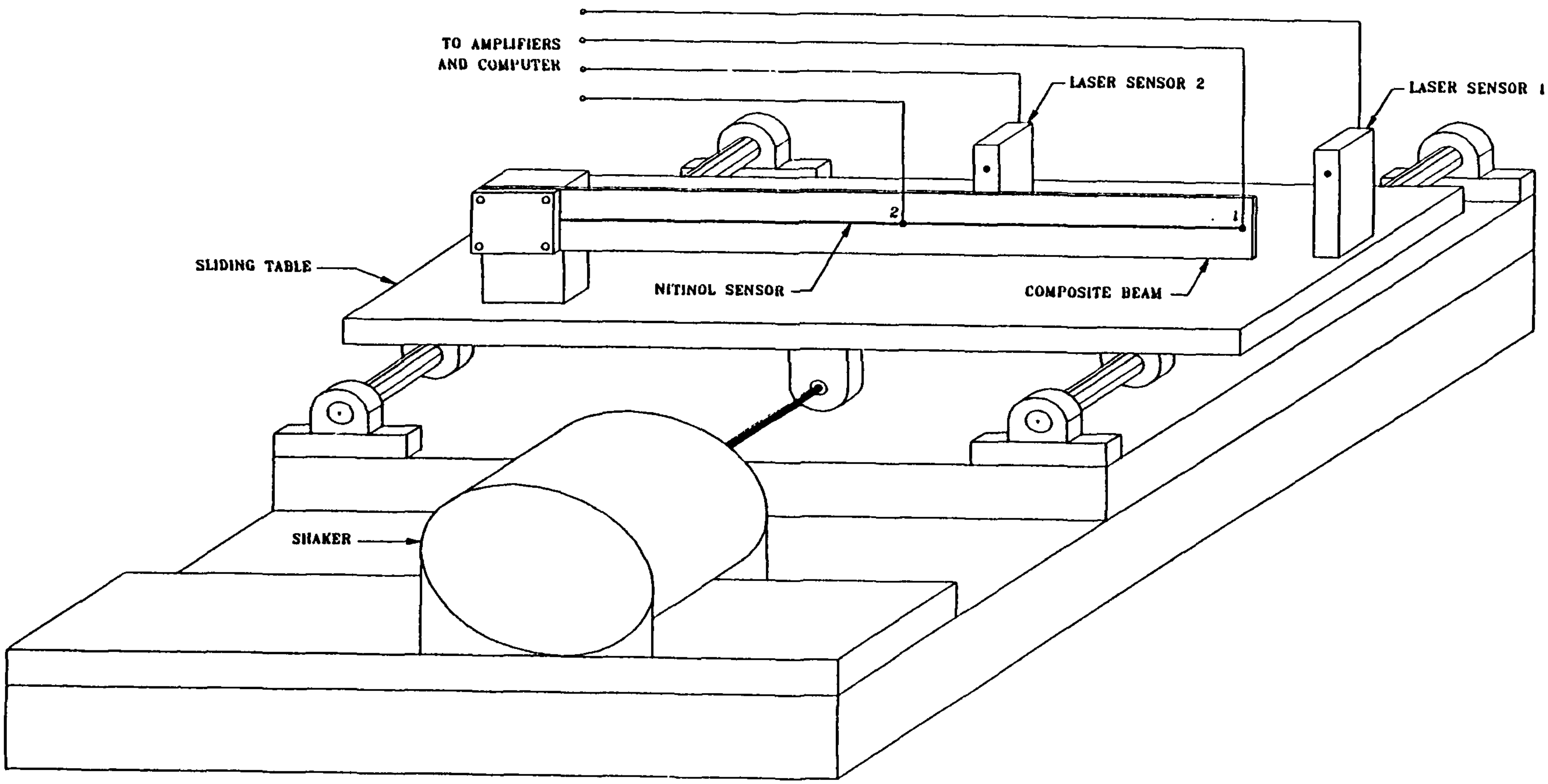

Figure (2) - Schematic drawing of the experimental set-up used in testing the **SMA** sensor.

in evaluating the performance of the **SMA** distributed sensor in both the time and frequency domain. The sensor is made of a 0.125 mm diameter **SMA** wire embedded inside a composite beam whose physical, geometrical and dynamical properties are given in Table 1. The **SMA** wire itself is manufactured from a super-elastic **Nickel-Titanium** alloy called **NITINOL** which has a resistivity of 0.644×10^{-6} ohm/m. Such an alloy is selected because its super-elasticity allows the wire to experience large deformations, about ten times more than conventional materials, and still completely spring back to its original undeformed shape [18]. This feature makes the sensor suitable for monitoring the vibration of very flexible structures without exhibiting any plastic deformations.

Table 1 - Physical, geometrical and dynamical properties of test composite beam

Length (cm)	Width (cm)	thickness (cm)	density (gm/cc)	Young's Mod. (GN/m^2)	1st Mode (Hz)	2nd Mode (Hz)	3rd Mode (Hz)
48.0	5.0	0.25	0.73	4.35	1.88	11.75	33.15

The composite beam, with the embedded **SMA** sensor, is mounted in a cantilevered manner on an oscillating platform which can oscillate freely on two guide rails. The rails are set parallel to the transverse vibration direction of the beam. A shaker (Wilkoxon Research model F3/F9, Bethesda, MD) is driven with a sinusoidal function generator to provide controlled vibration of the platform and in turn the composite beam. The resulting beam vibration is monitored by the **SMA** sensor which is provided with only two segments. The first segment extends between the beam tip **1** and its fixed root whereas .e second segment extends between the beam mid-span point **2** and the fixed base. The resistances of the two segments are measured using amplifiers model P-3500 from Measurements Group, Raleigh, North Carolina. The amplifiers operate with 9 Volt DC power source. The conditioned outputs of the amplifiers are sampled by a 386-microprocessor via an input/output board (model DASH-16 from METRABYTE, Taunton, MA). The sampling rate used is 190 Hz with an accuracy of 12 bits which corresponds to 4.88×10^{-3} mm. The displacements of the first and second modes are computed from the measurements of the resistance of the two segments using equation (15). Also, the physical displacements of the beam tip and mid-span are computed, in the microprocessor, using equation (19). The physical displacements obtained from the **SMA** sensor are compared with those measured by two laser sensors (model IIIB-LA40HR , Aromat Corp., New Providence , NJ). The laser sensors are placed on the oscillating platform facing the beam tip and mid-span points. The sensors have accuracy of 20 μm over a frequency band between 0-1000 Hz.

The calibration of the **SMA** sensor is carried out by comparing the sensor output with the output of the laser sensors according to the procedure outlined in the appendix. Such a procedure is important to account for errors in the sensor's parameters as the fiber position **a** and segments length L_i^s. The laser sensors are calibrated by reflecting their light beam off a micrometer head. The spacing between the head and the laser emitter is varied and the output of the laser sensor is recorded.

3.2. Performance of the SMA sensor

3.2.1. in the time domain

The composite beam with the embedded **SMA** sensor is subjected to three different initial sinusoidal excitations at 1.9, 7 and 11.8 Hz respectively. The first and third excitation frequencies are selected in order to resonant the beam at its first and second modes of vibration. Following the initial excitation period, the shaker driving the platform is turned off and the beam is left to vibrate freely. The signals of the **SMA** sensor and the laser sensors are then sampled by the computer over a period of 1.5 seconds. All the sampling and the results, reported in this study, are carried out during the transient period which follows the steady-state excitation by the shaker.

Figure (3) shows the corresponding length changes of the two **SMA** wire segments at the three excitation conditions. These length changes ΔL are used along with equation (19) to compute the physical displacements at the tip and mid-span of the beam. Figure (4) shows the computed physical displacements as obtained by the **SMA** sensor along with the corresponding displacements of the laser sensors when the first vibration mode of the beam is excited. Such a comparison indicate excellent agreement between the measurements of the **SMA** and the laser sensors.

Figures (5) and (6) display similar comparisons between the displacements of the **SMA** and the laser sensors, at the beam tip and mid-span, when the excitation frequencies are 7 and 11.8 Hz respectively. The two figures clearly demonstrate the accuracy of the **SMA** in monitoring the vibration of the beam in the time domain.

It is essential to note that all the measurements and the calculations of the modal and physical displacements are carried out, in real time, with a sample interval of 5.2 ms. This interval is corresponding to a sampling rate of 190 Hz which is at least 8 times greater than the Nyquist frequency limit necessary to avoid aliasing.

3.2.2. in the frequency domain

The performance of the **SMA** in the frequency domain is evaluated by impacting the composite beam with a modally tuned impact hammer (model PCB- GK291B02, PCB Piezotronics, Depew, NY). The response

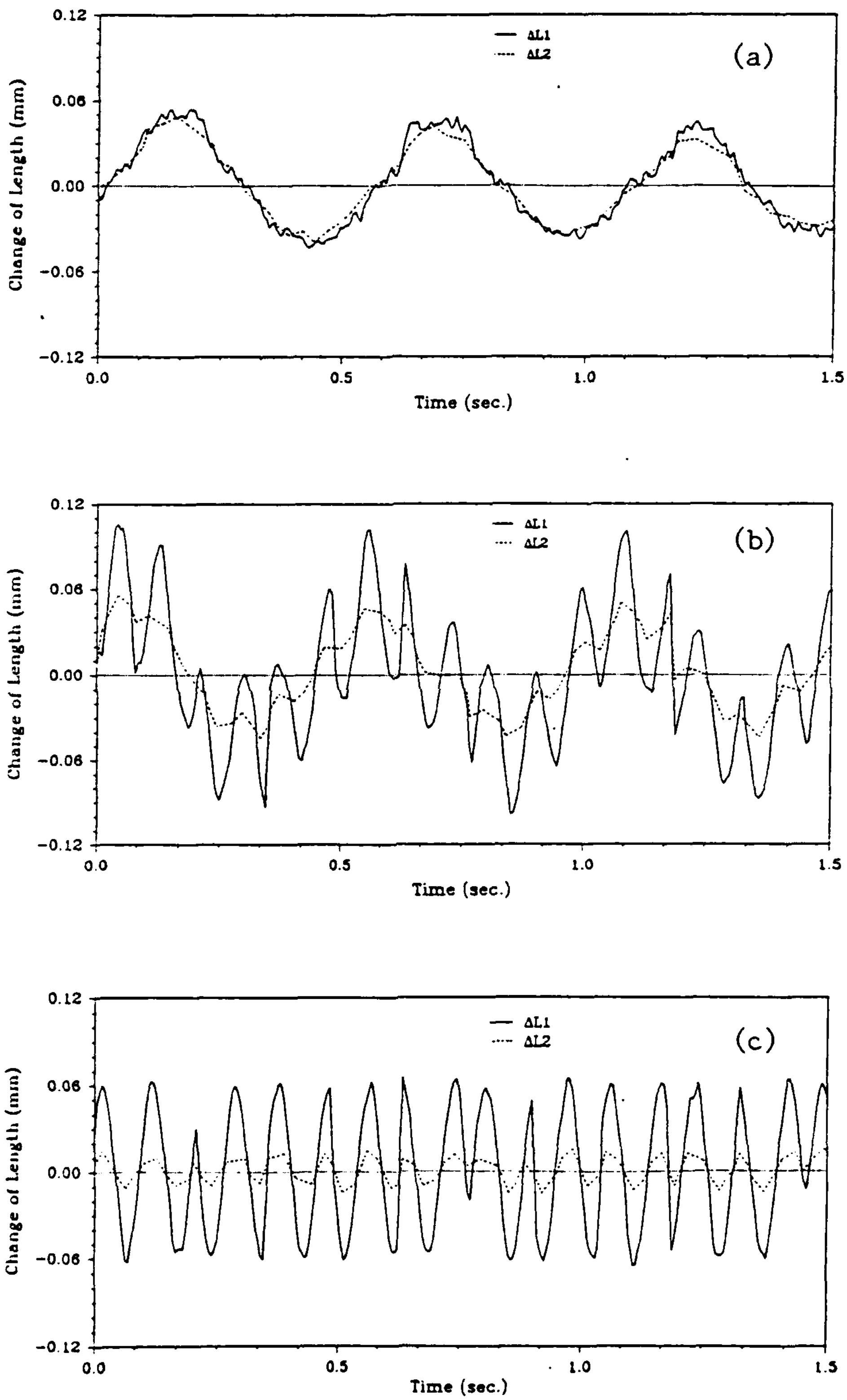

Figure (3) - Time history of changes in SMA wire length when beam is subjected to:
a. 1.9 Hz , b. 7 Hz and c. 11.8 Hz.

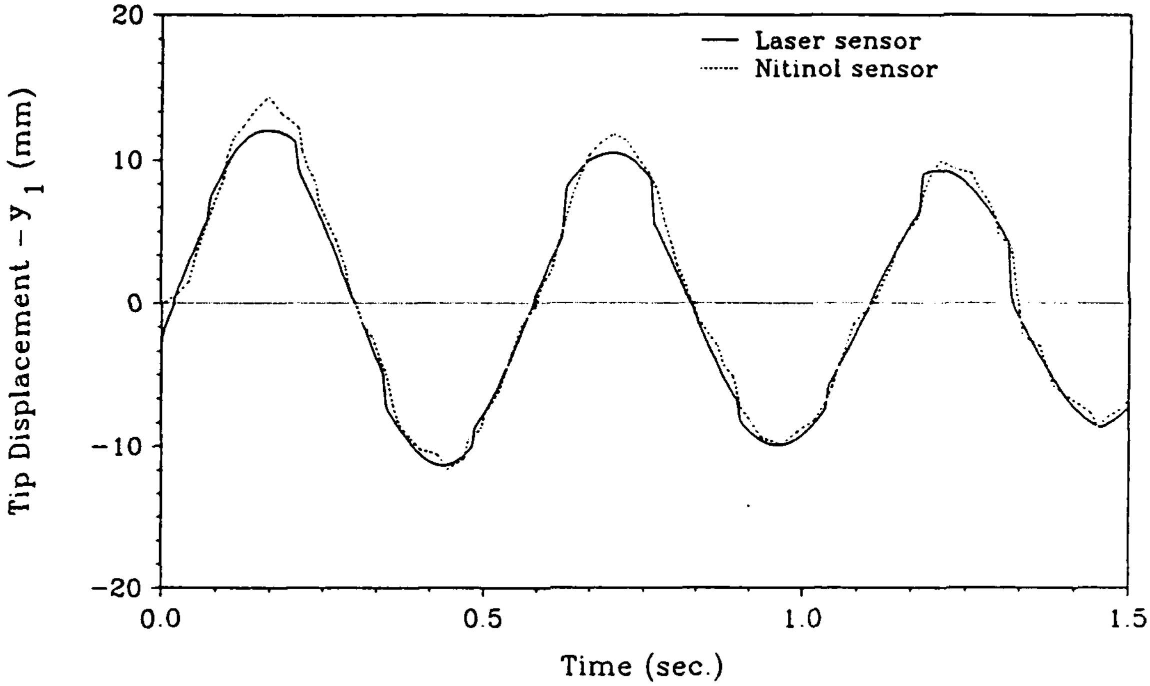

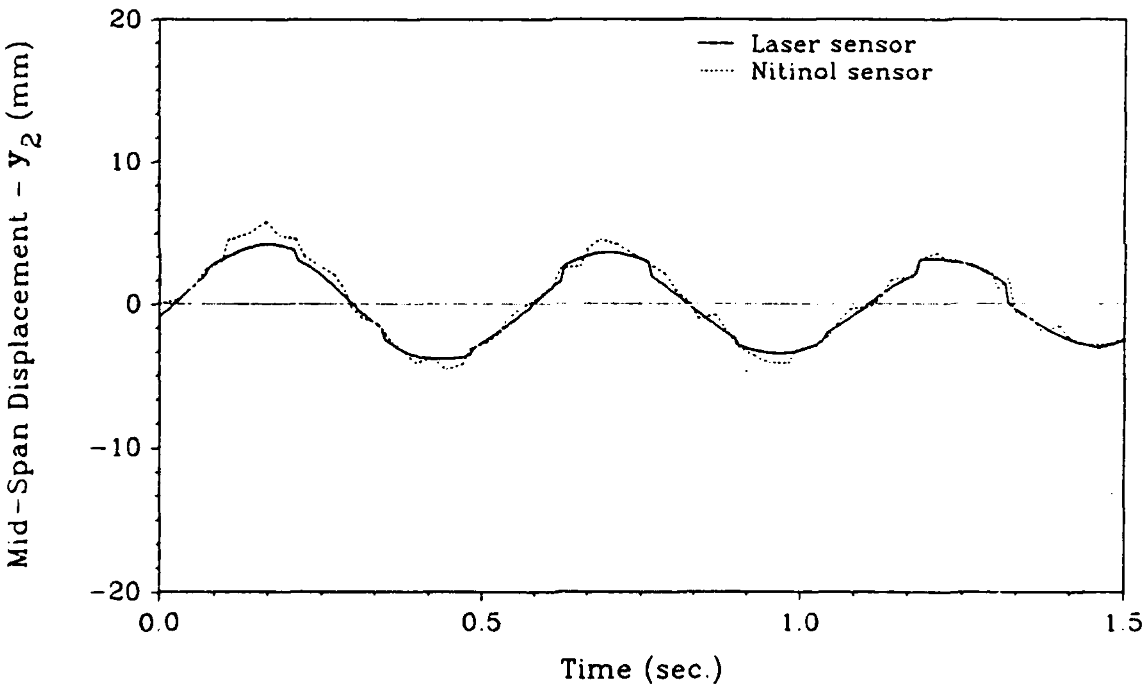

Figure (4) - Comparison between displacement measurements of SMA and laser sensors at tip and mid-span of beam when subjected to sinusoidal exciatation of 1.9 Hz.

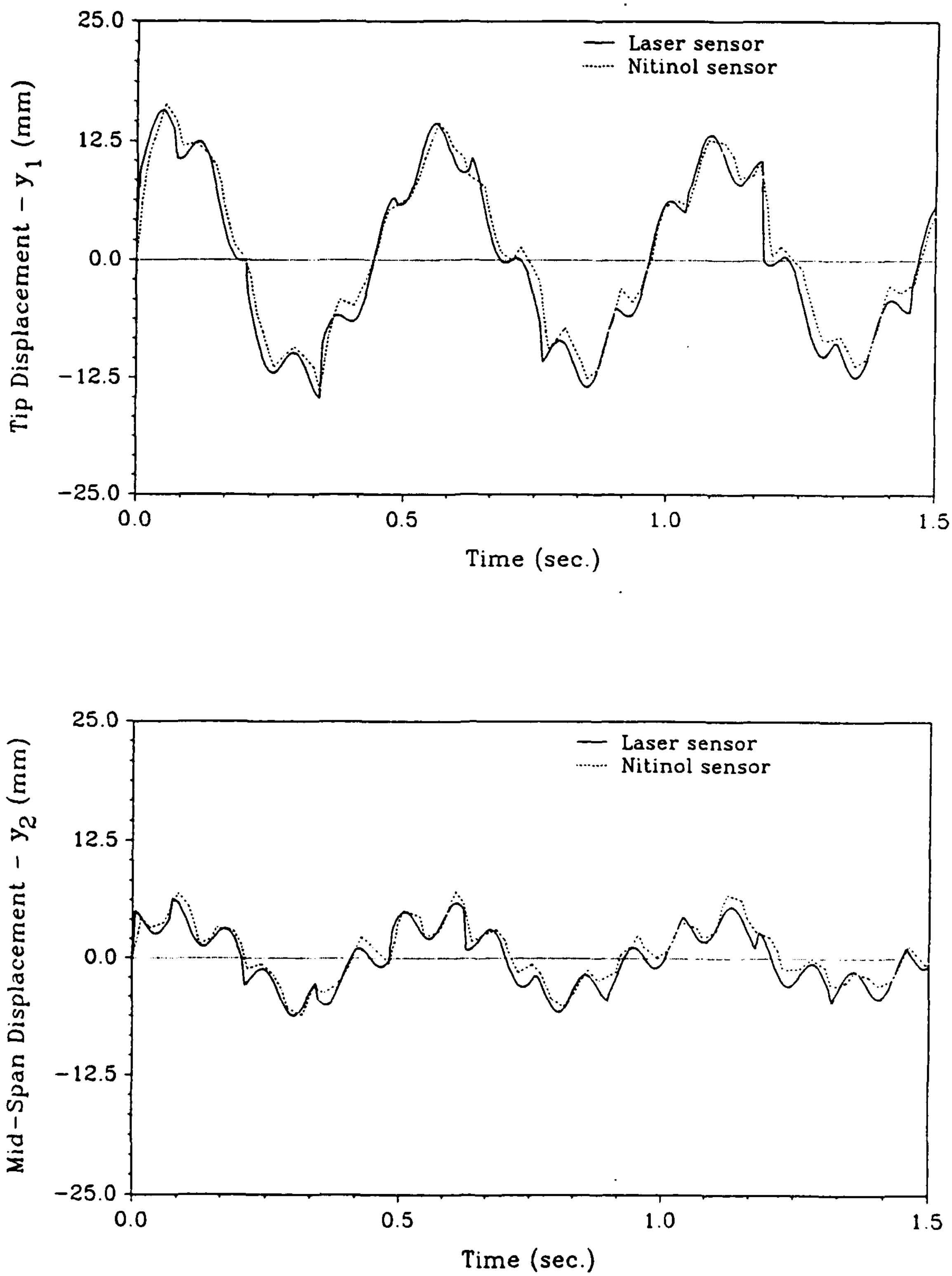

Figure (5) - Comparison between displacement measurements of SMA and laser sensors at tip and mid-span of beam when subjected to sinusoidal exciatation of 7.0 Hz.

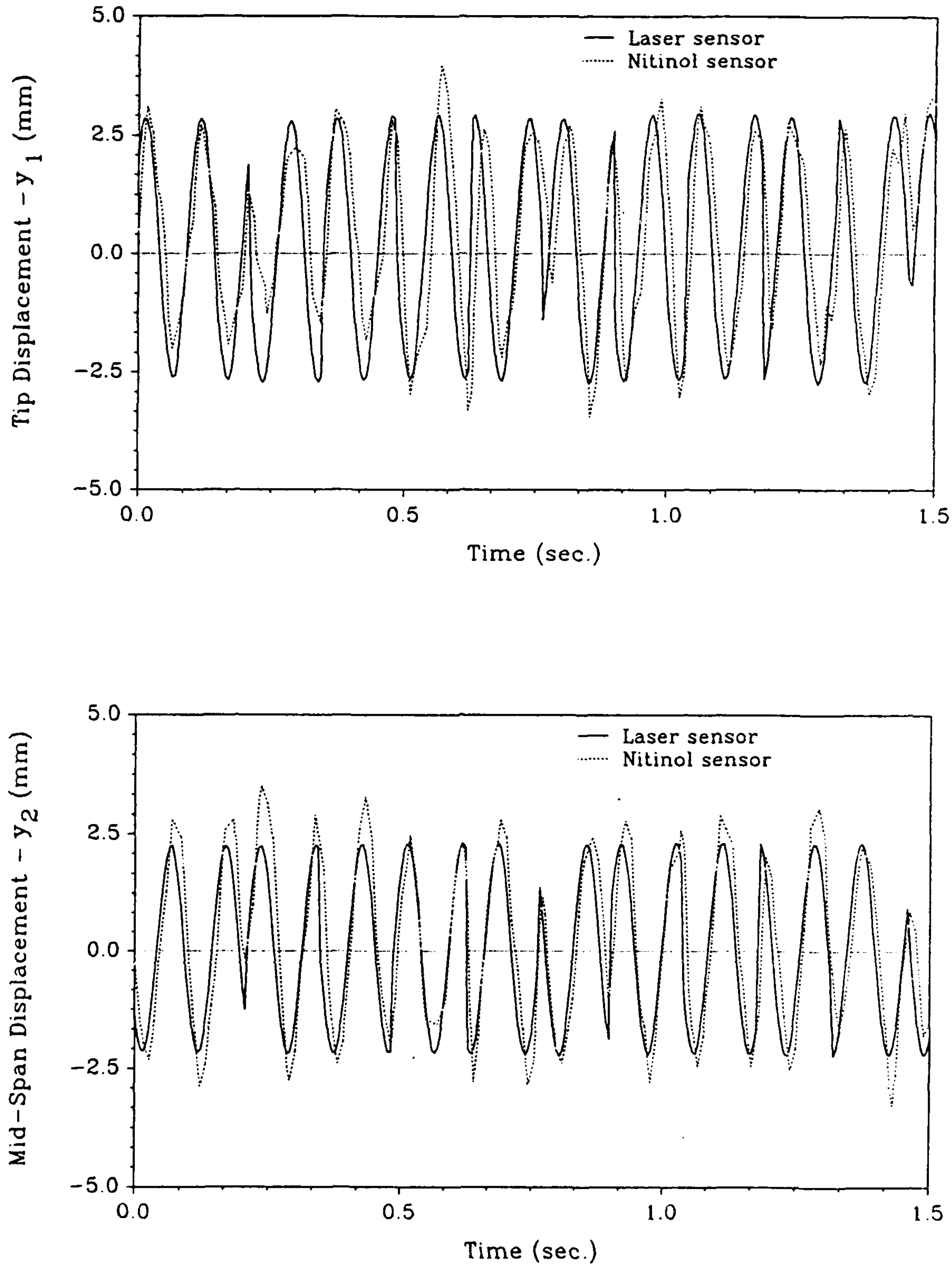

Figure (6) - Comparison between displacement measurements of SMA and laser sensors at tip and mid-span of beam when subjected to sinusoidal exciatation of 11.8 Hz.

of the **SMA** sensor as well as that of the laser sensors to such impacts are analyzed using a dual channel spectrum analyzer. These responses are used to predict the frequency response of the different vibration modes. Figures (7) and (8) show the normalized power spectra of the **SMA** and the laser sensors outputs at the beam tip and its mid-span respectively. It is evident that the response of the **SMA** sensor matches that of the laser sensors in the frequency domain. Furthermore, the experimental frequencies obtained by the analysis of the **SMA** sensor output are in close agreement with the theoretical predictions ω_i which are given by

$$\omega_i = (k_i\ L_1)^2 / \ (L_1^{\,2})\ (EI/\rho A)^{1/2} \tag{20}$$

where k_i is the wave number of the ith mode given by equation (7). In particular, the first three modes are found experimentally to be 1.875, 11.76 and 33.15 Hz whereas the corresponding theoretical predictions are 1.89, 11.85 and 33.18 Hz respectively.

However, it is essential to note that the bandwidth of the prototype **SMA** sensor is limited by the fact that it has two sampling points. This implies that it can only measure excitations up to the second mode of vibration which is 11.8 Hz.

4. CONCLUSIONS

The feasibility of a new class of distributed **SMA** sensors in measuring modal and physical displacements of composite beams is successfully demonstrated. The sensors utilize **SMA** wires which are embedded inside the matrix of the composite beams. Such an arrangement can be augmented with sets of embedded actuators, as **SMA** or

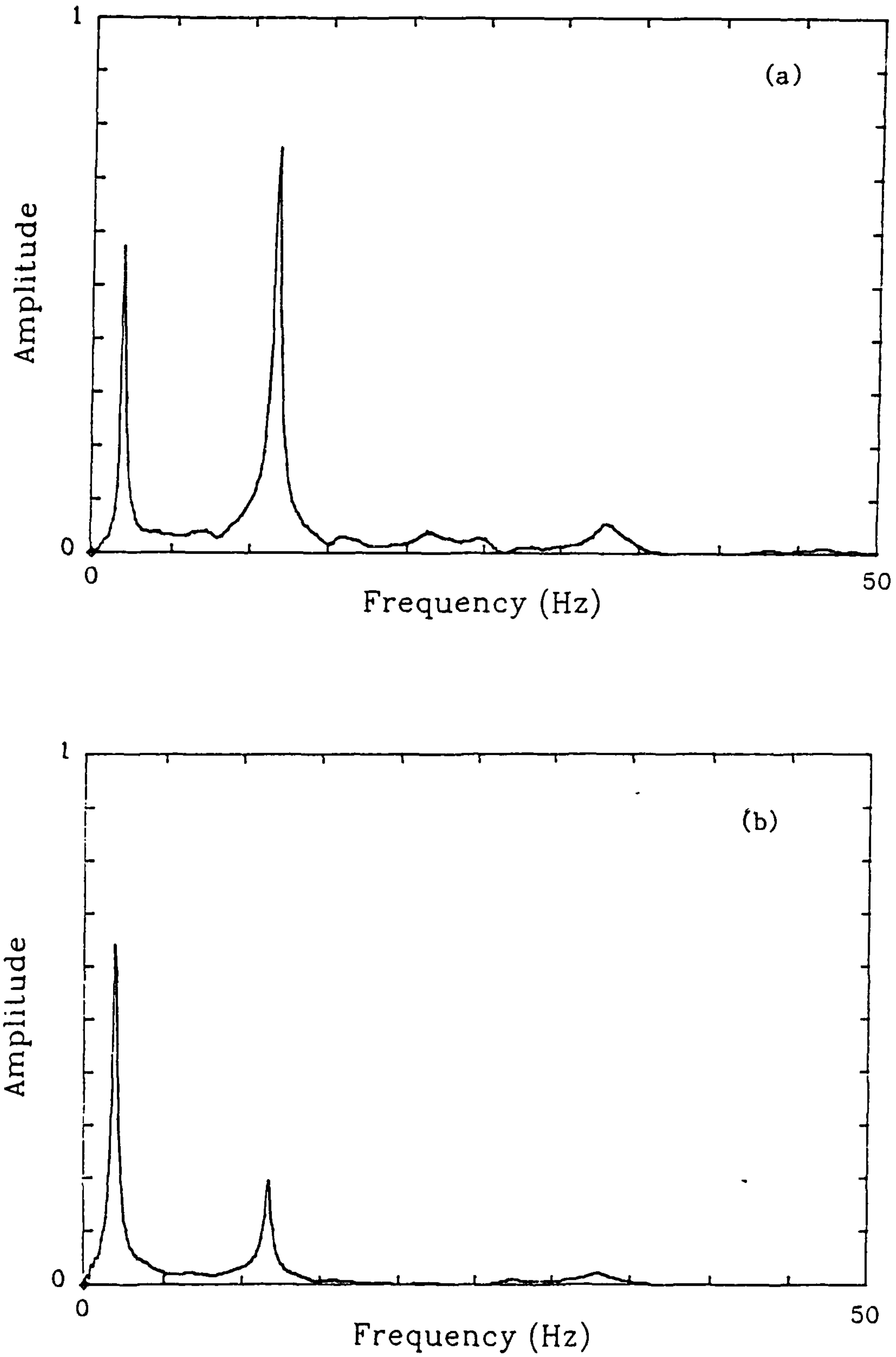

Figure (7) - Comparison between frequency response of **SMA** and the laser sensors at tip of beam when impacted with an impact hammer.

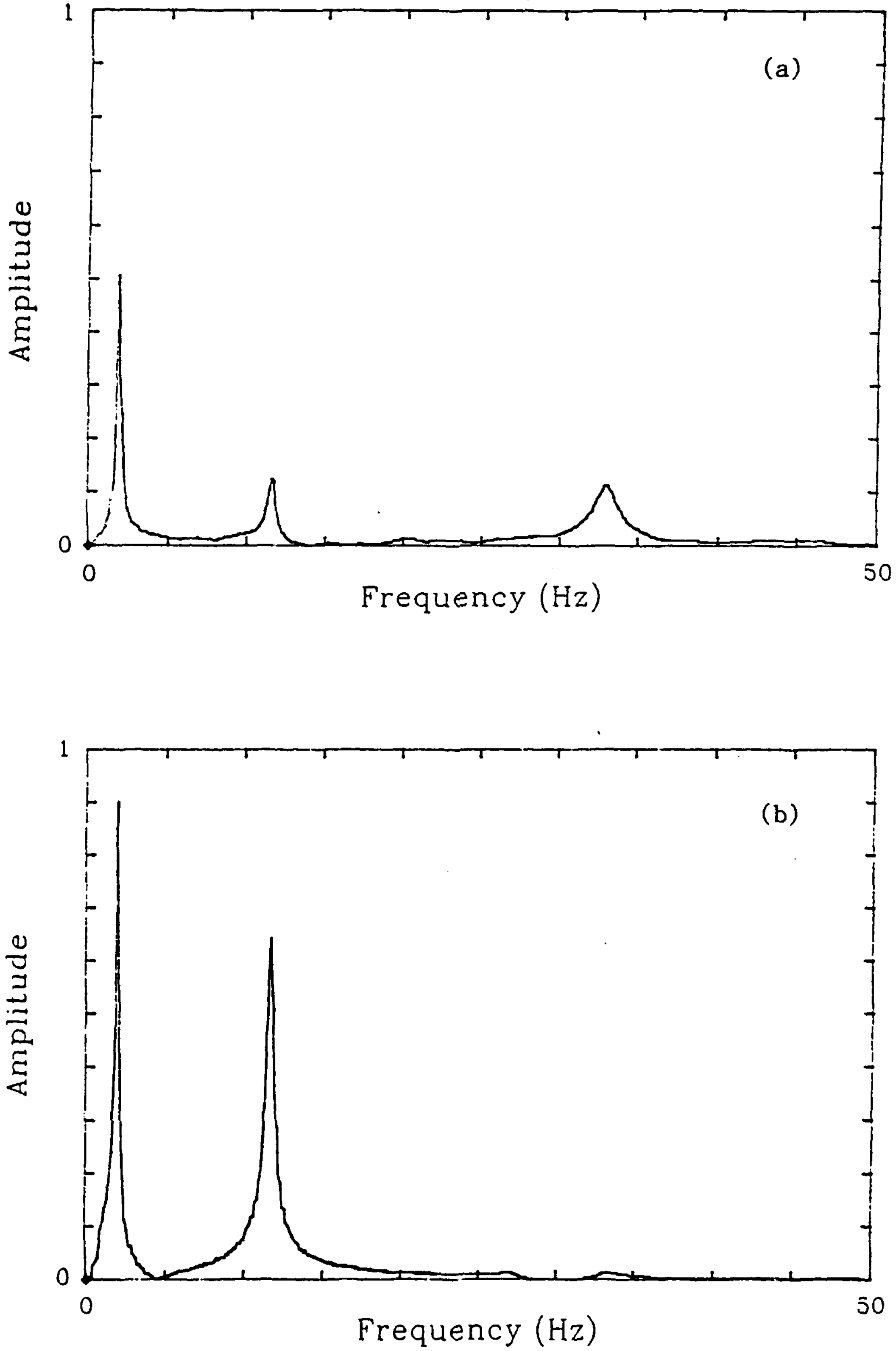

Figure (8) - Comparison between frequency response of **SMA** and the laser sensors at mid-span of beam when impacted with an impact hammer.

piezo-electric, in order to develop a class of **SMART** composite beams which have built-in vibration and shape control capabilities. These capabilities can be utilized along with any of the modal control algorithms, such as those developed by Baz et al [15-16], to control the structural vibrations and shape of these **SMART** composites.

The general theory of operation of the distributed sensor is presented for monitoring **N** modal and physical coordinates. The experimental validation of the sensor performance is demonstrated for a composite beam where the first two modes of vibrations dominate its dynamic response. The physical displacements of the beam tip and mid-span as obtained by the two-mode distributed sensor are found to be in excellent agreement with the measurements of conventional laser sensors. Emphasis however should be placed on the fact that the distributed sensor is tested with excitations within its frequency band capabilities. If the sensor is designed to monitor low frequency excitations and the external frequency band exceeds its maximum frequency limit, then it is essential to use low pass filters to filter out the high frequency contents in the sensor signals in order to avoid conventional observation spillover problems [19] and spatial aliasing [17]. This typical instrumentation problem can be avoided by proper selection of the sensor's bandwidth to be compatible with the expected excitation frequency band. However, for more accurate monitoring of the displacements it is recommended to provide the **SMA** sensor with more bandwidth than the excitation frequency band, i.e number of sampling points **N** should be greater than the number of displacements **P** to be determined. In this manner, equation (15) becomes:

$$\bar{\mathbf{U}} = [u_1 \ u_2 \ .. \ u_P]^T = \rho_e/A \ [\bar{\mathbf{C}}^T \ \bar{\mathbf{C}}]^{-1} \ \bar{\mathbf{C}}^T \ \Delta\mathbf{R} \tag{21}$$

where $\bar{\mathbf{U}}$ is the vector of **P** modal displacements, $\bar{\mathbf{C}}$ is a matrix (PxN) whose entries are given by equation (10) and $[\bar{C}^T \bar{C}]^{-1} \bar{C}^T$ is the pseudo-inverse of $\bar{C}$. Such a statistical approach, as **N>P**, of the over determined equation $\bar{C}\ \bar{U} = \rho_e/A\ \Delta R$ ensures that the modal displacements $\bar{U}$ extracted are the least-squares estimates. This will be particularly important in the case of noisy measurements. The modal displacements $\bar{U}$ extracted can then be used to compute the physical displacements **Y** of the beam using the following transformation equation

$$Y = \bar{\Phi}\ \bar{U} \tag{22}$$

where $\bar{\Phi}$ is the mode shape matrix (NxP) whose entries ϕ_{ij} correspond to the shapes of the jth mode at location **i**.

It should be pointed out also that the theory developed in this study can be easily extended to utilize the distributed **SMA** sensor to monitor the vibration of two or three dimensional motions as for example of plates or more complex structures.

ACKNOWLEDGEMENTS

This work is funded by a grant from the US Army Research Office (Grant number DAAL03-89-G-0084). Special thanks are due to Dr. Gary L. Anderson, Chief of the Structures and Dynamics Branch of the ARO for his invaluable and continuous technical inputs.

REFERENCES

1. D.COX, D.THOMAS, K.REICHARD, D.LINDNER and R.O.CLAUS 1989 *Proc. of SPIE on Fiber Optic Smart Structures and Skins II*, Vol. 1170, 372-383. Modal domain fiber optic sensor for closed loop vibration control of a flexible beam.

2. K.MURPHY, M.MILLER, A.VENGSARKAR and R.O.CLAUS 1991 *J.of Composites Technology & Research*, Vol.13, 29-35. Elliptical-core, dual-mode, optical fiber strain and vibration sensors for composite material laminates.

3. CHIH-KUNG LEE 1987 *Ph.D. thesis, Cornell University*. Piezoelectric laminates for torsional and bending modal control: Theory and experiments.

4. C.K.LEE, T.C.O'SULLIVAN and W.W.CHIANG 1991 *Proc.of 32 SDM Conference*. Paper AIAA-91-1064-CP, 2197-2207. Piezoelectric strain rate sensor and actuator designs for active vibration control.

5. C.FULLER, C.A.ROGERS and H.H.ROBERTSHAW 1989 *Proc. of SPIE Conference on Fiber optic Smart Structures and Skins II*, Vol. 1170, 338-358. Active structural acoustic with smart structures.

6. D.WILSON, J.ANDERSON, R.REMPT and R.IKEGAMI 1990 *Proc. of SPIE Conference on Fiber Optic Smart Structures and Skins III*, Vol.1370-25. Shape memory alloys and fiber optics for flexible structure control.

7. C.E.LEE and H.F.TAYLOR 1989 *Proc. of SPIE Conference on Fiber optic Smart Structures and Skins II*, Vol. 1170, 113-122. Fiber optic sensor research at Texas A&M University.

8. KEXING LIU, SUZANNE M.FERGUSON and R.M.MEASURES 1989 *Proc. of SPIE Conference on Fiber optic Smart Structures and Skins II*, Vol. 1170, 205-210. Damage detection in composites with embedded fiber optic interferometric sensors.

9. MARTIN AFROMOWITZ and KAI-YUEN LAM 1989 *Proc. of SPIE Conference on Fiber optic Smart Structures and Skins II*, Vol. 1170, 138-142. Optical properties of curing epoxies and applications to the fiber optic composite cure sensor.

10. G.P.SENDECKYJ and C.A.PAUL 1989 *Proc. of SPIE Conference on Fiber optic Smart Structures and Skins II*, Vol. 1170, 2-10. Some smart structures concepts.

11. L.MEIROVITCH and H.BARUH 1985 *J.of Guidance & Control*, **8**, **6**, 707-716. The implementation of modal filters for control of structures.

12. M.TAKEDA, M.HASHIMOTO and K.SATO 1986 *J.of Robotic Systems*, **3**, 441-450. A new displacement sensor using pseudoelastic titanium-nickel alloy wire.

13. L.MEIROVITCH 1967 *Analytical Methods in Vibration*. New York:Macmillan.

14. A.BAZ, S.POH and P.STUDER 1987. *Proc. of Sixth Symposium on Dynamics of Large Structures*, Blacksburg, VA, 217-235. Optimum vibration control of flexible beams by piezo-electric actuators.

15. A.Baz, S.POH and J.FEDOR 1989. *Proc. of Seventh Symposium on Dynamics of Large Structures*, Blacksburg, VA, 553-567. Independent modal space control with positive position feedback.

16. A.BAZ and S.POH 1990. *J.of Sound & Vibration*, **139**, **1**, 133-149. Experimental implementation of the modified independent modal space control method.

17. C.R.FULLER, C.H.HANSEN and S.D.SNYDER 1991. *J. of Sound & Vibration*, **145**, **2**, 195-215. Active control of sound radiation from a vibrating rectangular panel by sound sources and vibration inputs: An experimental Comparison.

18. T.W.DUEING and R.ZADNO 1990 *Engineering Aspects of Shape Memory Alloys* ed.by T.DUERIG, K.MELTON, D.STOCKEL and C.M.WAYMAN. London, England: Butterworth-Heinemann, Ltd. 369-393. An engineer's prespective of psuedoelasticity.

19. M.J.BALAS 1978 *J.of Optimization Theory and Application*, **25**, **3**, 415-436. Active control of flexible systems.

20. D.J.EWINS 1984. *Modal Testing:Theory and Practice*. Letchworth, England: Research Studies Press, Ltd.

APPENDIX

CALIBRATION OF THE SMA DISTRIBUTED SENSOR

The linear nature of the **SMA** distributed sensor, as defined by equations (15) and (19), makes its calibration a rather simple process. Such a calibration is necessary to account for errors in the parameters of the sensor such as the position and length of the **SMA** wire and its different segments. The calibration procedure is based on the use of a conventional laser sensor placed at location **i** along the beam to monitor the beam physical displacement $\mathbf{y}_{ik}$ at time sample k. The beam is subjected to a general excitation and the corresponding resistance changes ΔR_k of the different wire segments are determined at the same sample interval k. The collection of a set of **z** measurements of the physical displacement $\mathbf{y}_{ik}$ and the resistance changes ΔR_k may be concatenated, based on equation (19), to form the following equation:

$$Y_i = \Delta\mathcal{R} \quad C_i \tag{A-1}$$

where

Y_i = vector of concatenated physical displacement measurements given by

$$= \begin{bmatrix} y_{i(k)} & y_{i(k+1)} & \cdots & y_{i(k+z-1)} \end{bmatrix}^T, \tag{A-2}$$

$\Delta\mathcal{R}$ = matrix of concatenated resistance changes, given by

$$= \begin{bmatrix} \Delta R_{1(k)} & \Delta R_{2(k)} & \cdots & \Delta R_{N(k)} \\ \Delta R_{1(k+1)} & \Delta R_{2(k+1)} & \cdots & \Delta R_{N(k+1)} \\ \cdots & \cdots & \cdots & \cdots \\ \Delta R_{1(k+z-1)} & \Delta R_{2(k+z-1)} & \cdots & \Delta R_{N(k+z-1)} \end{bmatrix}, \tag{A-3}$$

and $\mathbf{C}_i$ = vector of sensor parameters at location i, given by

$$= \begin{bmatrix} c_{i1} & c_{i2} & \cdots & c_{iN} \end{bmatrix}^T. \tag{A-4}$$

The elements of the vector $\mathbf{C}_i$ can then be computed using the least mean squared estimates as follows

$$\mathbf{C}_i = [\Delta\mathcal{R}^T \, \Delta\mathcal{R}]^{-1} \, \Delta\mathcal{R}^T \, Y_i \tag{A-5}$$

The above procedure is repeated by moving the laser sensor to location j and estimating the vector $\mathbf{C}_j$ of sensor parameters in a similar manner. When all the rows $\mathbf{C}_i{}^s$ are estimated, the matrix $\mathbf{C}$ is formed and the calibration process of the distributed sensor is completed provided that the modal shape matrix Φ is already known or is experimentally determined using the classical modal analysis methods [20].

NOMENCLATURE

Latin letters

a	distance between SMA wire and neutral axis
A	cross sectional area of wire
A_b	cross sectional area of beam
$\underline{C}$	matrix given by equation (10) (NxN)
$\bar{C}$	matrix given in equation (21) (PxN)
C_i	ith row of C matrix
E	Young's modulus of composite beam
F	force acting on beam
I	area moment of inertia of beam
k	sample order
k_i	the wave number for the ith mode given by equation (7)
L_i	length of ith segment
M	moment acting on beam
N	number of wire segments, number of measured modes, and number of measured physical coordinates
P	number of accurate modal displacements
R_i	resistance of ith wire segment
t	time
T	beam thickness
u_i	modal coordinate of ith mode
$\underline{U}$	modal coordinate vector (Nx1)
$\bar{U}$	accurate modal coordinate vector (Px1)
x	distance along the neutral axis of beam
y	deflection in transverse direction
Y	vector of physical deflection of tapping points
Y_i	vector of concatenated physical displacements at ith location
z	number of calibration samples

Greek letters

α_i	constant for ith mode given by equation (6)
ΔL_i	change in length of ith segment
ΔL	vector of length changes (Nx1)
ΔR_i	changes in resistance of ith segment
ΔR	vector of resistance changes (Nx1)
$\Delta \mathcal{R}$	matrix of concatenated resistance changes
ε	strain in SMA wire
ρ	mass density of composite beam
ρ_e	electrical resistivity of SMA wire
ϕ_i	mode shape for ith mode
$\underline{\Phi}$	modal shape matrix (NxN) given in equation (17)
$\bar{\phi}$	modal shape matrix (NxP) given in equation (22)
ω_i	the ith mode

To appear in J. of Sound & Vibration

THE STATIC AND DYNAMIC CHARACTERISTICS OF NITINOL-REINFORCED COMPOSITE BEAMS

A. BAZ, S. POH, J. RO and J. GILHEANY
Department of Mechanical Engineering
The Catholic University of America
Washington, DC 20064

ABSTRACT

The static and dynamic characteristics of flexible fiberglass composite beams are controlled by activating optimal sets of shape memory alloy (**NITINOL**) wires which are embedded along the neutral axes of these beams. The underling phenomena influencing the behavior of this class of composite structural members are presented. The individual contributions of the fiberglass-resin laminate, the NITINOL wires and the shape memory effect to the overall performance of the composite beam are determined at different operating temperatures and initial preloads of the wires. The modes of vibration of the fiberglass beams are measured with and without the NITINOL reinforcement at various operating conditions. With properly designed NITINOL reinforcement, it is shown that the beams can become stiffer and less susceptible to buckling. The modes of vibrations of the activated Nitinol-reinforced composite beams can also be shifted to higher frequency bands relative to those of the unactivated or un-reinforced beams. Finite element models are developed to describe the static, dynamic and thermal interaction between the NITINOL wires and the fiberglass-resin laminates. Close agreement is obtained between theoretical predictions and experimental results. With such tunable characteristics, the NITINOL-reinforced composite beams can be effective in attenuating the vibrations induced by various external disturbances.

1. INTRODUCTION

Considerable attention has recently been devoted to the utilization of the Shape Memory NIckel-TItanium alloy (**NITINOL**) in developing **SMART** composites that are capable of adapting intelligently to external disturbances (Ikegami et al. [1], Rogers et al. [2], and Baz et al. [3-4]). Such wide acceptance of **NITINOL** stems from its unique behavior when it is subjected to particular heating and cooling strategies. For example, the alloy becomes soft when it is cooled below its martensite transformation temperature and becomes about four times stiffer when it is heated above its austenite transformation temperature (Funakubo [5]). Furthermore, when the alloy is trained to have a particular shape while in its austenite phase, it will memorize this shape. If the alloy is then cooled to its martensite phase and subject to plastic deformation, it will return to its **memorized** shape when it is heated above the austenite transformation temperature. The phase transformation from martensite to austenite produces significant forces as the alloy recovers its original shape. The alloy acts as an actuator transforming thermal energy into mechanical energy (Perkins [6] and Duerig et al. [7]). Accordingly, if the **NITINOL** fibers are embedded inside a composite matrix at optimal locations, they can be used to control the static and dynamic characteristics of the resulting **SMART** composite. The control action is generated by the described stiffening of the NITINOL fibers and/or the shape memory effect. With such built-in control capabilities, the performance of the **SMART** composites can be optimized and tailored to match changes in operating conditions.

Emphasis is placed in the present work on using the shape memory effect of the NITINOL fibers to control the performance of fiberglass composite beams. The NITINOL fibers are embedded inside vulcanized rubber sleeves placed along the neutral axes of these composite beams as shown in Figure (1). In this arrangement, the fibers are free to move during the phase transformation process in order to avoid degradation and/or destruction of the shape memory effect which may result when the fibers are completely bonded to the composite matrix.

The basic phenomena governing the static and dynamic performance of the NITINOL-reinforced composites will be presented, both theoretically and experimentally in this paper.

The paper is organized in five sections. In section **1**, a brief introduction is given. In sections **2** and **3**, the finite element models describing the static and dynamic characteristics of the NITINOL-reinforced beams are introduced respectively. The experimental validation of the finite element models is presented in section **4** and the conclusions are summarized in section **5**.

2. STATIC CHARACTERISTICS OF NITINOL-REINFORCED BEAMS

The static characteristics of NITINOL-reinforced composite beams are primarily governed by their stiffness. The beam stiffness is made up of different components which include: the flexural rigidity of the beam, the geometric stiffness that accounts for the axial and thermal loading, as well as the stiffness imparted by the elasticity of the NITINOL fibers. The individual components of the beam stiffness can be determined by considering the NITINOL-reinforced beam element shown in Figure (2) with the forces acting on it and the associated displacements. The combined stiffness of the element can be obtained using the principle of conservation of energy and equating the work done by external loads to the strain energies stored in the element. In the present analysis, the theory of Bernoulli-Euler beams is used with the assumption of small deflections.

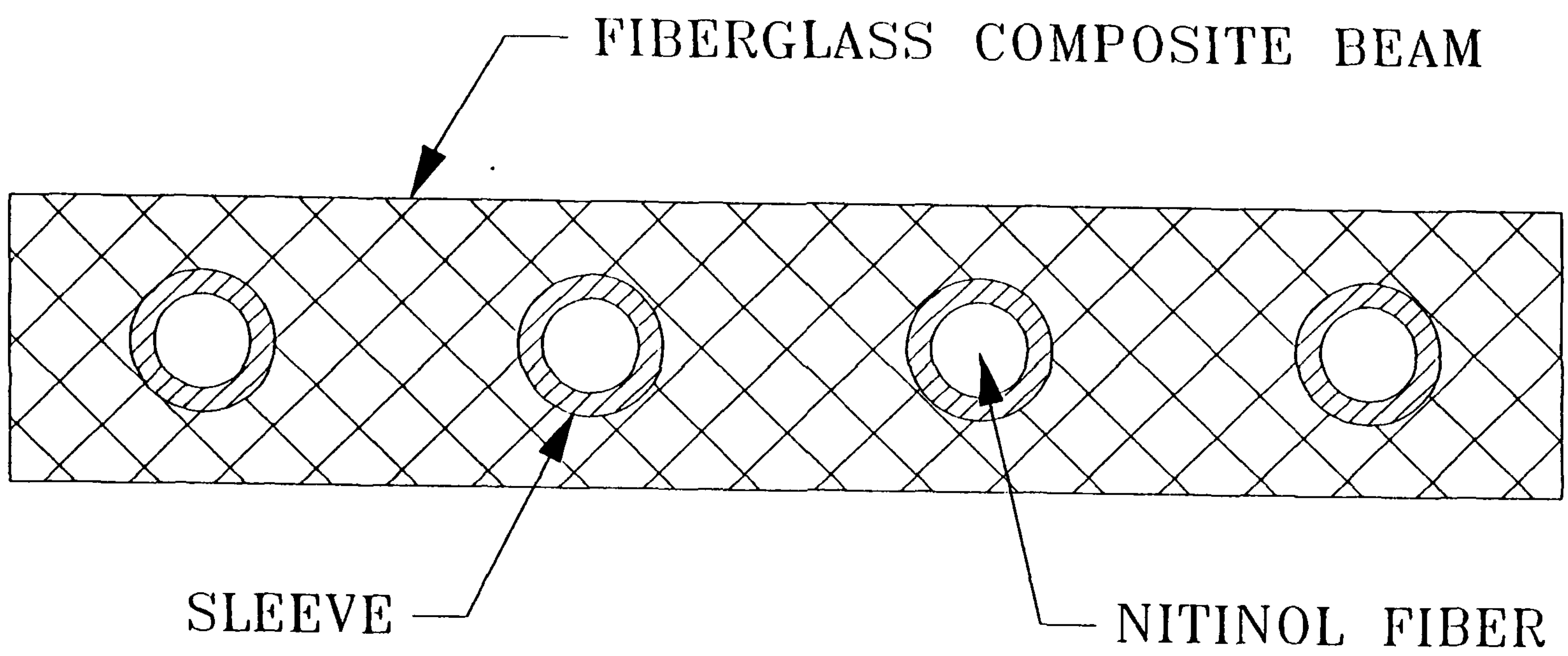

Figure (1) - A schematic drawing of the cross section of a NITINOL-reinforced composite beam.

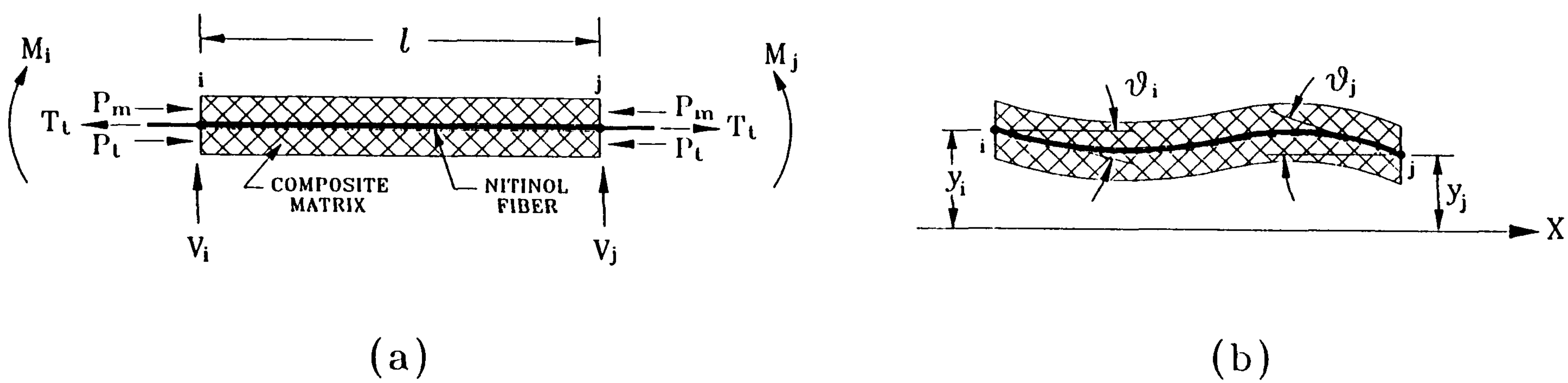

Figure (2) - NITINOL-reinforced beam element with forces and resulting displacements.

2.1. EXTERNAL WORK

The work done by the external loads includes:

a. work done by transverse loads and moments (W_1)

This work is given by

$$W_1 = 1/2\ [\delta]^T\ [F], \tag{1}$$

where $[\delta]$ and $[F]$ are the displacement and transverse loads vectors, respectively, given by

$$[\delta] = [w_i \quad \vartheta_i \quad w_j \quad \vartheta_j]^T, \tag{2}$$

and

$$[F] = [V_i \quad M_i \quad V_j \quad M_j]^T, \tag{3}$$

where w_i and ϑ_i are the linear and angular deflections of node i, respectively and V_i and M_i are the shear and moment acting at node i, respectively.

b. work done by the axial mechanical loads (W_{2m})

W_{2m} is given by [8] as

$$W_{2m} = P_m / 2 \int_0^L (dw/dx)^2\, dx, \tag{4}$$

where P_m is the external axial compressive load acting along the neutral axis of the beam element.

c. work done by the axial thermal loads (W_{2t})

W_{2t} represents the work done by the thermal loads P_t on the beam element due to changes in the temperature $\Delta\Theta$ of the element caused by changes in the ambient temperature or during the activation and de-activation of the NITINOL fibers. It is given by

$$W_{2t} = P_t / 2 \int_0^L (dw/dx)^2\, dx, \tag{5}$$

where P_t is given by

$$P_t = \alpha\, \Delta\Theta\, E_m\, A_m, \tag{6}$$

where α is the thermal expansion coefficient of the composite, E_m is its modulus of elasticity and A_m is the beam cross sectional area.

2.2. STORED STRAIN ENERGY

The stored strain energy consists of two components:

a. strain energy of beam (W_3)

The energy stored in the beam element due to its bending [9] is given by

$$W_3 = E_m I_m / 2 \int_0^L (d^2w/dx^2)^2 \, dx \tag{7}$$

where $E_m I_m$ is the flexural rigidity of the beam.

b. strain energy of NITINOL fibers (W_4)

Considering the NITINOL fiber as a string, as shown by Baz et al [10], with a tension **T** which is displaced laterally a di ance **w** from the neutral axis of the beam, then its stored strain energy W_4 is given by [9]

$$W_4 = T / 2 \int_0^L (dw/dx)^2 \, dx. \tag{8}$$

Equating the sum of the work done by the external forces **F**, P_m and P_t to the sum of the strain energies stored in beam and NITINOL fibers gives

$$W_1 + W_{2m} + W_{2t} = W_3 + W_4. \tag{9}$$

Substituting equations (1), (4), (5), (7) and (8) into equation (9) yields

$$[\delta]^T[F] = E_m I_m \int_0^L (d^2w/dx^2)^2 \, dx - P_n \int_0^L (dw/dx)^2 \, dx, \tag{10}$$

where P_n is the net axial force give by

$$P_n = (P_m + P_t - T). \tag{11}$$

Defining a cubic displacement function for the composite beam element, of the following form

$$w = a + b\,x + c\,x^2 + d\,x^3, \tag{12}$$

where a, b, c and d are constants that can be calculated in terms of the deflections of the nodes **i** and **j** bounding the beam element, equation (12) can be rewritten as

$$w = [A]\ [\delta], \tag{13}$$

where the elements of matrix [A] are function of x (Fenner [11]).

Accordingly, dw/dx and d^2w/dx^2 can be obtained by differentiating equation (13) with respect to x to yield

$$dw/dx = [C]\ [\delta] \quad \text{and} \quad d^2w/dx^2 = [D]\ [\delta], \tag{14}$$

where the matrices [C] and [D] are given by

$$[C] = \frac{d}{dx}\,([A]) \qquad \text{and} \qquad [D] = \frac{d^2}{dx^2}\,([A]). \tag{15}$$

The following relationships can also be obtained from equation (14)

$$(dw/dx)^2 = [\delta]^T[C]^T[C][\delta] \quad \text{and} \quad (d^2w/dx^2)^2 = [\delta]^T[D]^T[D][\delta]. \tag{16}$$

If the stiffness matrix $[K_e]$ of the element is defined by the following relationship

$$[F] = [K_e]\ [\delta], \tag{17}$$

then, $[K_e]$ can be determined by combining equations (10), (16) and (17) as follows

$$[K_e] = E_m\, I_m \int_0^L [D]^T[D]\ dx - P_n \int_0^L [C]^T[C]\ dx. \tag{18}$$

It can be seen from equation (18), that the element stiffness matrix $[K_e]$ consists of two components: the conventional transverse stiffness and the geometric stiffness that combines the effect of the axial mechanical loads, axial thermal loads and the tension of the NITINOL reinforcing fibers. Equation (18) also represents the basic equation for understanding the role that the NITINOL fibers can play in controlling the static characteristics of the composite beam. For example, if the beam is not reinforced by NITINOL fibers (i.e. $T = 0$) and the mechanical and thermal loads induce compressive stresses in the beam, then the geometric stiffness will increase and the total element stiffness will decrease. When the combined effect of the mechanical and thermal loads reaches a critical magnitude such that the geometric stiffness becomes equal to the flexural stiffness of the beam, the beam stiffness vanishes and the beam becomes elastically unstable. Subjecting the beam under this condition to any additional external disturbance will cause the beam to buckle.

It should be pointed out that the thermal loading, as it increases the geometric stiffness, also decreases the flexural stiffness of the beam because it reduces its effective modulus of elasticity E_m. Such a dual effect makes the beam buckle under smaller thermal loads than under pure mechanical loads.

However, the critical load of the un-reinforced beam can be increased by embedding pre-strained NITINOL fibers into the beam. If the tension T, resulting from the pre-strain alone, is high enough to counter-balance the mechanical and thermal effects then the beam stiffness can be maintained unchanged. For higher pre-strain levels, the beam stiffness can be enhanced. Further enhancement can be achieved when the shape memory effect of the NITINOL fibers is activated by heating the fibers above their austenite phase transformation temperature. The additional tension, induced into the fibers by the phase recovery forces makes the net axial load P_n negative, and accordingly increases the overall stiffness of the beam element. However, it is essential that the total tension in the NITINOL fibers, i.e., the sum of the tension due to the pre-strain and the phase recovery force, must exceed the mechanical and thermal loads and compensate for the softening effect produced in the matrix by the heating the NITINOL fibers. Therefore, effective control of the stiffness of NITINOL-reinforced composites can be achieved by proper selection of the initial pre-strain level of the NITINOL fibers. This selection is particularly crucial as the pre-strain level determines the generated levels of recovery forces [10].

The finite element model of the NITINOL-reinforced beams describes the interaction between the external loads, operating conditions and the geometrical and physical parameters of the composite beam and the NITINOL fibers. It defines how the NITINOL fibers can be utilized to tailor the stiffness of the composite to compensate for environmental and operating conditions and disturbances. The stiffness obtained for the individual elements of the beam can be assembled using the classical finite element approach (Fenner [11]). The assembled model can then be subjected to the appropriate boundary conditions in order to compute the deflections corresponding to particular external loading conditions. The analysis presented is for an orthotropic laminate that has a single layer of unidirectional NITINOL fibers. Such an analysis can be used along with the classical laminate theory (Vinson and Sierakowski [12]) to assemble the stiffness matrix for a multi-laminate composite beam. A similar approach has been carried out for modeling the static and dynamic characteristics of NITINOL-reinforced composite plates (Baz, Ro and Gilheany [13]). The finite element model developed will be validated with experimental results obtained with fiberglass composite beams.

3. DYNAMIC CHARACTERISTICS OF THE NITINOL-REINFORCED BEAMS

The dynamic characteristics of NITINOL-reinforced beams are obtained by combining the stiffness matrix $[K_e]$ with the mass matrix $[M_e]$ of the beam to form the following element equations of motion

$$[M_e]\ [\ddot{\delta}] + [K_e]\ [\delta] = [F], \tag{19}$$

where $[\ddot{\delta}]$ is the nodal acceleration vector. The elements $m_e(i,j)$ of the element mass matrix $[M_e]$ are obtained using the consistent mass formulation (Zienkiewicz and Taylor [14]) as follows

$$m_e(i,j) = \rho_m\ A_m \int_0^L A_i\ A_j\ dx, \tag{20}$$

where A_i and A_j are the ith and jth elements of the vector A given by equation (13).

The classical finite element approach is used to form the equations of motion of the assembly of several beam elements and the appropriate boundary conditions are then applied. The solution for the eigenvalues of the resulting homogeneous equations give the natural frequencies of the composite beam as influenced by the properties of the composite matrix and the NITINOL fibers. It is important to note that these properties are influenced by the temperature distribution inside the beam which is developed by virtue of activating and de-activating the NITINOL fibers.

4. EXPERIMENTAL VALIDATION

4.1 Test facility and experimental beam

The characteristics of NITINOL-reinforced beams are computed using the developed static and dynamic models. The theoretical predictions are compared with experimental results obtained with a composite beam made of randomly oriented glass fibers embedded in a low cure temperature polyester resin. The beam is 30 cm long, 2.5 cm wide and 0.156 cm thick and is mounted with fixed-fixed boundary conditions. The temperature dependence of the modulus of elasticity of the beam, shown in Figure (3), is obtained experimentally using the Dynamic, Mechanical, and Thermal Analyzer (**DMTA**) of Polymer Laboratories, Ltd [15].

Four NITINOL 55 fibers, that are 0.55 mm in diameter, are embedded inside the beam through vulcanized rubber sleeves that have outer diameter of 0.95 mm. Two sets of NITINOL fibers were used. The first set consisted of trained fibers that have an austenite transformation temperature of 50°C. However, the second set is untrained and the shape memory effect has not been imparted to it. The two sets are inserted, one at a time, inside the sleeves and the effect of the shape memory and the associated phase recovery forces on the performance of the composite beam are monitored when the beam is exposed to different ambient temperatures. The experimental set-up, shown in Figure (4), is placed inside a temperature-controlled chamber to determine the natural frequencies of the fixed-fixed beam as a function of the ambient temperature. In the set-up the NITINOL-reinforced beam is fixed at both ends, whereas the NITINOL fibers are clamped in a holder at one end and connected to a load cell at the other end. The load cell monitors the pre-strain level of the fibers when they are in their martensitic phase, as well as continuously measuring the recovery force when the fibers undergo phase transformation. In this arrangement, the fibers are activated thermally by controlling the temperature of the environmental chamber. The measurements are carried out after steady-state

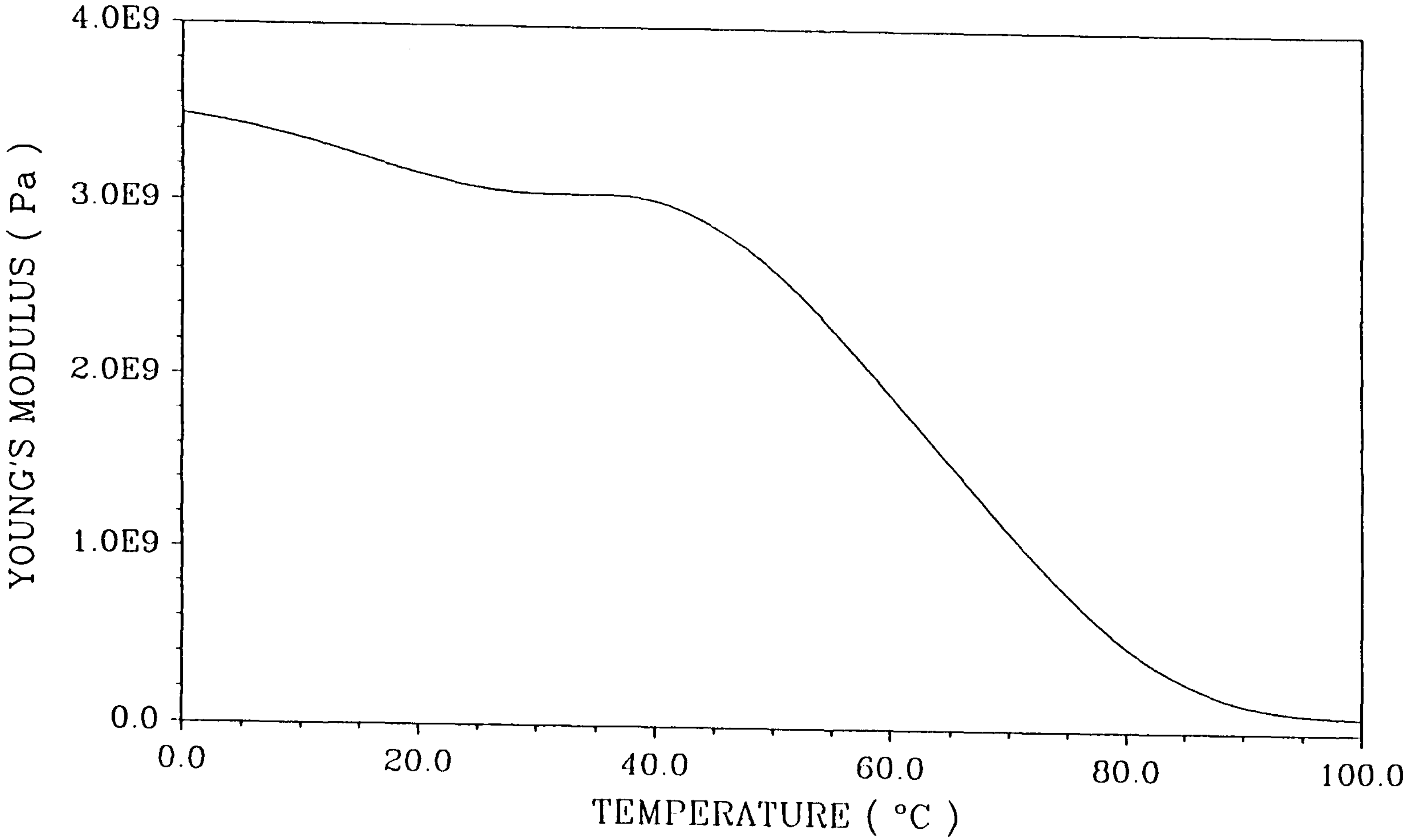

Figure (3) - Effect of operating temperature on modulus of elasticity of the test fiberglass composite beam.

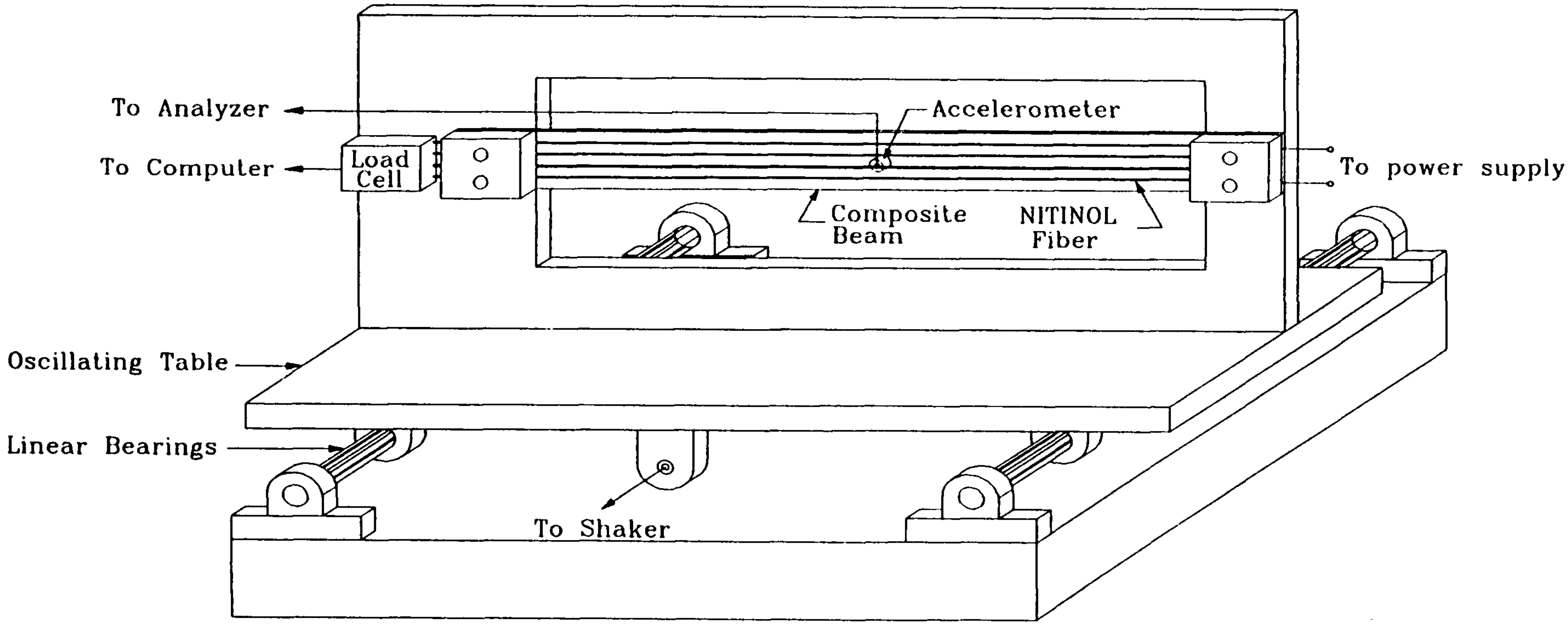

Figure (4) - Experimental set-up used in monitoring the performance of NITINOL-reinforced beams.

and thermal equilibrium conditions are attained. Under these conditions, the composite matrix and the NITINOL fibers are all at the same equilibrium temperature. At each equilibrium temperature, the composite beam is subjected to random vibrations and the resulting response is monitored by an micro-accelerometer bonded to the beam. The response is analyzed in the frequency domain to determine the modes of vibration of the composite beam.

4.2 Natural frequencies of NITINOL-reinforced beams

Figure (5-a) shows the measured changes in the first natural frequency of the beam when it is reinforced with untrained NITINOL fibers which are pre-strained at different levels. The changes are normalized with respect to the natural frequency ω_b of the un-reinforced beam measured at 25^{o}C, i.e. 50.1 Hz. The normalized characteristics of the un-reinforced beam are also plotted to serve as a datum for defining both the effect of reinforcing the beam with NITINOL fibers and the effect of the pre-strain level. It can be seen that the frequency of the un-reinforced beam drops as the ambient temperature increases and the beam losses its elastic stability and start to buckle when the temperature exceeds 40^{o}C . The drop in the natural frequency of the un-reinforced beam is attributed to the softening of the matrix which is clearly demonstrated by the loss in the modulus of elasticity of the beam as shown in Figure (3).

Reinforcing the beam with pre-strained untrained NITINOL fibers considerably increases the natural frequency of the beam. The extent of the upward shift in natural frequency increases with increased pre-strain level. An increase of about 40% is obtained at room temperature when the pre-strain level is only 0.26%. However, as the ambient temperature increases the frequency shift drops in a manner similar to the characteristics of the plain un-reinforced beam. Such a drop is again

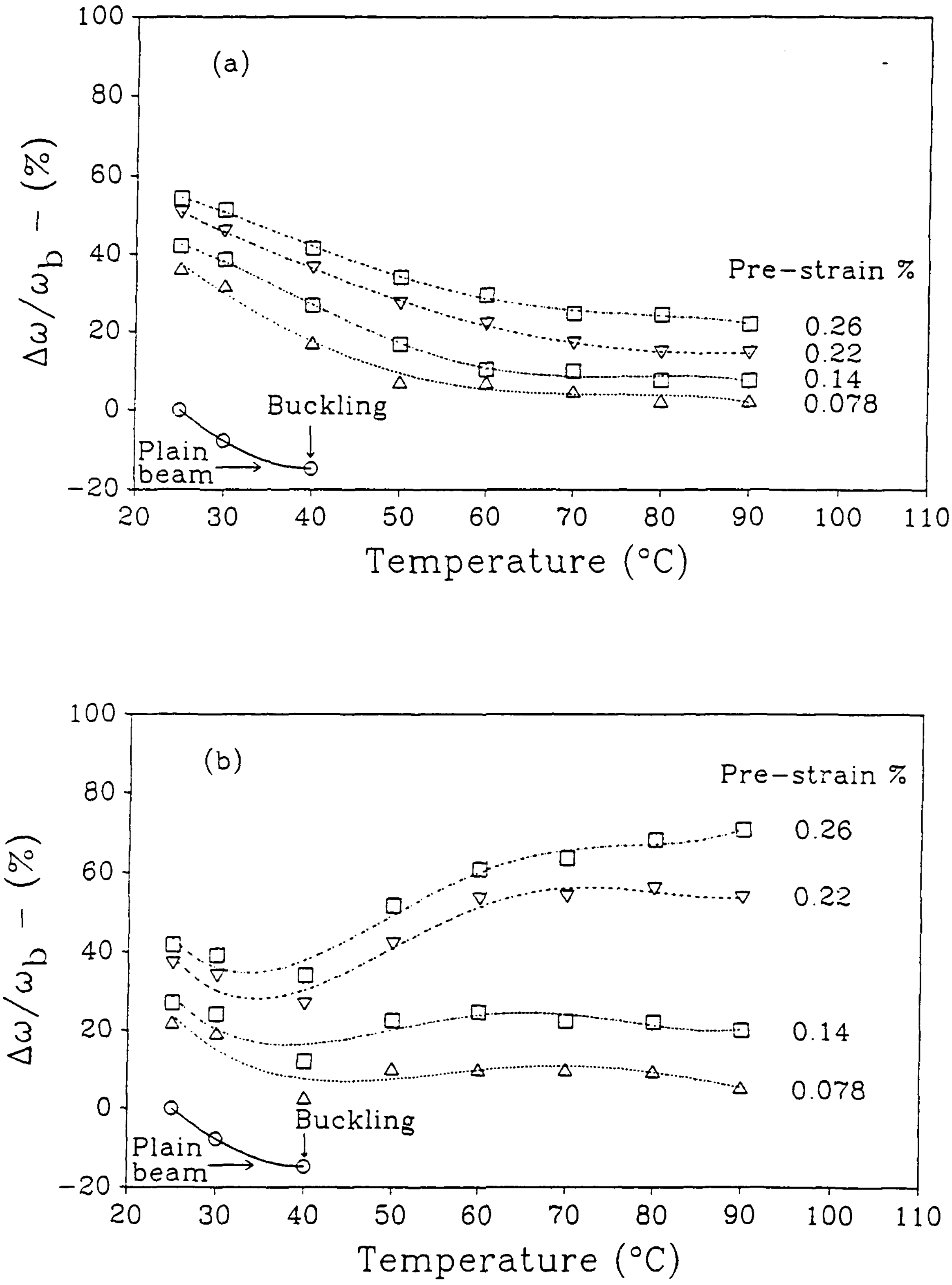

Figure (5) - Effect of the ambient temperature and pre-strain level on enhancing the first mode of vibration of fixed-fixed composite beam reinforced with NITINOL fiber without (a) and with (b) shape memory.

attributed to the softening effect of the matrix and the fact that the untrained NITINOL fibers act as a static pre-tensioning device that produce constant tension which is independent of temperature. Therefore, the frequency enhancement is only generated by the reinforcement and the pre-strain effects, and not by the shape memory effect. It is important to note that considerably higher increases in the natural frequencies can be obtained by further increases of the pre-strain level up to its maximum permissible level of 6%.

However, a greater frequency shift can be achieved by imparting the shape memory effect to the NITINOL fibers. The fibers are trained over 250 cycles using the procedure outlined by Johnson [16]. The trained fibers are inserted into the composite beam to replace the untrained set and the frequency shifts become significant, particularly at high ambient temperatures. This is clearly demonstrated in Figure (5-b). For temperatures between room temperature and $40^{o}C$, the frequency shifts obtained are similar to those with the untrained fibers within experimental accuracy. Once the ambient temperature exceeds the $50^{o}C$, i.e. the austenite phase transformation temperature of the NITINOL fibers, the frequency shift characteristics changes from a gradually decaying trend to one that is a gradually increasing. Such a sudden change is the result of the contribution of the phase recovery forces developed by the shape memory effect which is illustrated in Figure (6).

The shape memory effect generates strain energy in the NITINOL fibers to counterbalance the softening effect of the composite matrix with increasing temperature. As the amount of strain energy developed depends on the initial pre-strain level, it can merely compensate for the softening effect to maintain the beam frequency at nearly a constant value which is independent of ambient temperature as shown for pre-strain level of 0.078%.

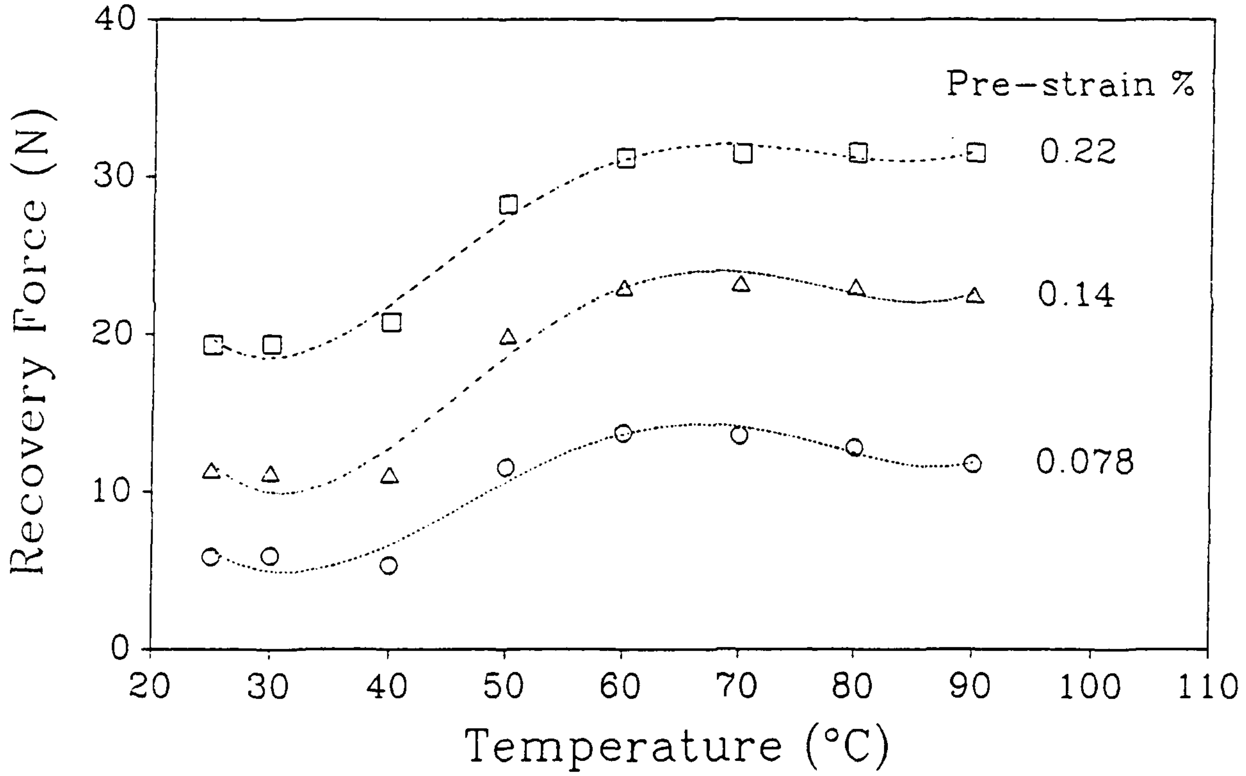

Figure (6) - Effect of pre-strain level and ambient temperature on the phase recovery forces of trained NITINOL fibers.

It can also increase the beam frequency as the ambient temperature increases as indicated for pre-strain levels of 0.22 and 0.26%. For a pre-strain level of 0.26% and ambient temperature of 90°C, the frequency increase reaches about 70% as compared to an 18% increase when untrained fibers are used. In this manner, the individual contributions of the pre-strain, matrix softening and shape memory effect on the frequency shift are isolated. This facilitates checking the validity of the mathematical models against the experimental results.

Comparisons between the theoretical predictions and the measurements are shown in Figures (7-a) and (7-b) for NITINOL fibers without and with shape memory effect, respectively. The figures include comparisons for the first and second modes of vibrations. Close agreement between theory and experiments is evident.

5. CONCLUSIONS

The static and dynamic characteristics of NITINOL-reinforced composite beams have been presented. The fundamental issues governing the behavior of this new class of **SMART** composites have been introduced. Applications of NITINOL reinforcing to control the static and dynamic behavior of composite beams have been successfully demonstrated.

Emphasis has been placed in the presentation on the actuation capabilities of the NITINOL fibers. However, extensive efforts are in progress to use the NITINOL fibers to extract modal and physical displacements of structures with multi-modes of vibration (Baz, Poh and Gilheany [17]).

With such built-in sensing and controlling capabilities, NITINOL-reinforced composites can provide a means for continuously tuning

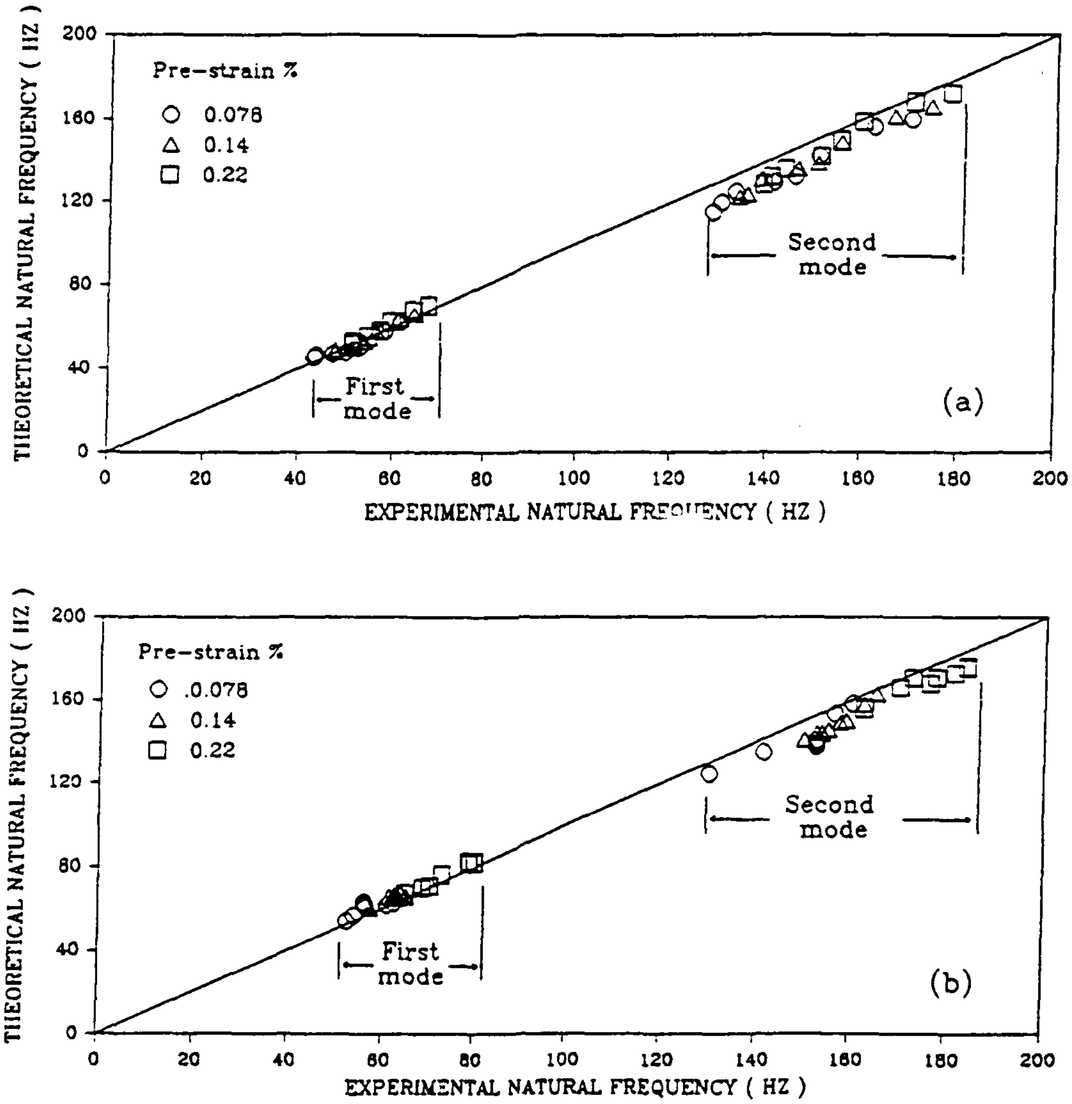

Figure (7) - Comparison between the theoretical and experimental frequencies of composite beam reinforced with NITINOL fibers without (a) and with shape memory (b).

the structural characteristics to adapt to changes in the operating conditions. These features will be particularly useful in many critical structures that are intended to operate autonomously for long durations in isolated environment such as defense vehicles, space structures and satellites.

ACKNOWLEDGEMENTS

This work is funded by a grant from the US Army Research Office (Grant number DAAL03-89-G-0084). Special thanks are due to Dr. Gary Anderson, the technical monitor and Chief of the Structures and Dynamics Branch of ARO, for his invaluable and continuous technical inputs.

NOMENCLATURE

[A]	interpolating function of beam deflection
A_i	ith element of [A]
A_m	cross sectional area of beam
[C], [D]	first and second derivatives of interpolating function of beam deflection
E_m	Young's modulus of beam
[F]	vector of external loads acting on beam
I_m	area moment of inertia of beam
$[K_e]$	stiffness matrix of beam element
L	length of beam element and NITINOL fiber
M_i	external moment acting at ith node
$[M_e]$	mass matrix of beam element
$m_e(i,j)$	the element i,j of the mass matrix
$P_{m,n,t}$	mechanical, net and thermal axial loads acting on beam
q_n	generalized coordinate of the nth vibration mode of NITINOL fiber
$\ddot{q}_n$	generalized acceleration of the nth vibration mode of NITINOL fiber
t	time
T_o	initial tension in a NITINOL fiber
T_t	total tension in a NITINOL fiber
V_i	shear force acting at the ith node
w	transverse deflection of beam and NITINOL fibers
W_1	work done by transverse loads
W_{2m}	work done by mechanical axial loads
W_{2t}	work done by thermal axial loads
W_3	strain energy of beam
W_4	strain energy of NITINOL fiber
x, y, z	cartesian coordinates along beam neutral axis and cross section respectively

Greek letters

$[\delta]$	the deflection vector of beam element
$\Delta\Theta$	axial temperature difference
ϑ_i	angular deflection of ith node
ϕ_n	mode shape of the nth mode
ω_n	natural frequency of the nth mode

REFERENCES

1. **IKEGAMI, R., WILSON, D. and LAAKSO, J.** 1990. *Edwards AFB Technical Report* # AL-TR-90-022 (F04611-88-C-0053). Advanced composites with embedded sensors and actuators (ACESA).
2. **ROGERS, C., LIANG, C. and JIA, J.**, 1991. *Computers & Structures*, **38**, 5/6, 569-580. Structural modification of simply-supported laminated plates using embedded shape memory alloy fibers.
3. **BAZ, A., and TAMPE, L.** 1989. *Proc. of ASME Design Technical Conference*, Montreal, Canada, **DE-16**, 211-218. Active control of buckling of flexible beams. Proc.of ASME Design Technical Conference, Montreal, Canada, Vol. DE-16, pp.211-218, Sept. 1989.
4. **BAZ, A., IMAN, K. and McCOY, J.**. 1990. *J. of Sound & Vibration*, 140, 3, 437-456. Active control of flexible beams using shape memory actuators.
5. **FUNAKUBO, H.**, 1987.*Shape Memory Alloys*, Gordon and Breach Science Publishers.
6. **PERKINS, J.** 1975. *Shape Memory Effect in Alloys*, Plenum Press, New York.
7. **DUERIG, T.W., MELTON, K.N., STOCKEL, D., and WAYMAN, C.**, 1990. *Engineering Aspects of Shape Memory Alloys*, Butterworth and Heinemann Ltd., London.
8. **CHAJES, A.** 1974. *Principles of Structural Stability Theory.* Prentice-Hall, Inc., Englewood Cliffs, N.J.
9. **BICKFORD, W.B.** 1990. *A First Course in The Finite Element Method.* Irwin, Homewooa, IL.
10. **BAZ, A., POH, S., RO, J., MUTUA, M. and GILHEANY, J.** 1991 *Intellingent Structures & Systems.* Edited by H.S.TZOU, Kulwer Academic Publishers. Dordrecht, The Netherlands. Active control of NITINOL-reinforced composite beams.
11. **FENNER, R.T.** 1975. *Finite Element Methods for Engineers.*, Macmillan Press Ltd., London.
12. **VINSON, J.R. and SIERAKOWSKI, R.L.** 1987. *The Behavior of Structures Composed of Composite Materials.* Martinus Nijhoff Publishers, Dordrecht, The Netherlands.
13. **BAZ, A., RO, J. and GILHEANY, J.** 1991. *Fourth Workshop on Dynamics and Aeroelastic Stability Modeling of Rotorcraft Systems*, University of Marlyand, College Park. The thermal and dynamic characteristics of NITINOL-reinforced plates.
14. **ZIENKIEWICZ, O.C. and TAYLOR, R.L.**, 1989. *The Finite Element Method.* Vol.1, Fourth Edition, McGraw-Hill Book Co., New York.
15. **POLYMER LABORATORIES LTD.**, 1990. Loughborough, United Kingdom. PL-DMTA, MKII dynamic mechanical thermal analyser.
16. **JOHNSON, A.**, 1984. *US Patent* number 4,435,229. Method of preparing a two-way shape memory alloy.
17. **BAZ, A., POH, S. and GILHEANY, J.**, 1991. *ASME Winter Annual Meeting*, Atlanta, GA. A multi-mode distributed sensor for vibrating beams.

ASME Winter Annual Meeting
Anaheim, CA - Nov. 1992.

ADAPTIVE CONTROL OF FLEXIBLE STRUCTURES USING MODAL POSITIVE POSITION FEEDBACK

A. Baz and Jong-Tai Hong

Mechanical Engineering Department
The Catholic University of America
Washington, DC 20064

ABSTRACT

An Adaptive Modal Positive Position Feedback (**AMPPF**) method is presented for controlling the vibration and shape of flexible structures. The proposed strategy combines the attractive attributes of the Independent Modal Space Control (IMSC) of Meirovitch and Positive Position Feedback (PPF) of Goh and Caughy. The controller is designed in the uncoupled modal space using only modal position signals to damp the vibration of undamped modes. The parameters of the **AMPPF** controller are also adjusted in an adaptive manner in order to follow the performance of an optimal reference model. In this way, optimal damping and zero steady-state errors can be achieved even in the presence of uncertain or changing structural parameters.

The adaptation laws governing the stable variation of the **AMPPF** controller parameters are derived using Lyapunov stability theorem. The effectiveness of the AMPPF in controlling the vibration and shape of a variable mass cantilevered beam is demonstrated experimentally. The performance obtained with the AMPPF algorithm is compared with those of other classical control algorithms. The results obtained emphasize the potential of the AMPPF algorithm as an efficient means for controlling flexible structures with uncertainties in real time.

1. INTRODUCTION

Considerable emphasis has been recently placed on the development of wide variety of adaptive control algorithms to effectively control the vibration and shape of large flexible structures. Such algorithms aim at compensating for the problems arising from the uncertainty of accurately modeling the dynamics of these structures, truncation of their dynamic models and the associated control spillover from the residual modes, variation of the structural parameters and nonstationarity of the disturbances acting on the structures. Without the appropriate adaptation to these problems, fixed gain controllers become totally inadequate to meet the control objectives and the desired performance requirements.

Distinct among the recently developed adaptive control algorithms is that of Bar-Kana and Kaufman [1] which relied in its operation on collocated pairs of sensors/actuators and on feeding back position and velocity outputs. The controller employed the direct reference model approach to theoretically control the vibration of beams, plates and frames. Similar approach, but with proportional and integral controller, has been utilized by Ih et al [2] to experimentally control a 5.6 m antenna at the JPL. K.Ossman et.al. [3] have theoretically developed an adaptive model following controller, for SCOLE, in which position and velocity outputs are forced via a variable structure control to track reference position and velocity paths. K.Ossman et.al. developed also an indirect adaptive controller in which the system parameters are estimated by a recursive least-squares and an LQ controller is designed to quickly damp out the vibration [3]. The effect of the spillover from the unmodeled modes is found to cause the control inputs of this algorithm and the system outputs to grow without bound. Silverberg and Norris [4] devised a self-tuned indirect adaptive controller which identifies the structural dynamics and updates the associated control gains to uniformly damp out the vibration of the structure.

In all the above algorithms, the indirect adaptive controllers and the direct reference models are designed in the physical-coupled space. For large structures this presents serious computational challenges particularly when Kalman filtering is needed as in Ref. [2]. In the present study, the proposed Adaptive Modal Positive Position Feedback (**AMPPF**) controller and its reference model are designed completely in the independent modal space with the open-loop equations of the system remaining uncoupled even after including the modal controller. Also, the **AMPPF** uses only modal position signals to obtain stable and damped performance. Such performance is attained by positively feeding back the position signals through tuned first order filters. The performance of the **AMPPF** algorithm is enhanced by augmenting it with a "time sharing" strategy that utilizes small number of actuators to control larger number of modes. The **AMPPF** algorithm is based on the fixed parameter Modal Positive Position Feedback (**MPPF**) algorithm developed by Baz et.al. which has been successfully utilized to control the vibration of simple beams [5] and more complex structures [6].

The present study aims at developing the adaptation laws of the **AMPPF** algorithm and experimentally evaluate its effectiveness in controlling the vibration and shape of a cantilevered beam.

This paper is organized in five sections. A brief introduction is given in section **1**. The concept of the **MPPF** and the **AMPPF** algorithms are presented in sections 2 and 3 respectively. Section **4** includes the experimental evaluation of the algorithm along with comparisons with other algorithms. Section 5 summarizes the conclusions of this study.

2. MODAL POSITIVE POSITION FEEDBACK (MPPF)

2.1. Concept

The basic concept of the MPPF method can be clearly understood by considering the diagram shown in Figure (1), where the controller is used to control the i^{th} mode of an undamped flexible structure in the independent modal space. The controller feeds back positively the modal displacement u_i through a first order filter that has a time constant τ_i. The filter output Y_i is added to the desired reference modal displacement u_{Ri} and resulting signal is amplified by a proportional controller gain K_i. This gain is set equal to $\gamma_i\omega_i^2$ to be in a form similar to that of Goh and Caughey's [7], where ω_i is the natural frequency of the i^{th} mode. The amplified signal f_i, i.e. the modal control action, is then sent to control the i^{th} mode of the structure.

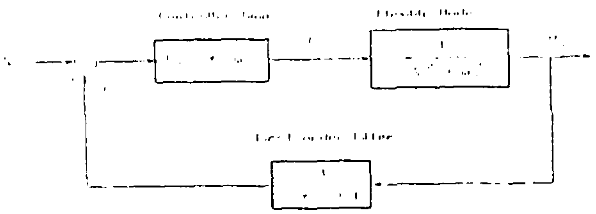

Figure (1) - Block diagram of the MPPF controller.

Mathematically, the interaction between the structural mode and the controller can be described as follows:

$$\text{Structure:}\quad \ddot{u}_i + \omega_i^2 u_i = f_i = \gamma_i \omega_i^2 (Y_i + u_i), \qquad (1)$$

$$\text{Filter:}\quad \tau_i \dot{Y}_i + Y_i = u_i . \qquad (2)$$

The above structure-filter system has the following closed-loop transfer function

$$u_i/u_{Ri}=\gamma_i\omega_i^2(\tau_i s+1)/[\tau_i s^3+s^2+\tau_i\omega_i^2 s+\omega_i^2(1-\gamma_i)], \qquad (3)$$

where s is the Laplace operator. Applying Routh's stability criterion, the system is asympotically stable for value of $0 \le \gamma_i \le 1$ and $\tau_i \ge 0$. Accordingly, it is possible for an undamped system to attain asymptotic stability by feeding positively its position signal through a simple first order filter without the need for any velocity feedback. This constitutes the basic premise of the present control algorithm. Conceptually, the algorithm possesses this favorable stable performance because the first order filter is in effect equivalent to an integral controller with negative feedback. It is also important to note that if the modal position signal is fed back negatively, instead of positively, through the first order filter, the system will always be unstable.

2.2. Parameters of MPPF

2.2.1 controller gain (γ_i)

The implementation of this modal control algorithm requires the selection of two design parameters, i.e., γ_i and τ_i. Actually, only the time constant τ_i of the filter needs to be selected since γ_i must assume a fixed value γ_i= 0.5 to eliminate the controller steady-state error as indicated by equations (1) and (2). Such a value is < 1 and satisfies the asymptotic stability condition previously discussed. Therefore, this algorithm can be equally used for accurate shape control ($u_{Ri} \neq 0$).

2.2.2. filter time constant (τ_i)

The optimal value of the time constant τ_i of the filter is determined by dividing the numerator and denominator of equation (3) by $\tau_i\omega_i^3$ to yield the following equation

$$u_i/u_{Ri}=\gamma_i\alpha_i(\bar{s}/\alpha_i+1)/[\bar{s}^3+\alpha_i\bar{s}^2+\bar{s}+(1-\gamma_i)\alpha_i], \qquad (4)$$

where $\alpha_i = 1/\tau_i\omega_i$ and $\bar{s} = s/\omega_i$. The above system has the following characteristic equation

$$\bar{s}^3 + \alpha_i\bar{s}^2 + \bar{s} + (1-\gamma_i)\alpha_i = 0, \qquad (5)$$

which has the root locus plot shown in Figure (2) for γ_i = 0.5 and $0<\alpha_i<\infty$. The corresponding damping ratio ζ_i of the closed-loop system obtained from the root locus plot, is shown in Figure (3) as a function of α_i which is the only design parameter of the system. Figure (3) indicates that the damping ratio attains a maximum value of 20.07 % when α_i = 1.18. This optimal value is very close to the PPF results obtained experimentally by Fanson and Caughey [8].

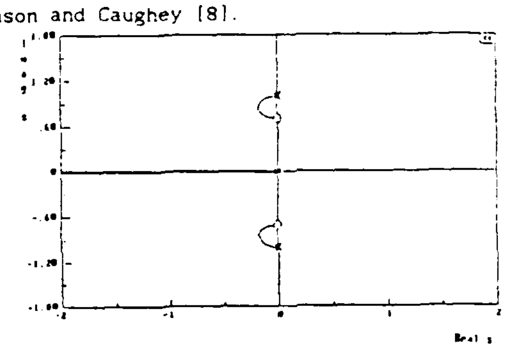

Figure (2) - Root locus of the **MPPF** method with γ_i=0.5.

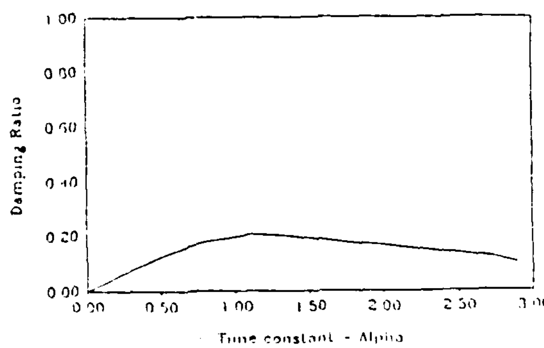

Figure (3) - Effect of α_i on closed-loop damping of **MPPF** method with γ_i=0.5.

In summary, using first order filters, instead of the second order filters of Goh and Caughey, has simplified the design without compromising the damping characteristics of the controller. More importantly, since the analysis presented is applicable to any mode, **uniform damping** for all the modes results if all their filters are tuned to satisfy the optimal tuning condition (α_i = 1.18). Accordingly, a damping ratio of 20.07 % can be maintained for any mode i, that has natural frequency ω_i, by selecting the time constant τ_i of its filter such that

$$\tau_i = 1 / 1.18\ \omega_i \qquad \text{for } i = 1,2,\ldots N, \qquad (6)$$

where N is the number of controlled modes.

3. ADAPTIVE-MPPF with PARAMETER ADAPTATION (AMPPF)

3.1. Need for parameter adaptation

In order to effectively utilize the **MPPF** method in controlling the shape and vibration of flexible structures in an optimal manner, it is essential to investigate other inherent features of the method. Such features can be easily revealed by considering the root locii of the **MPPF** characteristic equation (5), shown in Figure (4), for different values of the gain γ_i as α_i is varied from 0 to ∞. It is evident that increasing γ_i beyond 0.5 while maintaining it below the stability limit (i.e. $\gamma_i \leq 1$) results in significant changes in the shape of the root locii. More importantly, the branches of the root locii converge towards the real axis of the $\bar{s}$ plane indicating that higher closed-loop damping ratios can be achieved. Figure (5) shows the combined effect of γ_i and α_i on the attainable damping ratios as extracted from the plots of Figure (4). It is clear that for any value of the controller gain γ_i there is an optimal value of α_i for which the closed-loop damping ratio assumes its maximum. In section 2, it was shown that if γ_i is set equal to 0.5 to ensure zero steady-state error; a maximum damping ratio of 0.207 is attained when α_i is 1.18. Increasing γ_i to 0.9 requires that α_i be 1.768 to reach a maximum damping ratio of 1.00. Such a significant increase in the damping ratio occurs however at the expense of increasing the steady-state error, $(1-u_i/u_{Ri}) = 1-1/(1/\gamma_i-1)$, to 800%. Therefore, increasing the damping ratio above 0.207 cannot be achieved without compromising the steady-state error. This will only occur if the two parameters γ_i and α_i are maintained constant throughout the control process at values other than 0.5 and 1.18 respectively. However, it is possible to combine the high damping and zero steady-state error characteristics by adjusting the parameters γ_i and α_i in an adaptive manner. Specifically, one would start the control process with the highest damping possible (i.e. the largest value of γ_i) and as the process approaches its completion the gain γ_i is adjusted to be as close as possible to 0.5 in order for the structure to reach its final shape or state with zero steady state error. During the process of adjusting the gain γ_i the parameter α_i is also adjusted accordingly in order to achieve the maximum damping.

Accordingly, the **AMPPF** method capitalizes on the inherent interaction between the controller parameters to optimize the transient performance of the system. In this manner, although the structural parameters are time invariant, better transients can be achieved by adaptively making the controller parameters (γ_i and α_i) time varying. The desired time response can be obtained by selecting a desired reference behavior and change the controller to make the system follow the reference model.

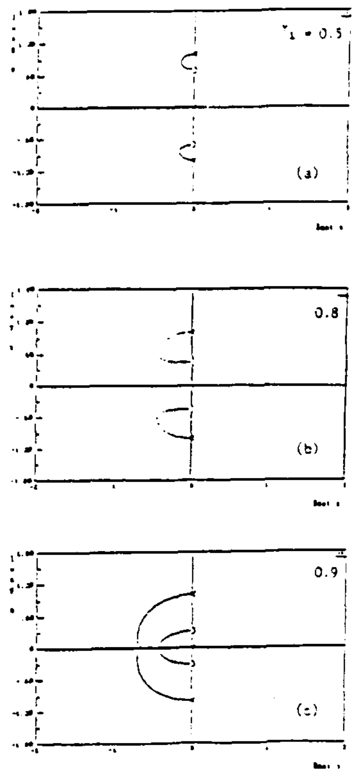

Figure (4) - Effect of γ_i on shape of root locus of the **MPPF** method.

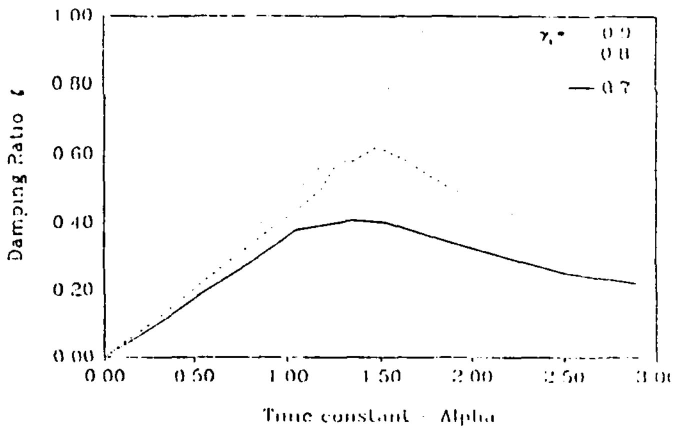

Figure (5) - Effect of α_i on closed-loop damping of **MPPF** method for different gains γ_i.

The interaction between the reference model and the structure-filter systems is shown in the block diagram of Figure (6). The laws governing the adaptation of the controller parameters γ_i and α_i (or τ_i) are derived in the following section.

3.2. Adaptation laws

Mathematically, the dynamics of the structure and its model reference are given by the following equations:

A. Structural system

Structure dynamics: $\ddot{u}_p + \omega_n^2\, u_p = \gamma_i \omega_n^2\, (Y_p + u_{Ri})$, (7)

Filter dynamics: $\tau_i\, \dot{Y}_p + Y_p = u_p$. (8)

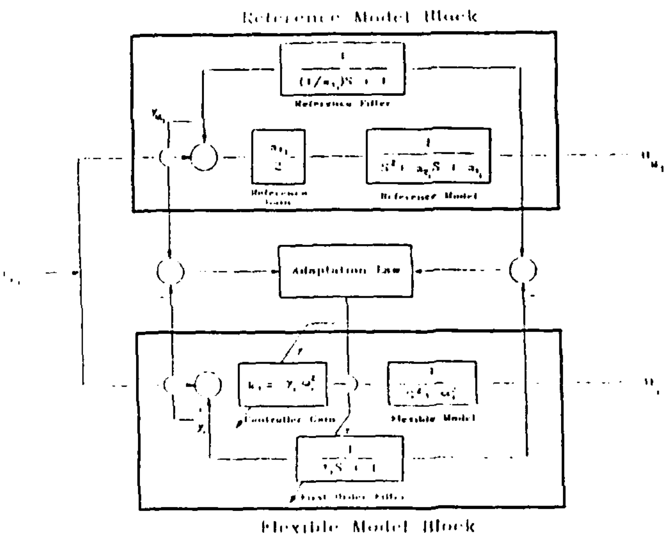

Figure (6) - Block diagram of the **AMPPF** method with parameter adaptation.

B. Reference system

Reference model: $\ddot{u}_m - a_2\dot{u}_m - a_1 u_m = -a_1/2\ (Y_m + u_{R1})$. (9)

Reference filter: $\dot{Y} + a_3 Y_m = a_3 u_m$. (10)

The reference model, described by equation (9), is structured to be damped in contrast to the undamped structural model and its gain is selected to ensure stability and zero steady-state error (i.e. = 1/2).

The interaction between the structure dynamics and the reference model dynamics is displayed in the block diagram of Figure (6). Defining the state vector X_p and X_m as $X_p = [u_p\ \ \dot{u}_p\ \ Y_p]^T$ and $X_m = [u_m\ \ \dot{u}_m\ \ Y_m]^T$, the structure and reference systems can be written as

Structure system $\dot{X}_p = A_p X_p + B_p u_{R1}$. (11)

Reference system $\dot{X}_m = A_m X_m + B_m u_{R1}$. (12)

where,

$$A_p = \begin{bmatrix} 0 & 1 & 0 \\ -\omega_1^2 & 0 & \gamma_1\omega_1^2 \\ 1/\gamma_1 & 0 & -1/\gamma_1 \end{bmatrix}, \qquad B_p = \begin{bmatrix} 0 \\ \gamma_1\omega_1^2 \\ 0 \end{bmatrix},$$

$$A_m = \begin{bmatrix} 0 & 1 & 0 \\ a_1 & a_2 & -.5a_1 \\ a_3 & 0 & -a_3 \end{bmatrix} \quad \text{and} \quad B_m = \begin{bmatrix} 0 \\ -.5a_1 \\ 0 \end{bmatrix} \qquad (13)$$

The matrices A_m and B_m of the reference model are given in terms of the three coefficients a_1, a_2 and a_3.

Defining the error vector e and its derivative $\dot{e}$ as

$$e = X_m - X_p \quad \text{and} \quad \dot{e} = \dot{X}_m - \dot{X}_p. \qquad (14)$$

and subtracting equation (11) from (12) yields

$$\dot{e} = A_m e + (A_m - A_p)X_p + (B_m - B_p)u_{R1} = A_m e + \bar{f}, \qquad (15)$$

where, $\bar{f} = (A_m - A_p)X_p + (B_m - B_p)u_{R1}$. (16)

Letting $A_m - A_p = \bar{\phi}$ and $B_m - B_p = \bar{\psi}$, then

$$\dot{e} = A_m e + [\bar{\phi}\ \ \bar{\psi}] \begin{bmatrix} X_p \\ u \end{bmatrix}. \qquad (17)$$

To calculate the adaptation law, the following Lyapunov function is defined:

$$V = e^T P e + h(\bar{\phi}, \bar{\psi}) > 0, \qquad (18)$$

where $$h(\bar{\phi}, \bar{\psi}) = \sum_{i=1}^{n} \bar{\phi}_i^T \bar{\phi}_i + \sum_{i=1}^{m} \bar{\psi}_i^T \bar{\psi}_i. \qquad (19)$$

For stable adaptation, $\dot{V}$ has to be strictly negative [9], i.e.

$$\dot{V} = \dot{e}^T P e + e^T P \dot{e} + \dot{h} < 0. \qquad (20)$$

Substituting $\dot{e}$ from equation (15) gives

$$\dot{V} = e^T [A_m^T P + P A_m] e + 2 e^T P \bar{f} + \dot{h} \qquad (21)$$

To have stable adaptation ($\dot{V} < 0$), the following two conditions must be satisfied:

(a) $2 e^T P f + \dot{h} = 0$ (22)

(b) select a stable reference model satisfying the following Lyapunov equation:

$$A_m^T P + P A_m = -Q, \qquad (23)$$

where Q is a positive definite matrix, then equation (21) reduces to

$$\dot{V} = -e^T Q e. \qquad (24)$$

Equation (22) gives the necessary adaptation laws for varying γ_1 and τ_1 such that the stability is ensured, i.e. Lyapunov stability theorom [9] is satisfied. This adaptation law can be determined by considering the characteristic equation of the reference system which can be written as

$$s^3 - (a_2 - a_3)s^2 + [-a_2 a_3 - a_1]s + [-0.5a_1 a_3] = 0. \qquad (25)$$

If it is desired that the system should behave like an optimal **ITAE** (Integral of Time multiplied by Absoulte Error) third order system, then it should have following characteristic equation [10]:

$$s^3 + 1.75\,\omega_o s^2 + 2.15\,\omega_o^2 s + \omega_o^3 = 0. \qquad (26)$$

Selecting $\omega_o = \omega_1$ of the system, and matching the coefficients of two characteristic equations (25) and (26), a_1, a_2 and a_3 can be found.

The parameter error matrices $\bar{\phi}$ and $\bar{\psi}$ can be formed as follows;

$$\bar{\phi} = A_m - A_p = \begin{bmatrix} 0 & 0 & 0 \\ a_1 + \omega_1^2 & a_2 & -(0.5a_2 + \gamma_1\omega_1^2) \\ (a_3 - 1/\tau_1) & 0 & -(a_3 - 1/\tau_1) \end{bmatrix}, \qquad (27)$$

$$\bar{\psi} = B_m - B_p = \begin{bmatrix} 0 \\ -(0.5a_1 + \gamma_1\omega_1^2) \\ 0 \end{bmatrix}. \qquad (28)$$

Forming h using equation (19) yields

$$h = \sum_{i=1}^{3} \bar{\phi}_i^T \bar{\phi} + \sum_{j=1}^{3} \bar{\psi}_j^T \bar{\psi}_j$$

$$=(a_1+\omega_1^2)^2+2(a_3-1/\tau_1)^2+a_2^2+(0.5a_1+\gamma_1\omega_1^2). \qquad (29)$$

Differentiating equation (29) with respect to time yields:

$$\dot{h}= 4\ (a_3 - 1/\tau_1)\ \dot{\tau}_1/\ \tau_1^2+ 4\ (0.5a_1 + \gamma_1\omega_1^2)\ \omega_1^2\dot{\gamma}. \qquad (30)$$

and defining the error vector **e**

$$e = X_m - X_p = \begin{bmatrix} X_{1m} \\ X_{2m} \\ Y_m \end{bmatrix} - \begin{bmatrix} X_{1p} \\ X_{2p} \\ Y_p \end{bmatrix} = \begin{bmatrix} e_1 \\ e_2 \\ e_3 \end{bmatrix}, \qquad (31)$$

then equation (22) becomes

$$(e_1p_3+e_2p_4+e_3p_5)\left[(a_1+\omega_1^2)X_{1p}+a_2X_{2p}-(.5a_1+\gamma\omega_1^2)(Y_p+u_{R1})\right]$$

$$+(e_1p_3+e_2p_5+e_3p_6)\left[(a_3-1/\tau_1)(X_{1p}-Y_p)\right]$$

$$+2(a_3-1/\tau_1)\dot{\tau}_1/\tau_1^2+2(.5a_1+\gamma_1\omega_1^2)\ \omega_1^2\ \dot{\gamma}_1 = 0. \qquad (32)$$

The above equation yields the following two adaptation laws :

$$\dot{\tau}_1=-0.5\tau_1^2(e_1p_3+e_2p_5+e_3p_6)(\ X_{1p} - Y_p\ ), \qquad (33)$$

and

$$\dot{\gamma} =-0.5(e_1p_2+e_2p_4+e_3p_5)\ \times$$

$$\left[\frac{(a_1+\omega_1^2)X_{1p}+a_2X_{2p}-(.5a_1+\gamma_1\omega_1^2)(Y_p+u_{R1})}{\omega_1^2(0.5a_1+\gamma_1\omega_1^2)}\right] \qquad (34)$$

which depend on the elements of the **P** matrix. The elements of the **P** matrix depend in turn on the **Q** matrix of the Lyapunov equation (23) and on the parameters a_1, a_2 and a_3 of the reference model as indicated in the appendix.

4. EXPERIMENTAL PERFORMANCE OF OPTIMAL MPPF ALGORITHM

4.1 EXPERIMENTAL SET-UP

A thin rectangular cantilevered beam is constructed to validate the developed algorithm . The design parameters of the beam are given in Table 1. The beam is controlled by one piezo-electric bimorph made from G1195- ceramic. The actuator is available commercially (model number R205) from Piezo-Electric Products, Inc., Metuchen, NJ 08840-4015 . Table 2 lists the main design parameters of the actuator.

The experimental beam and the piezo-actuator are arranged as shown in Figure (7). The beam is divided into three active elements. Bonded to the first element, near the fixed end of the beam, is the piezo-actuator. Three non-contacting position sensors are used to monitor the physical displacements of the three nodes in the transverse direction. The position signals are sampled by a 386-based micro-processor provided with an input/output board which has a conversion time of 15 μs and a resolution of 12 bits. The board analog outputs have a settling time of 30 μs.

The micro-processor uses the three sampled signals to compute the beam angular deflections and the linear and angular velocities of the nodes . The computed state variables are used to calculate the modal coordinates of the flexible system, the mode that has the highest modal energy, the corresponding optimal modal control force f_1, the physical control force F_c and the necessary voltage v to be sent to the piezo-actuator. The implementation of these calculations , i.e. the **AMPPF** algorithm , is carried out in real time in 3.04 ms.

Figure (8) outlines a flow chart of the **AMPPF** algorithm indicating its main steps.

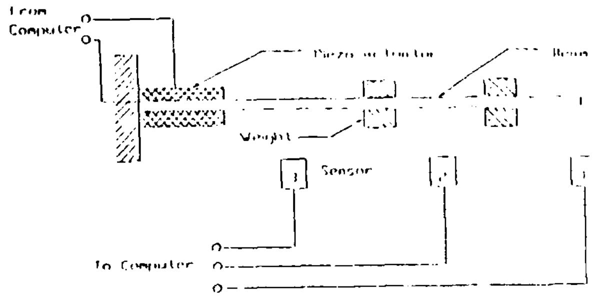

Figure (7) - Schematic drawing of the experimental beam, piezo-actuator and sensors.

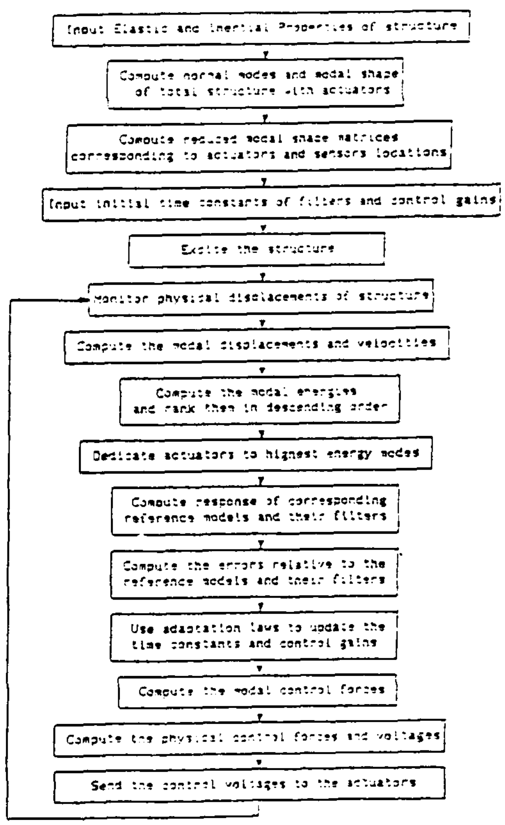

Figure (8) - Flow chart of the **AMPPF** method.

4.2 Modal characteristics of the beam-actuator system

The modal characteristics of the experimental beam are determined theoretically [5] and validated experimentally using classical modal analysis technique. A comparison between the theoretical and the experimental values of the first five vibration modes of the beam-actuator system is given in Table 3. The table gives also the modal damping as calculated from the experimental results using the half power approach [11].

4.3 Experimental results

In all the experiments conducted in this study, the beam is excited at its second mode of vibration by applying sinusoidal excitation of 20 volts in magnitude to the piezo-actuator. The excitations are maintained for a period of 0.15 seconds. The beam is either left to vibrate freely (i.e. Uncontrolled) or under the action of one modal control algorithm or another. The above excitation form is selected in order to excite the second mode of vibrations. Excitation of modes higher than the second would require faster micro-processor in order to sample at least 10 sample per period to achieve meaningful control. The uncontrolled performance is used as datum for judging the effectiveness of the different control algorithms.

4.3.1 Vibration control

The time response of the uncontrolled beam is shown in Figure (9-a) indicating a very low natural damping characteristics. Figure (9-b) shows the beam time response when it is controlled by the **AMPPF** algorithm. The values of the controller parameters γ_1, τ_1, γ_2 and τ_2, for the first and second modes of vibrations, are initially set at 0.99, 0.836, 0.99 and 0.0138 respectively. These initial values of the γ_i's and the α_i's are selected to ensure maximum initial damping. During the adaptation process, the resulting time variations of the gains $\gamma_{1,2}$ and the filter time constants $\tau_{1,2}$ are shown in Figures (10-a) and (10-b) respectively. The figures indicate that all the adaptive gains and time constants converge to stable values to ensure zero steady-state errors. Also, the corresponding time histories of the modal displacements of the beam are shown in Figures (11-a) and (11-b) for the first and second modes respectively. The figures demonstrate the effectiveness of the **AMPPF** algorithm in following the dynamics of the desired reference modal model.

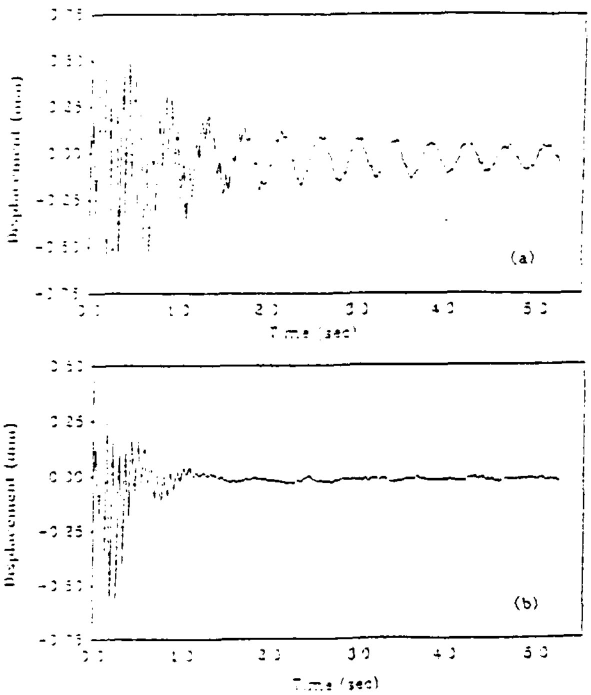

Figure (9) - Time response of beam
a. uncontrolled and
b. controlled with **AMPPF**

A better insight into the effectiveness of the **AMPPF** algorithm can be gained by considering the Fast Fourier Transform (**FFT**) of the beam response. Figure (12) shows the frequency content of the response of the uncontrolled beam in comparison with the controlled beam. These characteristics are obtained by sampling the beam tip position signal by a spectrum analyzer and performing on it an **FFT** analysis. The figure effectiveness of the **AMPPF** method in simultaneously suppressing the vibration of the first two modes of vibration using a single piezo-electric actuator.

Comparisons between the theoretical and experimental time responses of the uncontrolled and controlled beam are shown in Figures (13-a) and (13-b) respectively. The displayed results show close agreements between theory and experiments.

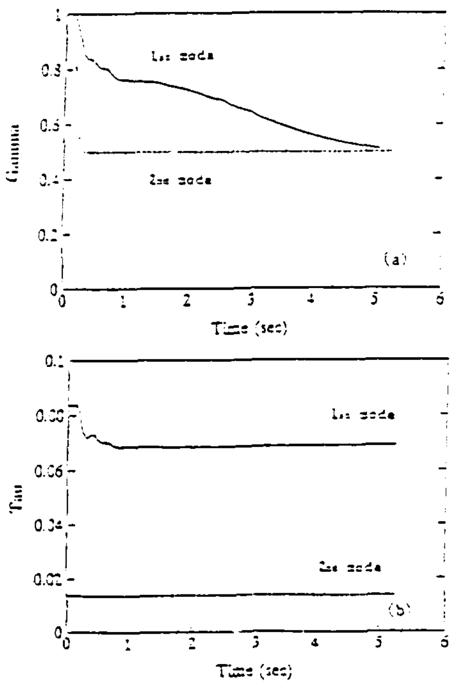

Figure (10) - Time history of the control parameters
a. gain $\gamma_{1,2}$ and b. time constant $\tau_{1,2}$

4.3.2 Vibration control of a variable mass system

A better insight of the effectiveness of the adaptive control algorithm can be gained by adaptively controlling a variable mass system. The mass variation of the flexible system is achieved by adding a mass to the free end of the beam. This additional mass changes the first mode of vibration by 20 %.

Figure (14) shows the time response of the controlled beam when an additional mass weighing 5.5 gm attached to the free end of the beam. Figures (15-a) and (15-b) show the corresponding time histories of the adaptive gains $\gamma_{1,2}$ and time constant $\tau_{1,2}$ of the variable mass system.

It is evident that the **AMPPF** algorithm has successfuly adapted to the mass changes and has effectively controlled the beam vibrations.

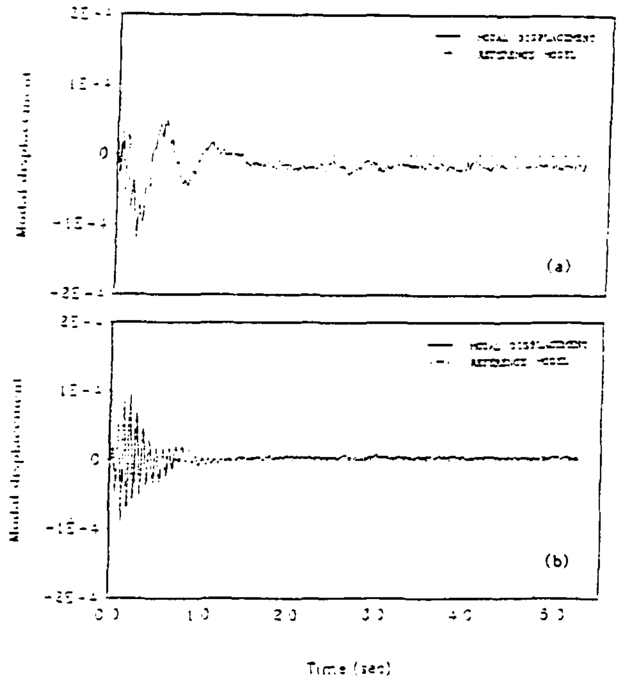

Figure (11) - Time history of the modal displacements of beam and reference model
a. for first mode and b. for second mode

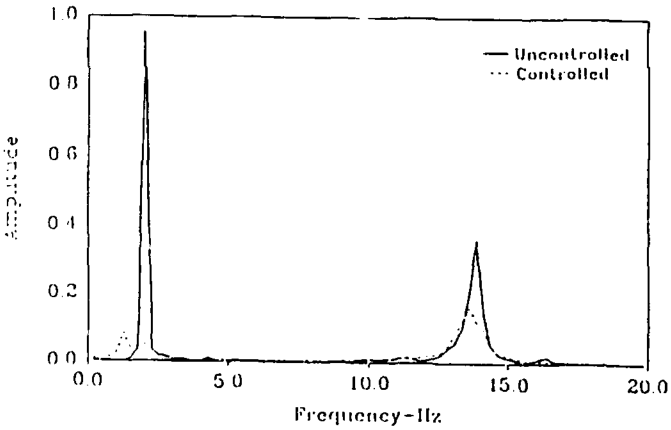

Figure (12) - Frequency response of the free end of the controlled and uncontrolled beam

4.3.3 Shape control

The use of the **AMPPF** algorithm in controlling the shape of the beam system is demonstrated in Figure (16) when the beam is deflected 0.1 mm off its initial zero-load position. The resulting time response of the beam and the corresponding control voltage are shown in Figures (16-a) and (16-b) respectively. The two figures clearly demonstrate that the applied control voltage reaches a steady-state value after the required shapes are attained. The model following capability of the **AMPPF** algorithm is indicated in Figure (16-c) where the modal displacement at the first mode of vibration is shown to track the desired reference model output

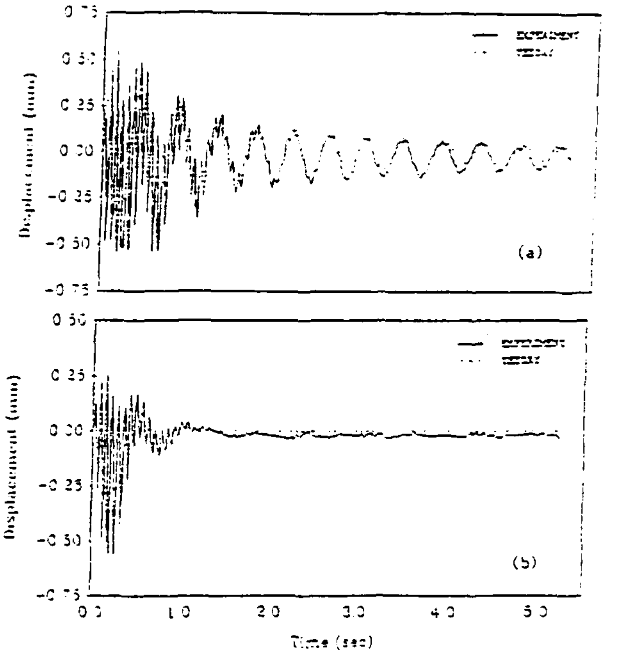

Figure (13) - Comparison between theoretical and experimental time response of the beam
a. uncontrolled and b. controlled

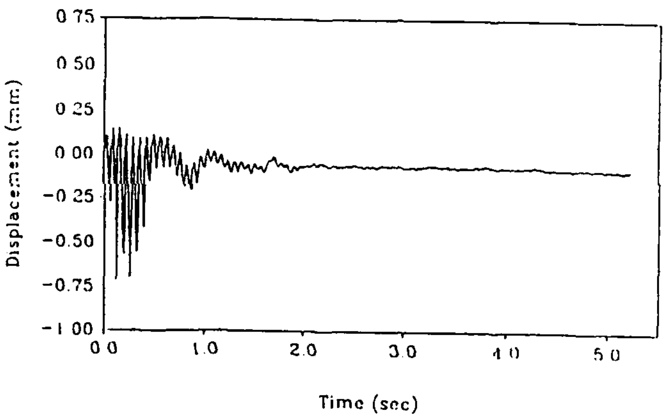

Figure (14) - Time response of the variable mass beam.

4.3.4 System comparison

Figure (17) shows the time response of the beam when the beam is controlled by the non-adaptive **MPPF** method. A comparison with the beam response with the **AMPPF**, shown in Figure (9-b), indicates that the adaptation results in improving the system performance considerably. Quantitative comparison between the two methods can be obtained by considering the displacement index U_d defined as the summation of the squared position error of the beam tip over time:

$$U_d = \sum_{t=0}^{t^*} y_{tip}^2(t) \quad , \tag{35}$$

and the control votage index U_r given by

$$U_r = \sum_{t=0}^{t^*} v^2(t) \quad , \tag{36}$$

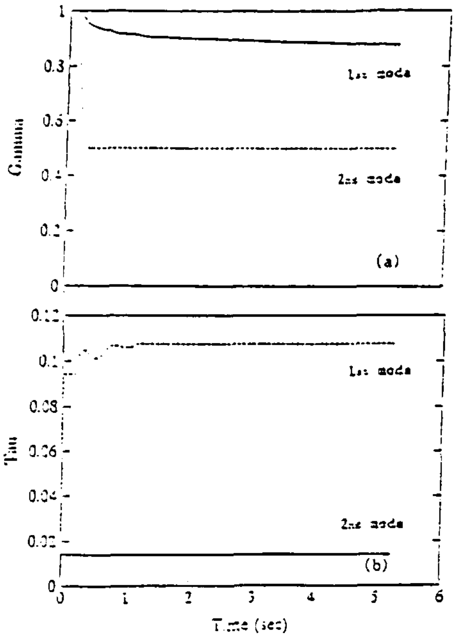

Figure (15) - Time history of the control parameters for the variable mass beam
a. gain $\gamma_{1,2}$ and b. time constant $\tau_{1,2}$

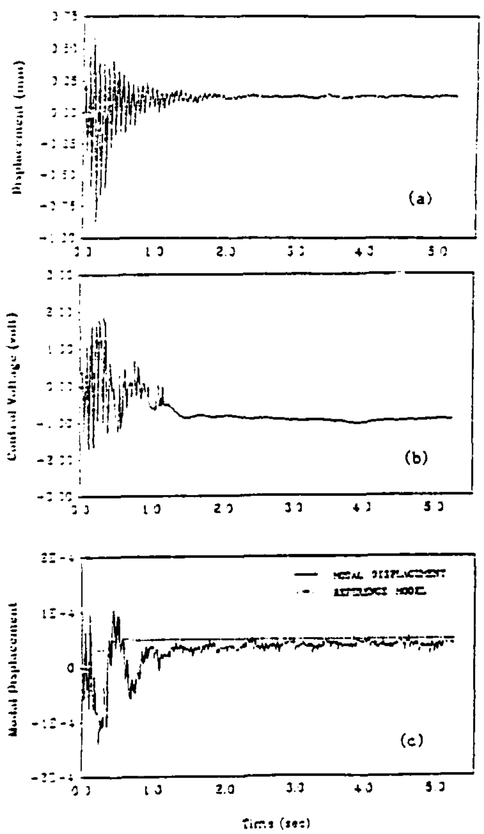

Figure (16) - Time response of the beam during shape control process
a. tip displacement, b. control voltage and c. modal displacement

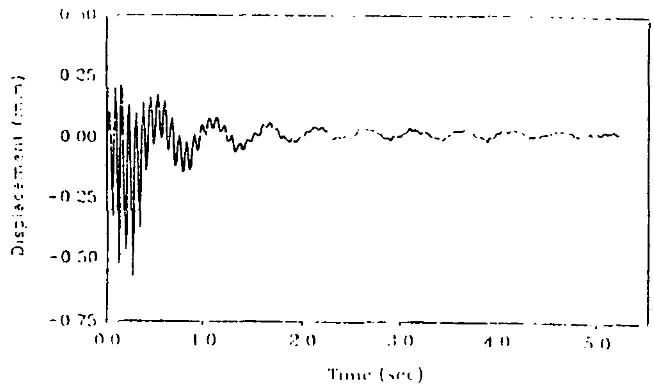

Figure (17) - Time response of the beam when controlled with MPPF method

where t^{*} is the time of each experimental run. Table 4 lists the displacement and control voltage indices for the different algorithms.

The experimental results obtained indicate the effectiveness of the AMPPF algorithm in suppressing structural vibrations and controlling the shape of flexible structures in the presence of modeling errors and structural system changes. Comparisons, carried out between the new algorithm and the non-adaptive MPPF method, emphasizes its favorable vibration damping and shape control characteristics.

5. CONCLUSIONS

This study has presented an adaptive modal control algorithm which is based on the Positive Position Feedback method. The algorithm utilizes only modal position signals, fed through first order filters, to damp out the vibration of undamped flexible systems. The theory behind the algorithm is presented. The adaptation laws necessary for tuning the filters and the controller gains are obtained, for all the controlled modes, using Lyapunov's stability theory. The algorithm is validated experimentally using a single piezo-electric actuator to control the vibration and shape of a flexible cantilevered beam. The results obtained indicate the effectiveness of the adaptation in improving the performance of the controller particularly when it is used to control beams with varying structural parameters.

The study demonstrates clearly the simplicity and potential of the method as an effective method for controlling large number of vibration modes with a smaller number of actuators . These features have important practical implications that make the algorithm viable for controlling large structures in real time.

ACKNOWLEDGEMENTS

This study was supported by a grant from the US Army Research Office (Grant number DAAL03-89-G-0084). Special thanks are due to Dr. Gary Anderson, the technical monitor and Chief of the Structures and Dynamics Branch of ARO, for his invaluable and continuous technical inputs.

REFERENCES

1. Bar-Kana I. and Kaufman H.,"Some Applications of Direct Adaptive Control to Large Structural Systems", *AIAA J. of Guidance, Control & Dynamics*, Vol 7, No.6, pp.717-724, 1984.
2. Ih, C.-H., Bayard, D., Ahmed, A. and Wang, S., "Experiments in Multi-Variable Adaptive Control of A Flexible Structure", *NASA Tech. Brief*, Vol.15, No.2, Item # 36, 1991.
3. Ossman, K., Yurkovich and Özgüner, Ü, "Adaptive Control Techniques for The SCOLE Configuration", *Proc. of 6th VPI&SU/AIAA Symposium on Dynamics and Control of Large Structures*, pp.343-363, 1987.
4. Silverberg, A. and Norris, M., " Self-Tuning Algorithms for Uniform Damping Control of Spacecraft", *AIAA Paper Number* AIAA-90-1174-CP, 1990.
5. Baz, A., S.Poh and J.Fedor, "Independent modal space control with positive position feedback", *ASME Journal of Dynamic systems, Measurements and Control*, **114**, 1, 96-103 (1992).
6. Poh, A. and A.Baz, "Active control of a flexible structure using a modal positive position feedback controller", *Journal of Intelligent Material Systems and Structures*, 1, 3, 273-288 (1990).
7. Goh C.J. and Caughey T.K. "On the Stability Problem Caused By Finite Actuator Dynamics in The Collocated Control of Large Space Structures", *Intl.J. Control*, Vol.41, pp.787-802, 1985.
8. Fanson J.L. and Caughey T.K. "Positive Position Feedback Control For Large Space Structures", AIAA paper Number 87-0902, 1987.
9. Chalam V.V. *Adaptive Control Systems Techniques and Applications*. Marcel Dekker Inc, New york, 1988.
10. Shinners S. *Modern Control System Theory and Application* Addison-Wesley Co. Reading, Massachusetts, 1972.
11. Ewins, D.J., *Modal Testing : Theory and Practice*, Research Studies Press Ltd., Letchwoth, England, 1984.

Table 1 - Main design parameters of test beam

Length (cm)	Width (cm)	Thickness (cm)	Young's modulus (GN/m²)	density (gm/cm³)
25.19	3.75	0.075	2.96	1.31

Table 2 - Main design parameters of the actuator

Length (cm)	width (cm)	thick (cm)	charge coeff. (m/v)	max. volt (v/mil)	Young's mod. (GN/m²)	density (gm/cm³)
4.85	1.375	0.1	190×10^{-12}	25	63	7.8

Table 3 - Modal characteristics of the beam system

Mode number	1	2
Theor. mode - Hz	2.25	13.57
Exper. mode - Hz	2.20	13.75
Error - %	2.22	1.10
Modal damping	.031	.018

Table 4 - Displacement and control voltage indices

Algorithms	Displacement Index(mm²)	Voltage Index (volt²)
AMPPF	0.36	27.83
MPPF	0.73	36.97

APPENDIX - A

ELEMENTS OF A_m and P MATRICES

A.1. Elements of A_m matrix

The parameters a_1, a_2 and a_3 which define the elements of the A_m matrix are obtained by matching the coefficients of the characteristic equation (25) of the reference system with the coefficients of the optimal ITAE characteristic equation (26). This gives a_1 as the negative real solution of the following equation

$$a_1^3 + 2.15\,\omega_o^2\,a_1^2 + 3.5\,\omega_o^4\,a_1 + 4\,\omega_o^6 = 0 \qquad \text{(A-1)}$$

where ω_o is the natural frequency of the optimal reference system.

The parameters a_2 and a_3 can then be determined from:

$$a_2 = -1.75\,\omega_o + a_3 \qquad \text{(A-2)}$$

and

$$a_3 = -2\,\omega_o^3 / a_1 \qquad \text{(A-3)}$$

A.2. Elements of P matrix

The matrix P is given by

$$P = \begin{bmatrix} p_1 & p_2 & p_3 \\ p_2 & p_4 & p_5 \\ p_3 & p_5 & p_6 \end{bmatrix} \qquad \text{(A-4)}$$

where the elements p_1 through p_6, are obtained by solving the Lyapunov equation (23) which becomes:

$$\begin{bmatrix} 0 & 2a_1 & 2a_3 & 0 & 0 & 0 \\ 1 & a_2 & 0 & a_1 & a_3 & 0 \\ 0 & -a_1/2 & -a_3 & 0 & a_1 & a_3 \\ 0 & 2 & 0 & 2a_2 & 0 & 0 \\ 0 & 0 & 1 & -a_1/2 & a_2-a_3 & 0 \\ 0 & 0 & 0 & 0 & -2a_1 & -2a_3 \end{bmatrix} \begin{bmatrix} p_1 \\ p_2 \\ p_3 \\ p_4 \\ p_5 \\ p_6 \end{bmatrix} = - \begin{bmatrix} Q_{11} \\ Q_{12} \\ Q_{13} \\ Q_{22} \\ Q_{23} \\ Q_{33} \end{bmatrix} \qquad \text{(A-5)}$$

where Q_{ij}'s are the elements of the positive definite matrix Q which are assumed by the control system designer. Equation (A-1), (A-2), (A-3) and (A-5) can then be used to compute the elements p_i's of the P matrix.

NOMENCLATURE

$a_{1,2,3}$	parameters of reference model
$A_{m,p}$	reference and structure-filter system matrices
$B_{m,p}$	reference and structure-filter system input matrices
e, $\dot{e}$	error vector and its derivative
e_i	ith error component (i=1-3)
f_i	modal control force of the ith mode
$\underline{f}$	vector defined by equation (16)
F_c	physical force vector
h, $\dot{h}$	positive definite function defined by equation (19) and its derivative.
K_i	controller gain
P	matrix satisfying Lyapunov equation
p_i	ith element of matrix P
Q	positive definite matrix defined in Lyapunov equation (23)

$s,\ \bar{s}$	Laplace and normalized Laplace operators
t	time
t^*	duration of experimental run
$U_{d,c}$	displacement and control effort indices
$u_i, \dot{u}_i, \ddot{u}_i$	modal displacement, velocity and acceleration of ith mode
$u_m, \dot{u}_m, \ddot{u}_m$	modal displacement, velocity and acceleration of ith mode of reference model.
$u_p, \dot{u}_p, \ddot{u}_p$	modal displacement, velocity and acceleration of ith mode of structure.
u_{Ri}	reference modal displacement of ith mode
v	voltage applied across actuator
$V,\ \dot{V}$	Lyapunov function and its derivative
$X_{1,2}$	position and velocity state variables.
$X_{m,p}$	state vectors of reference and structure-filter systems
$Y_i,\ \dot{Y}_i$	output of ith mode filter and its derivative
y_{tip}	transverse displacement of beam tip.

Greek Symbols

α_i	dimensionless time constant of filters
γ_i	dimensionless gain of the controller
τ_i	time constant of the ith mode
$\underline{\phi}$	parameter error of A matrix
ψ	parameter error of B matrix
ω_o	frequency of reference model
ω_i	frequency of the ith mode

— To appear in J. of Optimal Control —

OPTIMAL VIBRATION CONTROL
WITH
MODAL POSITIVE POSITION FEEDBACK

A. Baz and S. Poh

Mechanical Engineering Department
The Catholic University of America
Washington, DC 20064

S U M M A R Y

The vibrations of flexible structures are controlled by an Optimal Modal Positive Position Feedback (**OMPPF**) algorithm whose control forces are generated by only using modal position signals to provide damping action to undamped structural modes. The sub-optimal parameters of the **OMPPF** controller are obtained by casting the synthesis problem as an optimal control problem with incomplete state feedback. The performance of the **OMPPF** algorithm is enhanced by augmenting it with a **"time sharing"** strategy to share a small number of actuators between larger number of vibration modes. The effectiveness of the algorithm in damping out the vibration of flexible structures is validated experimentally using a cantilevered beam whose multi-modes of vibration are controlled by a single piezo-electric actuator. Theoretical performance predictions are found to be in close agreement with experimental results.

KEY WORDS: *Active vibration control*
Modal Positive Position Feedback
Incomplete state feedback
time sharing of actuators

1. INTRODUCTION

Considerable emphasis has been placed, during the past few years, on actively controlling the vibration of a wide variety of flexible structures. Several control algorithms have been considered ranging from the simple velocity feedback control law [1,2] to the more imaginative methods such as the Independent Modal Space Control (IMSC) of Meirovitch [3,4] and the Positive Position Feedback (PPF) of Goh and Caughey[5]. 1988, Baz and co-workers [6,7] modified the **IMSC** to account for the control spillover and devised a **time sharing** strategy to share small number of actuators between larger number of modes. The Modified **IMSC** method (**MIMSC**) has been shown to have favorable vibration damping characteristics as compared to the **IMSC** and the Pseudo-Inverse (PI) methods[8]. However the **IMSC**, **PI**, **MIMSC** and other modal control methods, rely in their operation on feeding back both the modal position and velocity signals of the controlled modes to achieve the required vibration damping . Extraction of these signals from physical measurements is both time consuming and computationally intensive especially when dealing with large structures. In 1989, Baz et.al.[9,10] developed the Modal Positive Position Feedback (**MPPF**) method to combine the attractive attributes of the **IMSC**, **MIMSC** and the **PPF** methods. In the **MPPF** method, the controller is designed completely in the independent modal space with the open-loop equations of the system remaining uncoupled even after including the modal controller. Also, the **MPPF** uses only the modal position signals to obtain stable and damped performance. Such performance is attained by positively feeding back the position signals through tuned first order filters. Closed-form expressions are given for determining the controller gains and the time constants of the filters in order to ensure stability, zero steady-state errors and maximum closed-loop damping ratio. The attractive features of the **MPPF** method have been successfully demonstrated by controlling the vibration of simple beams[9] and more complex structures[10]. However, no attempt has been made to develop optimal control strategies to enable the selection of the controller parameters in such a way that weighs the relative merits of the vibrational energy vis-a-vis the control effort.

It is therefore the goal of this study to develop such strategies and experimentally evaluate the effectiveness of the Optimal Modal Positive Position Feedback (**OMPPF**) algorithm in controlling the vibration of a cantilevered beam.

This paper is organized in five sections. A brief introduction is given in section **1**. The concept of the **OMPPF** algorithm and the selection of its optimal parameters are presented in sections **2** and **3** respectively. Section **4** includes the experimental evaluation of the algorithm along with comparisons with other algorithms. Section **5** summarizes the conclusions of this study.

2. THE CONCEPT OF THE "MPPF" ALGORITHM

The proposed method can be clearly understood by considering the block diagram shown in Figure (1). In the figure, the controller is used to control, in the independent modal space, the ith mode of an undamped flexible structure.

The controller feeds back positively the modal displacement $\mathbf{q}_i$ through a first order filter that has a time constant τ_i. The filter output $\mathbf{Y}_i$ is amplified by a proportional controller gain $\mathbf{K}_i$ which is set equal to $\gamma_i\ \omega_i^2$, where ω_i is the natural frequency of the ith mode. The amplified signal $\mathbf{f}_i$, i.e. the modal control action, is then sent to control the ith mode of the

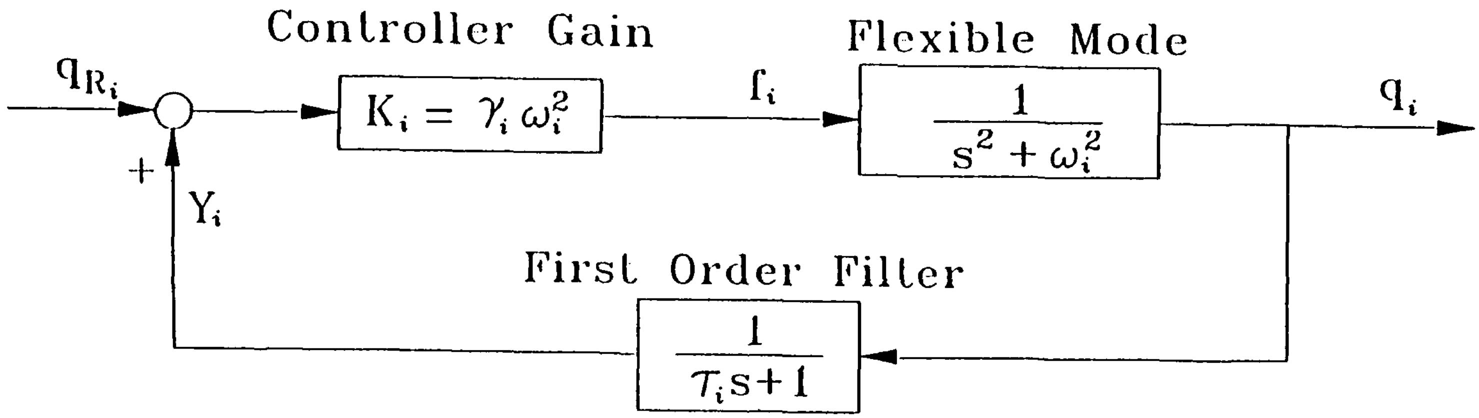

Figure (1) - Block diagram of the MPPF controller.

structure.

Mathematically, the interaction between the structural mode and the controller can be described as follows :

$$\textbf{The structure} \qquad \ddot{q}_i + \omega_i^2 q_i = f_i = \gamma_i \omega_i^2 Y_i \tag{1}$$

$$\textbf{The filter} \qquad \tau_i \dot{Y}_i + Y_i = q_i \tag{2}$$

where the dots denote differentiation with respect to time **t**.

Defining a normalized time $t^* = \omega_i t$, then equations (1) and (2) reduce to:

$$\textbf{The structure} \qquad q_i'' + q_i = \gamma_i Y_i \tag{3}$$

$$\textbf{The filter} \qquad Y_i' + \alpha_i Y_i = \alpha_i q_i \tag{4}$$

where the primes denote differentiation with respect to the normalized time $\mathbf{t}^*$ and α_i defines a dimensionless time constant of the filter which is given by

$$\alpha_i = 1 / (\tau_i \omega_i) \tag{5}$$

Equations (3) and (4) can be combined in the following equation:

$$q_i''' + q_i' = \mathbf{u} = - \alpha_i (1 - \gamma_i) q_i - \alpha_i q_i'' \tag{6}$$

The selection of the optimal gain γ_i and dimensionless time constant α_i of the filter can be achieved by considering the following state-space representation of equation (6):

$$\mathbf{X}' = \mathbf{A X + B u} \tag{7}$$

and $$y = C\,X \tag{8}$$

such that $$u = D\,X \tag{9}$$

where

$$X = \begin{bmatrix} q_i \\ q_i' \\ q_i'' \end{bmatrix}, \quad A = \begin{bmatrix} 0 & 1 & 0 \\ 0 & 0 & 1 \\ 0 & -1 & 0 \end{bmatrix}, \quad B = \begin{bmatrix} 0 \\ 0 \\ 1 \end{bmatrix},$$

$$C = [1 \quad 0 \quad 0] \quad \text{and} \quad D = [d_1 \quad 0 \quad d_2] \tag{10}$$

with $$d_1 = -\,\alpha_i\,(1 - \gamma_i) \quad \text{and} \quad d_2 = -\,\alpha_i \tag{11}$$

Considering the output matrix **C**, it is evident that the above state representation conforms with the premise that only the modal displacement $\mathbf{q}_i$ is accessible for measurements. Also, the right hand side of equation (6) and equation (9) define a fictitious control action **u** which is based on an **incomplete** state feedback as the second element of the gain matrix **D** is zero as indicated by equation (10). Once the gains $\mathbf{d}_1$ and $\mathbf{d}_2$ of the fictitious controller are optimally determined, as will described in section 3, the gain γ_i and the dimensionless time constant α_i of the original modal controller can be realized and the algorithm can be implemented according to equations (1) and (2).

3. SELECTION OF THE OPTIMAL CONTROL PARAMETERS

3.1. Formulation of the optimal control problem

The optimal gains $\mathbf{d}_1$ and $\mathbf{d}_2$ are determined by considering first the following optimal control problem:

$$
\left\langle
\begin{array}{llcl}
 & \multicolumn{3}{c}{\text{Find the control action } \mathbf{u}} \\
 & \multicolumn{3}{c}{\text{to minimize the quadratic performance index}} \\
 & \multicolumn{3}{c}{J = \int_{0}^{T} [\, y^T Q\, y + u^T R\, u \,]\, dt^{*}} \\
\text{such that} & \dot{\mathbf{X}} & = & (\mathbf{A} - \mathbf{B}\,\mathbf{D})\,\mathbf{X}, \\
 & \mathbf{y} & = & \mathbf{C}\,\mathbf{X}, \\
 & \mathbf{u} & = & -\,\mathbf{D}\,\mathbf{X}, \\
\text{and} & X(0) & = & \mathbf{X}_o
\end{array}
\right\rangle
\qquad (12)
$$

In the above problem, it can be easily shown[11,12] that the performance index **J** can be expressed as a quadratic form of the initial state $\mathbf{X}_o$ as follows

$$\mathbf{J} = \mathbf{X}_o^T\, \mathbf{P}(0)\, \mathbf{X}_o \qquad (13)$$

where **P** is symmetric and positive-definite matrix which is a solution of the following Lyapunov matrix equation:

$$\dot{\mathbf{P}} = (\mathbf{A} + \mathbf{B}\,\mathbf{D})^T\, \mathbf{P} + \mathbf{P}\,(\mathbf{A} + \mathbf{B}\,\mathbf{D}) + \mathbf{C}^T\, Q\, \mathbf{C} + \mathbf{D}^T\, \mathbf{R}\, \mathbf{D} \qquad (14)$$

such that P(T) = 0. For time invarying and stable systems, **P** approaches a constant value determined by setting $\dot{\mathbf{P}} = 0$. Equation (14) is obtained by differentiating the performance index with respect to time and using equations (7) through (9).

It is important to note that the above optimal control problem, given by equation (12), can not be directly solved using the solution $(\mathbf{D} = -\,\mathbf{R}^{-1}\, \mathbf{B}^T\, \mathbf{P})$ of the classical linear quadratic regulator problem[11] as the control action **u** is based on an incomplete state feedback. For this class of problems, the solution is found to depend on the initial state of the system[12-14]. This results in time varying feedback which is not efficient to implement particularly for large systems. Furthermore, it is not at all certain that a system optimized for one initial disturbance will perform satisfactorily for another disturbance. In order to ensure the acceptability of the system performance for all initial conditions, the performance of the worst case is optimized. This is achieved by considering the following performance index **M** instead of the original performance index **J**:

$$\mathbf{M} = \max_{\mathbf{x}_0} \; J \,/\, (X_o^T X_o) \tag{15}$$

This performance index normalizes the original performance index **J** with respect to the initial state of the system X_o. Substituting equation (13) into equation (15) gives:

$$\mathbf{M} = \max_{\mathbf{x}_0} \; (X_o^T P(0) X_o) \,/\, (X_o^T X_o) \tag{16}$$

It can be shown, as outlined in appendix **A**, that **M** is equal to the maximum eigen value of the **P** matrix

$$\mathbf{M} = \lambda_{max}(\mathbf{P}) \tag{17}$$

Therefore, the normalized performance index **M** becomes independent of the initial states of the system and the optimal control problem, given by equation (12), can be rewritten as

$$\left\langle \begin{array}{c} \text{Find the controller gains } \mathbf{d_1} \text{ and } \mathbf{d_2} \\ \text{to minimize the performance index } \mathbf{M} \\ \mathbf{M} = \lambda_{max}(\mathbf{P}) \\ \text{such that:} \\ (\mathbf{A} + \mathbf{B}\,\mathbf{D})^T \mathbf{P} + \mathbf{P}\,(\mathbf{A} + \mathbf{B}\,\mathbf{D}) + \mathbf{C}^T \mathbf{Q}\,\mathbf{C} + \mathbf{D}^T \mathbf{R}\,\mathbf{D} = 0 \end{array} \right\rangle \tag{18}$$

where **A**, **B**, **C** and **D** are as given in equation (10).

In other words, the above optimal control problem reduces to finding the sub-optimal fictitious controller gains $\mathbf{d}_1$ and $\mathbf{d}_2$ which minimize the maximum eigen value of the matrix **P** that satisfies the steady-state Lyapunov equation. The solution of such min-max problem yields $\mathbf{d}_1$ and $\mathbf{d}_2$ which can be used along with equation (11) to compute the optimal gain γ_i and filter time constant α_i of the **MPPF** algorithm.

3.2. Solution of the optimal control problem

The solution of the optimal control problem, given by equation (18), is carried out according to the flow chart shown in Figure (2). For a given weighting parameter **R** and an initial guess of the control gains $\mathbf{d}_1$ and $\mathbf{d}_2$, the elements of the matrix **P** are computed as outlined in appendix **B**. The positive definiteness of the matrix **P** is checked and its eigen values λ_i are computed using the Jacobi method[15]. The eigen values computed are ordered to determine the maximum value λ_{max_j}. This value is minimized by an optimization routine based on Powell's conjugate direction method[16]. The subroutine modifies the initial guess by finding an improved combination of $\mathbf{d}_1$ and $\mathbf{d}_2$. The improved gains are used again to compute the elements of **P** and find the corresponding $\lambda_{max_{j+1}}$. If the resulting $\lambda_{max_{j+1}}$ is smaller than the initial value λ_{max_j}, the process is repeated again. When no further improvement can be attained, the optimum is reached.

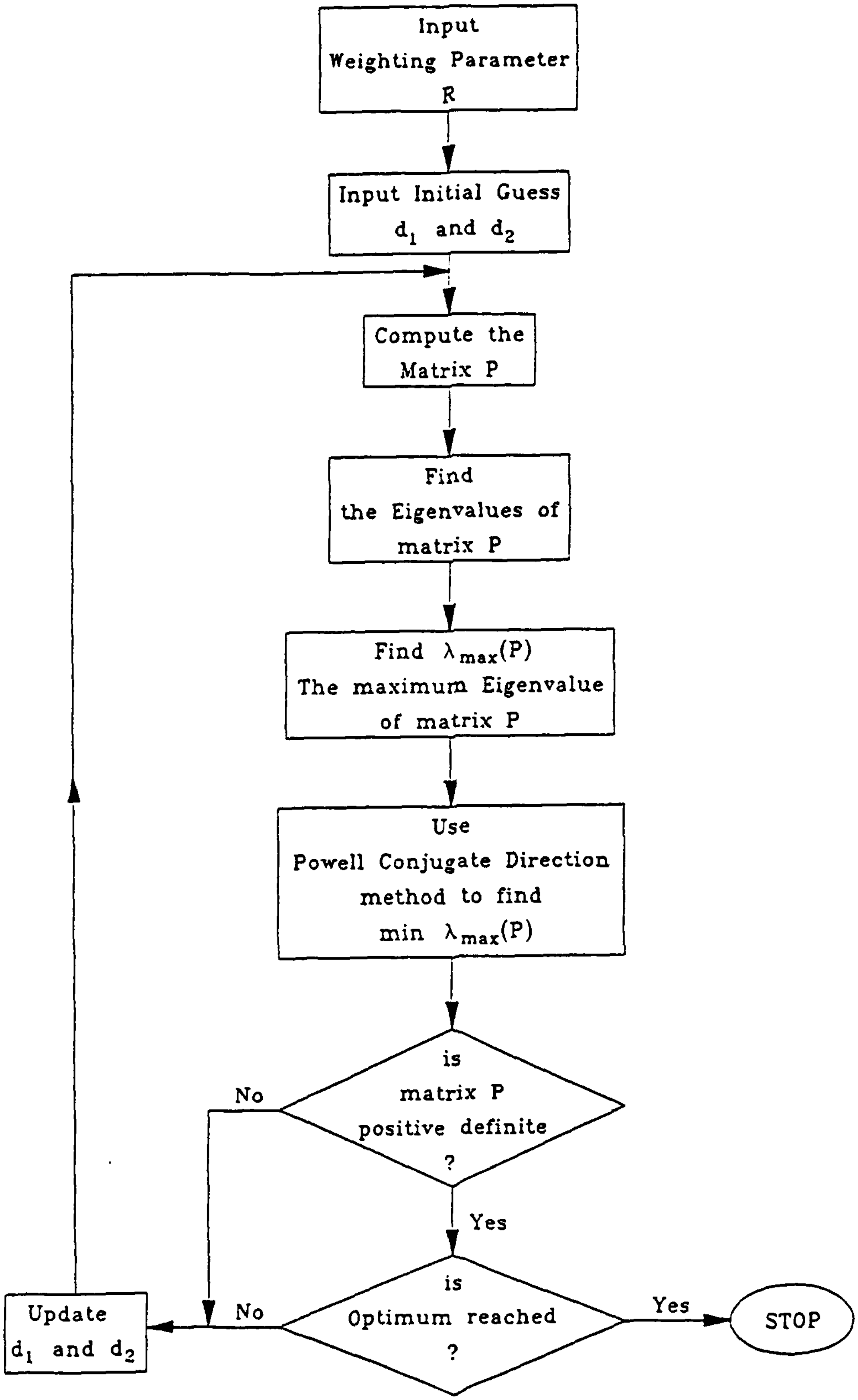

Figure (2) - Flow chart of the computation of the optimal parameters.

3.3. Optimal parameters

Figure (3) shows the contours of constant maximum eigen values (λ_{max}) of the matrix **P** drawn, as a function of $\mathbf{d}_1$ and $\mathbf{d}_2$, in the γ_i and α_i plane when the weighting parameter **R** = 0.01. The figure shows also the path followed from an initial guess (γ_i=0.9 and α_i=2.5) until the optimum is attained. Table 1 summarizes the optimal values of γ_i and α_i for different values of the weighting parameter **R**.

Table 1 indicates that the optimal value of the control gain γ_i remains nearly at 0.5 irrespective of the value of the weighting parameter **R**. This optimal value ensures both stability and zero steady-state error of the controller as can be seen from equations (1) and (2). However, the optimal values of the dimensionless filter time constant α_i are found to decrease as the weighting parameter **R** is increased. For a given mode of vibration ω_i, this means that the filter time constant τ_i increases with increasing **R** as indicated by equation (5). Therefore, if attenuation of the vibration is weighted to be more important than the control energy, i.e. **R** is small, then the filter should be very fast and τ_i should be small. Conversely, when the control energy is considered to be more important then the damping of the vibration, i.e. **R** is large, then the filter is tuned to be slow and its time constant τ_i is accordingly large.

It is very important to note that the presented analysis being applicable to any mode, results in the same **optimal tuning conditions** for all the modes of vibration. Accordingly, optimal vibration control can be achieved for any mode **i**, that has natural frequency ω_i, by selecting the

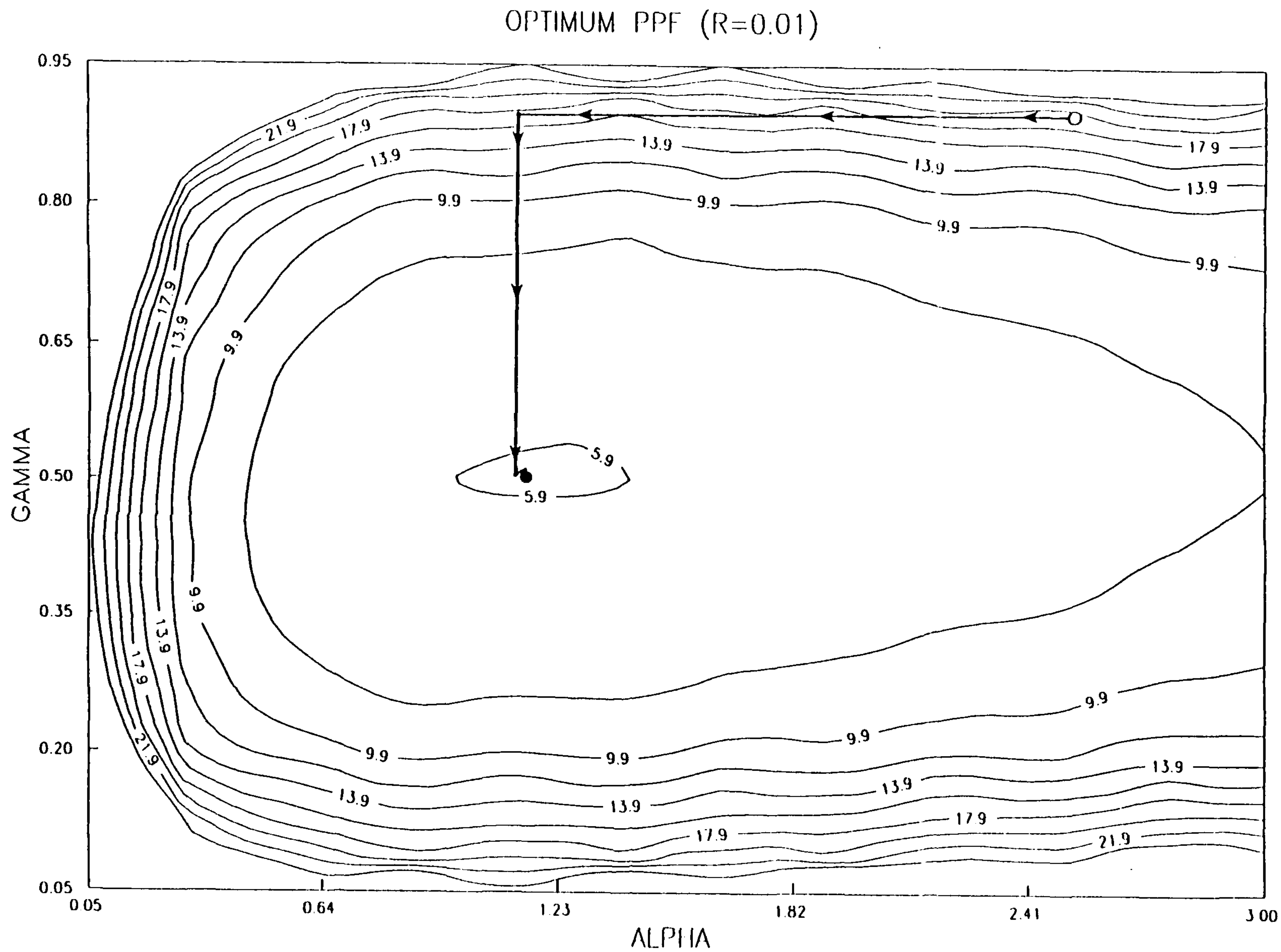

Figure (3) - Contour map and optimal path for R = 0.01.

optimal control gain γ_i to be equal to 0.5 and the **optimal** time constant τ_i of its filter such that

$$\tau_i = \alpha_i \; / \; \omega_i \qquad \text{for } i=1,\ldots, N \tag{19}$$

where N is the number of controlled modes and α_i is the optimal dimensionless filter time constant given in Table 1.

Figure (4) shows a flow chart of the proposed **OMPPF** algorithm. The algorithm performance is enhanced by augmenting it with a **"time sharing"** strategy to share a small number of actuators to control larger number of vibration modes. Such **"time sharing"** strategy has been shown[9-11] to be very effective in controlling large structures with a small number of actuators. This is unlike the classical **IMSC** method of Meirovitch[3,4] where the number of actuators needed must be equal to the number of modes to be controlled. The effectiveness of the **OMPPF** algorithm in damping the vibration of flexible systems is validated experimentally in the what follows.

4. EXPERIMENTAL PERFORMANCE OF OPTIMAL MPPF ALGORITHM

4.1 EXPERIMENTAL SET-UP

A thin rectangular cantilevered beam is constructed to validate the developed algorithm . The design parameters of the beam are given in Table 2. The beam is controlled by one piezo-electric bimorph made from G1195-ceramic. The actuator is available commercially (model number R205) from Piezo-Electric Products, Inc., Metuchen, NJ 08840-4015 . Table 3 lists the main design parameters of the actuator.

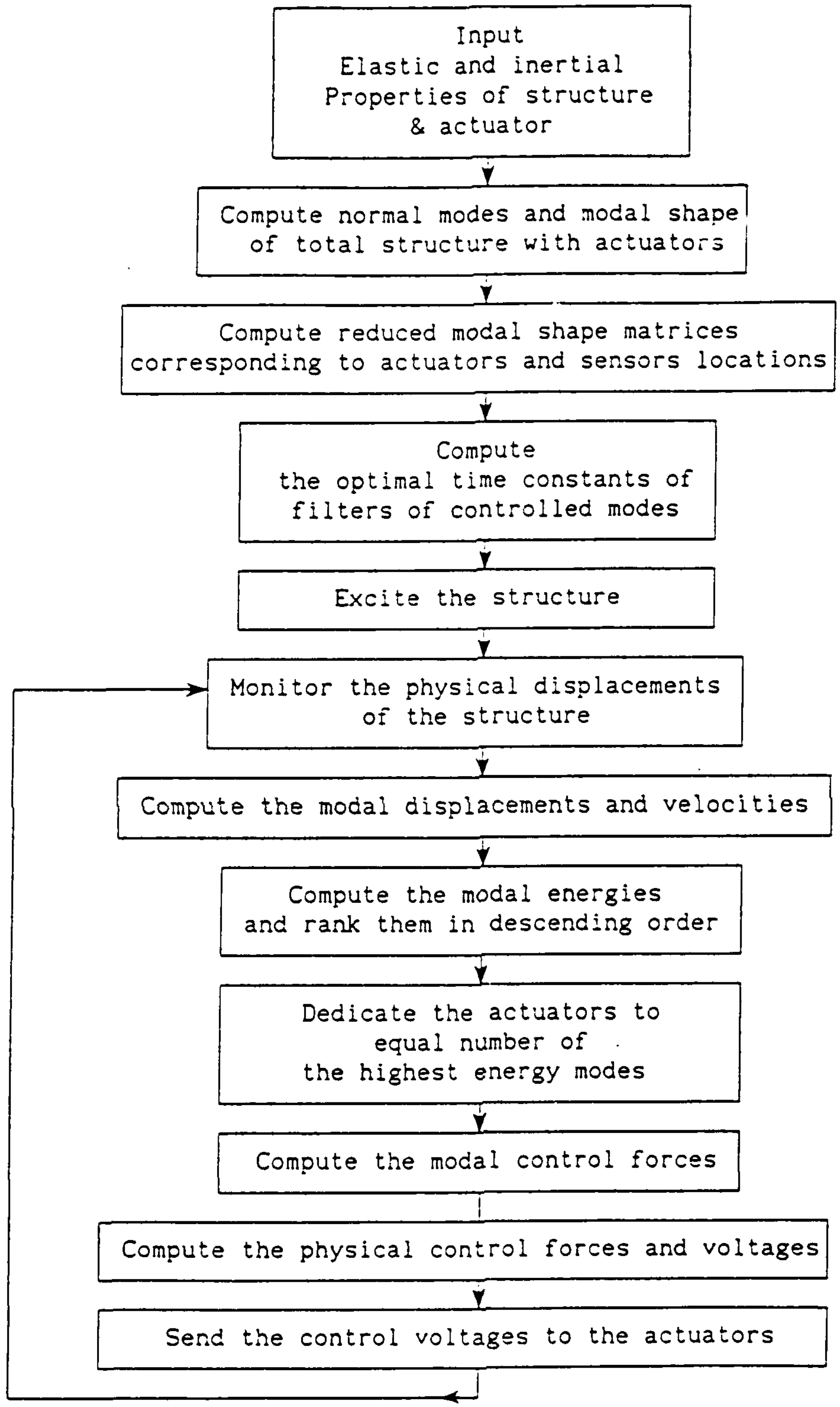

Figure (4) - Flow chart of the OMPPF algorithm.

The experimental beam and the piezo-actuator are arranged as shown in Figure (5). The beam is divided into three finite elements . Bonded to the first element, near the fixed end of the beam, is the piezo-actuator. Three non-contacting position sensors are used to monitor the physical displacements of the three nodes in the transverse direction. The position signals are sampled by a 386-based micro-processor provided with an input/output board which has a conversion time of 15 μs and a resolution of 12 bits. The board analog outputs have a settling time of 30 μs.

The micro-processor uses the three sampled signals to compute the beam angular deflections and the linear and angular velocities of the nodes . The computed state variables are used to calculate the modal coordinates of the flexible system, the mode that has the highest modal energy, the corresponding optimal modal control force $\mathbf{f}_i$, the physical control force $\mathbf{F}_c$ and the necessary voltage $\mathbf{v}$ to be sent to the piezo-actuator. The implementation of these calculations , i.e. the **OMPPF** algorithm , is carried out in real time in 3.04 ms.

4.2 Modal characteristics of the beam-actuator system

The modal characteristics of the experimental beam are determined theoretically[9] and validated experimentally using classical modal analysis technique. A comparison between the theoretical and the experimental values of the first five vibration modes of the beam-actuator system is given in Table 4. The table gives also the modal damping as calculated from the experimental results using the half power approach[17].

4.3 Experimental results

In all the experiments conducted in this study, the beam is

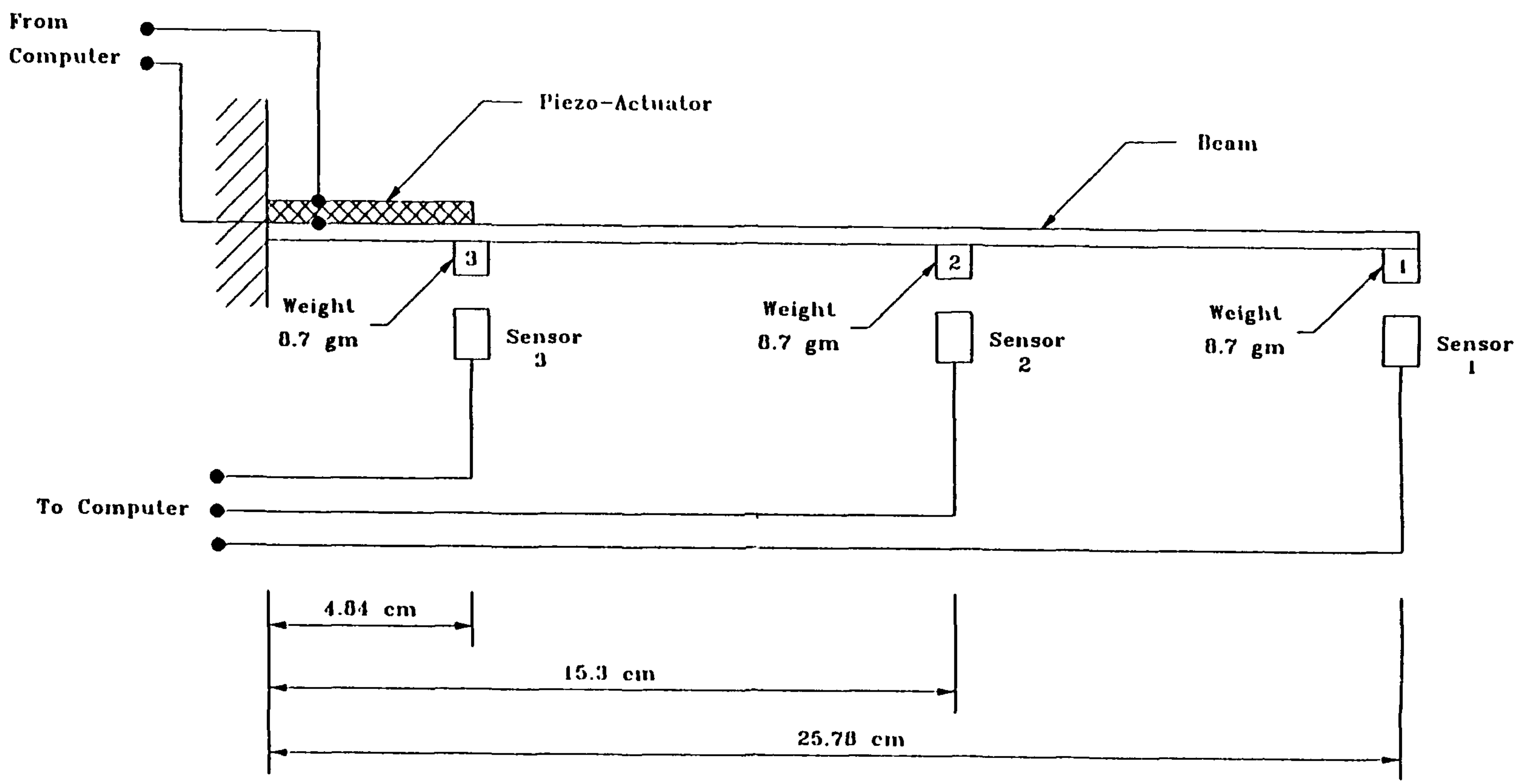

Figure (5) - Schematic drawing of the experimental beam, piezo-actuator and sensors.

excited at its second mode of vibration by applying sinusoidal excitations of 20 volts in magnitude to the piezo-actuator. The excitations are maintained for a period of 0.3 seconds. The beam is either left to vibrate freely (i.e. uncontrolled) or under the action of one modal control algorithm or another. The uncontrolled tip displacement, shown in Figure (6-a), is used as a datum for judging the effectiveness of the control algorithm.

Figures (6-b) and (6-c) show the corresponding time response of the beam when it is optimally controlled by the **OMPPF** algorithm with the weighting parameter **R** set at 0.01 and the piezo-actuator is dedicated either to the first mode alone or time shared between all the modes respectively. It is evident that time sharing the actuator is more effective in damping out the beam vibration. Such effectiveness comes about because the actuator is dedicated to control the mode that has the highest instantaneous modal energy. This is not necessarily the lowest mode of vibration as it depends on the nature of the external disturbance.

Figure (7-a) and (7-b) show the corresponding optimal control voltage sent to the piezo-actuator when it is used to control the lowest mode or when it is time shared between the modes respectively. The figures indicate that higher control voltage is needed when the actuator is time-shared between modes. This is attributed to the need for fast response filters to control higher order modes, as implied by equation (5), which results in turn in higher control actions as indicated by equation (6).

The effect of varying the weighting parameter **R** on the performance of the **OMPPF** algorithm, with its time sharing capability, is shown in Figure (8). Increasing **R** results in slower vibration damping as more emphasis is

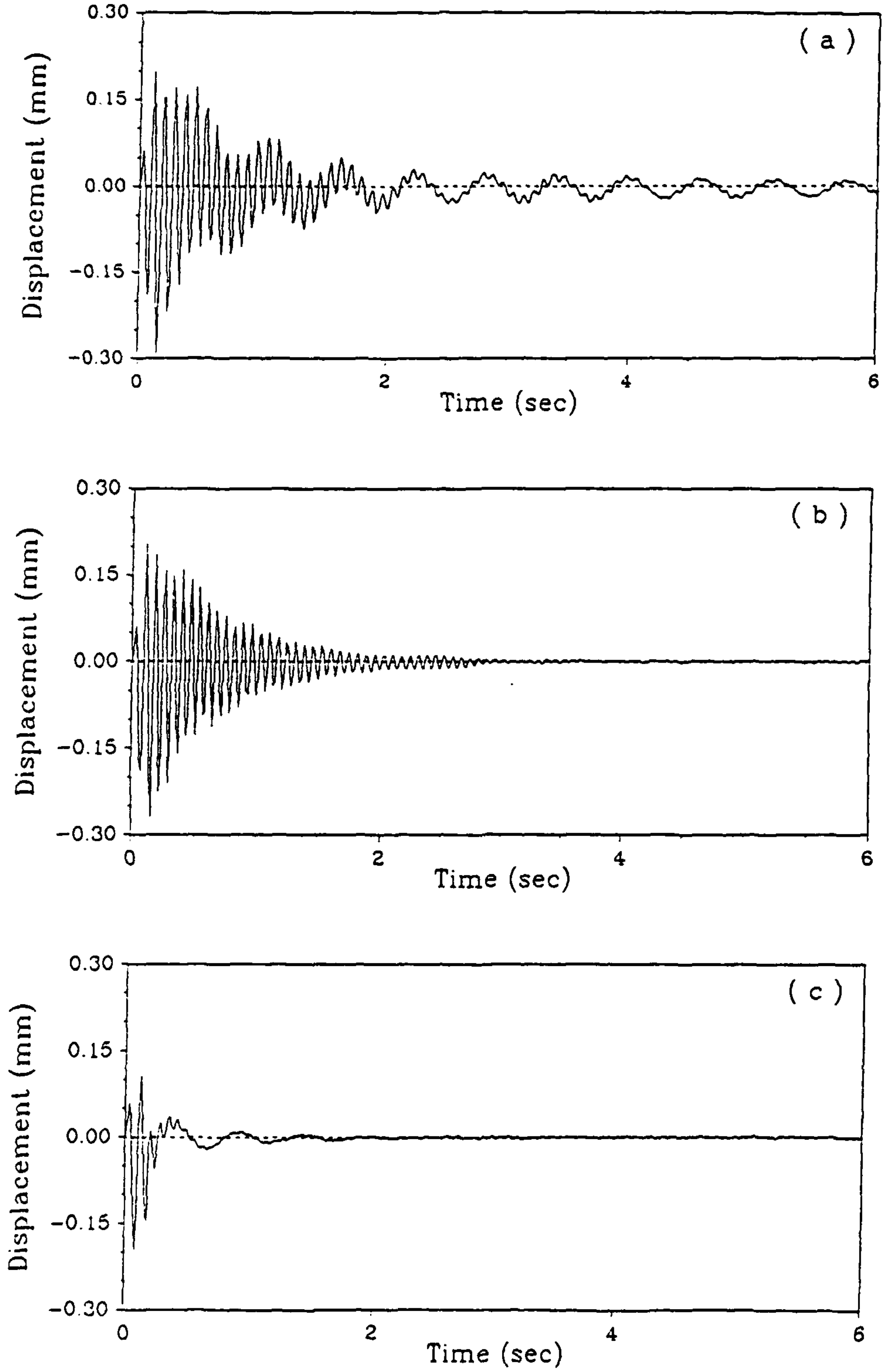

Figure (6) - Time response of beam
a. uncontrolled
b. optimally controlled without time sharing (R=0.01)
c. optimally controlled with time sharing (R=0.01)

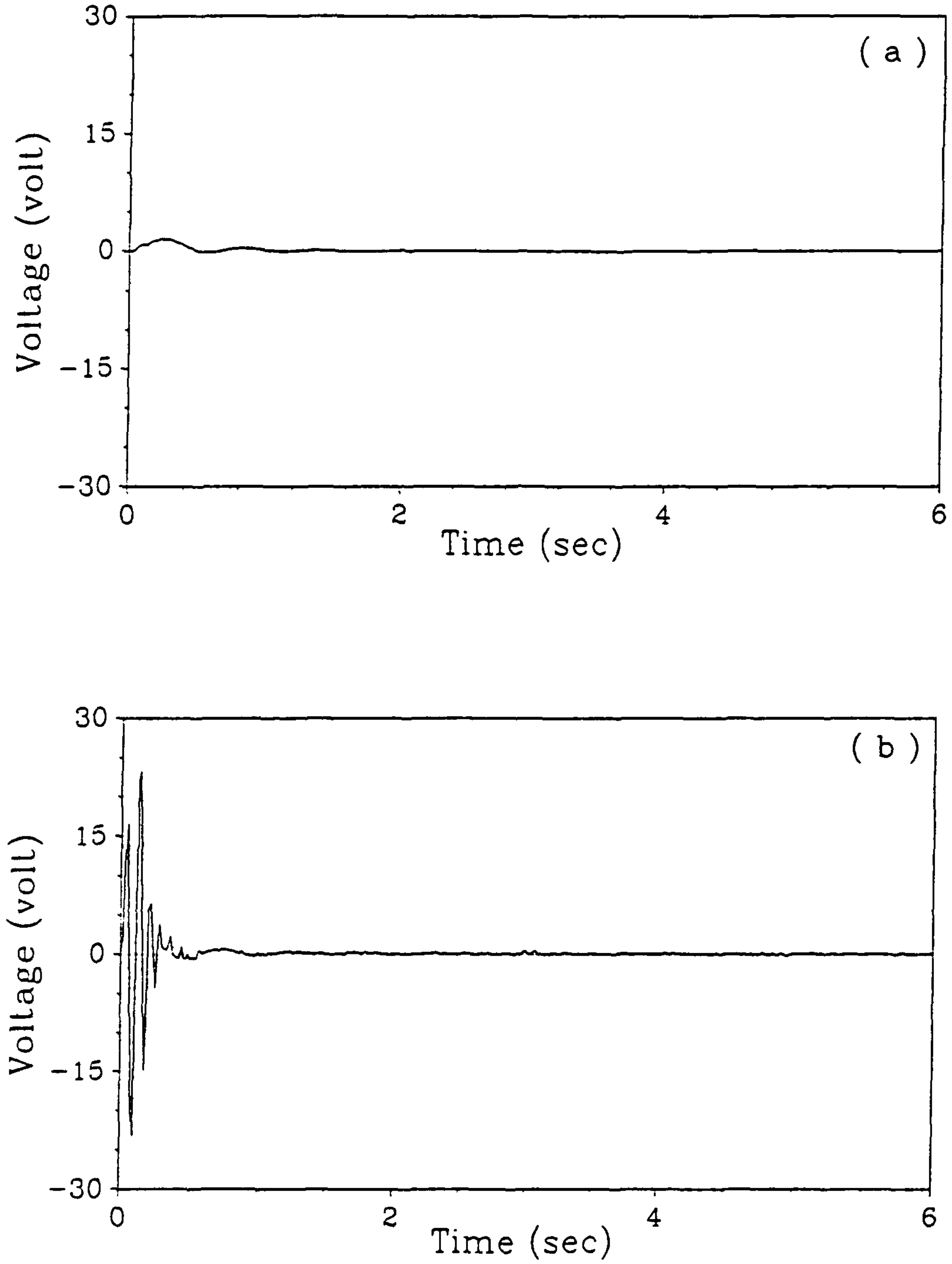

Figure (7) - Time history of the optimal control voltage
a. without time sharing (R=0.01)
b. with time sharing (R=0.01)

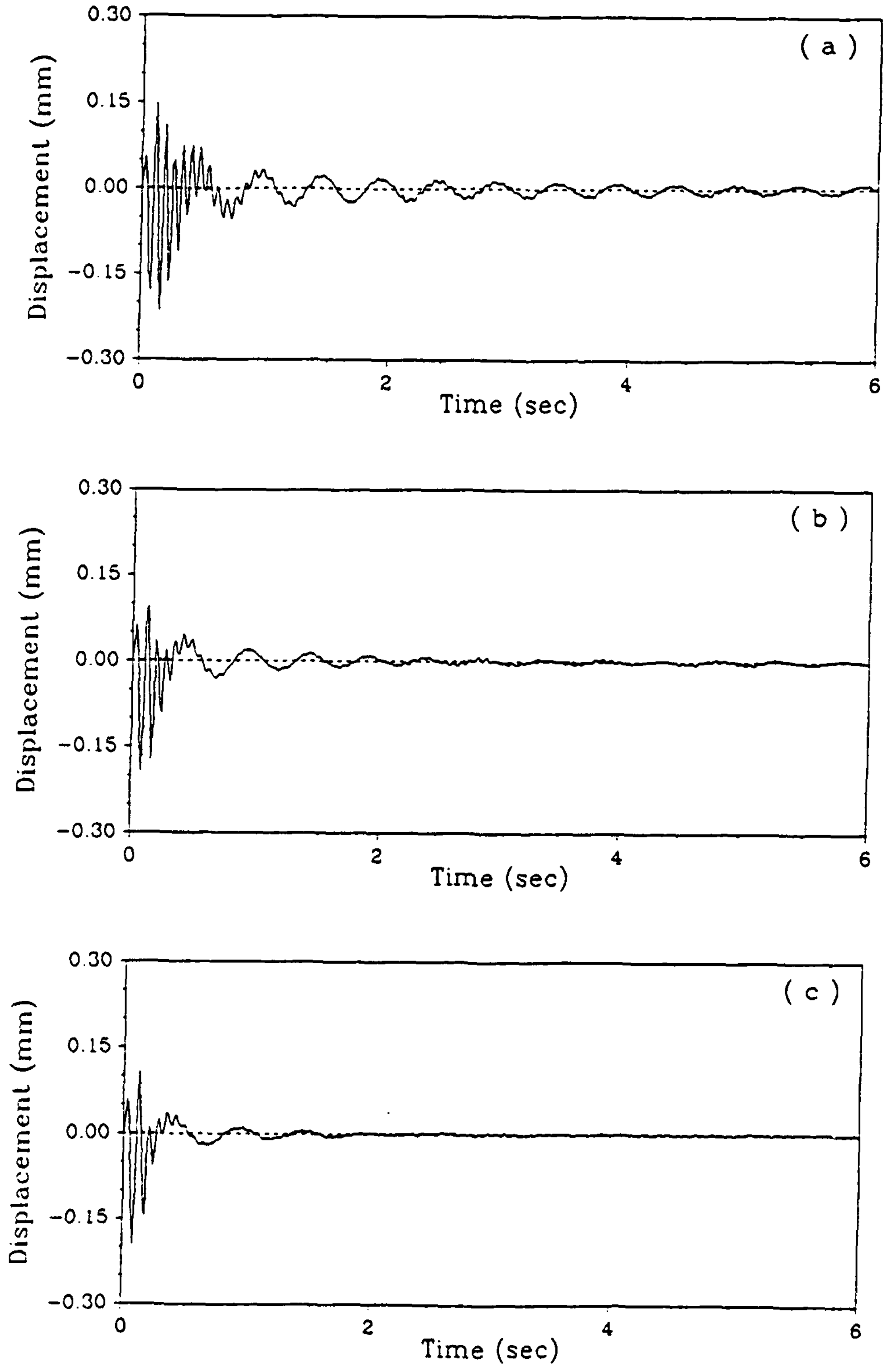

Figure (8) - Time response of the optimally controlled beam with time sharing
a. R=100, b. R=10 and c. R=0.01

placed on the importance of the control effort over the vibration energy. This emphasis is manifested by the decrease in the control voltages as **R** is increased as indicated in Figure (9).

A better insight into the effectiveness of the **OMPPF** algorithm can be gained by considering the Fast Fourier Transform (**FFT**) of the beam response. Figure (10) shows the frequency content of the response of the uncontrolled beam in comparison with the optimally controlled beam. These characteristics are obtained by sampling the beam tip position signal by a spectrum analyzer and performing on it an **FFT** analysis. The Figure emphasizes the effectiveness of the new algorithm particularly when **R** is increased and when it is augmented with the time sharing capability.

Comparisons between the theoretical and experimental time responses of the uncontrolled and optimally controlled beam (with **R**=0.01) are shown in Figures (11-a) and (11-b) respectively. The displayed results show close agreements between theory and experiments.

5. CONCLUSIONS

This study has presented an optimal modal control algorithm which is based on the Positive Position Feedback method. The algorithm utilizes only modal position signals, fed through first order filters, to damp out the vibration of undamped flexible systems. The theory behind the algorithm is presented. Optimal tuning of the filters and the controller gains are obtained, for all the controlled modes, using optimal control theory for systems with incomplete state feedback. The algorithm is validated experimentally using a single piezo-electric actuator to control the

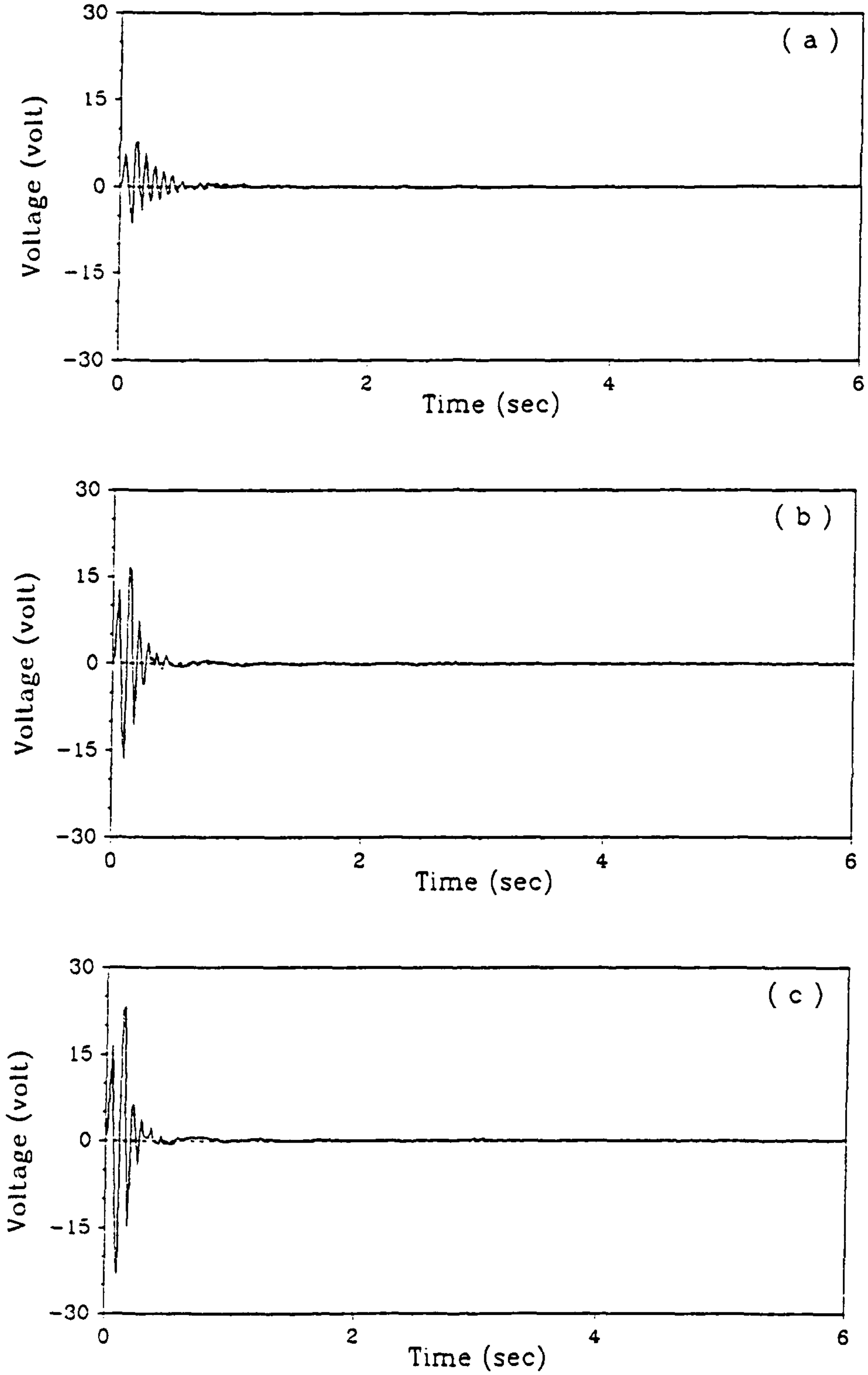

Figure (9) - Time history of the optimal control voltage with time sharing
a. R=100, b. R=10 and c. R=0.01

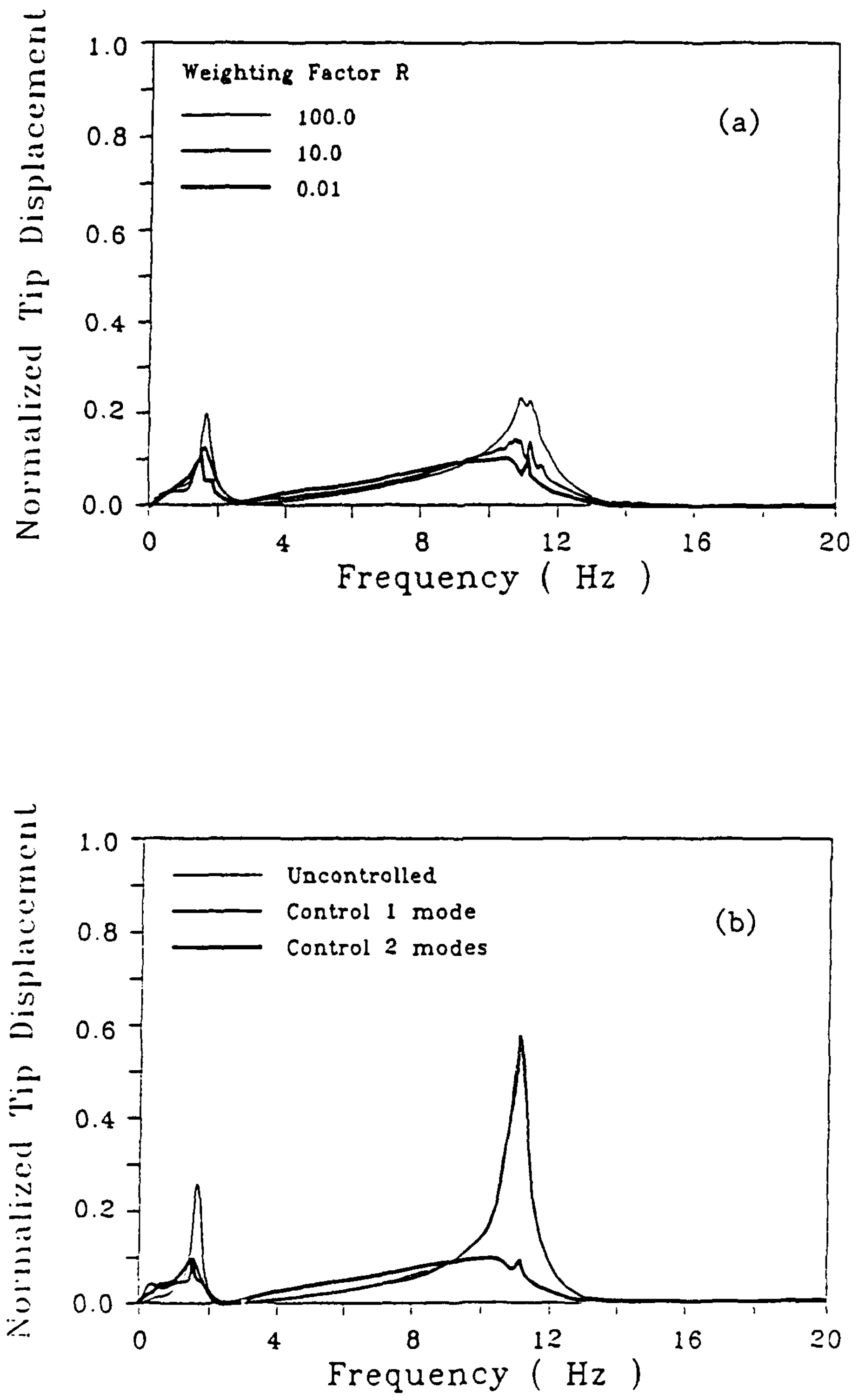

Figure (10)- Frequency response of optimally controlled beam
a. at different R
b. with and without time sharing

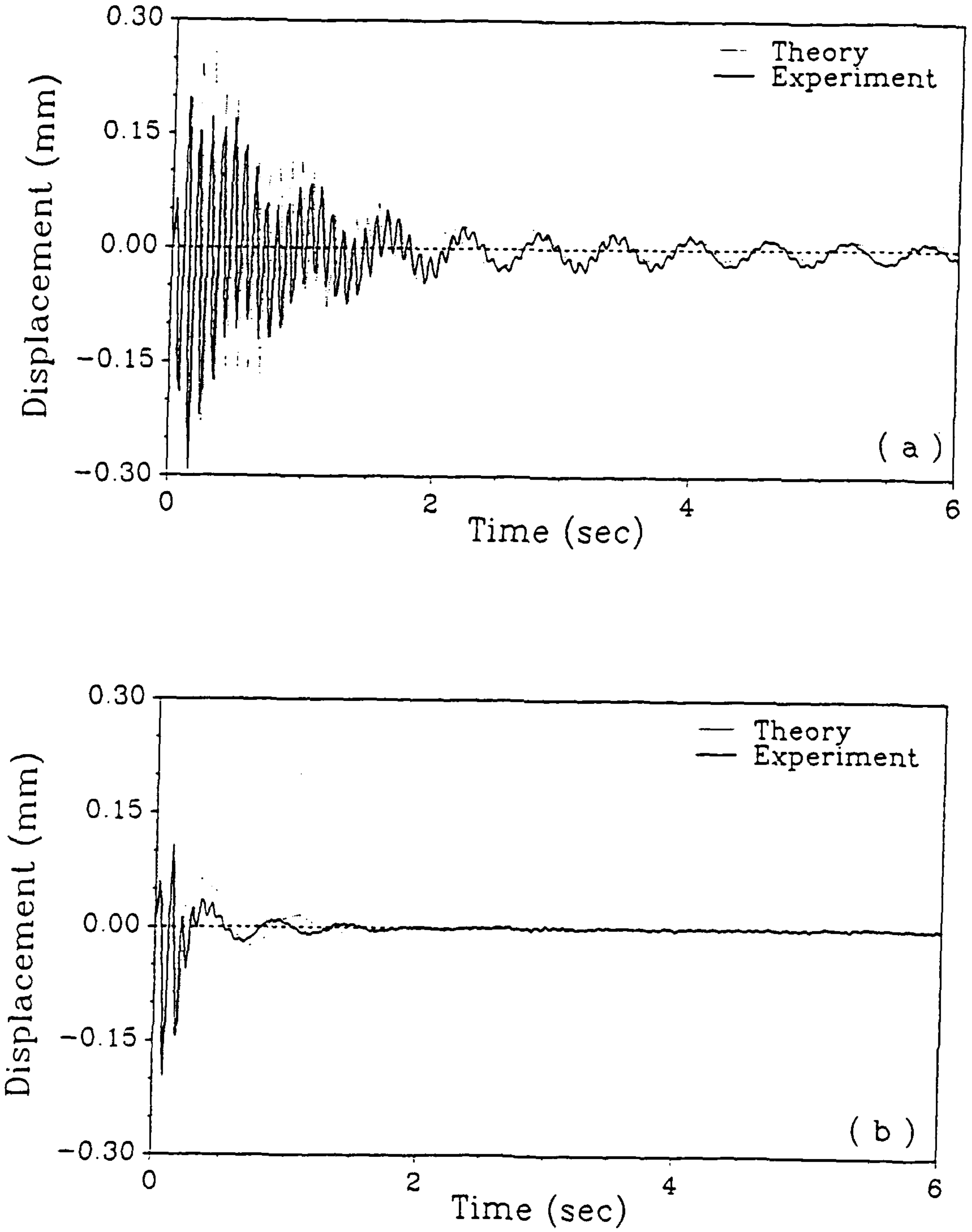

Figure (11)- Comparison between theoretical and experimental time response of the beam
a. uncontrolled and b. controlled with R=0.01

vibration of a flexible cantilevered beam. The results obtained indicate its effectiveness in suppressing structural vibration particularly when it is provided with **time sharing** capabilities.

The study demonstrates clearly the simplicity and potential of the method as an effective method for controlling large number of vibration modes with a smaller number of actuators . These features have important practical implications that make the algorithm viable for controlling large structures in real time.

ACKNOWLEDGEMENTS

This study was supported by a grant from the US Army Research Office (Grant number DAAL03-89-G-0084). Special thanks are due to Dr. Gary Anderson, the technical monitor and Chief of the Structures and Dynamics Branch of ARO, for his invaluable and continuous technical inputs.

REFERENCES

1. Balas, M., "Direct velocity feedback control of large space structures", *J. of Guidance and Control* **2**, 252-253 (1979).

2. Forward, R.L., "Electronic damping of orthogonal bending modes in a cylindrical mast", *Journal of Spacecraft* **18**, 11-17 (1981).

3. Meirovitch, L. and H.Baruh, "Control of self-adjoint Distributed - parameter systems", *Journal of Guidance and Control* **5** , 59-66 (1981).

4. Meirovitch, L., H.Baruh and H.Oz, " Comparison of Control Techniques for large flexible systems", *Journal of Guidance and Control* **6**, 302-310 (1983).

5. Goh, C.J. and T.K. Caughey, "On the stability problem caused by finite actuator dynamics in the collocated control of large space structures", *Int.J.Control*, 41, 787-802 (1985).

6. Baz,A., S.Poh and P.Studer, "Modified independent modal space control method for active control of flexible systems.*Journal of The Institution of Mechanical Engineers , Part C*, **203**, 103-112 (1989).

7. Baz, A and S.Poh, "Experimental implementation of the modified independent space control method", *Journal of Sound and Vibration*, **139**, **1**, 133-149 (1990).

8. Baz, A. and S.Poh, "Comparison between MIMSC, IMSC and PI in controlling flexible systems", *NASA Technical report number N*87-25605 (1987).

9. Baz, A., S.Poh and J.Fedor, "Independent modal space control with positive posiyion feedback", *ASME Journal of Dynamic systems, Measurements and Control*, **114**, **1**, 96-103 (1992).

10. Poh, A. and A.Baz, "Active control of a flexible structure using a modal positive position feedback controller", *Journal of Intelligent Material Systems and Structures*, **1**, **3**, 273-288 (1990).

11. Lewis, F.L. *Optimal Control*. John Wiley & Sons, Inc, New York, 1986.

12. Kalmann, R.E. and J.E.Bartram, "Control system analysis and design via the 'second' method of Lyapunov", *ASME Journal of Basic Engineering*, **82**, 371-400 (1960).

13. Jameson, A., "Optimization of linear systems of constrained configuration", *Intl. Journal of Control*, **11**, **3**, 409-421 (1970).

14. Moerder, D.D. and A.Calise, "Convergence of a numerical algorithm for calculating optimal output feedback gains", *IEEE Trans on Automatic Control*, **AC-30**, **9**, 900-903 (1985).

15. Meirovitch, L., *Computational methods in structural dynamics*, Sijthoff & Noordhoff, The Netherlands, 1980.

16. Reklaitis, G.V., A.Ravindran and K.M.Ragsdell, *Engineering optimization: Methods and applications*, John Wiley & Sons, Inc., New York, 1983.

17. Ewins, D.J., *Modal Testing : Theory and Practice*, Research Studies Press Ltd., Letchwoth, England, 1984.

APPENDIX - A

The Performance Index (M)

The performance index **M** is given by

$$\mathbf{M} = \max_{x_0} \; J \,/\, (X_o^T X_o) \tag{A-1}$$

This performance index normalizes the original performance index J with respect to the initial state of the system X_o. Substituting equation (13) into equation (A-1) gives:

$$\mathbf{M} = \max_{x_0} \; (X_o^T P(0) X_o) \,/\, (X_o^T X_o) \tag{A-2}$$

As **P** is symmetric, it has real eigen values λ_i and the corresponding eigen vectors ω_i may be formed as an orthonormal set. If **V** is the eigen vector matrix , then

$$\mathbf{V}^T \mathbf{V} = \mathbf{I}, \tag{A-3}$$

and

$$\mathbf{V}^T \mathbf{P(0)} \mathbf{V} = \Lambda \tag{A-4}$$

where Λ is a diagnoal matrix with elements λ_i. Assume that:

$$X_o = \mathbf{V} z \tag{A-5}$$

then,

$$J \,/\, (X_o^T X_o) = (X_o^T P(0) X_o) \,/\, (X_o^T X_o)$$

$$= (z^T \Lambda z) \,/\, (z^T z)$$

$$= (\sum \lambda_i z_i^2) \,/\, (\sum z_i^2) \tag{A-6}$$

but as,

$$\lambda_{min} \sum z_i^2 \le \sum \lambda_i z_i^2 \le \lambda_{max} \sum z_i^2 \tag{A-7}$$

then, from equations (A-1), (A-6) and (A-7) we have

$$\mathbf{M} = \lambda_{max} (\mathbf{P}) \tag{A-8}$$

A P P E N D I X - B

ELEMENTS OF MATRIX P

The matrix **P** is given by

$$\mathbf{P} = \begin{bmatrix} p_1 & p_2 & p_3 \\ p_2 & p_4 & p_5 \\ p_3 & p_5 & p_6 \end{bmatrix} \tag{B-1}$$

where the elements p_1 through p_6, which satisfy the steady-state Lyapunov equation (14), are given by

$$p_1 = p_3 - d_1\, p_5, \tag{B-2}$$

$$p_2 = d_2 \;/\; [\; 2d_1\; (1-d_1/d_2)\;], \tag{B-3}$$

$$p_3 = -\;(\; 1 \;/\; d_1 - d_1\, R\;) \;/\; 2, \tag{B-4}$$

$$p_4 = p_6 - d_2\, p_5 - p_3, \tag{B-5}$$

$$p_5 = p_2, \tag{B-6}$$

and

$$p_6 = -\;(\; d_2\, R \;/\; 2 - p_5 \;/\; d_2\;) \tag{B-7}$$

with R denoting a scalar weighting factor.

For a given d_1 and d_2, p_2 and p_3 can be calculated first, then P_5 followed by p_1, p_6 then p_4.

NOMENCLATURE

A	structure-filter system matrix (3x3)
B	input matrix (3x1)
C	output matrix (1x3)
D	fictitious controller gain matrix
d_1, d_2	fictitious controller gains
f_i	controlled modal force of the ith mode
F_c	Physical force vector
I	identity matrix (3x3)
J	performance index
K_i	controller gain
M	normalized performance index
P	matrix satisfying Lyapunov equation (3x1)
p_i	ith element of matrix P
Q	weighting matrix
$q_i, \dot{q}_i, \ddot{q}_i$	modal displacement, velocity and acceleration of ith mode
R	weighting parameter
T	final time
t	time
t^*	dimensionless time
u	control effort
v	voltage applied across actuator
ϑ_i	ith eigen vector of matrix P
V	eigen vector matrix of matrix P
X	state vector of structure-filter system (3x1)
X_o	initial state vector
y	system output
Y_i	the output of the ith filter
z	any vector (3x1)

Greek Symbols

α_i	dimensionless time constant of filters
γ_i	dimensionless gain of the controller
$\lambda_{max}, \lambda_{min}$	maximum and minimum eigenvalues of P matrix
Λ	matrix of eigen values of P (3x3)
τ_i	time constant of the ith mode
ω_i	frequency of the ith mode

Superscripts

1 dots on letter denote differentiation with respect to time
2 primes on letter denote differentiation with respect to dimensionless time

Table 1 - optimal values of γ_i and α_i for different **R**

R	0.01	1.00	10.00	100.00
α_i	1.139	1.043	0.598	0.1999
γ_i	0.505	0.503	0.5001	0.4988

Table 2 - Main design parameters of test beam

Length (cm)	Width (cm)	Thickness (cm)	Young's modulus (GN/m^2)	density (gm/cm^3)
25.78	3.75	0.075	2.96	1.31

Table 3 - Main design parameters of the actuator

Length (cm)	width (cm)	thick. (cm)	charge coeff. (m/v)	max. volt (v/mil)	Young's mod. (GN/m^2)	density (gm/cm^3)
4.85	1.375	0.1	190×10^{-12}	25	63	7.8

Table 4 - Modal characteristics of the beam system

Mode number	1	2	3	4	5
Theor. mode - Hz	1.62	11.0	64.7	87.4	157.7
Exper. mode - Hz	1.55	10.1	49.5	80.5	167.5
Error - %	4.3	8.1	23.5	7.9	-6.2
Modal damping	.038	.022	.016	.015	.010

SUPPLEMENTARY

INFORMATION

vibration of the beam when all the four NITINOL fibers are activated or unactivated. It is evident that the activation of the NITINOL fibers shifts the first three modes of vibration to higher frequency bands and that the enhanced damping characteristics of the heated beam result in considerable vibration attenuation for all the modes.

A summary of the amplitude attenuation obtained at different flow speeds is given in Figure (33). Attenuations of about 40% are observed for the three modes of vibration over the speed range considered.

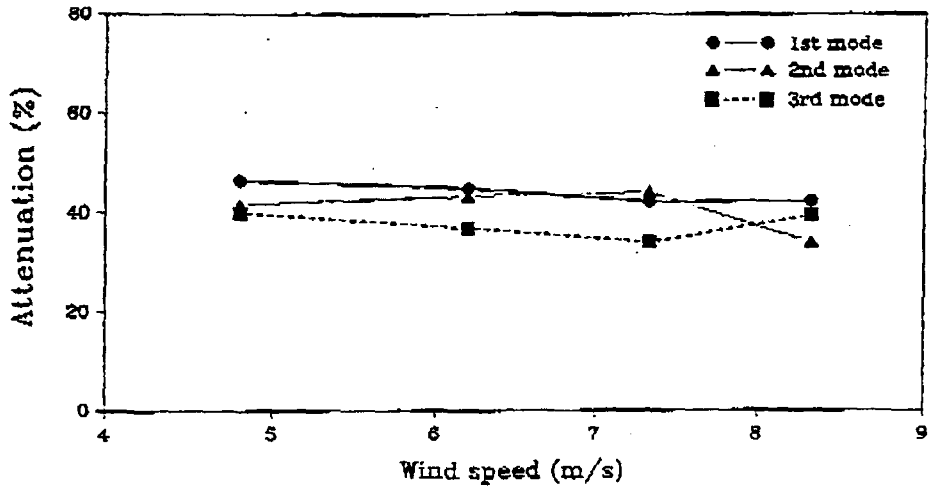

Figure (33) - Amplitude attenuation at different flow speeds

The effect of activating different number of fibers on the attenuation of the flow-induced vibrations is shown in Figure (34) at flow speed of 8.32 m/s. Increasing the number of activated fibers results in a proportionate reduction in the amplitude of vibration.

A summary of the effect of number of activated NITINOL fibers on the amplitude of vibration normalized with respect to the amplitude of vibration of the uncontrolled beam, is shown in Figure (35).

The results obtained demonstrate the effectiveness of NITINOL-reinforced composites in suppressing flow-induced vibrations over a wide range of flow speeds.

5. SUMMARY

The static, dynamic and thermal characteristics of NITINOL-reinforced composite beams have been presented. The fundamental issues governing the behavior of this new class of SMART composites have been introduced. Applications of NITINOL reinforcing fibers in the control of buckling and flow-induced vibrations are successfully demonstrated.